The spectroscopic properties of melanin

A thesis submitted for the degree of Doctor of Philosophy
to the University of Queensland
November 2007

Jennifer Riesz
Physical Sciences

Typeset in LaTeX 2_ε.

Statement of my contribution to jointly-published work and contributions by others

Chapter 2: The broadband absorption spectrum of melanin

The broad ideas presented in this chapter were also summarised in the publication "P. Meredith, B. J. Powell, J. J. Riesz, S. Nighswander-Rempel, M. R. Pederson and E. Moore. *Towards structure-property-function relationships for eumelanin*, Soft Matter **2**, 37 (2006)". The discussion in that publication is largely by Paul Meredith (with contributions from Ben Powell), but the discussion presented in this thesis is my own and figures are attributed as referenced.

Chapter 3: The structure of melanin

The work presented in this chapter came out of many in-depth discussions with my supervisors Paul Meredith, Ross McKenzie and Ben Powell. I performed the majority of the literature searching and research under their guidance and wrote the review presented here. I was not involved in the TEM work that is presented in this chapter, and include it merely to show a complete representation of the advances in this area.

Chapter 4: Quantitative scattering of eumelanin solutions

This chapter is an almost complete representation of the publication "J. Riesz, J. Gilmore and P. Meredith. *Quantitative scattering of melanin solutions*. Biophysical Journal **90(11), 1 (2006)**". The idea for this work was my own, and the theory was developed in close collaboration with Joel Gilmore. I designed the experimental setup and performed all measurements, and did all of the data manipulation to produce the figures included. Paul Meredith was involved throughout with discussion of the data and review of written work. I wrote the published paper, and the discussion included in this thesis is very similar (with some exceptions where material was repeated earlier in the introductory sections).

Chapter 5: The dipole strength of eumelanin

This chapter is an almost complete representation of the publication "J. Riesz, J. Gilmore, R. H. McKenzie, B. J. Powell, M. R. Pederson and P. Meredith. *The transition dipole strength of melanin*. Submitted to Physical Review E (2007)". This work was inspired by discussion between myself, Ross McKenzie, Ben Powell and Paul Meredith. The theory and modifications to NRLMOL to perform dipole strength calculations were developed in close collaboration with Mark Pederson during my two week visit to his laboratory in 2005. I performed all data manipulations and analysis, with input of thoughts and ideas from Ross McKenzie, Ben Powell, Paul Meredith and Joel Gilmore during our many meetings to discuss this work. I wrote the final publication, and Paul Meredith made modifications to the introductory section. Joel Gilmore contributed a paragraph on solvent effects. The discussion included in this thesis is very similar to the published paper (with some exceptions where material was repeated earlier in the introductory sections).

Chapter 6: The challenge of spectroscopy with melanin

This chapter follows closely work that has been published as "P. Meredith and J. Riesz. *Radiative relaxation quantum yields for synthetic eumelanin.* Photochemistry and Photobiology **79(2)**, 211 (2004)". The idea for this work was Paul Meredith's, and I performed all measurements and data manipulation. The correction procedure was developed in close collaboration between myself and Joel Gilmore. The publication was written by Paul Meredith with figures produced by myself; however the discussion presented in this thesis is my own.

Chapter 7: The radiative quantum yield map

This chapter follows closely work that has been published as "S. Nightswander-Rempel, J. Riesz, J. Gilmore and P. Meredith *A quantum yield map for synthetic eumelanin.* The Journal of Chemical Physics **123**, 194901 (2005)". This work was inspired by discussions between myself and Joel Gilmore, in which we jointly developed the theory reported. I developed the experimental method (with some assistance from Joel Gilmore for data retrieval) and took the initial measurements. The data was discussed at meetings attended by Paul Meredith, Joel Gilmore and Stephen Nighswander-Rempel, all of whom contributed their ideas and thoughts. Several later repetitions of these measurements were taken by Stephen Nighswander-Rempel, and he performed subsequent data processing according to the theory developed by Joel and myself to produce figures 7.2, 7.3, 7.7 and 7.6. I wrote an early draft of the publication with a detailed description of the theory and some introductory material and discussion of results; this draft was later refined and added to by Stephen Nighswander-Rempel. The discussion in the published paper is largely Stephen's, although the discussion included in this thesis is entirely my own.

Chapter 8: Radiative relaxation in synthetic pheomelanin

This chapter is an almost complete representation of the publication "J. Riesz, T. Sarna and P. Meredith. *Radiative relaxation in synthetic pheomelanin.* Journal of Physical Chemistry B. **110(28)**, 13985 (2005)". This work was inspired by Tadeusz Sarna's offer of a sample of pheomelanin for us to perform some measurements on. I performed all measurements and data manipulation, and discussed the results with Paul Meredith. I wrote the final publication with assistance and review from Paul Meredith (and contributions from Tadeusz Sarna), and the discussion included in this thesis is very similar (with some exceptions where material was repeated earlier in the introductory sections).

Chapter 9: Quantitative spectroscopy of DHICA, a key eumelanin monomer

Indu Mahadevan synthesised and characterised the DHICA samples which were used for spectroscopic analysis, and wrote the paragraphs included here describing the process. I thought of and designed the spectroscopic work as a summer project for an undergraduate student (Aaron Coutts). Coutts was supervised by Paul Meredith on a weekly basis, and I provided daily (constant) mentorship and training. The experimental measurements were

taken by Coutts. Coutts performed some of the data manipulation and analysis under my guidance, and I did the rest to create the figures included in this chapter. The analysis of these figures was discussed at meetings of myself with Paul Meredith, Ross McKenzie, Ben Powell and Joel Gilmore. We later enlisted the assistance of Seth Olsen who performed a series of sophisticated calculations to develop the theory summarised briefly in this chapter, and published as "S. Olsen, J. Riesz, I. Mahadevan, A. Coutts, J. P. Bothma, B. J. Powell, R. H. McKenzie, S. C. Smith and P. Meredith. *Convergent proton-transfer photocycles violate mirror-image symmetry in a key melanin monomer.* Journal of the American Chemical Society (2007)". This publication included several of the figures I created which are included in this chapter.

Chapter 10: Spectroscopic observation of eumelanin formation

I thought of and designed this work as a summer project for an undergraduate student (Aaron Coutts). Coutts was supervised by Paul Meredith on a weekly basis, and I provided daily (constant) mentorship and training. Approximately three quarters of the experimental measurements were taken by Coutts (with the rest taken by myself after his vacation scholarship ran out). Coutts performed some of the data manipulation and analysis, and I did the rest to create the figures included in this chapter.

Chapter 11: Inelastic neutron scattering spectroscopy

Paul Meredith thought of this work and obtained funding for us both to travel to the ISIS facility to perform these measurements. I prepared all the samples and performed all the INS measurements under the close supervision and expert guidance of John Tomkinson. I performed the inital literature review and analysis of the INS results for indole, which were later completed in a much more sophisiticated manner by John Tomkinson, published as "J. Tomkinson, S. Parker, J. Riesz and P. Meredith. *The vibrational spectrum of indole: an inelastic neutron scattering study.* J. Biomolecular Structure and Dynamics (2006)". The work included in this thesis is a summary of that publication in my own words. I analysed the results for the other molecules listed, with a large amount of assistance and training from John Tomkinson via email. These results will soon be submitted for publication as "J. Riesz, J. Tomkinson, I. Mahadevan, and P. Meredith. *Inelastic neutron scattering of indole-2-carboxylic acid and DHICA (dihydroxyindole-2-carboxylic acid), a key melanin monomer* (2007)". This has been largely written by myself (with paragraphs contributed by John Tomkinson and Ben Powell on the computational and experimental methods). The work included here follows this publication very closely.

Statement of originality

Except where acknowledged in the Statement of Contribution to Jointly-published Work and Statement of Contribution by Others, the material presented in this thesis is, to the best of my knowledge, original and has not been submitted in whole or part for a degree in any university.

Jennifer Riesz
Author

Assoc. Prof. Paul Meredith
Principal Advisor

Acknowledgements

Huge thanks must go to Joel Gilmore for all of his intellectual contributions to the work included here, and his constant willingness to help with any problem, no matter how big or how small. I believe that collaboration with Joel produced the best work included in this thesis. Also, I owe a massive thank-you to Paul Meredith for all his leadership and support over the years; he has been an excellent PhD advisor, and I would certainly recommend him to my friends and respected peers. I cannot emphasise enough how significant Paul's contribution has been towards making my PhD an enjoyable and extremely productive learning experience. Thank-you also to my advisors Ross McKenzie and Ben Powell for their time spent sharing their expert knowledge, and for always keeping me focused on the big questions. John Tomkinson's expert assistance with the INS analysis was invaluable, and the work would not have been possible without his patience and ongoing enthusiasm. Thank-you to Aaron Coutts for being a wonderfully patient and careful summer student, and to Jacques Bothma for his consistently inspiring and enlightening conversations (I look forward to seeing the impressive contributions that Jacques is going to make wherever he ends up). Thank-you also to Paul Cochrane for the use of his thesis layout and style files. This work has been supported by the Australian Research Council (ARC), the UQ Centre for Biophotonics and Laser Science, and the University of Queensland (RIF scheme), the ARC Linkage Scheme, the AMRF fund through DEST, the Queensland Smart State PhD scholarship program and an Australian Postgraduate Award.

List of Publications

- P. Meredith and J. Riesz *Radiative relaxation quantum yields for synthetic eumelanin.* Photochemistry and Photobiology **79(2)**, 211-216 (2004)
- J. Riesz, J. Gilmore and P. Meredith *Quantitative photoluminescence of broad band absorbing melanins: a procedure to correct for inner filter and re-absorption effects.* Spectrochimica Acta A **61(9)**, 2153-2160 (2005)
- P. Meredith, B. J. Powell, J. Riesz, R. Vogel, D. Blake, S. Subianto, G. Will and I. Kartini *Broad Band Photon-harvesting Biomolecules for Photovoltaics.* in Artificial Photosynthesis: From Basic Biology to Industrial Application (ed: A.F. Collings and C. Critchley) **Ch3**, p37 (2005)
- Stephen Nighswander-Rempel, J. Riesz, Joel Gilmore, and Paul Meredith *A quantum yield map for synthetic eumelanin.* The Journal of Chemical Physics **123**, 194901 (2005). Also selected for the November 15 issue of Virtual Journal of Biological Physics Research.
- Stephen Nighswander-Rempel, J. Riesz, Joel Gilmore, Jacques Bothma and Paul Meredith *Quantitative fluorescence excitation spectra of synthetic eumelanin.* Journal of Physical Chemistry B **109(43)**, 20629-20635 (2005)
- Paul Meredith, Ben Powell, J. Riesz, Stephen Nighswander-Rempel, Mark Pederson and Evan Moore *Towards structure-property-function relationships for eumelanin.* Soft Matter **2**, 37-44 (2006)
- J. Riesz, Tadeusz Sarna, and Paul Meredith *Radiative relaxation in synthetic pheomelanin.* Journal of Physical Chemistry B **110(28)**, 13985-13990 (2005)
- J. Riesz, Joel Gilmore, Paul Meredith *Quantitative scattering of melanin solutions.* Biophysical Journal **90(11)**, 1-8 (2006)
- J. Tomkinson, S. Parker, J. Riesz, P. Meredith *The vibrational spectrum of indole: an Inelastic Neutron Scattering study* (in press, J. Biomolecular Structure and Dynamics) (2006)
- S. Olsen, J. Riesz, B. J. Powell, R. H. McKenzie, S. Smith, I. Mahadevan, P. Meredith *Dual excited state intermolecular proton transfer photocycles explain mirror image rule violation in a key eumelanin monomer* (Accepted as rapid communication in Journal of the American Chemical Society (JACS)) (2007)

- J. Riesz, J. Gilmore, R. H. McKenzie, B. J. Powell, M. Pederson, P. Meredith *The transition dipole strength of eumelanin* (in press, Physical Review E) (2007)

Abstract

Melanin exhibits a broadband absorbance spectrum that appears to be unique amongst functional biomolecules. Explaining the origin of this spectrum is one of the primary challenges facing this field. Three main theories have been proposed: 1) The optical density is due to scattering, 2) Melanin is an amorphous semiconductor which then naturally exhibits broadband absorbance, or 3) Melanin has a large amount of chemical heterogeneity (or disorder) which leads to a broadband absorbance spectrum through superposition of the absorbance spectra of many species (the chemical disorder model). We discuss these models and the experimental evidence for each. We report direct experimental evidence that the optical density is not a consequence of scattering processes, and is due to true absorbance. Distinguishing between the two remaining explanations leads us to a discussion of the molecular structure of melanin, an issue which remains unresolved. We include a literature review, summarising the important structural findings for melanins, and conclude that the evidence suggests that melanin consists of a heterogeneous collection of small oligomers, which points towards the chemical disorder explanation for broadband absorbance. We caution, however, that the amount of chemical disorder obviously prevalent in this system is often neglected in discussions of the structure of melanin. We show that the oscillator strengths of melanin and its fundamental components are naturally explained by the chemical disorder model, as are their emission and excitation spectra and their radiative quantum yields. We show that the emission properties of melanin are not consistently reported in the literature, which is in part due to the strong re-absorption that occurs in this system, and we emphasise the importance of correcting for this effect in any measurement of the fluorescence of melanin. The emission properties of synthetic pheomelanin are reported, and are found to be different to those for eumelanin, suggesting different energy dissipation processes for these pigments. We also report a careful study of the spectroscopic properties of DHICA (5,6-dihydroxyindole-2-carboxylic acid), a key melanin monomer, and propose, based on these results, that proton transfer processes contribute to energy dissipation in this molecule. The radiative yield of melanin is measured to be extremely small ($< 0.1\%$), which is consistent with melanin's biological role as a photoprotectant, and suggests that non-radiative energy dissipation processes are very important for melanin. As a result of this finding we measure the vibronic structure of eumelanin related molecules using inelastic neutron scattering and accurately assign the vibrational modes using density functional theory calculations. This provides an important first step towards understanding the non-radiative processes in melanin energy dissipation and its biological functionality.

Contents

List of Figures

List of Tables

List of Abbreviations

General:

ESIPT	excited state intramolecular proton-transfer
FWHM	full width at half maximum (of a gaussian)
HOMO	highest occupied molecular orbital
IRF	instrument response function (time resolved spectroscopy)
LUMO	lowest unoccupied molecular orital
PL	photoluminescence (fluorescence as a function of emission energy)
PLE	photoluminescence excitation (fluorescence as a function of excitation energy)
UV	ultra-violet

Experimental techniques

AFM	atomic force microscopy
EELS	electron energy loss spectroscopy
HPLC	high performance liquid chromatography
HRTEM	high resolution transmission electron microscopy
INS(S)	inelastic neutron scattering (spectroscopy)
IR	infrared (spectroscopy)
MALDI	matrix assisted laser desorption/ionization (mass spectrometry)
NEXAFS	near edge X-ray absorption fine structure
NMR	nuclear magnetic resonance
SANS	small angle neutron scattering

SAXS	small angle x-ray scattering
SEM	scanning electron microscopy
TEM	transmission electron microscopy
TLC	thin-layer chromatography
WAXS	wide angle x-ray scattering

Computational terminology:

DFT	density functional theory
G98	gaussian98 (density funtional theory software)
GGA	generalised gradient approximation
NRLMOL/NL	naval research laboratory molecular orbital library (density functional theory software)
PBE	perdew, burke and ernzerhof (exchange correlation functional)
PP	porezag-pederson (density functional theory basis sets)
TDDFT	time dependant density functional theory

Chemical compounds:

CDM	cysteinyldopa-melanin (synthetic pheomelanin)
DHI	5,6-dihydroxyindole (an eumelanin monomer)
DHICA	5,6-dihydroxyindole-2-carboxylic acid (an eumelanin monomer)
DM	dopa-melanin (eumelanin synthesised by oxidative polymerisation of dopa)
DMF	dimethyl formamide (organic solvent)
DMSO	dimethyl sulfoxide (organic solvent)
Dopa	dihydroxyphenylalanine
EDTA	ethylenediamine tetraacetic acid
ICA	indole-2-carboxylic acid
PBSA	phosphate-buffered saline (without calcium and magnesium)

1

Introduction

Melanin is a dark biological pigment found throughout nature. It is a predominantly indolic macromolecule [1], although the name conveys no chemical information, and means simply 'black' [2]. There are many different types of melanin, including eumelanin, pheomelanin, neuromelanin and allomelanin. Eumelanin and pheomelanin are both found in the skin, hair and eyes of many animal species, including humans, where they act as photoprotectants (absorbing harmful ultraviolet and visible radiation). Eumelanin is known to be a macromolecule of 5,6-dihydroxyindole (DHI) and 5,6-dihydroxyindole-2-carboxylic acid (DHICA), and is black to brown in colour [3]. Eumelanin is the most extensively studied of all melanins since it is the primary pigment found in human skin, although it also forms the major component of squid ink and is responsible for the dark colouration in feathers [4]. Pheomelanin is a sulfur containing macromolecule composed of 1,4-benzothiazine units, and is red to yellow in colour (pheomelanin is responsible for the colouration of human red hair and chicken feathers [5, 6]). This thesis deals largely with eumelanin, although pheomelanin will be discussed in more detail in chapter 8.

The other varieties of melanin (including allomelanins and neuromelanins) shall not be dealt with in detail in this thesis, but briefly allomelanins are pigments found largely in plants such as certain fungi and seeds, and also in soil. Neuromelanin is found in the brainstem and inner ear of humans and higher primates where its role is unknown, although it is thought to have some biological significance; neuromelanin is decreased or absent in individuals with Parkinson's disease, for example [7, 8]. It is not clear whether the relationship between neuromelanin and Parkinson's disease is causal, although it is suggested that the pigment might modulate neurotoxic processes through interaction through iron, binding of drugs or reaction with free radicals and free radical producing species [9]. Additionally, albinism often leads to deafness in animals, suggesting biological functionality [10].

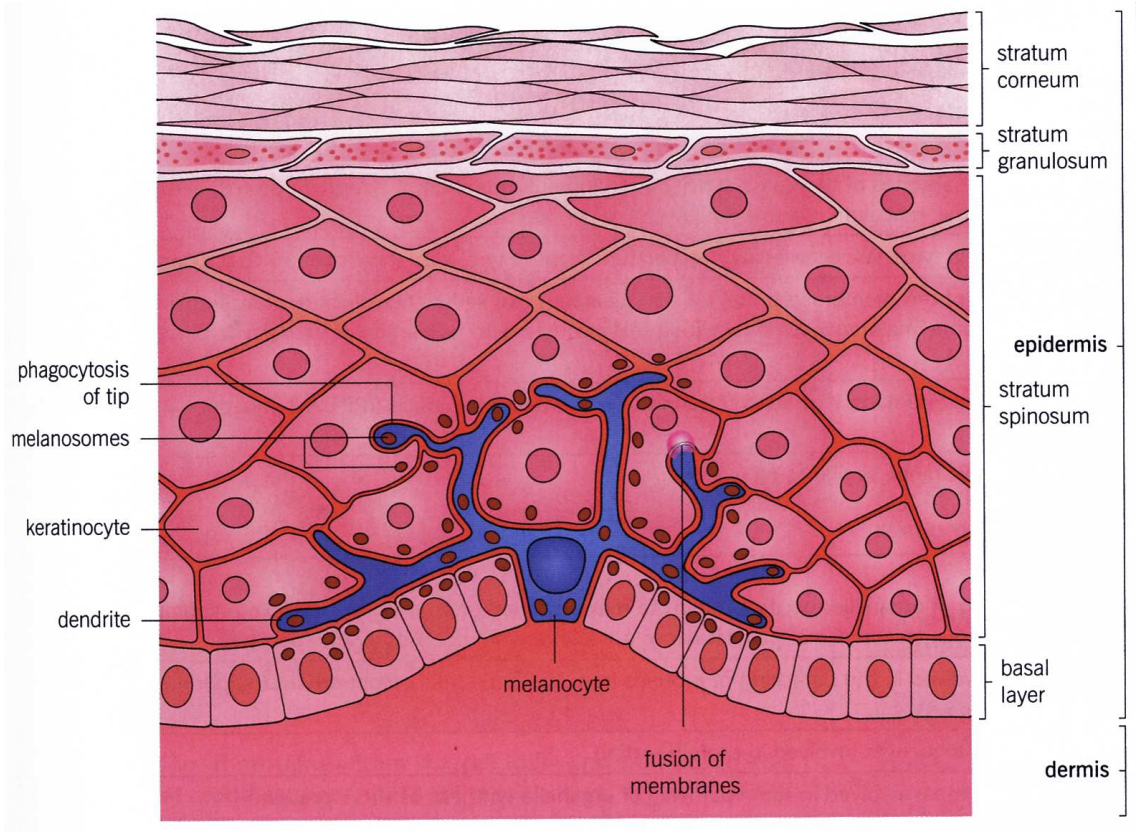

FIGURE 1.1: A melanocyte residing in the basal layer of the epidermis. In normal skin, approximately every tenth cell in the basal layer is a melanocyte. Melanosomes are transferred from the dendrites of the melanocyte into neighbouring keratinocytes (from [14]).

1.1 Melanin in human skin

Three main pigments contribute to the colour of healthy human skin: melanin, oxygenated haemoglobin (red) and reduced haemoglobin (blue); absorption spectra of these are shown in figure 2.2. Of these, it is the size, type and distribution of melanin particles that varies between individuals and leads to differences in colouration.

A cross section of human skin is shown in figure 1.1. The stratum corneum is approximately 0.01 to 0.02 mm thick and consists mainly of dead cells which scatter light but do not have significant absorbance for wavelengths longer than 300 nm (for wavelengths shorter than 300 nm protein and nucleic acid absorption become significant). Below this lies the stratum spinosum, which is 0.027 to 0.15 mm thick. This is the layer that contains melanin pigment in cells called keratinocytes. Below the stratum spinosum is the dermis, which is 0.6 - 3 mm thick [11, 12]. Melanin is synthesised in specialised cells called melanocytes, which are located in the basal cell layer, between the stratum spinosum and the dermis. The melanin is packaged into particles called melanosomes (which also contain structural protein [13]), and then transported via melanocyte dendrites into keratinocytes. Keratinocytes then move outwards to distribute melanin throughout the epidermis [7].

Melanin pigmentation of human skin has two major components - constitutive skin colour

(the natural colouration of skin in the absence of irradiation by light), and facultative skin colour (hyperpigmentation of the skin in response to direct exposure to ultraviolet light, or "tan"). This hyperpigmentation has two components, a short-lived immediate tanning reaction, and a delayed reaction [15]. The mechanism by which these tanning processes occur is not well understood, but is known to include melanosome formation, melanin production and melanosome transfer, as well as an increase in the number of melanocytes [4].

1.2 Interest in melanin

Paradoxically, although melanin is a photoprotectant it has also been implicated in the chain of events that lead to malignant melanoma skin cancer [16–18], although this link is very poorly understood. Highly pigmented skin is more protected from carcinogenesis than unpigmented skin [19], but it has been suggested that pheomelanin may actually function as a photosensitizer [20], and has been shown to actually enhance DNA damage in cells in response to ultraviolet radiation [21, 22]. The skin is the most common site of cancer in humans [19], and although melanoma is one of the rarer types of skin cancer, it causes the majority of skin cancer related deaths [23]. According to the World Heath Organisation, approximately 48,000 melanoma related deaths occur each year [24]. This makes understanding the biological functionality of melanin and its role in melanoma a health priority, particularly for countries with high levels of solar radiation such as Australia. Melanin also plays a central role in a variety of highly visible and inconvenient pigmentary disorders such as albinism and vitiligo [25].

Melanin is also of interest as a model system for understanding disorder in biological systems. Disorder is thought to be an essential part of the biological functionality of melanin, which is unlike other much more thoroughly studied biomolecular systems such as DNA and proteins. Disordered systems in biology have yet to recieve a great deal of attention, likely due to the difficulties inherent in studying them. This makes melanin a fascinating novel system with the potential for development of techniques applicable to a wide range of important biosystems [26–28].

As a third point of interest, melanin exhibits interesting physical and chemical properties such as anti-oxidant and free-radical scavenging behaviour, metal and drug binding properties [29–32], broad band ultraviolet and visible absorption and strong non-radiative relaxation of photo-excited electronic states [33]. Apart from making melanin fascinating to study, these properties make it a potentially useful material for devices and other technologies. Possible examples include highly efficient broadband single photon counters (superconductor based bolometers with a thin eumelanin film as the sensitising pigment), extremely sensitive humidity sensors (based on the extreme sensitivity of eumelanin solid state conductivity to hydration [34]), organic semiconductor electronics and solar cells [35, 36]. A fundamental understanding of the functioning of the pigment and how its molecular scale structure influences its macroscopic properties is essential for these applications. Establishing the relationship between eumelanin structures and properties forms the core theme of this thesis.

1.3 Synthesis of eumelanin and pheomelanin

Biologically, eumelanin is derived from tyrosine in a reaction catalysed by the enzyme tyrosinase, as outlined in the scheme depicted in figure 1.2. Analysis of this synthetic process and final eumelanin structure is extremely difficult due to the highly unstable nature of the reaction intermediates, and extremely stable and insoluble nature of the final product [4]. Nevertheless, intermediates have been identified, largely due to the pioneering work of Raper and Mason [37, 38]. The enzyme tyrosinase acts on dopa and tyrosine to produce dopaquinone, which reacts to form dopachrome (a red compound). Dopachrome is rather stable, but will spontaneously decompose to form DHI (5,6-dihydroxyindole), giving off CO_2. If the enzyme dopachrome tautomerase is present (Dct), dopachrome will instead tautomerise to give mostly DHICA (5,6-dihydroxyindole-2-carboxylic acid), retaining the carboxylic acid group [39]. Hence the availability of Dct will determine the relative amounts of DHI and DHICA produced, and therefore the ratio of these components in the final eumelanin macromolecule. This ratio will also be affected by other enviromental factors, and hence varies widely depending upon the source of the eumelanin under study [40].

It is widely accepted that eumelanin is a heterogeneous macromolecule of DHI and DHICA, and pheomelanin is a heterogeneous macromolecule of the sulphur containing cysteinyldopa (CD), as illustrated in figure 1.2. The manner in which these monomer units bind to form the macromolecular structure will be discussed further in chapter 3.

Melanin must be extracted from biological systems for study, and the extensive amount of bound protein must be removed. This is often achieved via harsh processes such as acid/base treatment, which is known to severly disrupt the properties of the pigment [41]. Much milder enzymatic methods are also available to extract melanin from hair, skin and eye tissue yielding melanin that is closer to its natural state [42]. It has become common practice to use eumelanin extracted from the ink sac of the cuttlefish *Sepia officinalis* as a model eumelanin pigment since it is readily available and easily extracted via mild techniques which yield a uniform black pigment that is appropriate for use as a standard [43].

Material that is termed 'synthetic melanin' is also often used as a standard for natural melanins. Synthetic melanin is formed under a variety of conditions *in vitro* including:

- Biomimetic conditions - oxidation of DHI with enzyme tyrosinase in aqueous buffer at neutral pH. This would seem to be the best synthetic method since it is closest to the natural system, but unexpectedly eumelanin formation occurs very slowly under these conditions, even in the presence of large amounts of enzyme [44]. Additionally, it is challenging to control and measure the activity of tyrosinase during this reaction, giving poor reproducibility [3]. Enzymatic preparations may also be performed with the alternate substrates of dopa and tyrosine.

- Autoxidative dopa eumelanin may be prepared by simply allowing alkaline solutions of dopa to come into contact with air. The solution may then be acidified to precipitate the eumelanin [4].

- A peroxidase/H_2O_2 couple induces a complete and rapid conversion of DHI to eumelanin in aqueous buffer at biomimetic pHs [44]. Similarly, a synthetic eumelanin is

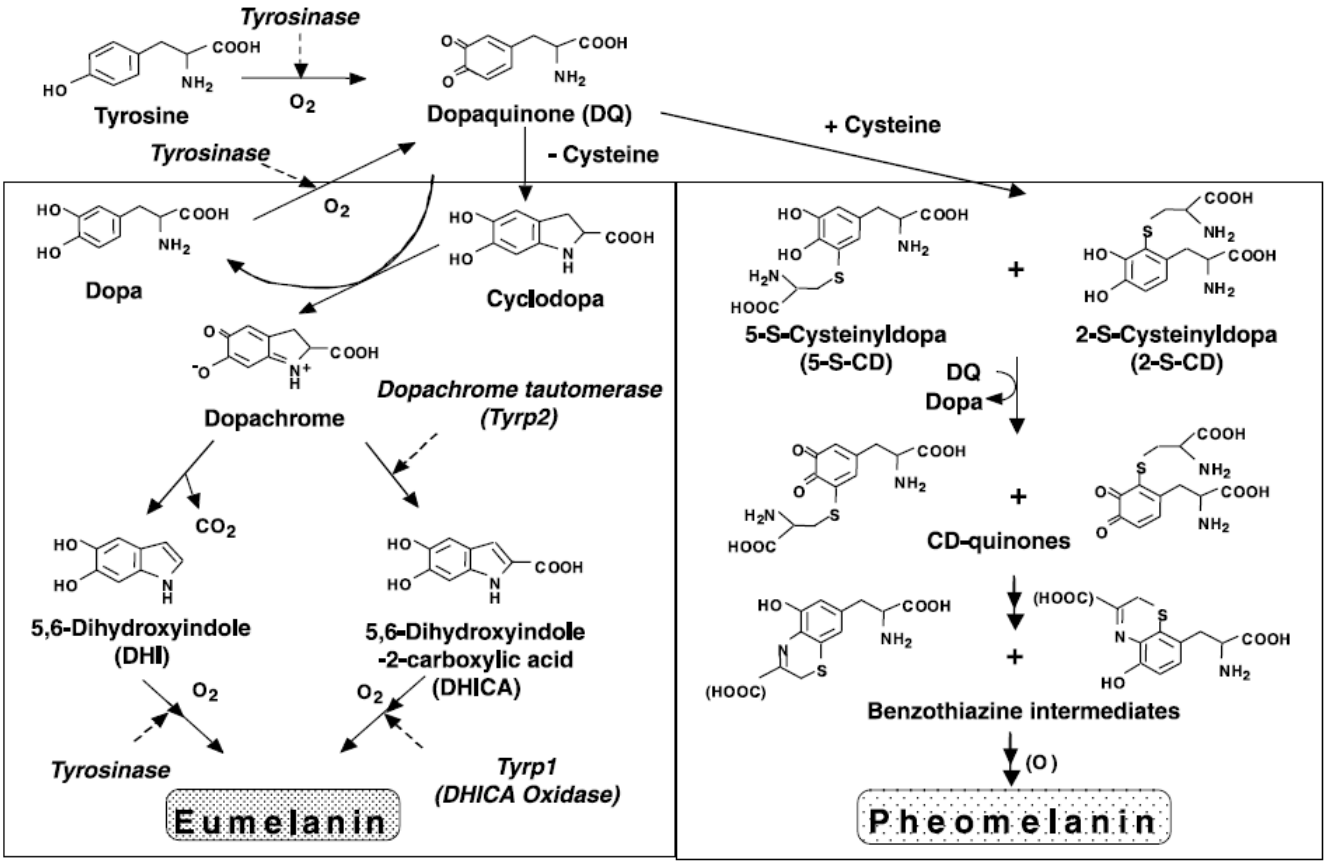

Figure 1.2: Melanin biosynthesis (from [39]). The eumelanin scheme is largely credited to Raper for his pioneering work on eumelanin biosynthesis in 1927 [37, 38].

commercially available that has been prepared by persulfate or peroxide oxidation of tyrosine [4].

The resulting black pigments show great similarity to natural eumelanin, although proof that they are identical to natural eumelanin remains lacking [2, 3]. Synthetic eumelanin is convenient as a model system for pioneering new methods or theories to treat this difficult material, and since they are produced under controlled conditions and contain known monomeric units they offer advantages for analysis over the more complex naturally extracted melanins. However, if substantiation of biological hypotheses is required care should be taken to use naturally derived melanins extracted using mild treatments [4, 42].

Throughout this thesis we use autoxidative dopa eumelanin as a synthetic analogue for natural eumelanin. Because we use a synthetic compound we avoid many of the problems of working with the natural pigment (such as incomplete removal of proteins, complex secondary structures and lack of experimental repeatability), and this allows us to make better progress towards understanding the structural and spectroscopic properties of this difficult system. We strongly caution the reader, however, that synthetic eumelanin should not be assumed to be identical to natural eumelanin. The experimental techniques and insight that we have gained from working with the synthetic system should be independantly verified in the natural system before any conclusions about biofunctionality are made.

1.4 The structure of this thesis

This thesis is organised into two parts. The first part deals with the absorption processes in eumelanin. Chapter 2 begins with a discussion of the broadband absorption spectrum of eumelanin, and outlines possible explanations for this spectrum. The significance of understanding the molecular structure of eumelanin is outlined, which leads into chapter 3; this chapter contains a comprehensive review of the literature concerning the molecular structure of eumelanin. These early chapters do not include new research, but instead provide a critical framework for the work presented in this thesis.

Part one of this thesis continues with two pieces of original work concerning the absorbance spectrum of eumelanin. Chapter 4 deals with the contribution of scattering to the optical density of eumelanin. This has been a problem plaguing spectroscopic research on melanins for decades, and is effectively resolved with the measurements and theory reported here. Significantly, this work also eliminates one of the possible explanations for the broadband absorbance of melanin, leaving two remaining models for analysis. The work contained in this chapter was published in the Biophysical Journal in a form very similar to that presented here (reference [45]).

Chapter 5 presents a study of the oscillator strength of eumelanin. Nature typically designs molecular systems that are extremely efficient at fulfilling their functions, so one might expect that as a biological absorber, eumelanin might have an exceptionally strong oscillator strength. Interestingly, this was not found to be the case, suggesting that eumelanin fulfils its biological role through more primitive means. The work contained in this chapter was published in Physical Review E in a form very similar to that presented here (reference [46]).

The second part of this thesis deals with energy dissipation processes in melanin. The early chapters deal with radiative emission (an effective non-invasive probe of molecular properties). Chapter 6 presents a careful study of the steady state emission properties of eumelanin, corrected for reabsorption and inner filter effects, the significance of which has been long neglected in spectroscopic literature regarding eumelanin. This chapter was published in a similar form in Photochemistry and Photobiology ([47]). The thesis continues with an in-depth study of the radiative yield of eumelanin as a function of excitation and emission wavelength in chapter 7; these results were published in a similar form in the Journal of Chemical Physics [48]. Chapter 8 presents a careful study of the steady state emission properties of pheomelanin pigment, and a discussion of the significance of the differences between pheomelanin and eumelanin; these results have been published in the Journal of Physical Chemistry B in a form very similar to that presented here (reference [49]). These studies on the bulk melanin pigments highlighted the significance of understanding the properties of the fundamental melanin components, DHI and DHICA, which have been spectroscopically very poorly characterised to date. This inspired a quantitative study of the absorption and emission properties of DHICA (chapter 9), and the spectroscopic observation of DHICA as it polymerises to form melanin (chapter 10). Some of the most significant results in chapter 9 formed the basis for a sophisticated theoretical study on DHICA and were included in the publication of these results in the Journal of the American Chemical Society (reference [50]).

The last chapter of this thesis (chapter 11) presents inelastic neutron scattering measurements on key melanin monomers; this research begins to delve into the non-radiative processes that are thought to be the predominant form of energy dissipation in this system. Future research based on these initial careful studies should shed light on the vibrational processes that are so essential for the functioning of this pigment. The final chapter contains a discussion of possible future research directions (chapter 12).

Part I

Explaining the broadband absorbance of melanin

2

The broadband absorption spectrum of melanin

2.1 Measuring absorption

The Beer-Lambert law describes the exponential attenuation of light as it passes through an absorbing medium

$$I = I_0 e^{-\alpha d} \tag{2.1}$$

where I_0 is the initial intensity of the light and I is the intensity after passing through a distance d of material with an absorption coefficient α (note that this is the manner in which the absorption coefficient is defined). The experimentally measured absorbance of a material will typically be reported as one of the following three quantities: the absorbance, A (also called the optical density, OD)

$$A = \log_{10}\left(\frac{I_0}{I}\right) \tag{2.2}$$

the absorption coefficient, α

$$\alpha = \frac{1}{d}\ln\left(\frac{I_0}{I}\right) \tag{2.3}$$

$$= \frac{A}{d}\ln(10) \tag{2.4}$$

or the (molar) extincition coefficient, ϵ

$$\epsilon = \frac{1}{Cd}\log_{10}\left(\frac{I_0}{I}\right) \tag{2.5}$$

$$= \frac{1}{Cd}A \tag{2.6}$$

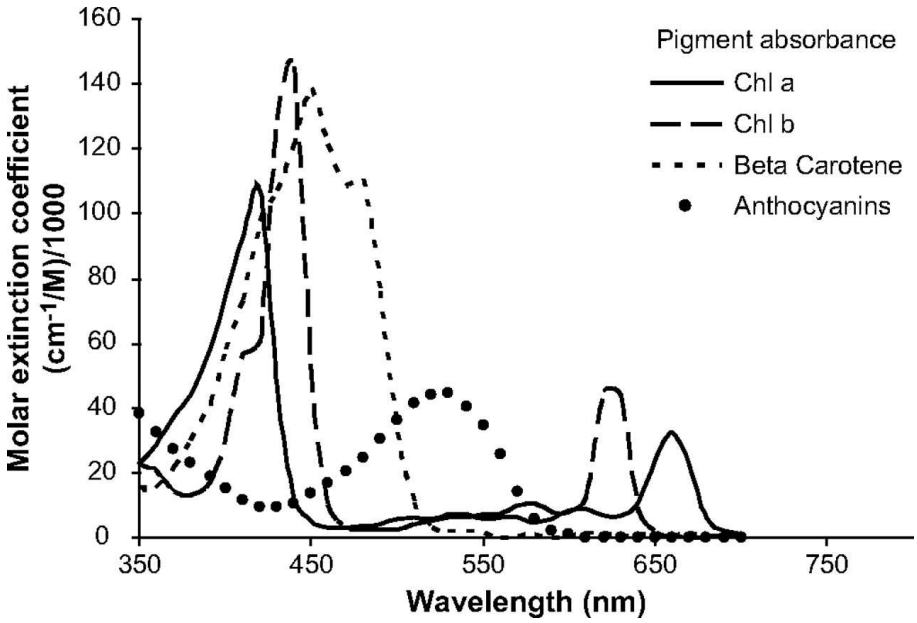

FIGURE 2.1: Absorbance spectra of the major plant pigments (from [51]). Chl a: Chlorophyll a, Chl b: Chlorophyll b. Note that all spectra are clearly peaked in nature, as is typical of most chromophores.

where C is the concentration of the absorbing species (this can be measured in a variety of units, and care must be taken to ensure that the dimensionality of the above expressions is maintained). ϵ is unique to a particular substance and independent of experimental parameters such as concentration [1] and pathlength, whereas α will vary depending upon the experimentally used concentration, and A will vary depending upon the concentration and the path length. Which of these is used in a particular situation depends upon which is most convenient and informative for that particular application.

2.2 The broadband absorption spectrum of melanin

Most biological pigments exhibit distinct absorption bands. For example, consider the UV/visible absorbance spectra of some of the most significant plant pigments shown in figure 2.1 (from reference [51]). The chlorophylls (Chl a and b) are the primary pigments responsible for photosynthesis in plants, beta carotene is a type of carotenoid that also absorbs incident radiation and contributes energy to photosynthesis, and anthocyanins are the third major group of pigments in leaves, but their biological function is not widely agreed upon [51]. Most significantly, all of these important biopigments have distinct absorbance peaks, as is typical of biomolecules. These peaks are associated with transitions between discrete electronic energy levels.

The major pigments found in animal tissues (including human skin) are melanin and

[1] The extinction coefficient is independent of concentration in the low concentration limit. At high concentrations (much higher than those used throughout this thesis) effects including (but not limited to) multiple scattering may cause non-linearity in the absorption coefficient with concentration.

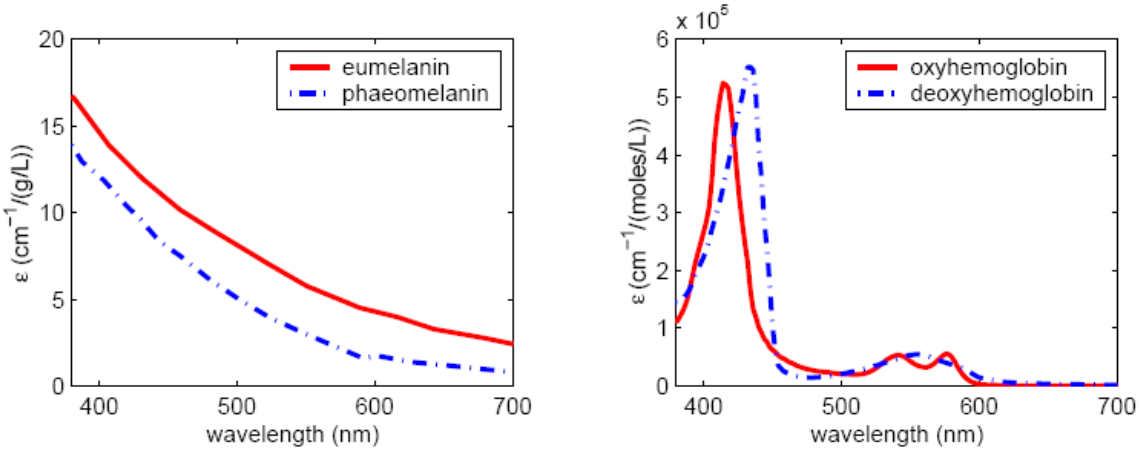

Figure 2.2: Absorbance of the major pigments found in human skin, measured *in vitro* (from [52]). Note that due to the unknown molecular structure of melanin a molar extinction coefficient cannot be defined in the same manner, hence it is represented on a different scale.

haemoglobin, the absorbance spectra of which are shown in figure 2.2. Spectra of bilirubin and β-carotene, other pigments found in skin, are also included (bilirubin is a breakdown product of normal haem catabolism which is responsible for the yellow colouration of subjects suffering from jaundice). With the exception of melanin, all the skin pigments shown have clearly peaked absorption spectra. Melanin, however, exhibits an unusual broadband absorption spectrum. The broadband nature of the melanin spectrum is likely due to its photoprotective role (a peaked spectrum would transmit photons of certain wavelengths). The absorbance of melanin increases monotonically towards higher energies, probably to give increased protection against the most damaging high energy photons. Interestingly, the spectrum of melanin in the visible range is very close to exponential when plotted against wavelength, as demonstrated in figure 2.3; the significance of this simple dependance is unknown. Absorbance lineshapes are expected to be broadened in a gaussian manner when plotted against *energy* (rather than wavelength), so a simple dependance of lineshape upon wavelength is unexpected, and possibly coincidental.

The origin of the broadband absorption spectrum of eumelanin has long been the topic of scientific debate, which continues to this day. There are three main alternative models:

1. The broadband absorbance is primarily a scattering phenomenon, and not due to electronic absorption [54].

2. Melanin is an amorphous semiconductor, which naturally results in a broadband absorption spectrum [55].

3. Melanin consists of many chemically distinct species and the broadband spectrum is formed by the superposition of the peaked spectra of these species. This is the so called "chemical disorder model" [53].

Chapter 4 of this thesis deals entirely with the first of these models; our measurements show that the eumelanin absorption spectrum is not due to scattering and is due to true electronic absorbance. We will discuss the two remaining models here.

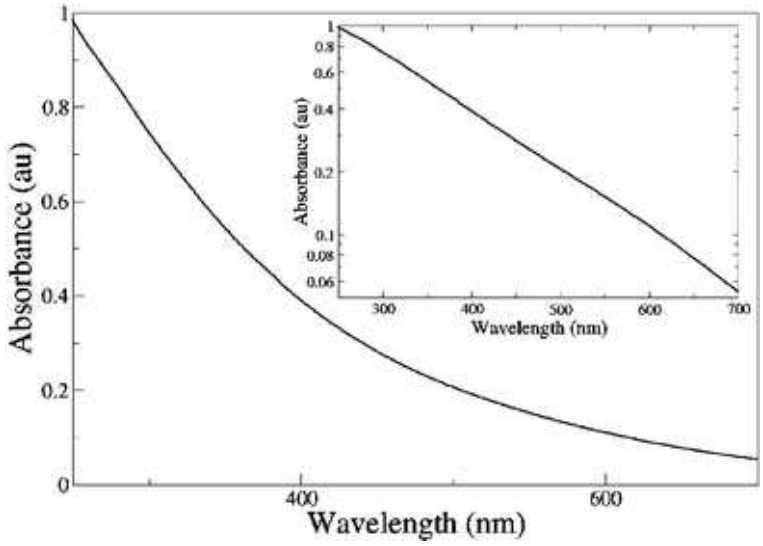

FIGURE 2.3: Absorbance spectrum of synthetic eumelanin solution in pH 10 NaOH (0.0025% by weight eumelanin, 1 cm pathlength cuvette). The same data is shown inset on a log-linear scale showing the exponential nature of the spectrum (from [53]).

2.3 Melanin as a semiconductor

It was first suggested in 1960 by Longuet-Higgins that an amorphous semiconductor model naturally explains the black colour of eumelanin (broadband absorbance) [55]. In this model, eumelanin consists of a large indole heteropolymer which has a delocalised π system. This leads to an amorphous semiconductor band structure and therefore a broadband absorption spectrum. Further support of this model was published in 1974 when McGinness et al. reported amorphous semiconductor switching behaviour in eumelanin films, which had only been previously observed in inorganic materials [56]. Also in favour of the semiconductor model, later reports suggest that eumelanin exhibits the thermoelectric effect with a negative charge carrier (under vacuum) [57, 58], and show that increasing temperature increases the conductivity of eumelanin samples [59]. In 1961 Pullman and Pullman applied Huckel π-electron theory to a hypothetical eumelanin polymer model and showed that they could successfully explain the electron-acceptor and semiconducting properties of eumelanin in this model [60]; this work was later extended by Galvao and Caldas [61–64]. This extensive body of research in favour of the heteropolymer semiconductor model for melanins has led to it becoming a strongly accepted paradigm in the field.

Unfortunately the semiconductor model fails to explain other observed properties of melanin. Measurements of the Hall effect under ambient conditions suggest a positive charge carrier [65], as do measurements of the thermoelectric effect under ambient conditions (as opposed to the negative sign observed under vacuum) [57], and coulombmetric studies suggest that protons in fact form 65% of the charge carriers in eumelanin [66]. Also a problem for the semiconductor model, non-ohmic behaviour has been observed [58, 67]. Additionally, in this model we would expect to see a band gap manifesting as a low energy band edge; this has never been observed in absorption spectra of eumelanin solutions or in solid state

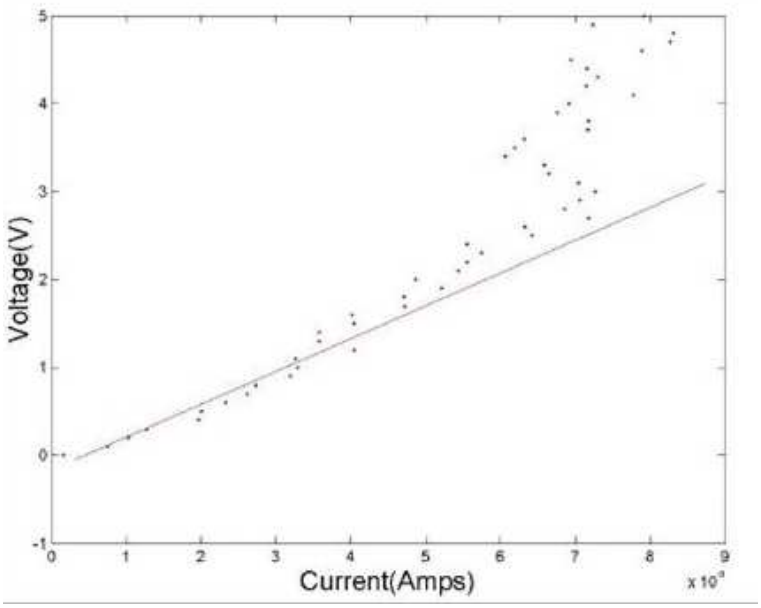

Figure 2.4: Melanin I-V curve, showing non-ohmic behaviour at high voltages (from [34]).

transmittance and reflectance measurements. Proponents of this model suggest that the apparent lack of a band gap may be explained by scattering and/or the band edge tails that are observed in amorphous systems.

Assuming an amorphous semiconductor model, several authors have attempted to predict the solid state energy gap from the shape of the absorption spectrum using a Tauc approach (the slope of a plot of $(\alpha E)^{1/2}$ vs E gives the energy gap, where α is the measured absorption coefficient and E is the excitation energy). Varied energy gap estimates have resulted, from 3.4 eV [68] to 1.2 ± 0.2 eV [69]. Photopyroelectric spectroscopy provides an alternative probe of the energy gap; recent measurements suggest there may be a fundamental "partial" gap at 1.7 eV [70, 71]. The disparity in these results suggests that the absorption spectrum of eumelanin is not a sensitive probe of electronic structure, or alternatively that eumelanin should not be modelled as an amorphous semiconductor.

Recent measurements from our group confirm the non-ohmic behaviour of eumelanin at high voltages (figure 2.4), which is inconsistent with the semiconductor model. Also, measurements of eumelanin conductivity as a function of relative humidity (figure 2.5) show that it varies in a manner unlike a hydrated semiconductor (see figure 2.6 for comparison).

Many organic semiconductors have been well studied, some oligomeric such as pentacene, anthracene and rubrene, others polymeric, such as poly(3-hexylthiophene), polyacetylene and poly(p-phenylene vinylene). All are highly conjugated, containing either a high proportion of carbon-carbon double bonds, or a large amount of aromaticity. This predominance of π-bonding gives sufficient delocalisation to produce semiconducting behaviour and therefore broadband absorbance through an electronic band structure. Most importantly, most organic semiconductors are highly structurally ordered, and small oligomeric organic semiconductors are ordered to the point of being crystalline in nature. We propose then that in order to have convincing evidence that eumelanin should be described as an amorphous semiconductor we

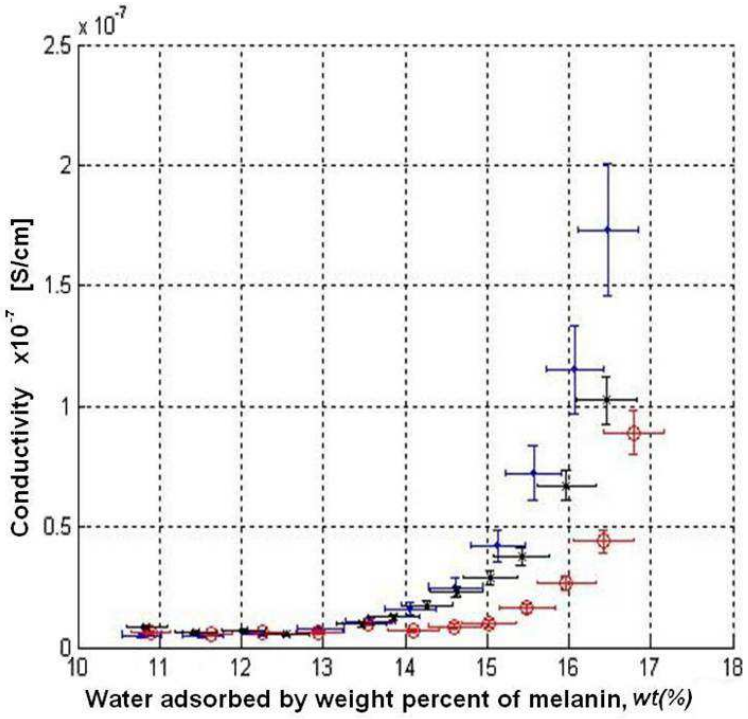

FIGURE 2.5: Melanin conductivity vs hydration (from [34]). Compare with figure 2.6.

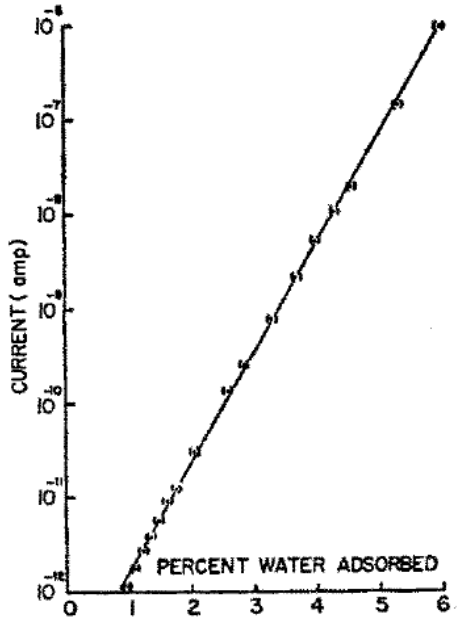

FIGURE 2.6: Conductivity of crystalline bovine haemoglobin (a known organic semiconductor) as a function of the percent of water absorbed (for a constant voltage, conductivity is directly proportional to current) (from [72]).

must show that it consists either of highly ordered oligomeric units, or of large polymeric chains (possibly with some disorder). As shall be discussed in detail in chapter 3 there is a wealth of experimental evidence suggesting that eumelanin is not highly ordered; in fact, disorder is known to dominate this system. There is also significant evidence that eumelanin is oligomeric in nature, with oligomers of between 4 and 8 monomer units. These observations make the amorphous semiconductor model of eumelanin seem unlikely, but we cannot rule it out without further evidence.

2.4 The chemical disorder model

It has been proposed that chemical disorder could provide an alternative explanation for the broadband absorption spectrum of eumelanin [35, 53, 73–76]. Since there are several different eumelanin monomers that may crosslink through various different sites, it is possible that a sample of eumelanin may consist of a large number of distinct chemical species which we shall term 'oligomers' (without meaning to imply anything about the size of these species) [62]. Density functional theory calculations suggest that each distinct oligomer may be expected to have a slightly different HOMO-LUMO energy gap [64, 73, 74, 77–80]. A disordered collection of oligomers may therefore exhibit broadband absorbance, since the spectrum will be the sum of many absorbance peaks at slightly different energies [53, 76]. Figure 2.7 demonstrates how only a small number of peaks with typical solvent broadening are necessary to reproduce the observed broadband spectrum of eumelanin (we plot against energy since solvent broadening should produce peaks that are gaussian in energy, rather than wavelength).

As will be discussed in the later chapters of this thesis, all of the observed properties of eumelanin are consistent with the chemical disorder model. Emission and excitation spectra exhibit unusual features that are naturally explained by this model, and similarly for the radiative quantum yield of melanin.

At this point we wish to note that the term 'oligomer' is typically used for small fragments of polymers. The size that is small enough to be considered an oligomer depends upon the system under discussion (an oligomer is typically much smaller than the polymer of interest, and may contain anywhere between two and hundreds of monomer units). In real eumelanin systems the size of the oligomer will likely be limited by the solubility of the pigment under the conditions in which it was formed, and hence it will vary depending upon the source. Whether eumelanin should be called 'polymeric' or 'oligomeric' in nature is really a concern of nomenclature (and comes down to how large an oligomer must be before we define it as a polymer). The size of oligomers is not of primary importance for the chemical disorder model, it is simply important that there are enough distinct species to produce broadband absorbance. Hence in the context of melanins, we will take the term 'oligomer' to mean simply a specific eumelanin macromolecule that may contain any number of monomers, even very large numbers.

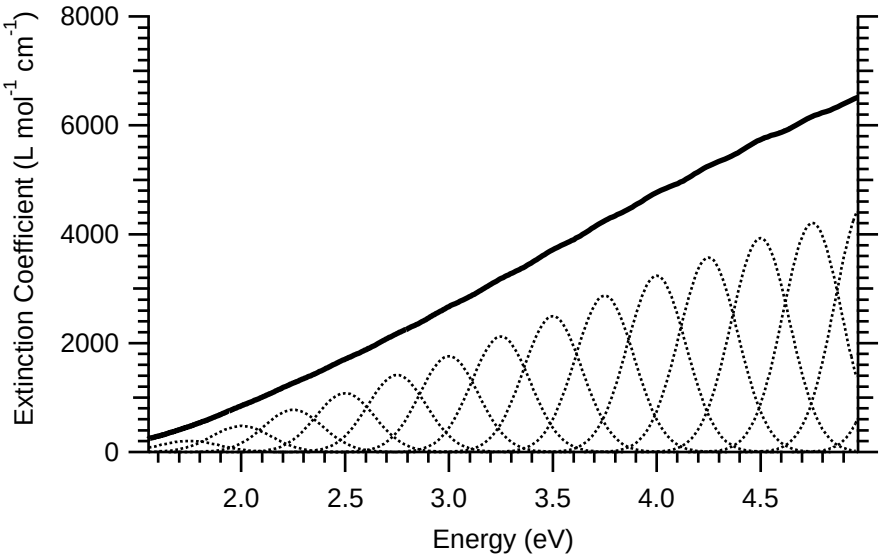

FIGURE 2.7: The absorbance spectrum of eumelanin vs energy (extinction coefficient calculated per monomer, with monomer molecular weight being the average of that of DHI and DHICA). The summation of a small number of gaussians (here 15, shown in dotted lines) with typical solvent broadening produces the broadband absorption spectrum of eumelanin (solid thick line).

2.4.1 Theory supporting the chemical disorder model

There have been several theoretical studies of the viability of the chemical disorder model. In 2003 Bonchenek et al. calculated the absorption spectra of various eumelanin pentamers using the semi-empirical INDO (Intermediate Neglect of Differential Overlap) approach and showed that they could reproduce the broadband eumelanin spectrum by summation of these spectra [81]. Also in 2003, Stark et al. used density functional theory to predict likely oligomer structures (a variety of dimers, and a typical tetramer, pentamer and hexamer) and showed that the linear summation of the absorption spectra of these species was broadened and reproduced features of the experimental spectrum [73, 74]. In 2005 they investigated the effect of aggregation of oligomers (stacking of planar sheets via π interactions) and showed that this may also affect the absorption spectra (increasing chemical disorder) [80].

Most recently, a publication by Kaxiras et al. proposed ring structures for tetramers (figure 3.18) and reported absorption spectra for these molecules calculated using density functional theory [82]. These spectra are shown in figure 2.8, with the superposition included. Although the individual spectra are clearly peaked, the superposition is broadband and increases towards higher energies in a manner very similar to the eumelanin spectrum.

The ability of these models to reproduce the broadband spectrum of eumelanin is a strong indication of the viability of the chemical disorder model.

2.4.2 Redox states

Ito et al. have shown that the absorption maximum of DHICA oligomers is only slightly red-shifted from that of the DHICA monomer [83]. This suggests that some mechanism other

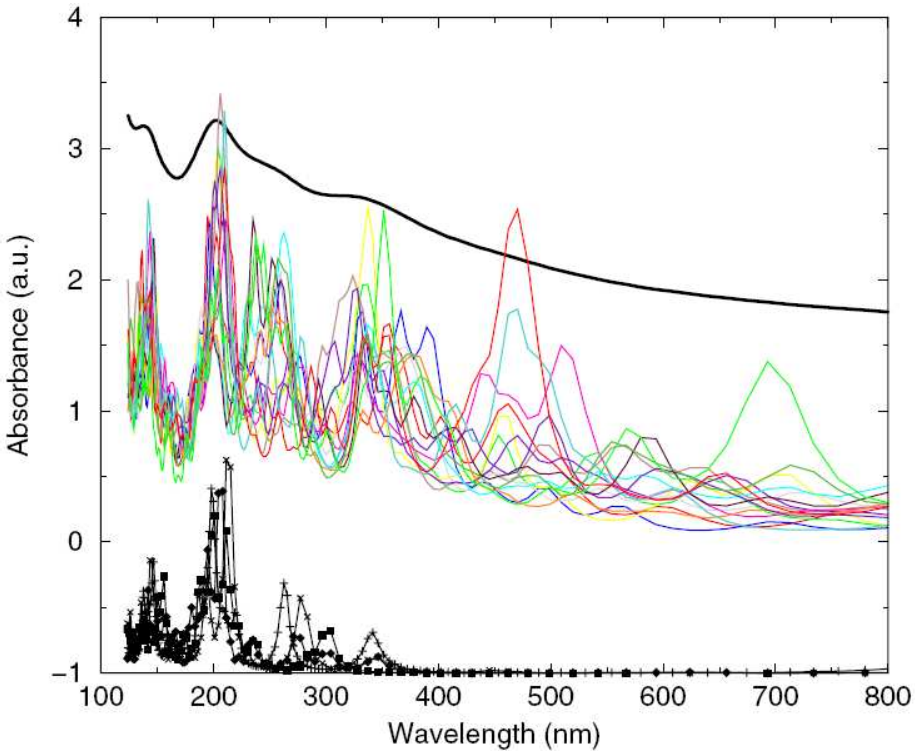

Figure 2.8: Absorption spectrum resulting from the superposition of the spectra of dominant tetramers, as calculated by density functional theory (thick black line, shifted up by 1.5 units for clarity). Individual tetramer contributions are given by the thin coloured lines, and monomer spectra are also shown (shifted down 1 unit for clarity). The broadband shape of the melanin absorption spectrum can be reproduced by summation of the spectra of various oligomers. Note that experimental spectra cannot be easily measured below 250 nm due to the high absorbance of water at higher energies, possibly explaining why the peak at ∼200 nm has not been observed experimentally. From [82].

than simply polymerisation must be present to produce sufficient diversity in absorption peaks for broadband melanin absorbance, and in particular, to produce significant absorption in the visible region of the spectrum.

It is important to note that eumelanin is thought to consist of DHI and DHICA in a variety of redox states. In addition to the commonly depicted reduced dihydroxyindole state (as illustrated in figure 1.2), the oxidised indolequinone and semiquinone states depicted in figures 2.9 and 2.10 are expected to be present in solution in quantities high enough to affect the absorption spectrum of eumelanin. Density functional theory calculations suggest that these redox states are likely to have very different HOMO-LUMO gap energies, and therefore significantly different absorption spectra. Powell et al. predicted the HOMO-LUMO gap energy of the DHI hydroquinone state to be 344 nm, whereas the indolequinone is significantly redshifted to 615 nm, and the semiquinone shows very large redshifting to 1110 nm [78]. Similarly for DHICA, the hydroquinone (state 1 in figure 2.10) was predicted to have a HOMO-LUMO gap energy of 409 nm, the indolequinone (state 3a in figure 2.10) was predicted to be redshifted to 634 nm, and the semiquinone (state 3b in figure 2.10)

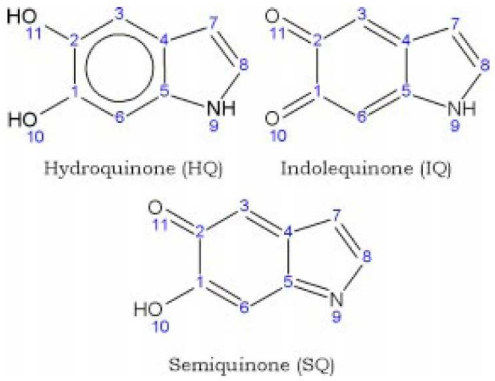

FIGURE 2.9: The redox states of DHI. From [78].

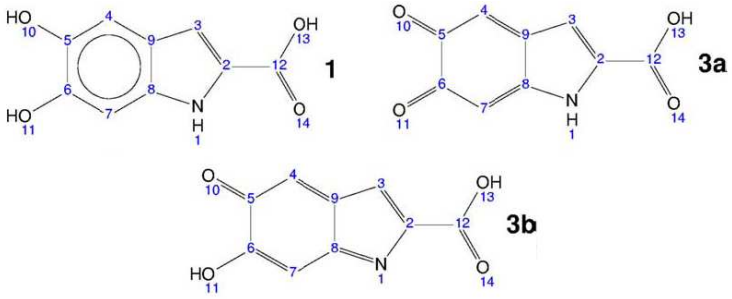

FIGURE 2.10: The equivalent redox states of DHICA. From [77].

shows very large redshifting to 1130 nm. These results suggest that while the absorption spectrum of DHICA may be only slightly redshifted from that of DHI, the absorption spectra of the various redox states are significantly varied. This has the important effect of increasing chemical disorder and allowing for a significantly greater number of distinct absorption peaks to contribute to broadband absorbance. In particular, the presence of significant quantities of indolequinone and semiquinone is likely to be essential for producing the observed absorbance of melanin in the visible part of the spectrum (due to their significantly redshifted HOMO-LUMO gap energies).

These results remain challenging to prove experimentally due to the difficulty of obtaining stable and well characterised samples for the measurement of absorption spectra. Edge et al. claim to have measured the absorption maxima of the DHI and DHICA quinone states to be 480 nm and 420 nm respectively [84], although we believe that they are likely to have instead been measuring the absorption spectra of a radical state of some description, since these HOMO-LUMO gap energies are outside of the uncertainty in the density functional theory calculated values (615 nm and 634 nm respectively). Further work in this area is required.

2.5 Chapter conclusions

The chemical disorder model is currently our favoured explanation for the broadband absorbance of eumelanin since it best explains the observed features. However, definitively distinguishing between the semiconductor model and the chemical disorder model requires a better understanding of the structure of melanin. For the semiconductor model to be likely, eumelanin should consist of either large polymeric species, or be relatively structurally ordered (if only small species are present). On the other hand, the chemical disorder model simply requires that eumelanin is composed of a large number of chemically distinct species. The following chapter shall discuss the structural evidence for each of these models.

3
The structure of melanin

3.1 Chapter introduction

At the cellular level, melanin is organised into organelles called melanosomes. Eumelanin melanosomes are ovoid in shape, whereas pheomelanin melanosomes are spherical and more fragile [85–88]. Melanosomes in negroid subjects are approximately 800 nm in length, whereas caucasian melanosomes are smaller, at approximately 400 nm in length [4, 89]. Melanin granules from the ink sacs of *Sepia officinalis* (often used as a model for human eumelanin) are spherical and much more varied in size than those extracted from humans [90, 91] (note that these melanin granules should not be termed melanosomes in this context [92]). Natural melanosomes have been shown to contain anywhere from 17.9% to 73.2% melanin and 5.4% to 61.4% protein, depending upon the source [93].

The structural arrangement of melanin and protein within melanosomes is very poorly defined. At the molecular level, eumelanin is known to be a macromolecule of DHI (5,6-dihydroxyindole) and DHICA (5,6-dihydroxyindole-2-carboxylic acid), with structures as depicted in figures 1.2 and 3.1. However, the manner in which these monomers covalently bind to form the melanin pigment is essentially unknown. A knowledge of structure at this level is essential for accurate quantum chemical modelling of melanin, and for evidence of either the semiconductor or chemical disorder model of melanin (the semiconductor model requires large heteropolymeric structures, whereas the chemical disorder model simply requires a chemically disordered collection of molecules). The structure of eumelanin at this molecular level has become a point of significant interest in the melanin community [33, 94], and there is a huge volume of literature relating to it. We will attempt, in this chapter, to summarise the most important findings.

In nomenclature borrowed from proteins, we shall discuss the structure of eumelanin in this thesis using the terms ‘primary and ‘secondary’ structure, and it is pertinent at this point to accurately define these terms with respect to eumelanin. By primary structure, we

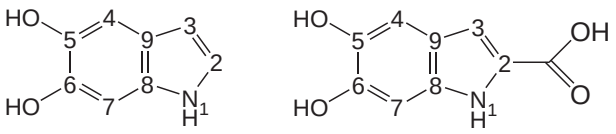

DHI DHICA

FIGURE 3.1: Chemical structures of the monomeric building blocks of eumelanin (DHI and DHICA). The standard numbering of bonding positions is illustrated and hydrogens have been left off the carbon skeleton for clarity.

mean the manner in which the monomeric units (DHI and DHICA) covalently bind. The structures of oligomers such as those depicted in figures 3.10, 3.5 and 3.18, or manner of covalent binding in large polymers are best described as structure at the primary level [1]. Secondary structure, then, is the manner in which these covalently bound units associate via non-covalent interactions (such as van der Waals forces or hydrogen bonding) to form larger structures. π-stacking of sheets, such as that depicted in figures 3.9 and 3.13 would fall into the category of secondary structure. These terms have been used somewhat loosely with respect to melanins in the past, but we believe that the definition outlined here is the most faithful to the meaning of the terms from the original context.

3.2 Covalent binding of monomers

An important first step towards elucidating the structure of eumelanin is to clearly identify the most likely binding sites of the monomeric units. From this the mode of polymerisation of eumelanin can be deduced, and the most likely molecular structures determined. Prota's group at Naples has been instrumental in making progress towards this goal through a large body of work (for a review see [96]). Early studies attempted to identify the most likely binding sites through degradation of the eumelanin pigment and subsequent analysis of the oxidised products [97]. More recent studies have focused on oxidative polymerisation of the eumelanin monomers (DHI and DHICA) under biomimetic conditions and isolation of the intermediate oligomers via methods such as HPLC (high performance liquid chromatography) [98]. This method allowed the successful isolation of the DHI dimers depicted in figure 3.2 [44]. The formation of these particular dimers suggests the prevalent mode of coupling for DHI is through the 2, 4, and 7 positions (with standard numbering of carbons, as depicted in figure 3.1). A similar method allowed the isolation of the DHICA dimers depicted in figure 3.3, which show that DHICA prefers to bind through the 4, 7 and 3 positions (binding through 2 is obviously prohibited due to the carboxylic acid occupying that site). Chiral linear trimers and tetramers of DHICA with binding through the 4 and 7 positions have also been isolated (representative structures are shown in figure 3.4) [99, 100].

The preferential binding of DHI through the 2-position was later confirmed via NMR of ^{13}C-labelled synthetic eumelanin [102]. This study also revealed binding of DHI through the 3 position (although to a lesser extent than the 2 position), and showed that these two sites

[1] By comparison, the primary structure of DNA and proteins defines the order in which the monomeric units (nucleic acids or amino acids) covalently bind to form a linear chain [95].

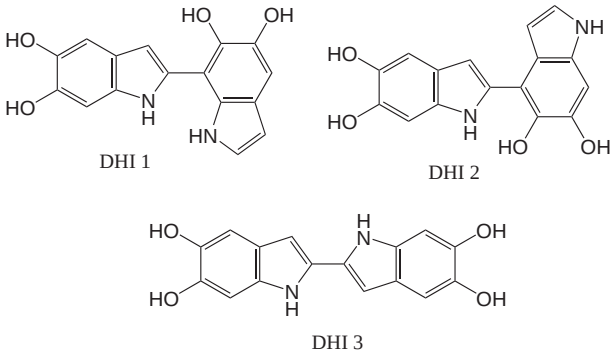

Figure 3.2: Dimers isolated from oxidised DHI [101]. The types of dimers formed indicates which binding sites are favoured for DHI (2, 4 and 7).

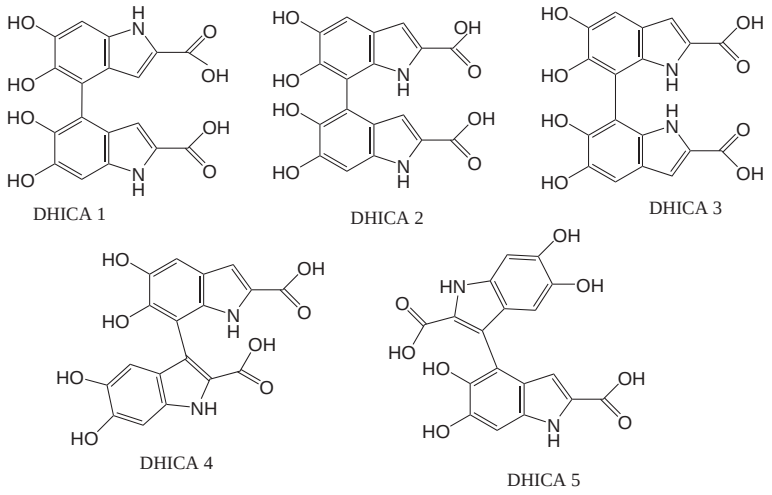

Figure 3.3: Dimers isolated from oxidised DHICA [98]. The types of dimers formed indicates which binding sites are favoured for DHICA (4, 7 and 3).

together (2 and 3) are responsible for three-quarters of the proton loss during polymerisation.

It is important to note that DHI and DHICA are thought to intimately copolymerise when the macromolecule forms [103, 104], so the possibility of a predominance of structures consisting exclusively of either DHI or DHICA is unlikely (except where the pigment is sythesised with only one type of monomer present). Most of the dimers identified thus far consist of only one monomer because the polymerisations were deliberately performed with only a single species present to produce the simplest possible macromolecular product. Mixed dimers have also been identified however, such as one that binds through the 2 and 4 positions [105], and bindings of this nature are thought to be common in naturally derived pigment. In particular, DHICA may be structurally important as an 'end-capping' group in eumelanin pigment, since the carboxylic acid group blocks polymerisation through the 2 position and makes the DHICA monomer more likely to exist at the ends and edges of structural units.

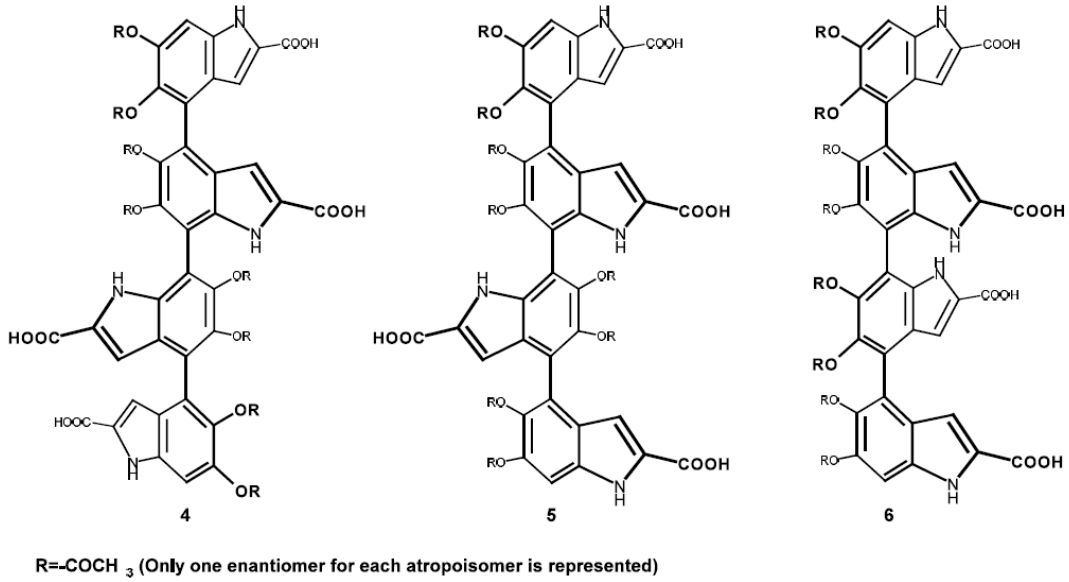

FIGURE 3.4: Chiral DHICA tetramers isolated by tyrosine catalyzed oxidation of DHICA under biomimetic conditions (from [100]).

3.2.1 Mass spectrometry (MALDI)

Matrix assisted laser desorption/ionization (MALDI) mass spectrometry has been successful at identifying some of the species present in eumelanin samples. Synthetic DHICA eumelanin and synthetic DHI eumelanin were studied, and were both found to contain a wide variety of oligomeric species with mainly low molecular weights (mass values in the range 500-1500 Da) [106, 107]. No species larger than hexamers were identified, with the most common being trimeric and tetrameric. The authors suggest that the size of the oligomers may be dictated by their solubility in the reaction medium during the chain elongation process, and hence is likely to vary depending upon the exact preparation conditions. This suggests that caution must be taken when comparing melanins prepared under different conditions and from different sources.

Representative structures of some of the species identified in DHICA eumelanin are shown in figure 3.5. Structure I shows bonding at the 4 and 7, consistent with the studies discussed above. Structure II contains some units that have been degraded by peroxidative fission (mainly by hydrogen peroxide) to produce pyrrolic chromophores. This degradation was found to be significant in both synthetic DHI and DHICA even under mild and controlled conditions, and offers a much more diverse range of possible oligomers than simple copolymerisation of eumelanin monomers. In this way, gradual degradation of the pigment may actually contribute to biological functionality by increasing chemical disorder (via the addition of pyrrolic chromophores and other compounds) and ensuring a broadband absorption spectrum (since pyrrole moieties introduce a new absorption maximum).

Similar structures to those shown in figure 3.5 were obtained for natural (*sepia*) eumelanin [108], again with low molecular weights (450 to 1200 Da), although the authors of that study note that a significant proportion of high molecular weight pigment components may not have been detected by MALDI due to the limitations of this method. Degradation was again

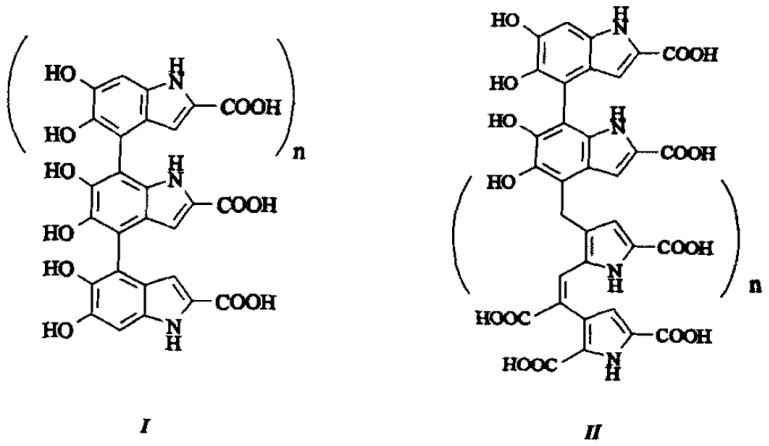

Figure 3.5: Representative structures of oligomers identified via mass spectrometry in synthetic DHICA eumelanin (no species larger than hexamers were observed). From [106].

shown to be a significant feature of the structures identified, confirming the relevance of the synthetic studies to the natural pigments.

The most important finding from mass spectrometry of eumelanin is that the majority of the literature shows mass units within or below $\sim 600 - 1200$ amu, which corresponds to oligomers of between 4 and 8 monomer units [107–112]. Large polymeric structures are not observed for any of the samples studied.

3.2.2 NMR

Although NMR is a blunt tool for studying the structure of polymers, clear differences have been demonstrated between the NMR spectra of different types of melanin indicating that NMR spectroscopy is sensitive to primary structure. Accurate interpretation of these spectra for specific structures is challenging since they contain a very large number of peaks (which are difficult to assign), and these peaks are broadened due to chemical heterogeneity [113, 114]. It has been suggested that high resolution liquid phase spectra would be more detailed and may yield more structural information than the solid state spectra that have been reported [115]. Nevertheless, NMR measurements yield important structural clues, such as the observation by Peter et al. that their sample contained a high proportion of catechol units which has important implications for the redox state of eumelanin, and therefore its covalent binding and optical properties [113].

^{13}C and ^{15}N solid state spectra confirm the presence of indolic structures in melanin, as well as pyrrolic species (probably from degraded indoles) [115]. It has also been noted that synthetic melanins degraded with H_2O_2 have very similar ^{13}C NMR spectra to natural *Sepia* eumelanin [114]. This either suggests that the method used to extract protein from the *Sepia* eumelanin was too harsh (and eumelanin was degraded in the process), or that degradation is significant in the natural system.

Aliphatic carbon residue resonances have been repeatedly reported in eumelanin NMR, which is somewhat unexpected (the carbons in eumelanin are thought to be predominantly aromatic in nature) [113, 115–117]. Herve et al. attributed these resonances to residual

proteinaceous material that was not removed in the extraction procedure since they did not observe them in their measurements of synthetic eumelanins [117], but Peter et al. report aliphatic carbon resonances in synthetic eumelanin isolated from dopamine and DOPA [113]. Golounin proposed instead that the aliphatic units are due to oxidative degradation of the aromatic rings, again highlighting the presence of degradation in eumelanin from both natural and synthetic sources [118]. The aliphatic region of the spectrum is difficult to interpret, however, and may perhaps be attributable to both degraded indole units and residual protein [119].

Several more recent studies focused on natural melanins (*Sepia* eumelanin or human hair melanin) and proposed some oligomeric structural models, although the spectra remain difficult to interpret unequivocally [119, 120].

3.2.3 Bicoupling and planarity

All of the chemical species isolated thus far exhibit monocoupling (a single covalent bond between the monomers). Some of these species are likely to be planar, stabilised by hydrogen bonding [73], although many may be non-planar (the second monomer may rotate out of the plane to reduce steric hinderance). Bicoupled dimers (dimers with two covalent bonds between the monomer units), on the other hand, will be constrained to be planar. Bicoupled dimers of DHICA have been investigated using density functional theory methods and were suggested to be as stable or perhaps even more stable than the monocoupled dimers [74, 76]. This is not an intuitive result, given that bicoupled dimers are sterically strained.

An NMR study of Herve et al. suggested that between 1.6 and 2.7 protons are lost from carbon atoms per monomer as DHI oxidises to form synthetic eumelanin [116]. This indicates that each monomer forms between 1.6 and 2.7 covalent bonds with its neighbours (depending upon the oxidation pathway). A similar measurement for natural pigment shows that they lose 2.5 protons per monomer. This result does not take into account loss of protons from hydroxyl groups, so the degree of covalent bonding may in fact be higher. These numbers suggest that bicoupling and tricoupling should be significant in eumelanin structures.

Thus the question arises of why no bicoupled dimers have been isolated experimentally. This has important implications for the secondary structure of eumelanin; as shall be discussed in the following sections, there is evidence that eumelanin self-assembles into planar sheets which then aggregate via π-stacking interactions. This is logical for planar oligomers, but it is difficult to see how the aggregation process would occur in this manner for non-planar species.

3.3 The size and shape of aggregates

3.3.1 Microscopy

It is natural to use high resolution microscopy techniques such as scanning tunnelling microscopy (STM), scanning electron microscopy (SEM) and atomic force microscopy (AFM) for the investigation of structure. These methods determine the size and shape of aggregates, but can only probe surfaces over small areas (not bulk properties). Microscopy techniques

are ideally suited to investigating the shapes and sizes of whole melanosomes (hundreds of nanometers, or micrometres in the case of *Sepia* eumelanin granules) [42, 90, 91, 121–124], but are at their limits for structures smaller than this (such as the identification of species of the sizes indicated by mass spectrometry measurements). The difficulty of analysis of melanins is increased greatly by the fact that the method of preparation is known to affect the structure, giving a variety of particle sizes for different samples [42, 125]. This makes repeatability a significant issue.

Several studies report particle sizes for *Sepia* eumelanin. Nofsinger et al. report SEM images showing asymmetric particles ranging from $\sim$ 3 to 286 μm in the long dimension, and other paticles with doughnut shapes. They determined that these consisted of smaller closely packed structures that varied in their lateral dimension from $\sim$ 45 to 230 nm. The transmission electron microscope images of Vitkin et al. were in agreement with this (they reported particle size distributions with a predominant particle diameter of 90 nm) [124], as did the results of Zeise et al. [16, 90].

The SEM measurements of Nofsinger et al. showed that these particles consisted of even smaller subunits that were $\sim$ 15 nm in diameter [126]. They believed these to be aggregates of oligomers that formed upon drying since they are still much larger than the particle sizes observed in mass spectrometry measurements. AFM measurements similarly demonstrate the presence of particles that are 15-25 nm in diameter [127].

Clancy and Simon published a more in depth AFM study of *Sepia* eumelanin deposited on a mica surface in 2001 [128], which was later also included in a review of the application of imaging technologies to eumelanin [129]. They showed that the most prevalent structure in *Sepia* eumelanin is an aggregate comprised of particles with diameters of 100-200 nm, as shown in figure 3.6. Filament structures were also observed on much of the surface (seen in figure 3.6, and shown in more detail in figure 3.7). These filaments were determined to have an average height of $\sim$ 5 nm and widths of tens of nanometers. Clancy and Simon used the AFM tip to physically deform an aggregate, cutting across its centre as shown in figure 3.8. The 100 nm particles were easily deformed, leaving a trough $\sim$ 30 nm deep and $\sim$ 30 nm wide, and forming a ridge of $\sim$ 20 nm along the sides of the cut. These data indicate that the tip displaces constituents that are small compared with the dimensions of the tip [129] (ie. the 100 nm particles are not the smallest subunit of this system). The authors show that these observations are consistent with previous experiments via the scheme depicted in figure 3.9. They use the eumelanin 'protomolecule' model proposed by Zajac et al. based upon WAXS measurements (as shall be described later in section 3.4.1) [130]. Flat sheets (of a size consistent with mass spectroscopy measurements) stack via π interactions to form the protomolecule, and they propose these may aggregate edgewise via hydrogen bonding interactions or stack further to form filaments.

Several microscopy studies report the observation of even smaller subunits which are more comparable to the particle sizes suggested by mass spectroscopy. Zajac et al. used STM to identify a eumelanin protomolecule of $\sim$ 20 Å lateral extent and $\sim$ 10 Å height, in agreement with the stacked oligomer model proposed based on WAXS data (figure 3.13) [130, 131]. Similarly, Gallas et al. used STM and AFM to image particles with average lateral dimensions of $\sim$ 23 Å and heights of $\sim$ 15 Å. These are proposed to be direct measurements of the fundamental unit of melanin, the 'protomolecule' [132].

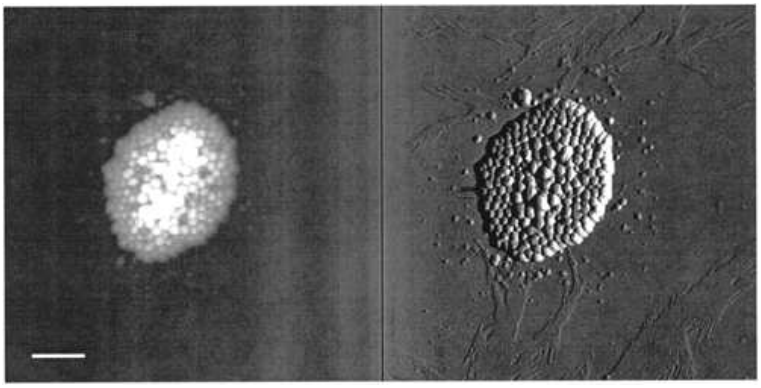

FIGURE 3.6: AFM images of a *Sepia* eumelanin aggregate deposited on mica from solution (left: contact mode, right: deflection mode). Scale bar is 970nm. The micron sized aggregate is surrounded by smaller eumelanin particles, and filaments are evident on much of the surface in the deflection image (from [128]).

3.3.2 Small angle X-ray scattering (SAXS)

SAXS is a powerful technique for determining the bulk size and shape of particles on a nanometer lengthscale, but is unable to discern features on angstrom lengthscales. Early SAXS measurements on melanins suggested that aggregates have a radius of gyration between 15 Å and 50 Å with shapes ranging from spheres to rods [133]. Later experiments suggest that eumelanin particles are sheet-like, with a mean thickness of 12.5 Å and a lateral extent of $\sim$ 54 Å [132]. These were shown to aggregate in the presence of copper ions to form long, rod-like structures with a radius of 32 Å which may aggregate further in higher concentrations of copper ions into sheets with a mean thickness of 51 Å. This study also reported small angle neutron scattering (SANS) measurements on non-deuterated eumelanin in H_2O and D_2O; these unfortunately had very poor statistical quality which is probably why SANS has not been extensively used to study melanins.

3.3.3 Wide angle X-ray scattering (WAXS)

A weak 'prepeak' was observed in WAXS measurements of the structure factor of melanin; this peak corresponds to a preferred spacing of 13 - 20 Å [134–136]. This length scale corresponds to the initial particle size of a colloidal eumelanin solution determined in another study [137], and hence was assumed to be the preferred aggregate size. It was noted that the prepeak height was dependant upon sample hydration (it decreased with drying), although the reason for this was unclear.

3.3.4 Summary

Based on the above evidence, we believe that, in a manner typical of polymers, the preferred aggregate size of eumelanin is likely to be determined by the solubility of the eumelanin in the particular solvent when it was forming, and hence this preferred aggregate size is likely to vary widely from sample to sample.

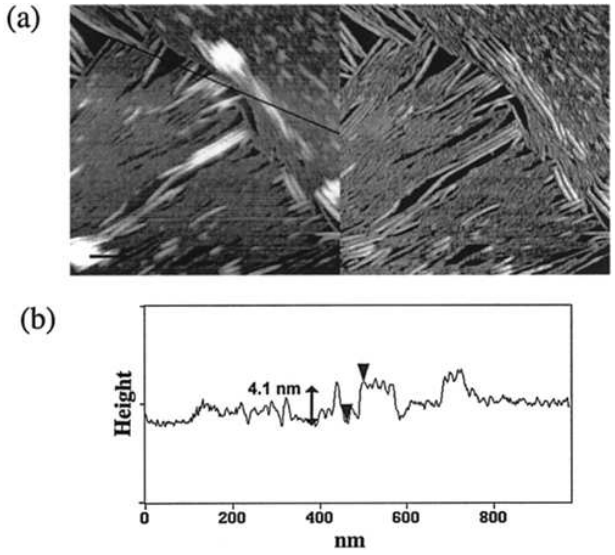

Figure 3.7: Tapping mode AFM images of eumelanin filaments dried on mica (left: height, right: phase). The scale bar is 125nm. Lower graph shows a cross section of the filaments in a plane taken along the black line in the height image. These data show that the filaments are $\sim 3-6$ nm in height and $\sim 15-50$ nm in diameter (from [128]).

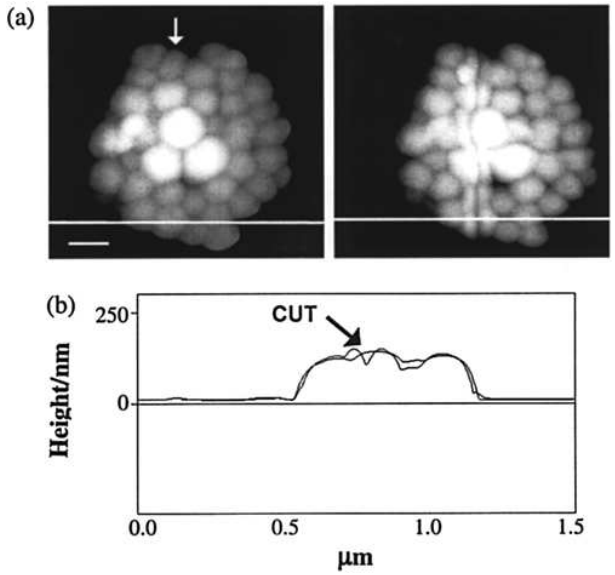

Figure 3.8: (A) Tapping mode AFM images of a *Sepia* eumelanin aggregate before (left) and after (right) the AFM tip was used to cut across the aggregate along the direction indicated by the white arrow. The scale bar is 210nm. (B) Cross-sections along the solid white line (perpendicular to the cut) shown in (A) before and after cutting the aggregate. These images show that the act of cutting displaces molecular constituents that are small compared with the dimensions of the AFM tip (from [128]).

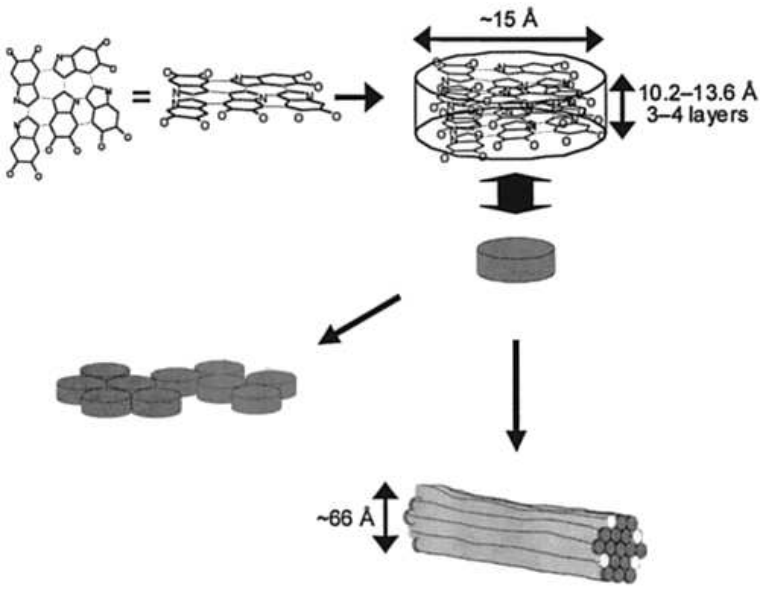

FIGURE 3.9: A schematic diagram of the initial assembly of eumelanin based on results from scattering and imaging studies. The fundamental molecular unit is taken to be a small planar oligomer built from approximately 5 DHI/DHICA units. This planar oligomer assembles through π-stacking and side-on interactions. The formation of filaments is demonstrated (from [128]).

3.4 Evidence for π-stacking in melanins

3.4.1 Wide angle X-ray scattering (WAXS)

Wide angle X-ray scattering measurements probe short length scales (around the lengths of covalent bonds in molecules). WAXS is therefore an excellent technique for examining structure on the primary scale. Additionally, WAXS can give some limited information about larger length scales such as intermolecular distances (secondary structure).

Early WAXS studies suggest that eumelanin is highly disordered, and that the monomeric units are arranged in lamellar (planar) structures that are stacked with an interlayer spacing of approximately 3.4 Å [134, 135, 137–140]. Work by Chio additionally suggested the presence of paracrystalline blocks linked together to form random aggregates [141]. Chio's measurements were consistent with lamellar structures of four to eight monomer units stacked up to three or four layers high in a manner similar to disordered graphite. The presence of paracrystalline blocks in naturally extracted melanosomes was confirmed by Bridelli et al. [142].

These WAXS results were confirmed and refined by measurements of Rayleigh scattering of Mossbauer radiation, a technique which allows separation of scattering contributions due to polymer structure and those due to bound water molecules (coordinated water contributes mostly to inelastic scattering, which is significant for eumelanin samples) [143]. The higher level of accuracy available with this technique gave confirmation of previously dismissed WAXS peaks and identified several that had not been previously observed, giving a more accurate definition of the details of eumelanin structure factor curves to match with later computational models.

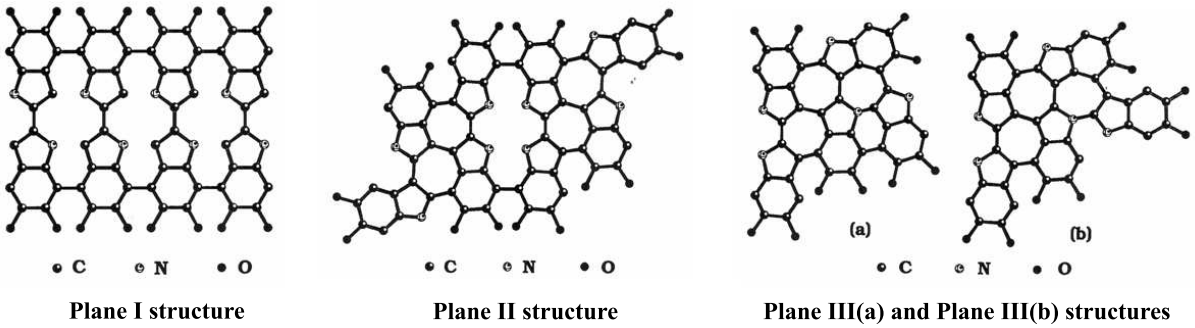

Figure 3.10: Structures investigated by Cheng et al. and compared to WAXS measurements (from [145])

All of these measurements culminated in the excellent WAXS study by Cheng et al. published in 1994 [136, 144, 145]. This work remains the state of the art, and it is unlikely that more structural information can be gleaned from WAXS measurements of eumelanin unless serious further advances are made in this technique. Cheng et al. report the first truly quantitative measurement of eumelanin WAXS (earlier studies were limited by Compton scattering and the energy of the X-ray radiation). To achieve this they apply very significant corrections to their WAXS data, firstly for Compton scattering (which is as much as five times greater than elastic scattering over the high q region because eumelanin consists of light elements), and secondly for coherent multiple scattering (melanin has a low X-ray absorption coefficient meaning that coherent multiple scattering accounts for up to 4% of the measured signal). The authors caution that due to the application of these large corrections the finer details of the structure factor should not be relied upon absolutely.

Cheng et al. reported the WAXS from natural *sepia* eumelanin, synthetic tyrosine eumelanin and synthetic L-dopa eumelanin, and showed that all three give very similar results, indicating that these synthetic eumelanins are appropriate models for natural eumelanin (at least as far as primary and secondary structure is concerned). All samples showed a characteristic spacing of 3.45 Å, which corresponds to the interlayer spacing of defective graphite [146], and hence was attributed to stacking of layers.

Cheng et al. published a second part to this WAXS study, where they proposed various molecular structures for eumelanin (shown in figure 3.10) and compared these to their WAXS results. All the proposed structures are planar (to allow for the observed stacking), and contain between 5 and 8 monomer units (to produce particles consistent with the observed preferred aggregate size). Highly symmetric structures (eg. Plane I) were dismissed since these give rise to sharp peaks not observed in the experimental structure factor. All structures with a relatively random arrangement of monomers (Planes II, III(a) and III(b)) adequately fit the experimental data, and the authors conclude that eumelanin probably consists of a statistical average of many molecular structures.

Structure factors [S(q)] and corresponding radial distribution factors [RDF(r)] calculated by Cheng et al. for two structures are shown in figures 3.11 and 3.12, with comparison to the experimental spectrum measured for tyrosine eumelanin. Figure 3.11 shows the fit with a theoretical structure of simply a single DHI monomer. Note that this structure

reproduces nearly all of the observed peaks, suggesting that WAXS is highly sensitive to the arrangement of atoms within the monomer unit, but less so to primary and secondary structure. This structure notably does not reproduce the first sharp diffraction peak; this peak does not appear in the structure factor until stacking of layers is included in the model (further evidence of π-stacking in eumelanin). This was done to produce figure 3.12. This shows the best fit that was obtained by Cheng et al., for a structure consisting of the Plane III(a) structure stacked four layers high with a gaussian distribution of spacing between layers centered around the average value of 3.45 Å, as illustrated in figure 3.13.

Cheng et al.'s work offers a significant insight into the structure of eumelanin. We caution, however, that it should not be accepted as the only possible structural model which will fit the experimental data. The authors of this study emphasise that although this structural model produces a good fit with experiment, other models may equally do so, and this data should be used predominantly for the rejection of structural models which do not agree. With the lack of further strong evidence to support or contradict this model in later experiments, it has developed into a dogma which is not founded strongly in the original experiment.

3.4.2 Effects of mild bleaching

Gallas et al. used scanning tunneling microscopy (STM) and tapping mode atomic force microscopy (TM-AFM) techniques to study the effects of mild bleaching on powdered eumelanin pigment deposited on various surfaces [147]. They discovered that bleaching had little effect on the lateral dimensions of the observed structures ($\sim$ 23 Å), whereas the height of the structures decreased significantly with bleaching (from $\sim$ 15 Å to $\sim$ 5 Å observed with STM and from $\sim$ 14 Å to $\sim$ 6 Å with AFM). They interpret this observation as the destacking of oligomer sheets with bleaching. Bleaching is expected to oxidise the oligomers, making them electron deficient and therefore not readily able to form π stacked sheets [147].

SAXS analysis of the effects of mild bleaching are consistent with these results [148]. Littrell et al. determined that before bleaching eumelanin particles are sheet-like with a thickness of $\sim$ 11 Å, and that the radius of gyration of the particles decreases from 16.5 to 12.5 Å with increased bleaching. They summarise their findings in the structural scheme illustrated in figure 3.14. The oligomers shown are covalently bonded planar sheets of monomers; these oligomers stack to form protomolecules with a spacing between layers of 3.4 Å. These protomolecules then aggregate edgewise during synthesis due to hydrogen bonding. During the bleaching process the authors propose that these hydrogen bonds are disrupted causing deaggregation and delamination. It should be empahsised that the details of this scheme are based on experimental evidence from other sources, and could not be determined from the SAXS measurements reported in this study alone.

These observations are consistent with π-stacking in eumelanins, but do not prove it unequivocally.

3.4.3 Melanin thin films

AFM analysis of eumelanin thin films prepared using an organic solvent-based synthesis shows that the films consist of relatively planar eumelanin structures [149]. These structures

generate surface steps with heights in the range 2-3 nm, and do not tend to form larger aggregates. This step height is two to three times larger than the proposed protomolecule height, possibly suggesting that this method of producing films of eumelanin leads to different surface structures than those observed in bulk eumelanin powders. However, these results do confirm the tendancy of eumelanin to form planar structures which would allow for π-stacking.

3.4.4 Transmission electron microscopy (TEM)

Very recent high resolution TEM images of synthetic dopa-derived eumelanin from our group confirm the prevalence of π-stacking in eumelanin[2]. Images revealed spherical particles of approximately 5.8 nm diameter which were formed from layers in a nano-aggregate onion-like manner, as shown in figure 3.15. The spacing between layers is measured to be ~ 3.8 Å, consistent with π-stacking distances in other indolic and porphyrin systems [151–153], and consistent with the earlier WAXS measurements of eumelanin [136].

π-stacking was also confirmed for natural eumelanin extracted from bovine epithelium[3], as shown in figure 3.16. This natural sample does not appear to have formed the nano-aggreate structures of the synthetic sample, but rather long continuous sheets. The stacking distance for the bovine eumelanin is also determined to be 3.8 Å, identical to the synthetic system. The 5.8 nm diameter particles are not evident in this sample, and interestingly, particles of the dimensions of the proposed eumelanin protomolecule are also not evident. It is possible that the image consists of protomolecules bonded edgewise to form long continuous sheets. Larger polymeric structures cannot be ruled out based upon these images, but seem unlikely based upon mass spectrometry results which suggest a predominance of low molecular weight species in these systems.

Eumelanin is notoriously insoluble, but our group has recently devised a method to solubilise synthetic eumelanin in the common organics solvents dimethyl formamide (DMF) and dimethyl sulfoxide (DMSO). Dissolving the eumelanin in these solvents does not appear to disturb its spectroscopic properties. This was done by treating the synthetic eumelanin with an aqueous solution of ammonia which is then combined with either DMF or DMSO. The

[2]Synthetic eumelanin was prepared and purified using the standard procedure outlined in reference [150] the result of which was a black powder with a solution a broad band monotonic spectrum characteristic of all melanins. The powder was ultra-sonicated in dichloroethane to create a dispersion, which was then deposited onto a lacy-carbon grid for high resolution TEM analysis.

[3]Bovine retinal epithelium (RPE) melanin was isolated and purified via the standard method outlined in reference [154]. Briefly, once the unnecessary portions of the bovine eye were discarded the RPE cells were gently brushed off Bruch's membrane. When freed, the cells were washed out of the eye cup with Dulbecco's phosphate-buffered saline without calcium and magnesium (PBSA). The cells were disrupted by mechanical homogenisation. Cellular debris was removed by centrifugation at 60 g for 7 min. The resultant low speed supernatant was centrifuged at 6000 g for 10 min to sediment the pigment granules. This sediment was re-suspended in 0.3 M sucrose and layered onto a discontinuous sucrose gradient and centrifuged on a MSE super speed centrifuge at 103,000 g for 1 hr. The melanosomes formed the pellet and were isolated and further purified by running a second identical gradient and the pellet obtained was washed four times with PBSA in order to remove the sucrose. The melanosomes obtained in this fashion were treated with hydrochloric acid to remove the protein and membrane components. The resultant melanin was washed with, and then re-suspended in PBSA.

ammonia and water are then removed under a partial vacuum to leave a solution containing the eumelanin in either DMF or DMSO. This is somewhat novel as simply sonicating eumelanin powder in either of these solvents doesn't give a solution but merely creates a suspension which settles over time. A typical TEM image for this solubilised eumelanin is shown in figure 3.17. To acquire this image the eumelanin was prepared as described previously and then precipitated by the addition of toluene. It can be clearly seen that the stacking of layers is no longer evident, indicating that dissolving the eumelanin in DMF has removed the stacking in the system. We believe, therefore, that the π-stacking of eumelanin is what causes its low solubility in most solvents.

Most significantly, these TEM images clearly demonstrate that π-stacking is present in both synthetic and natural eumelanins.

3.5 Other considerations

3.5.1 Disorder and variability

In analysing these studies it is important to remember that we are dealing with a highly heterogenous system (as evidenced by the majority of experimental data). This means that no one correct structure exists in the way that it does for specific proteins and DNA molecules, and we can deal only in statistical averages, probably best approached by using nomenclature borrowed from the science of disordered polymers. Also, we must remember that synthetic eumelanins are ultimately likely to be different from those in nature, and once we have a better grasp of the structure of the model synthetic eumelanins we must study separately the more complex natural system. Care must be taken in how the natural eumelanin is extracted, since harsh extraction techniques are known to damage the eumelanin [90].

The structure of the eumelanin is also likely to be strongly dependant on the source. Given the differences between their monomers, eumelanin will almost certainly have a different structure to pheomelanin. The ratio of DHI to DHICA in eumelanin is also known to vary widely between sources, and this will undoubtedly have a strong impact upon the primary and secondary structure. Enzymatically prepared eumelanin has been shown to contain $\sim 10\%$ DHICA, whereas natural eumelanins can contain up to 75% [40, 41].

3.5.2 Melanosomal proteins

Models of natural eumelanins must incorporate the extensive amount of protein that is known to be found in natural melanosomes. In 2003 Basrur et al. identified 56 proteins in melanosomes that are shared with other organelles and an additional 12 proteins that are specific to melanosomes [13]. The presence of melanosome-specific proteins strongly suggests that the protein in melanosomes is significant for the biological functioning of eumelanin. Light scattering studies also suggest that the enzyme tyrosinase (known to catalyse eumelanin synthesis) plays a crucial and complex role in creating the final structure of melanosomes [155]. The influence of these factors upon the structure of eumelanin has been thus far completely neglected.

3.5.3 Porosity and the uptake of metal ions

It has been shown that whole melanosomes can absorb up to 8% by weight of Fe(III) (one Fe(III) for every three to four monomeric units) without any change in morphology [156]. Additionally, a substantial amount of the metals naturally bound to eumelanin in whole melanosomes can be extracted without morphology change (more than 90% of the eumelanin is treated by suspension in water and use of a chelator such as EDTA). Both of these observations strongly suggest that the structural organisation of melanosomes allows efficient transport of metals throughout the particle [94]. Detailed structural models consistent with this are yet to be formulated, although it has been suggested that melanosomes may feature channels to allow the passage of metal ions [156]. Brunauer-Emmett-Teller surface area analysis and Barrett-Joyner-Halenda pore volume analysis indicate that the surface of the 150 nm granules observed by SEM imaging is not smooth, and that the interior of the granules is not porous, but rather that the aggregates of the granules (multi-μm sized) are porous [125].

A model recently proposed by Kaxiras et al. [82] suggested an arrangement of DHI monomers that forms a porphyrin-like structure, as shown in figure 3.18. This porphyrin-ring structure was proposed to explain the observed metal binding properties of eumelanin. Other studies, however, suggest that metal binding to eumelanin involves coordination to either the *o*-dihydroxyl groups (for Fe(III)), or to carboxylic acid groups (for Mg(II) and Ca(II)) [156]. A ring structure is therefore not necessary to explain metal binding in eumelanin.

3.5.4 Treatment with detergent

It was shown in 1973 that detergents cause dissolution of melanosomes [157]. This shows that there is significant non-convalent bonding in eumelanins, with dominant forces possibly being hydrophobic interactions. This finding is consistent with a general π-stacking model for eumelanins [94].

3.5.5 Hydration

Hydration is believed to be very important in dictating the physical and structural properties of eumelanin [41]. Some of the water contained in eumelanin is strongly bound, and removal of this water has been shown to result in increased susceptibility to autoxidation [158]. This suggests that bound water is structurally important in eumelanin. Optical scattering studies suggest that the amount of water found in eumelanin particles is dependant upon the pH at which aggregation occurs; an alkaline pH produces soft eumelanin polymers that contain a large quantity of water organised into internal cages that is difficult to extract, whereas an acidic pH produces denser granules hydrated mostly at the surface from which water can be easily desorbed [155]. The structure of eumelanin thin films also depends upon the solvent used for the deposition process, suggesting that water plays a fundamental role in determining the structure of eumelanin [149].

3.5.6 Fractal structure

Static and dynamic light scattering of the dynamics of aggregation of synthetic eumelanin reveals fractal structures in the precipitates [159]. The authors of this study identified two regimes of aggregation kinetics, one exhibiting diffusion limited aggregation (DLA, fractal dimension $d_f = 1.8$), the other reaction limited aggregation (RLA, $d_f = 2.2$). A later optical scattering study confirmed this fractal nature ($d = 2.38$) and showed that their natural eumelanin sample was characterised by particles of average molecular weight $\sim 10^6$ and a radius of gyration $R_g \sim 90$ nm, with spherical symmetry that did not have a high water content [155]. A more recent study used nitrogen adsorption isotherms to confirm again the fractal structure of eumelanin particles, and also showed that the surface structure of eumelanin is likely to be significant for the biological activity of eumelanin (porosity characteristics and surface area values suggest a strong involvement of adsorption processes) [160]. SAXS measurements also confirm the fractally rough nature of the surface of eumelanin particles [144].

3.6 Chapter conclusions

In light of the extensive challenges facing this field, it is hardly surprising that the primary and secondary structure of eumelanin remains thus far unresolved. We do, however, know the following:

- The eumelanin monomers bind preferentially through the 2, 4, 7 and 3 positions (for DHI) and 4, 7 and 3 positions (for DHICA)[4].
- Melanin consists of many chemically distinct low molecular weight species containing between 4 and 8 monomer units. Large polymeric structures have not been observed, but cannot be completely ruled out based upon the current evidence.
- Melanin is often observed to consist of particles with a lateral dimension of ~ 20 Å and a height of ~ 10 Å. However, larger particles are also frequently observed, and smaller particles are likely to be difficult to detect via many methods. We believe that the observed particle size is strongly dependant upon the solvent and environmental conditions under which the pigment was formed.
- Recent TEM images unequivocally show π-stacking is a predominant structural feature of both synthetic and natural eumelanin in a manner similar to amorphous graphite.
- Most significantly, the structure of eumelanin is highly disordered and any structural description must be a statistical average.

In light of these observations we believe that the stacked protomolecule model (figure 3.13) is the best description of the molecular structure of eumelanin, but we also caution that the extent of disorder in this system has been largely neglected thus far when this structure

[4]Note that DHI and DHICA are thought to intimately copolymerise in the natural pigment, as outlined in section 3.2

is assumed to dominate. We propose that the nomenclature that has been developed to describe disordered polymer systems could be effectively applied to describing the structure of eumelanin in a more accurate way. Polymer science may also provide insight into effective modelling techniques that incorporate this disorder more effectively.

Large polymer structures have not been directly observed in any structural measurements, and although many of the results could be consistent with polymer structures, it seems unlikely. Mass spectroscopy measurements, in particular, suggest that small oligomer structures dominate. Disorder is also shown to dominate in this system. We therefore believe, based upon this structural evidence, that the amorphous semiconductor model explanation for the broadband absorbance of eumelanin is unfounded, and the chemical disorder model is a much more likely explanation for broadband absorbance.

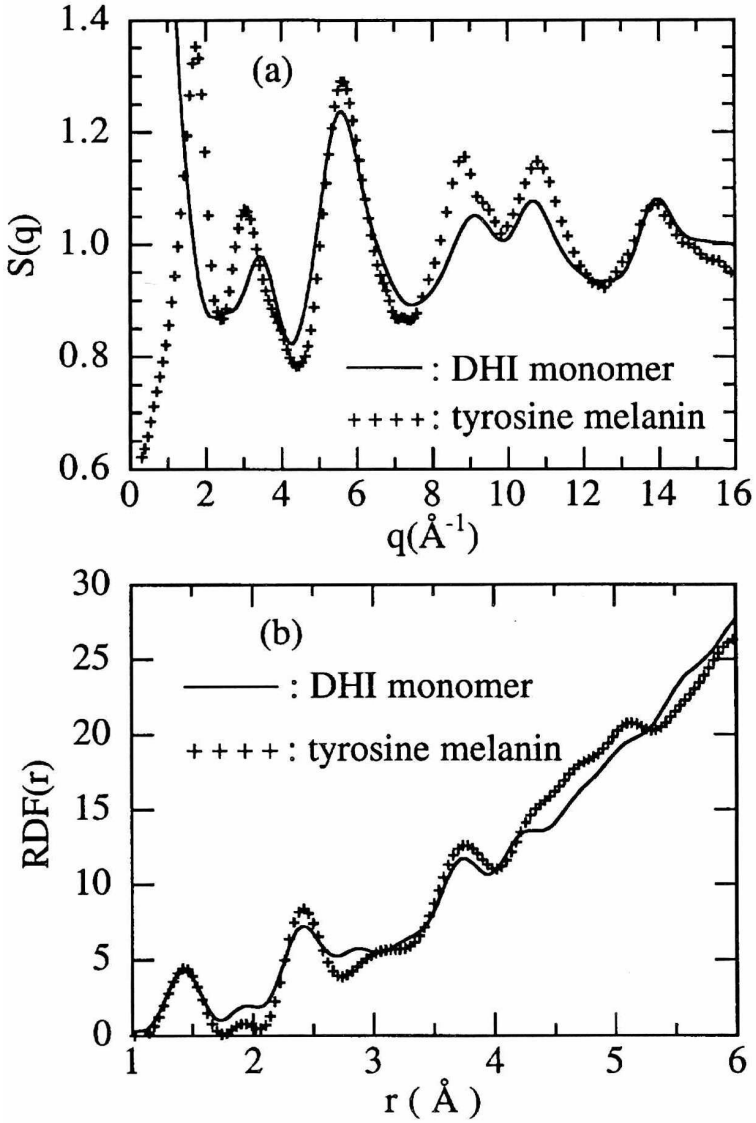

FIGURE 3.11: a) Structure factor, S(q) and b) radial distribution fuction, RDF(r) for a DHI monomer (solid line) compared with experimental WAXS measurement for tyrosine eumelanin. The structure of the monomer alone clearly reproduces most of the significant peaks, suggesting that WAXS is highly sensitive to the arrangement of atoms in the monomeric units, but less so to primary and secondary structure. (from [145]).

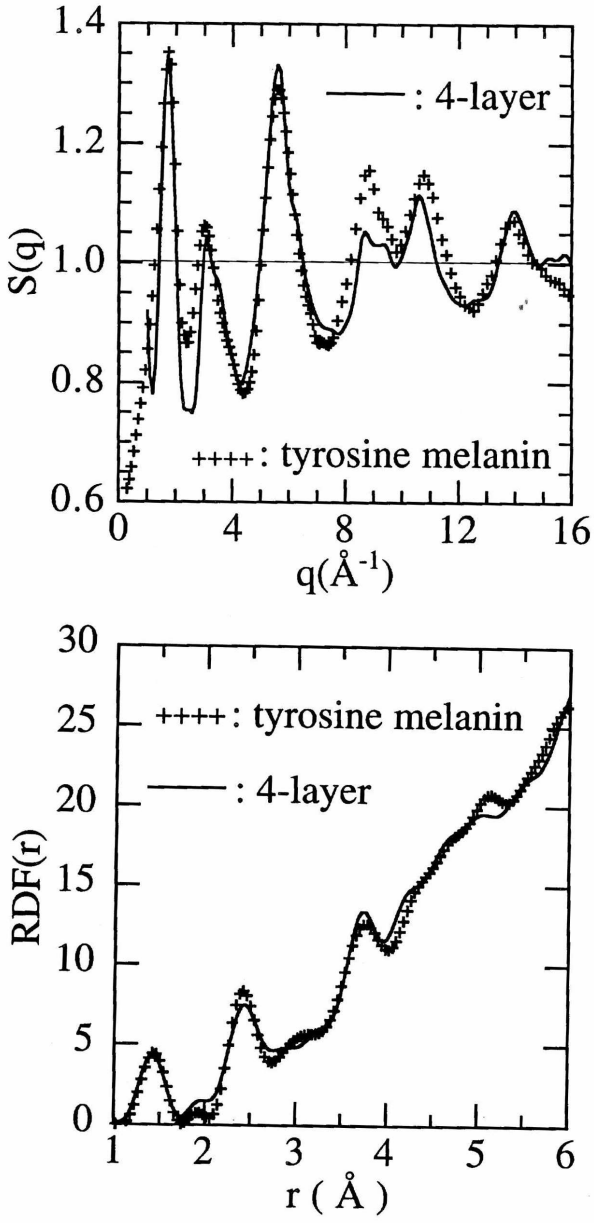

Figure 3.12: Structure factor, S(q) and radial distribution fuction, RDF(r) for a four layer aggregate model of eumelanin particles with a gaussian spacing distribution (solid line), compared with experimental WAXS data from tyrosine eumelanin (crosses). This structural model provides the best fit to the experimental data of those investigated (from [145]).

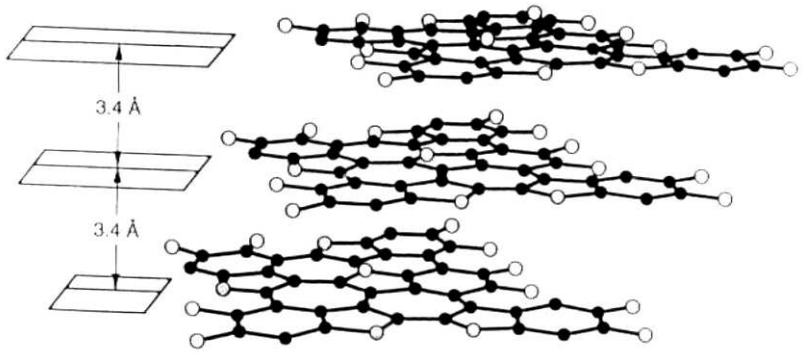

FIGURE 3.13: The oligomeric molecular model of eumelanin proposed by Zajac et al. consisting of three stacked oligomeric sheets. The overall dimensions are ~ 20 Å in lateral extent and ~ 7.6 Å in height. This has been termed the eumelanin 'protomolecule' (from [130]).

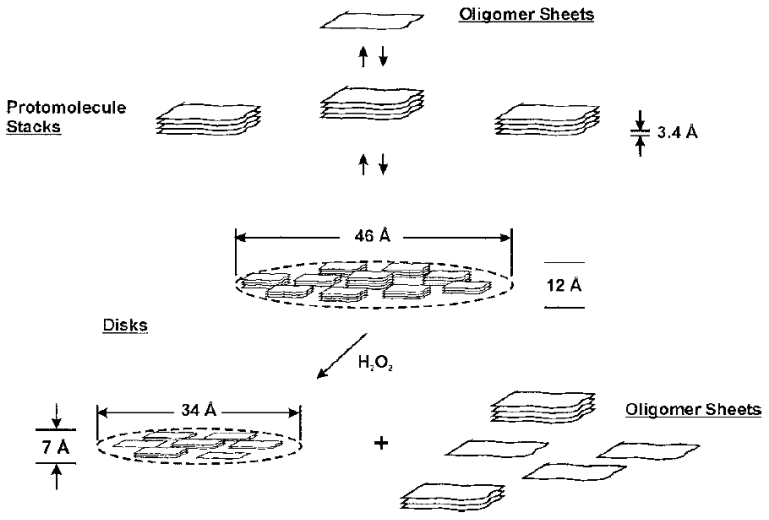

FIGURE 3.14: Structural scheme proposed by Littrell et al. indicating changes in eumelanin with bleaching. Based on evidence from other experiments they show oligomers as covalently bonded sheets which stack to form protomolecules. They propose that these protomolecules hydrogen bond edgewise into aggregates during synthesis. Hydrogen peroxide disrupts these hydrogen bonds leading to deaggregation and delamination during bleaching (from [148]).

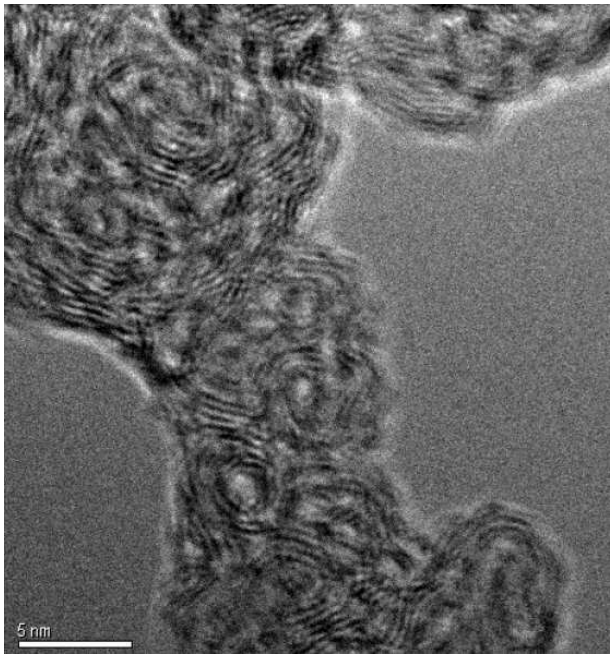

Figure 3.15: A high resolution phase contrast TEM image of synthetic dopa-derived eumelanin clearly demonstrating π-stacking of layers within onion structures. This image was obtained on material overhanging the lacy grid to remove the amorphous carbon background and increase the sample contrast.

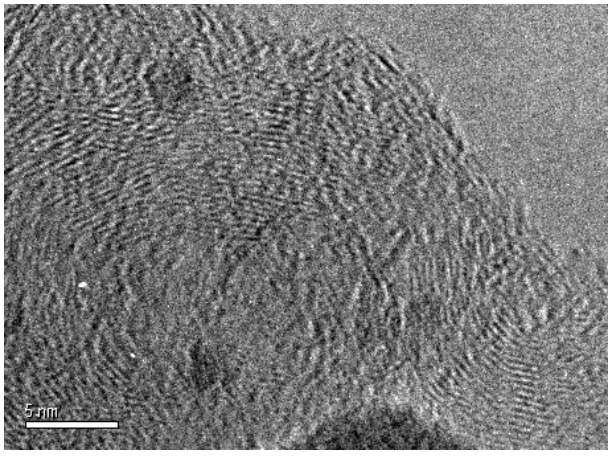

Figure 3.16: TEM image of bovine epithelium eumelanin clearly demonstrating π-stacking of layers. The lateral extent of the layers is much larger than that for the synthetic sample, likely due to different solvent conditions during formation.

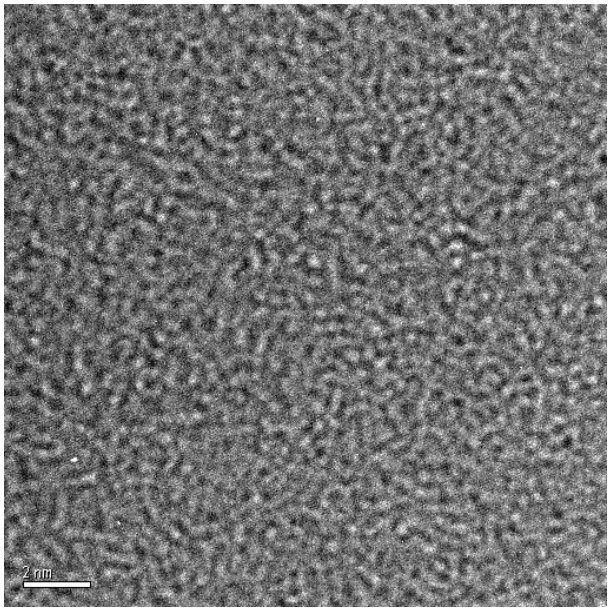

FIGURE 3.17: TEM image of synthetic eumelanin that has been fully solubilised. The stacking of layers is no longer evident, suggesting that the lack of solubility of eumelanin is due to π-stacking.

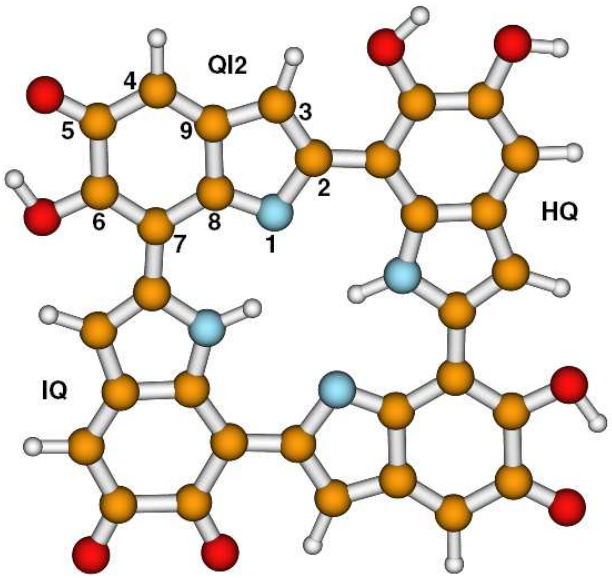

FIGURE 3.18: Hypothetical eumelanin tetramer proposed by Kaxiras et al. Gold = C, red = O, blue = N, white = H (from [82]).

4

Quantitative scattering of eumelanin solutions

4.1 Chapter abstract

We have accurately measured the optical scattering coefficient of a dilute, well solubilised eumelanin solution as a function of incident wavelength, and found to contribute less than 6% of the total optical attenuation between 210 and 325nm. At longer wavelengths (325nm to 800nm) the scattering was less than the minimum sensitivity of our instrument. This indicates that UV and visible optical density spectra can be interpreted as true absorption with a high degree of confidence. The scattering coefficient vs wavelength was found to be consistent with Rayleigh Theory for a particle radius of 38 ± 1nm.

4.2 Chapter introduction

Wolbarsht suggested in 1981 that the broadband absorption spectrum of melanin may be due to scattering, rather than electronic or physical properties of the eumelanin itself [54]. He noted that Rayleigh scattering would reproduce the broadband spectrum, and account for the increase in optical density at short wavelengths. This has very serious implications; if the measured shape of the absorption spectrum is dominated by scattering then great care must be taken when calculating optical properties. Despite several studies on the topic, optical scattering remains a significant concern. The published literature on the scattering of eumelanin solutions is sparse and not cohesive, hence it is useful at this point to briefly review past work.

The importance of optical scattering was noted by Nofsinger and Simon when they discovered that the shape of the eumelanin absorption spectrum is strongly dependant upon the particle size [17, 161]. Since scattering intensity is very strongly dependant upon particle size this could indicate that the optical density of eumelanin is dominated by scattering. To test this, they conducted photoacoustic measurments which suggested that the measured optical

density was not dominated by scattering for wavelengths longer than 400nm for any particle size fraction [17]. An earlier photoacoustic calorimetry measurement by Forest and Simon similarly suggested that scattering contributes no more than 15% of the total light extinction at 350nm [162]. Hence Nofsinger and Simon concluded that the observed dependance upon particle size was due to electronic and physical properties of the eumelanin.

Recently, a number of optical emission and excitation studies have been published, which report accurate quantitative measurement of key properties such as the radiative quantum yield as a function of wavelength [47–49, 163, 164]. Such studies provide valuable insight into energy absorption and dissipation mechanisms, as well as shedding light on the structural question. These measurements require the assumption that scattering is negligible. If this is not the case, the scattering coefficient should be measured and subtracted from the optical density to obtain the true absorption. This was attempted by Krysciak, who directly measured the optical scattering from a dilute eumelanin solution as a function of wavelength [165]. He found scattering to be negligible between 500 and 700nm, but also discovered the puzzling result of 'negative scattering' at shorter wavelengths. He suggested that this was due to multiple scattering events and absorption (which becomes very large at shorter wavelengths) decreasing the measured scattering below the previously measured baseline. Krysciak's results were non-conclusive, neither confirming nor excluding the prescence of scattering at optical wavelengths.

The following year, Kurtz reported on a theoretical prediction of the relative contributions of scattering and absorption to the optical density of eumelanin [166]. He used the real and imaginary parts of the refractive index of melanin measured in a previous study to determine the extinction, scattering and absorption cross sections over the visible spectrum. Kurtz found that in the Rayleigh regime (particle radii much less than the wavelength) absorption dominated over scattering, whereas for larger particles the two contributed equally. He emphasised the very strong dependance of scattering on particle size. The importance of this is experimentally apparent in a 2001 study by Sardar et al. where scattering and absorption coefficients were measured at four optical wavelengths between 633nm and 476nm [167]. They found that scattering far outweighed absorption at all wavelengths, contributing more than 99% of the optical density at 633nm. This result contradicts all previous studies, and is almost certainly due to the sample preparation, which resulted in what was described as 'a brown turbid suspension'. The authors state that the eumelanin particles were not solubilised and remained a particulate suspension. Under these conditions, the particle sizes would most likely be much larger than those in the well solubilised, dilute solutions typically used for spectroscopic studies [17, 47, 48, 161, 163, 164].

Other studies have attempted to use alternative methods to measure the absorption of eumelanin in the absence of scattering effects. Caiti et al. used photoacoustic phase angle spectroscopy of powdered eumelanin in the dry state [168]. This technique is insensitive to scattering, and confirmed unambiguously the decrease in the absorption of eumelanin with increasing wavelength. Unfortunately, the phase spectra do not correspond by visual inspection to absorption spectra, and interpretation remains difficult. Therefore, while this study sheds doubt on the Wolbarsht model, it does not allow correction of absorption spectra for scattering effects in a quantitative way. Similarly, a recent study by Albuquerque et al. used photopyroelectric spectroscopy to measure the optical absorption coefficient of eumelanin

in the solid state [71]. Again, the decrease in absorption with increasing wavelength was confirmed, although a direct comparison with solution measurements could not be made due to the different properties of the system. Interestingly, a band gap was observed at 1.70eV (730nm), which is possibly hidden in solution spectra by scattering.

A careful study by Vitkin et al. in 1994 gives the most quantitative estimate available of the scattering coefficient of a eumelanin solution [124]. Vitkin et al. conducted photometric measurements with a double integrating sphere system at 580nm and 633nm. They found that scattering contributed 12% and 13.5% of the total attenuation coefficient at each wavelength respectively. These values, while small, are enough to introduce significant error in the measurement of the radiative quantum yield and other optical parameters, and should ideally be corrected for. A measurement of the scattering coefficient as a function of wavelength would allow the subtraction of scattering effects from the optical density spectrum to achieve this.

If the scattering coefficient as a function of wavelength were known, the shape of the scattering spectrum could be compared with Rayleigh Theory. As discussed in chapter 3, there remains debate as to the primary and secondary structure of eumelanin: large heteropolymer, or oligomer [77, 78]. This is a most fundamental question, since it influences the interpretation of many other experiments. Since Rayleigh scattering is strongly dependant upon particle size, these scattering measurements can also be used to determine a fundamental particle size of eumelanin in solution. Hence we have conducted an integrated scattering measurement as a function of wavelength over the ultraviolet range, where scattering effects should be most significant.

In addition, the solutions used by Vitkin et al. (0.07% to 0.12% eumelanin by weight) were more concentrated than those best suited to fluorescence measurements. The broadband absorption spectrum of eumelanin gives rise to significant reabsorption and inner filter effects at concentrations above 0.0025% by weight [47, 163]. Although scattering should scale linearly with concentration it is feasible that there is less aggregation at lower concentrations, giving rise to less scattering. Hence we have made a direct measurement of the scattering coefficient at the ideal spectroscopic concentration.

In this chapter we:

1. Measure the integrated scattering from an optical spectroscopy grade eumelanin solution as a function of wavelength from 210nm to 325nm
2. Develop general equations to measure the scattering in broadband absorbing samples, and apply these to the specific case of a eumelanin solution
3. Show that the measured scattering is consistent with Rayleigh theory, and use this to estimate an approximate particle size

4.3 Experimental

4.3.1 Sample preparation

Synthetic eumelanin powder was purchased from the Sigma Chemical Co. (lot 60K1383, prepared by oxidation of tyrosine with hydrogen peroxide) and used without further purification

[1]. The powder was solubilized to form a 0.1% solution (by weight) in high purity $18.2M\Omega$ MilliQ de-ionised water adjusted to pH 11.5 with NaOH (since this is the minimum pH at which eumelanin is reliably soluble). The stock solution was gently heated and sonicated for 15 mins to ensure complete solubility.

The stock solution was then diluted to a concentration (by weight) of 0.0025%. Under such conditions a pale brown, apparently continuous eumelanin dispersion was produced. This is identical to the sample preparation used for spectroscopic analysis throughout this thesis. This concentration was selected because it maximises the weak fluorescence signal whilst minimising distorting re-absorption and probe beam attenuation effects (and hence is ideal for measuring emission).

4.3.2 Absorption spectrometry

An absorption spectrum between 200nm and 800nm was recorded for the synthetic eumelanin solution using a Perkin Elmer Lambda 40 spectrophotometer. An integration of 2nm, scan speed of 240nm/min and slit width of 3nm bandpass were used. The spectrum was collected using a quartz 1cm square cuvette. Solvent scans (obtained under identical conditions) were used for background correction.

4.3.3 Integrated scattering

Scattering measurements were made using a Perkin Elmer Lambda 40 spectrophotometer with an integrating sphere attachment (Labsphere RSA-PE-20 Reflectance spectroscopy accessory). The solution was contained within a 1mm path length quartz cuvette that was placed at the front and back of the sphere as shown in figure 4.1 b) and c) to measure the forwards and backwards integrated scattering respectively. Scattering anisotropy was not of concern for this study, since we are interested only in the total scattering signal. Measurements were taken with a scan speed of 120nm/min, a slit width of 4nm bandpass and 2nm smoothing. Since the scattering intensity was very low each scan was taken five times and averaged. The 100% reflectance intensity was determined using a labsphere certified reflectance standard, as shown in figure 4.1 a). The solvent alone was measured in both the front and back positions (figure 4.1 b) and c)) and subtracted after absorption correction (described in the following section). Some light was inevitably lost due to the non-zero size of the beam entry and exit holes in the sphere, and due to the width of the cuvette. This loss, along with the non-perfect reflectivity of the inside of the sphere was accounted for by the use of the 100% transmission measurement as a standard. A short path length cuvette (1mm) was used to minimise this loss.

4.4 Theory

Eumelanin solutions have strong, broadband absorbance, and all optical spectroscopic results are therefore affected by re-absorption (attenuation of fluorescence) and inner filter

[1]Please note that synthetic eumelanin is not necessarily identical to naturally occurring eumelanin, and comparison of results between the two systems should be made with caution, as discussed in section 1.3.

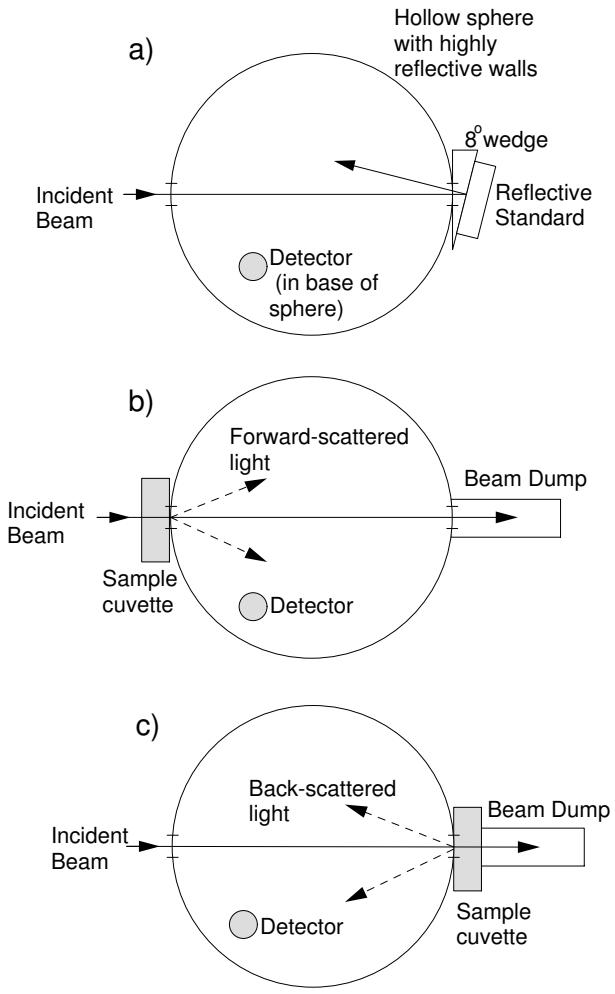

Figure 4.1: a) Geometry for 100% transmission standard. b) Geometry to collect forward scattered light c) Geometry to collect backwards scattered light.

(attenuation of the incident beam) effects[2]. Although a narrow cuvette and dilute concentration were used to minimise these effects, it was necessary to perform a careful analysis to account for attenuation of the measured scattering by absorption. We derive here a general method for correcting for absorption effects in scattering measurements that can be applied to any strongly absorbing solution.

We define α_{sf} to be the forward scattering coefficient, α_{sb} to be the backward scattering coefficient, and α_s to be the total scattering coefficient, such that $\alpha_{sf} + \alpha_{sb} = \alpha_s$. The absorption coefficient is given by α_a and the total attentuation coefficient is given by α_t. We assume that $\alpha_t = \alpha_a + \alpha_s$ (any attenuation not due to scattering is included in the absorption coefficient). Consider a cuvette of width d, with a beam of light incident from the left, as shown in figure 4.2. By definition, in a small region dx the attenuation of the beam due to each effect (forward scattering, backwards scattering or absorption) is proportional to each

[2]For a full discussion of these effects and the most basic form of the correction method please refer to chapter 6

αdx, and to the intensity of the beam in that region ($I(x)$). Therefore

$$\begin{aligned} dI(x) &= dI_{sf} + dI_{sb} + dI_a \\ &= -\alpha_{sf} I(x)dx - \alpha_{sb} I(x)dx - \alpha_a I(x)dx \\ &= -(\alpha_{sf} + \alpha_{sb} + \alpha_a) I(x)dx \\ &= -\alpha_t I(x)dx \end{aligned}$$

Integration then gives

$$I(x) = I_0 e^{-\alpha_t x} \tag{4.1}$$

which is the familiar Beer-Lambert Law, where I_0 is the intensity of light incident upon the cuvette. We want to find an expression for the total intensity of light scattered forward, I_{sf}. This will be given by the sum of the light scattered forward from each part of the cuvette, from $x = 0$ to $x = d$,

$$I_{sf} = -\int_0^d dI_{sf}$$

The negative here comes from the fact that we are summing the parts lost from the incident beam due to forward scattering to find the total amount that is scattered forwards. Using the definition of the forward scattering coefficient (α_{sf}) discussed above this is given by

$$I_{sf} = \int_0^d \alpha_{sf} I(x)dx$$

Using equation 4.1,

$$I_{sf} = \int_0^d \alpha_{sf} \left[I_0 e^{-\alpha_t x} \right] dx$$

Evaluating the integral then gives us an expression for the total amount of light scattered forwards:

$$I_{sf} = \frac{\alpha_{sf}}{\alpha_t} I_0 \left(1 - e^{-\alpha_t d}\right) \tag{4.2}$$

Similarly, the intensity of light scattered backwards (I_{sb}) is given by:

$$I_{sb} = \frac{\alpha_{sb}}{\alpha_t} I_0 \left(1 - e^{-\alpha_t d}\right) \tag{4.3}$$

4.4.1 Correction for absorption

We make the geometric approximation that the light scattered in the forward direction will travel a path length of $d - x$ to leave the cuvette (refer to figure 4.2). As the scattered light travels this distance through the eumelanin solution it will be attenuated by absorption. We assume that attenuation is only due to absorption here, and not scattering, since multiple scattering is known to be negligible for eumelanin solutions at this concentration[3]. Let the

[3]Multiple scattering is negligible if the total attenuation coefficient is linear in concentration [169, 170]. This has been shown to be the case for eumelanin solutions at the concentrations used in this study, as reported in chapter 6. Note that this is equivalent to saying that the inverse of the scattering coefficient (the average distance between two successive scattering events) is sufficiently larger than the cuvette dimension.

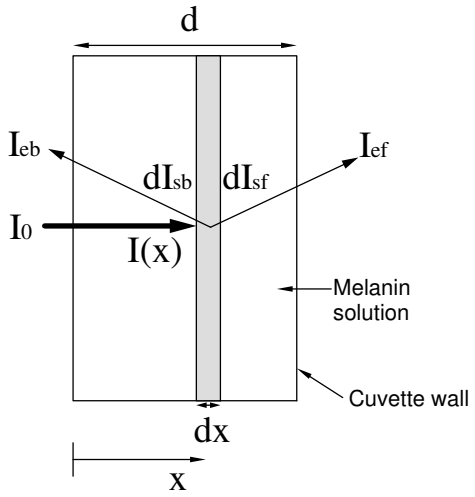

Figure 4.2: Cuvette geometry (rectangular cuvette viewed from above)

final intensity emitted forwards from the cuvette (attenuated by absorption) be given by I_{ef}. Using the Beer-Lambert Law (equation 4.1),

$$dI_{ef} = dI_{sf} e^{-\alpha_a (d-x)} \tag{4.4}$$

Therefore the total intensity of scattered light emitted forwards is given by

$$I_{ef} = -\int_0^d dI_{ef}$$

Substituting equation 4.4 gives

$$I_{ef} = -\int_0^d e^{-\alpha_a (d-x)} dI_{sf}$$

By the definition of α_{sf} we find

$$I_{ef} = \int_0^d e^{-\alpha_a (d-x)} \left(\alpha_{sf} I(x) dx\right)$$

Substituting equation 4.1 then gives

$$I_{ef} = \int_0^d e^{-\alpha_a (d-x)} \left(\alpha_{sf} I_0 e^{-\alpha_t x} dx\right)$$

Integration then yields an expression for the total amount of light emitted from the cuvette due to forward scattering (affected by absorption):

$$I_{ef} = \frac{\alpha_{sf}}{\alpha_t - \alpha_a} e^{-\alpha_a d} \left[1 - e^{-(\alpha_t - \alpha_a) d}\right] I_0 \tag{4.5}$$

Similarly, the final backwards scattered intensity emitted from the cuvette (I_{eb}) will be given by:

$$I_{eb} = \frac{\alpha_{sb}}{\alpha_t + \alpha_a} \left[1 - e^{-(\alpha_t + \alpha_a) d}\right] \tag{4.6}$$

where the absorption for back scattering occurs over a distance x (rather than $d - x$) as shown in figure 4.2.

To determine the amount of light that was originally scattered (I_{sf}) from the attenuated intensity that we measure (I_{ef}) we combine equations 4.2 and 4.5 to eliminate I_0

$$I_{sf} = \frac{\alpha_t - \alpha_a}{\alpha_t} \left(\frac{1 - e^{-\alpha_t d}}{e^{-\alpha_a d} - e^{-\alpha_t d}} \right) I_{ef} - B_f \tag{4.7}$$

where we must subtract off the background signal (B_f) which is measured from a blank cuvette (containing solvent only) to remove scattering from the solvent and cuvette walls. This process can be repeated in a very similar manner for the backwards scattering to find

$$I_{sb} = \frac{\alpha_t + \alpha_a}{\alpha_t} \left(\frac{1 - e^{-\alpha_t d}}{1 - e^{-(\alpha_t + \alpha_a) d}} \right) I_{eb} - B_b \tag{4.8}$$

where B_b is the background scattering in the backwards direction.

We have made several assumptions in the above derivations, which we will now summarise. First, it is assumed that the incident beam is scattered at a small enough angle (either forwards or backwards) that we can make geometric approximations of the path length, as described earlier. This is justified by the $cos^2(\theta)$ angular dependence of Rayleigh scattering, which therefore requires that the scattering particles are small enough to be within the Rayleigh regime (particle diameter much less than the incident wavelength). We also assume that we can define a scattering coefficient as an intensive property of a melanin solution (scattering per unit length). This is true only if multiple scattering is insignificant, which is true for sufficiently dilute solutions (as is the case here). Absorption of the scattered light, detection efficiency and background noise are all accounted for in the method outlined below. Thus, this method can be applied to any sample of small scattering particles (diameter much smaller than the wavelength of the incident light) sufficiently dilute such that the total attenuation is linear with concentration, where absorption is believed to be affecting the measured scattering intensity.

4.4.2 Comparison with experiment

We must now take into account the actual manner in which the intensity of the scattered light was measured. We define S to be the light received by the detector as a percentage of the maximum light received with a standard reflector in place of the beamdump (refer to figure 4.1).

$$S = \frac{I_{recorded}}{I_{max}} \times 100$$

Assuming the detector receives a constant fraction of the true scattered light, and 100% of the light is scattered by the standard reflector in the calibration test,

$$S = \frac{I_{scatt}}{I_0} \times 100 \tag{4.9}$$

where I_{scatt} is scattering in either the forwards or backwards direction. Thus S is the percentage of incident light scattered by the sample. However, the detected values are affected

by absorption. Let S_{mf} be the scattering signal actually measured (affected by absorption),

$$S_{mf} = \frac{I_{ef}}{I_0} \times 100$$

Since S is linear in I we can apply the recorrection given in equation 4.7 to obtain S_f, the true percentage of I_0 that is scattered forwards

$$S_f = \frac{\alpha_t - \alpha_a}{\alpha_t} \left(\frac{1 - e^{-\alpha_t d}}{e^{-\alpha_a d} - e^{-\alpha_t d}} \right) S_{mf} - S_{BGf} \tag{4.10}$$

where S_{BGf} is the background scattering signal measured in the forwards directions. Similarly for scattering backwards

$$S_b = \frac{\alpha_t + \alpha_a}{\alpha_t} \left(\frac{1 - e^{-\alpha_t d}}{1 - e^{-(\alpha_t + \alpha_a) d}} \right) S_{mb} - S_{BGb} \tag{4.11}$$

where S_b is the percentage of incident light scattered backwards, S_{mb} is this percentage attenuated by absorption, and S_{BGb} is the percentage scattered backwards in the background measurement. The total scattering, $S = S_f + S_b$ is then given by

$$S = \frac{\alpha_t - \alpha_a}{\alpha_t} \left(\frac{1 - e^{-\alpha_t d}}{e^{-\alpha_a d} - e^{-\alpha_t d}} \right) S_{mf} - S_{BGf} + \frac{\alpha_t + \alpha_a}{\alpha_t} \left(\frac{1 - e^{-\alpha_t d}}{1 - e^{-(\alpha_t + \alpha_a) d}} \right) S_{mb} - S_{BGb} \tag{4.12}$$

4.4.3 Determining the scattering coefficient

Finally, we must relate these to the total scattering coefficient, α_s. From equation 4.9 we see

$$S_f = \frac{I_{sf}}{I_0} \times 100$$

Combining this with equation 4.2 we find

$$\frac{S_f}{100} = \frac{\alpha_{sf}}{\alpha_t} \left(1 - e^{-\alpha_t d} \right)$$

Similarly for backwards scattering,

$$\frac{S_b}{100} = \frac{\alpha_{sb}}{\alpha_t} \left(1 - e^{-\alpha_t d} \right)$$

so that the total scattering, $S = S_f + S_b$ is then given by

$$\frac{S}{100} = \frac{\alpha_s}{\alpha_t} \left(1 - e^{-\alpha_t d} \right) \tag{4.13}$$

Combining equations 4.12 and 4.13 to eliminate S we find

$$\begin{aligned} \frac{\alpha_t - \alpha_a}{\alpha_t} \left(\frac{1 - e^{-\alpha_t d}}{e^{-\alpha_a d} - e^{-\alpha_t d}} \right) \frac{S_{mf}}{100} - \frac{S_{BGf}}{100} \quad &+ \quad \frac{\alpha_t + \alpha_a}{\alpha_t} \left(\frac{1 - e^{-\alpha_t d}}{1 - e^{-(\alpha_t + \alpha_a) d}} \right) \frac{S_{mb}}{100} - \frac{S_{BGb}}{100} \\ &= \quad \frac{\alpha_s}{\alpha_t} \left(1 - e^{-\alpha_t d} \right) \end{aligned} \tag{4.14}$$

Since $\alpha_a = \alpha_t - \alpha_s$ this equation has only one unknown (α_s) and can be solved (S_{mf}, S_{mb}, S_{BGf}, S_{BGb}, α_t and d are all measurable). This must be done numerically, since α_s appears non-trivially on both sides.

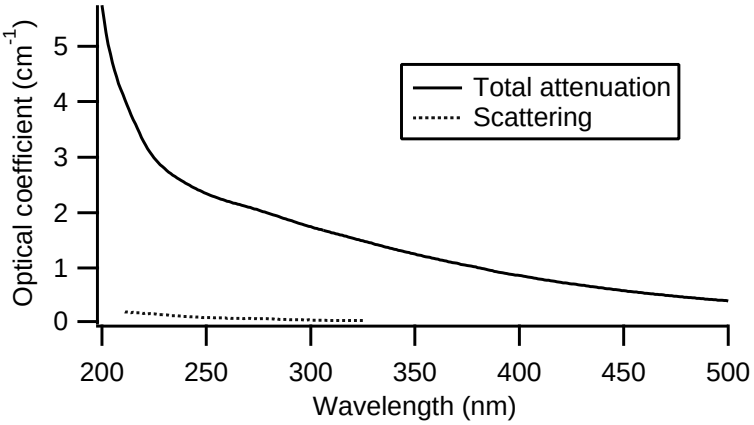

FIGURE 4.3: Total attenuation and scattering coefficients for a 0.0025% (by weight) solution of synthetic eumelanin.

4.5 Results and discussion

Figure 4.3 shows the absorption coefficient for a 0.0025% (by weight) solution of synthetic eumelanin over the visible and UV range. It is typically broadband, and in excellent qualitative agreement with previously published absorption spectra of eumelanins [17, 47, 54, 161, 165, 171–173]. The measured scattering coefficient for the same solution is also shown, as a function of wavelength between 210 nm and 325 nm (calculated using equation 4.14). For wavelengths longer than 325 nm the scattering coefficient was less than the minimum sensitivity of the instrument. We expect that scattering will decrease at longer wavelengths; Rayleigh scattering, for particles with radii smaller than ~ 50 nm has a λ^{-4} dependence, and Mie scattering, for larger particles (comparable to the wavelength of the light), is less strongly dependant upon wavelength. It is therefore reasonable to assume that the scattering coefficient is less than the measured values over the whole visible range.

The percentage of the total attenuation due to scattering ($\alpha_s/\alpha_t \times 100$) was calculated as a function of wavelength, and is plotted in figure 4.4. It can be shown that the ratio of the coefficients is equivalent to the ratio of the intensities

$$\frac{\alpha_s}{\alpha_t} = \frac{I_s}{I_s + I_a} \tag{4.15}$$

where I_a is the intensity of light lost due to absorption and I_s is the intensity of light lost due to scattering. Hence this quantity gives the percentage of the lost intensity that is due to scattering. It can be seen from figure 4.4 that scattering contributes less than 6% of the total loss at all wavelengths within the measured range. This means that measured absorption spectra (total loss spectra) of eumelanin can be assumed to be primarily due to actual absorption, and used for interpretation of spectroscopic data without further manipulation. This allows accurate determination of important quantities such as the radiative quantum yield of eumelanin [47]. This percentage is less than that measured by Vitkin et al. (12% at 580nm and 13.5% at 633nm) and possibly indicates less aggregation in our more dilute solutions [124].

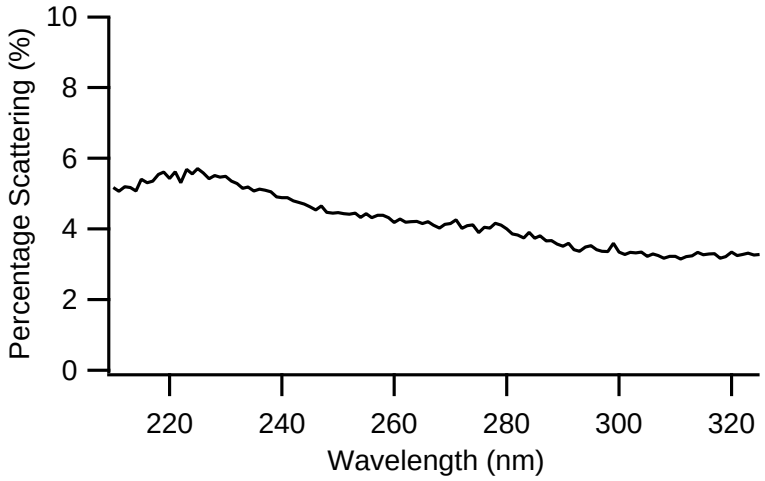

Figure 4.4: The scattering coefficient (as plotted in figure 4.3) as a percentage of the total attenuation coefficient for the same solution. We see that even over this short wavelength range where scattering should be most significant, it contributes less than 6% of the total attenuation.

4.5.1 Prediction of scattering coefficient

The scattering coefficient appears to exhibit a strong dependancy upon the wavelength (figure 4.5) which is suggestive of Rayleigh scattering, rather than Mie scattering (Mie scattering intensity exhibits only a weak dependence on wavelength for particle sizes comparable to the wavelength of the light). Let us therefore determine whether the measured scattering coefficient is consistent with Rayleigh scattering alone (no Mie scattering). As shown by Jackson [174], in the Rayligh limit (particles much smaller than the wavelength of the incident light), the scattering coefficient (α_s) for dielectric spheres of radius a with dielectric constant ϵ in a vacuum is given by

$$\alpha_s = \frac{128\pi^5}{3}\frac{Na^6}{\lambda^4}\left|\frac{\epsilon-1}{\epsilon+2}\right|^2$$

where λ is the wavelength of the illuminating light and N is the number of spheres per unit volume. This calculation can be repeated with the spheres in a solvent of dielectric constant ϵ_s to show that the scattering coefficient is then given by

$$\alpha_s = \frac{128\pi^5}{3}\frac{Na^6}{\lambda^4}\left|\frac{\epsilon-\epsilon_s}{\epsilon+2\epsilon_s}\right|^2 \tag{4.16}$$

Hence, knowing the way that the scattering coefficient depends upon the wavelength, we can estimate the size of the particles giving rise to scattering. Unfortunately, it is nontrivial to apply this to eumelanin, since the structure of the fundamental particles is unknown. This makes determining the number of particles per unit volume challenging. Nevertheless, we can make some assumptions about the structure to determine an estimate of the particle size.

In the absence of a better structural model, it is a fair assumption that eumelanin monomers form globular particles (approximately spherical). The volume of each particle will be equal to the number of monomers per particle (n_p) multiplied by the 'volume of

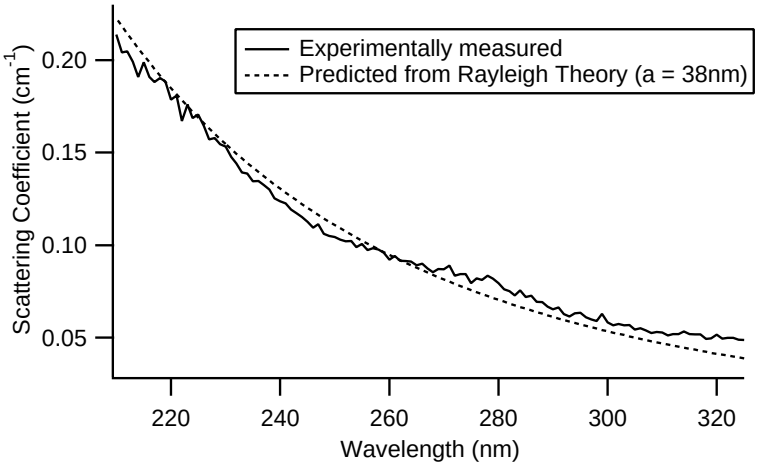

FIGURE 4.5: The eumelanin scattering coefficient, with the predicted Rayleigh scattering coefficient (from Eq. (4.17)). The best fit (plotted above) was obtained with a particle radius of 38nm.

a single monomer' (V_m) which can be estimated to be $1.2 \times 10^{-28} m^3$ [128, 136, 145]. Hence

$$n_p = \frac{4}{3}\pi a^3 \frac{1}{V_m}$$

The molecular weight of a dihydroxyindole monomer is 149g/mol. The molecular weight of an aggregate will therefore be $149 n_p$g/mol. Let C be the concentration of our solution in weight percent, such that $C = 2.5 \times 10^{-5}$ for a solution that is 0.0025% eumelanin by weight. Taking the density of the solvent (water) to be $1 g/cm^3$, $1 cm^3$ of solution will contain C grams of eumelanin, or $C/(149 n_p)$ moles of eumelanin aggregates. The number of aggregates per cm^3 of solution will then be given by

$$\begin{aligned} N &= \frac{N_A C}{149 n_p} \\ &= \frac{3 N_A C V_m}{596 \pi a^3} \end{aligned}$$

where $N_A = 6.02214 \times 10^{23}$ is Avogadros number. Applying this to Eq. (4.16) we find

$$\alpha_s = \frac{32}{447} N_A \pi^4 C V_m \frac{a^3}{\lambda^4} \left| \frac{\epsilon - \epsilon_s}{\epsilon + 2\epsilon_s} \right|^2 \tag{4.17}$$

The dielectric constant for eumelanin (ϵ) has been measured to be ≈ 2.72 at optical frequencies (633nm) [175, 176]. The dielectric constant for water (ϵ_s) is known to be ≈ 1.81 at optical frequencies [177, 178]. V_m has been estimated to be $1.2 \times 10^{-28} m^3$, as discussed above. Knowing these parameters we can fit the scattering coefficient vs wavelength curve by varying the particle size, a. Although we have used several very rough assumptions about the structure of eumelanin, the particle radius is to the third power in the equation for the scattering coefficient. The scattering is therefore strongly dependant upon the particle size and it can be determined somewhat accurately from a measurement of scattering.

This was done over the range 210 nm to 325 nm where accurate scattering data was available, as shown in figure 4.5. The best fit was found for a particle radius of 38 ± 1 nm. The good fit of the data to Rayleigh scattering theory suggests that we are in fact measuring scattering, and not another phenomemon (instrumental or otherwise). This particle size is larger than that predicted by Cheng et al. [136, 145]. Larger particles were measured by Vitkin et al., who report a particle size distribution for a similar sample preparation that has most particles with radii in the range 10-70nm [124].

We caution that this analysis assumes a monodisperse particle size in solution, which is likey to not be the case. If a distribution of particle sizes are present then the measured α_s will be proportional to the integrated particle size distribution ($f(a)$) multiplied by particle size to the third power:

$$a_s \propto \frac{1}{\lambda^4} \int_0^\infty f(a) a^3 da \tag{4.18}$$

Note that this expression is heavily weighted towards larger particles because of the a^3. This means that the mean particle size in our solution is in fact smaller than 38 nm, and may be consistent with that predicted by Cheng et al [136, 145]. Rather than being a mean particle size, this value should be interpreted as an upper bound for the mean particle size in our solution. Due to the integration we are unfortunately unable to extract a particle size distribution via this method, but alternative techniques such as dynamic light scattering may have this capability for this system (this is recommended as an avenue of future research).

It is not clear how these *in vitro* particle sizes relate to those *in vivo*. Biologically, eumelanin is synthesised in cellular organelles called melanosomes whose size and shape varies widely depending upon the species and where the cell is located in the organism. The ultrastructure of these melanosomes also varies widely, and is very poorly characterised [179]. The structure will also be heavily influenced by the protein to which eumelanin is strongly bound *in vivo*. By studying synthetic eumelanin samples (protein free, and much simpler than the complete biological system) we aim to understand the behaviour and structure of the fundamental eumelanin particles. This will hopefully shed light on the ultrastructure of melanosomes and therefore their biological functionality.

Melanosomes can be quite large (2 - 3 μm) and therefore could be expected to scatter light strongly (as will tissue generally, being a complex collection of organelles of varying sizes). It has been questioned whether this scattering could potentially contribute to photoprotection, or whether eumelanin absorption is solely responsible. If the outler layer of skin were highly scattering this would shield inner cells in an identical manner to an absorbing layer of the same optical density. In light of these results, however, we believe that eumelanin functions primarily by absorbing light and dissipating it non-radiatively, rather than scattering the incident radiation.

4.6 Chapter conclusions

The integrated scattering of a eumelanin solution was measured as a function of incident wavelength, and found to contribute less than 6% of the optical density between 210nm and 325nm. This means that eumelanin absorption spectra can be interpreted as actual absorption with a high degree of confidence, and allows the calculation of many other optical

spectroscopic quantities, such as the radiative quantum yield, without direct subtraction of scattering [47]. Hence, as long as eumelanin spectroscopic solutions are appropriately prepared and well solubilised, scattering is not a concern. The scattering coefficient vs wavelength was found to fit Rayleigh Theory with a particle radius of 38 ± 1nm, which forms an upper bound on the mean particle size in our solution. This is larger than the fundamental particle sizes previously reported from X-ray scattering and microscopy studies [128, 136, 145], and is therefore consistent. Knowing the physical structure of eumelanin particles is essential for interpretation of spectroscopic results, and therefore for understanding the de-excitation pathways in eumelanin and its biological functionality.

5
The dipole strength of eumelanin

5.1 Chapter abstract

We report the transition dipole strength of eumelanin in the ultra-violet and visible. We have used both theoretical (density functional) and experimental methods to show that eumelanin is not an unusually strong absorber amongst organic chromophores. This is somewhat surprising given its role as a photoprotectant, and suggests that the dark colouring *in vivo* (and *in vitro*) of the eumelanin pigment is a concentration effect. Furthermore, by observing the polymerisation of a principle precursor (5,6-dihydroxyindole-2-carboxylic acid) into the full pigment, we observe that eumelanin exhibits a small amount ($\sim 20\%$) of hyperchromism (i.e. the reaction process enhances the light absorption ability of the resultant macromolecule relative to its monomeric precursor). These results have significant implications for our understanding of the photophysics of these important functional biomolecules. In particular, they appear to be consistent with the chemical disorder model of eumelanins.

5.2 Chapter introduction

The work described in this chapter is motivated by a desire to probe the chemical disorder hypothesis and specifically investigate whether eumelanin as a pigment has an unusually high absorbance (relative to other organic and bio-organic chromophores) in the UV and visible. To the first order, if eumelanin was merely a disordered ensemble of chemically distinct macromolecules, one would expect the "system" to possess an integrated transition dipole moment similar to that of the sum of its individual parts. To this end, we have measured the extinction coefficients for a number of species, namely: synthetic eumelanin, DHICA (as a monomer and during its polymerization to eumelanin), tyrosine and fluorescein (a strongly fluorescent, well characterised dye, used here as a standard for comparison). Chemical structures of these molecules are shown in figure 5.1. From these spectra we have

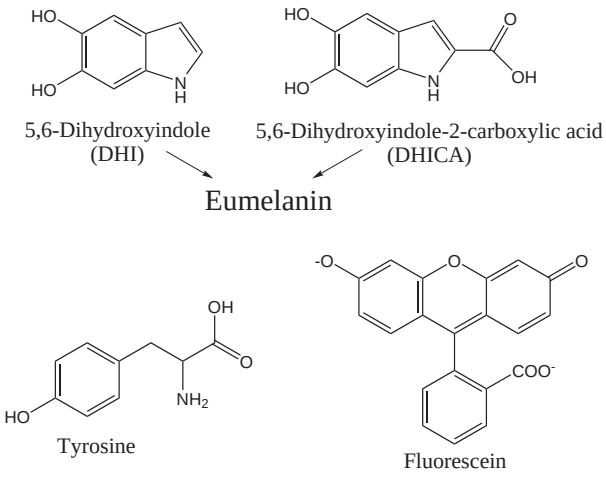

FIGURE 5.1: The chemical structures of molecules relevant to this study. DHI and DHICA are the basic monomeric building blocks of the eumelanin macromolecule, whereas tyrosine is an earlier precursor. Fluorescein is a commonly used organic dye and quantum yield standard.

extracted dipole strengths, transition dipole moments and oscillator strengths. In addition, we have measured fluorescence spectra for tyrosine, fluorescein and eumelanin and used these to determine radiative rates and lifetimes. These have been compared to literature values for verification of our methods. For a final comparison, transition energies and dipole strengths of these compounds have been predicted from first principles via density functional theory.

5.3 Theory

The dipole strength of an electronic transition (D, in units of C^2m^2) can be determined from an experimentally measured absorption spectrum via the following expression [180, 181]

$$D = \frac{3\epsilon_0 \hbar c}{\pi N_A} n \int_{\Delta\nu} \frac{\epsilon(\nu)}{\nu} d\nu \tag{5.1}$$

where all constants are in SI units, $\epsilon(\nu)$ is the extinction coefficient expressed in m^2mol^{-1} (as defined in equation 2.5, $\Delta\nu$ is the frequency range over which the transition occurs and n is the average refractive index of the solvent in a region of space around the chromophore of the order of an optical wavelength (we approximate this here by the refractive index of the bulk solvent). This calculation assumes that you can clearly identify and integrate over a single electronic transition (which is not always possible in an experimental spectrum). Note that 1 m^2mol^{-1} = 10 L mol^{-1} cm^{-1}. D may be converted to the commonly used units of $debye^2$ via 1 $debye^2 = 1.1127 \times 10^{-59} C^2m^2$. From the dipole strength one may then determine the magnitude of the transition dipole moment $\mu_{ij} = e\langle j|\vec{r}|i\rangle$ between two states $|i\rangle$ and $|j\rangle$,

$$D = |\mu_{ij}|^2. \tag{5.2}$$

Note that for clarity we have supressed the subscripts i and j on D and other parameters where they are understood. We can also determine the dimensionless oscillator strength, f,

$$f = \left(\frac{4\pi m_e \nu}{3e^2\hbar}\right) D \tag{5.3}$$

where e and m_e are the charge and mass of an electron respectively, ν is the frequency of the transition, and all values are in SI units (including D in C^2m^2).

5.3.1 Radiative rates

The radiative rate of a material in a medium of index n is given by the Strickler-Berg relation [180],

$$A = \frac{1}{4\pi\epsilon_0}\frac{64\pi^4 n\langle\nu^{-3}\rangle^{-1}}{3hc^3}D \tag{5.4}$$

where all quantities are in SI units (including D in C^2m^2). A is the radiative rate in s^{-1} and the angular brackets indicate an average weighted by the emission spectrum

$$\langle\nu^{-3}\rangle^{-1} = \frac{\int f(\nu)d\nu}{\int \nu^{-3}f(\nu)d\nu} \tag{5.5}$$

where $f(\nu)$ is the emission spectrum. A is also known as the Einstein coefficient of spontaneous emission [181]. The lifetime of the excited state (τ) is then given by

$$\tau = \frac{\Phi}{A} \tag{5.6}$$

where Φ is the radiative quantum yield (the ratio of photons emitted to photons absorbed by a material) [182].

5.3.2 The effect of the solvent

The dipole strength of a chromophore in solution may be changed from the intrinsic dipole strength of the isolated chromophore (gas phase). To a good approximation, although different solvents will change the position and width of the absorption peaks (and hence the extinction coefficient), in the absence of specific solute-solvent interactions (such as hydrogen bonding or conformational changes) the change in dipole strength of the chromophore in solution depends only on the solvent refractive index [183, 184]. This result can be obtained from "reaction field" type models [185], modelling the solvent as a bath of harmonic oscillators, for which sum rules can be obtained [186]. The dipole strengths obtained experimentally in this chapter are therefore expected to differ from those of an isolated molecule, as calculated by NRLMOL[1]. Corrections may be possible through a reaction field type calculation [183, 187].

[1]NRLMOL is the Naval Research Laboratory molecular orbital library, a piece of software designed to perform density functional theory calculations on isolated molecules. Our use of this program is explained more fully in section 5.4.4

5.4 Experimental

5.4.1 Sample preparation

Eumelanin

A eumelanin stock solution was prepared in a manner identical to that described in section 4.3.1. This stock solution was diluted to concentrations (by weight) of 0.001%, 0.0025% and 0.005%. The dipole strength was determined for each solution (via measurement of the absorption spectrum, as described below) over the frequency range indicated in table 5.1 and averaged to give the reported value.

DHICA

DHICA was synthesised as reported by Tran *et al.* [76]. It was solubilised in pH 9 NaOH at a 2 mM concentration. The absorbance was measured and scaled using a published value for the extinction coefficient at the 316 nm peak [188]. The oxidative polymerisation of this solution was monitored by the extraction of aliquots at 0, 0.5, 1, 2, 4, 8, 12, 24, 51 and 74 hrs. For a more complete experimental method see reference [76].

Tyrosine

D-Tyrosine (99%, batch 14424MA) was purchased from Aldrich and solublised in 1M HCl to a concentration (by weight) of 0.0025%.

Fluorescein

Fluorescein is known to have various forms, but at the pH used in this study it exists in the dianionic form as shown in figure 5.1 [189]. Fluorescein (Aldrich, F2456-100G, Batch 09014PA, Dye content ca. 95%) was solubilized in 0.1M NaOH solution and diluted to give 5 solutions of varying concentration (2×10^{-5}% to 5×10^{-6}% by weight). The dipole strength was determined for each solution over the frequency range indicated in table 5.1 and averaged to give the reported value.

5.4.2 Steady state spectroscopy

Absorbance spectra were measured in a manner identical to that described in section 4.3.2. Emission spectra were measured as described in chapter 6[2].

5.4.3 Time resolved fluorescence

The excited state lifetimes were measured as follows. The sample was excited with a Tsunami titanium sapphire laser (Spectra-Physics Lasers Inc, Model 3960C-X3BB) tuned to 780 nm, with a pulse length of 73 fs and power output of 7.50 W. A frequency doubling crystal was

[2]These emission spectra are discussed in more detail later in chapter 6, so we leave the experimental method with the complete discussion

used to produce a beam of 390 nm. A pulse picker on a 1/10 ratio gave an 8 MHz pulse train with an extinction ratio of approximately 400. The resulting beam was passed through a 390 nm bandpass filter, then used to excite the eumelanin solution contained within a quartz cuvette. The cuvette was measured inside the enclosed cuvette holder (PicoQuant GmbH Rudower Chausse 29, Fluotime 200) with inbuilt detection system (ScienceTech Inc Model no. 9030DS). Emission was detected at 475 nm with excitation and emission slits both 2 mm, the iris fully open to give the maximum signal level, and an acquisition time of 1000 s. A blank solution (solvent only) was measured for background subtraction. An instrument response function (IRF) was measured from a Ludox standard scattering solution at the incident wavelength (390 nm) with settings that produced a maximum intensity approximately equal to that of the eumelanin data (excitation and emission slits: 2 mm, acquisition time: 1 s, iris fully closed to prevent detector saturation). Data was deconvolved via an iterative reconvolution process using the multiexponential fluorescence decay fitting software 'PicoQuant FluoFit'.

5.4.4 Density functional theory calculation details

First principles density functional theory calculations were performed using the Naval Research Laboratory molecular orbital library (NRLMOL) [190–197]. NRLMOL performs massively parallel electronic structure calculation using gaussian orbital methods. We fully relaxed the geometry with no symmetry constraints using the Perdew, Burke and Ernzerhof (PBE) [198] exchange correlation functional, which is a generalized gradient approximation (GGA) containing no free parameters.

Minimum energy structures were calculated for DHICA, tyrosine and fluorescein (chemical structures shown in figure 5.1). We then calculated the strength of each absorption line as the sum over all states of both levels [199] (recall $\mu_{ij} = e\langle j|\vec{r}|i\rangle$).

$$S_{ij} = S_{ji} = \sum_{ij} \mu_{ij}.\mu_{ij} \tag{5.7}$$

This quantity can be related to the radiative rate A (the Einstein coefficient) via

$$A_{ji}g_j = \frac{64\pi^4\nu^3}{3hc^3}S_{ji} = \frac{2.02\times10^{18}}{\lambda'^3}S'_{ji} \tag{5.8}$$

where no summation over repeated indicies is implied. In the final expression λ' is measured in Angstroms and S'_{ji} is in atomic units [199]. The degeneracy g_j is treated explicitly by NRLMOL. The radiative rate A can be related to the dipole strength via equation 5.4 to give the following expression for the dipole strength

$$D_{ij} = 6.438S'_{ij} \tag{5.9}$$

where D is in debye^2 and S' is in atomic units. The dipole strengths of all transitions with energies in the experimental frequency ranges (see table 5.1) were summed to give the dipole strength values given in table 5.2.

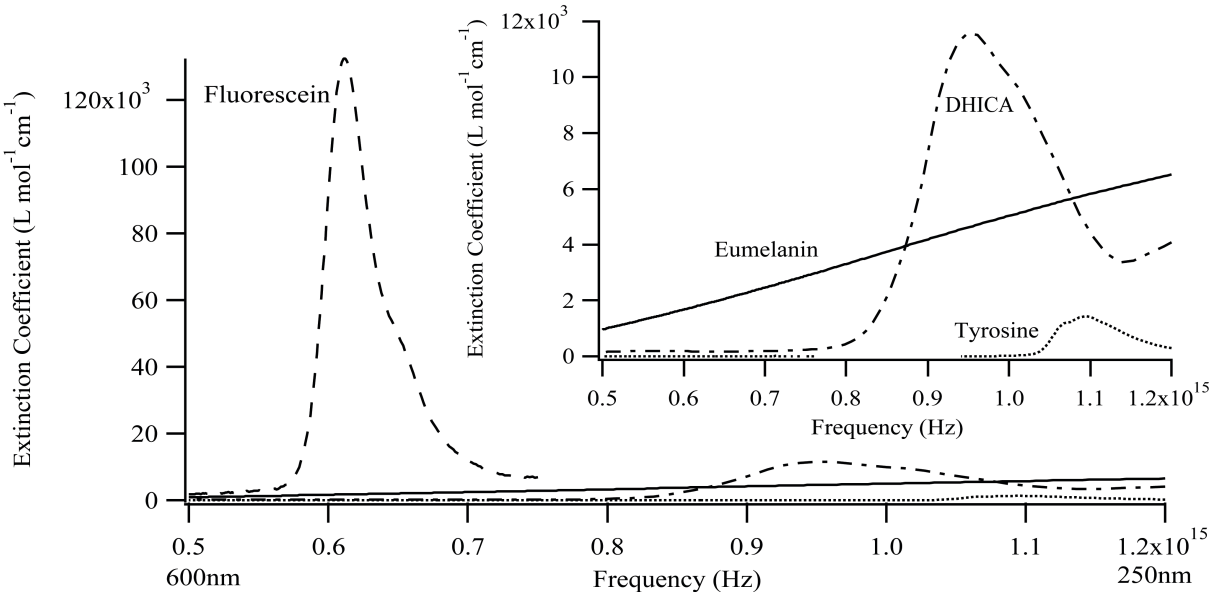

FIGURE 5.2: The extinction coefficients of synthetic eumelanin (solid), DHICA (dot-dash) tyrosine (dotted) and fluorescein (dashed). The inset shows DHICA, eumelanin and tyrosine data with a different vertical scale (not visible on full plot due to the order of magnitude greater extinction coefficient of fluorescein compared to the other samples). For eumelanin, the extinction coefficient is expressed *per monomer*. Note the unusual broadband shape of the eumelanin spectrum as compared with the peaked spectra of the other organic molecules. These spectra are in qualitative and quantitative agreement with those in literature [200–203]. The much greater magnitude of the fluorescein extinction coefficient is reflected in its much larger dipole strength (see Table 5.1).

5.5 Results and discussion

5.5.1 Extinction coefficients

Figure 5.2 compares the measured extinction coefficients for tyrosine, eumelanin, fluorescein and DHICA as determined experimentally according to equation 2.5. The extinction coefficients for all compounds are in good agreement with literature values [200–203], both qualitatively and quantitatively. The extinction coefficient of eumelanin is reported here *per monomer*, where the molar weight of a monomer is taken to be the average molar weight of DHI and DHICA (171g mol^{-1}), since we assume that our sample consists of an even mixture of these monomers [41, 99, 204]. For such a macromolecule, this is the most meaningful way to express the extinction coefficient. Note the broadband shape of the eumelanin spectrum compared with the more typical peaked spectra of the other organic chromophores. Knowing that our measured extinction coefficients are in good agreement with previously published values, we can now determine other parameters from this data with confidence.

5.5.2 Experimentally measured transition dipole strengths

Dipole strengths, transition dipole moments and oscillator strengths for each of these compounds were determined from the measured extinction coefficients according to Eqs. (5.1),

	D (debye^2)	μ (debye)	f (dimensionless)	$\Delta\nu$ (10^{15} Hz)
Tyrosine	1.6	1.3 [1.04]	0.027 [0.019]	0.375 to 1.2
Eumelanin	$37N$	$6.1\sqrt{N}$	$0.53N$	0.5 to 1.2
DHICA	31	5.6	0.46	0.5 to 1.2
Fluorescein	140	12 [7.0]	1.3 [0.46]	0.5 to 0.75

Table 5.1: Absorption parameters as defined in the theory section extracted from extinction coefficients in figure 5.2 (D: dipole strength, μ: transition dipole moment, f: oscillator strength). These are typically determined for a particular peak or transition, but this is not possible for a broadband spectrum such as that for eumelanin, hence the frequency ranges over which the integrations of experimental data were performed to determine the dipole strength and other parameters are as listed ($\Delta\nu$). Data in brackets are from reference [202] over the same frequency range for comparison. Discrepancies between these results and those found in literature may be attributed to difference in solvents (which can affect the dipole strength via second order effects) and uncertainty in concentration. Since the primary and secondary structure of eumelanin is unknown it is necessary to determine these parameters in terms of N, the average number of monomers per oligomer (as described in the text). The dipole strength per monomer of eumelanin (37) is comparable to that of DHICA (31), much larger than that of tyrosine (1.6), and much smaller than that of fluorescein (140). This suggests that eumelanin is not an exceptionally strong absorber as might have been assumed due to its photoprotective biological role.

(5.2) and (5.3), and are shown in table 5.1. For eumelanin the average molar weight is taken to be the average number of monomers per oligomer (N), multiplied by the average molar weight of the two forms of eumelanin precursor (171g mol^{-1}). The extinction coefficient and other parameters discussed in section 5.3 then become functions of N, and are expressed as such in tables 5.1 and 5.4. Values in brackets for tyrosine and fluorescein are from reference [202] for comparison. Our results are consistent with literature values; discrepancies can be attributed to differences in solvent (which may affect the dipole strength via second order effects). Refer to section 5.3.2 for more details.

Note that the parameters shown in table 5.1 are usually calculated over a particular single transition, whereas for eumelanin this is unachievable due to the broadband shape of the absorption spectrum. For typical compounds, the extinction coefficient is small outside of a clear peak, and hence increasing the integration range will not greatly affect the estimate of the dipole strength. For eumelanin, however, there is no clear peak, so increasing the integration range (particularly towards the UV) will increase the estimate of the dipole strength. We have chosen the relevant integration range 250 nm to 800 nm, which gives an order of magnitude estimate of the dipole strength in a critical range from a functional perspective. DHICA was integrated over the same range as eumelanin so that a direct comparison is possible. Tyrosine and fluorescein exhibit clear peaks, so that the integration range is not particularly important.

Transition dipole moments and oscillator strengths have also been included in table 5.1 since these are other commonly used measures of the same parameter. Note that if

eumelanin forms large polymer structures this would make the number of monomers per oligomer (N) very large, and hence the dipole strength very large. This does *not* mean, however, that the polymerisation process enhances the absorption of a solution of eumelanin relative to its precursors, since, as the polymerisation process occurs, the total number of species in the solution decreases. This means that, although the dipole strength increases, the concentration decreases in such a way that the optical density of the solution may stay approximately constant.

In summary, the dipole strength per monomer of eumelanin over the UV/visible range was determined to be approximately 40 debye^2 (table 5.1). This is greater than the dipole strength of tyrosine (1.6 debye^2), comparable to that of DHICA (31 debye^2), and less than that for fluorescein (140 debye^2). These results are consistent with the predictions of the chemical disorder model, and suggest that eumelanin is neither an exceptionally strong absorber (as one might expect due to its biological role as a photoprotectant), nor exceptionally weak.

5.5.3 Transition dipole strengths from density functional theory

First principles quantum chemistry calculations are routinely used as a standard tool for assessing such properties of materials as optical and electrical parameters, electronegativity, hardness, softness, molecular energetics and other properties [205]. Here we use density functional theory (DFT) to assess whether our experimentally determined optical parameters are in agreement with quantum chemical models for these systems. This provides important validation of our experimental results, and a benchmark for further use of DFT in studies of this nature.

The transition dipole strengths and energy gaps (listed as frequencies) of the structurally well characterised molecules examined here were calculated using DFT, and are listed in table 5.2. More than one transition was predicted to lie within the experimental frequency ranges, most of which had negligible dipole strengths. Hence only those predicted to have substantial magnitude are listed. The fourth column lists the main transitions that are predicted to make substantial contributions to the dipole strength. Note that for tyrosine the HOMO to LUMO transition has negligible intensity (and hence is not listed), whereas that transition dominates the dipole strengths of DHICA and fluorescein. Similarly, for both DHICA and fluorescein the HOMO-1 to LUMO transition makes the next most intense contribution to the dipole strength, and is located close in energy to the HOMO to LUMO transition. For tyrosine, however, all higher energy transitions with substantial intensity were far removed from the initial peak, occurring at much higher energies and close to the upper bounds of the experimental frequency range. With the known tendancy of DFT to underestimate energy gaps (as discussed below), we believe that these higher energy transitions were not related to the experimentally measured extinction coefficient peaks, and hence have not been considered in this analysis. It is curious that tyrosine differs qualitatively from DHICA and fluorescein; we believe this is an interesting topic for further investigation.

The electron densities calculated by DFT of the important molecular orbitals for these molecules are shown in figure 5.3. For DHICA and fluorescein the HOMO to LUMO and HOMO-1 to LUMO transitions are those predicted to make significant contributions to the

	D_{DFT} (debye^2)	$\nu(10^{15}$ Hz)	Transition
Tyrosine	11	0.987	HOMO to LUMO+1
DHICA	49	0.691	HOMO to LUMO
	10	0.743	HOMO-1 to LUMO
Fluorescein	90	0.454	HOMO to LUMO
	9.2	0.500	HOMO-1 to LUMO

Table 5.2: The transition dipole strengths (D_{DFT}) and frequencies (ν) for tyrosine, DHICA and fluorescein predicted by DFT. Only the most prominent transitions (those with significant magnitude) in the experimental ranges used in this study are listed. HOMO-LUMO gap for DHICA has been previously reported [77].

dipole strength. It is clear that the electron densities of each of these three important molecular orbitals for DHICA and fluorescein have nodes in the plane of the molecule, and therefore can be attributed to π orbitals. This suggests that both of these transitions are $\pi - \pi^*$, as would be expected for transitions at these energies for organic molecules of this type. It is interesting to note that while DHICA has a relatively even electron distribution in all states shown, fluorescein shows a significant movement of electron density from one part of the molecule to the other in both the HOMO to LUMO and HOMO-1 to LUMO transitions.

The electron densities for tyrosine are more difficult to interpret because this molecule has a non-planar section. All three molecular orbitals appear to have π character, however, indicating that the HOMO to LUMO+1 transition (the only transition of experimental relevance with significant intensity) is also a $\pi - \pi^*$ transition. Interestingly, both the HOMO and LUMO+1 appear to have the electron density localised largley on the aromatic group, whereas the LUMO (not involved in any significant transitions) has electron density localised on the non-aromatic tail group.

Transition dipole strengths and frequencies for each of these molecules calculated from DFT are shown in table 5.3, compared with those determined from the experimentally measured extinction coefficient for these molecules. It can be seen that PBE-DFT consistently underestimates the energy gap by $\sim 10 - 30\%$, as is typically observed [206]. Due to broadening of experimental data we must choose an integration range to achieve a quantitative comparison of these DFT predicted dipole strengths to experiment. Since there were multiple transitions predicted for the energy ranges used experimentally, the dipole strengths of all transitions in the range for DHICA and fluorescein were summed to give the value for comparision to experiment, as shown in table 5.3. For tyrosine, the positioning of the DFT predicted peaks suggested that only the HOMO to LUMO+1 transition should be compared to the experimental data (as discussed above).

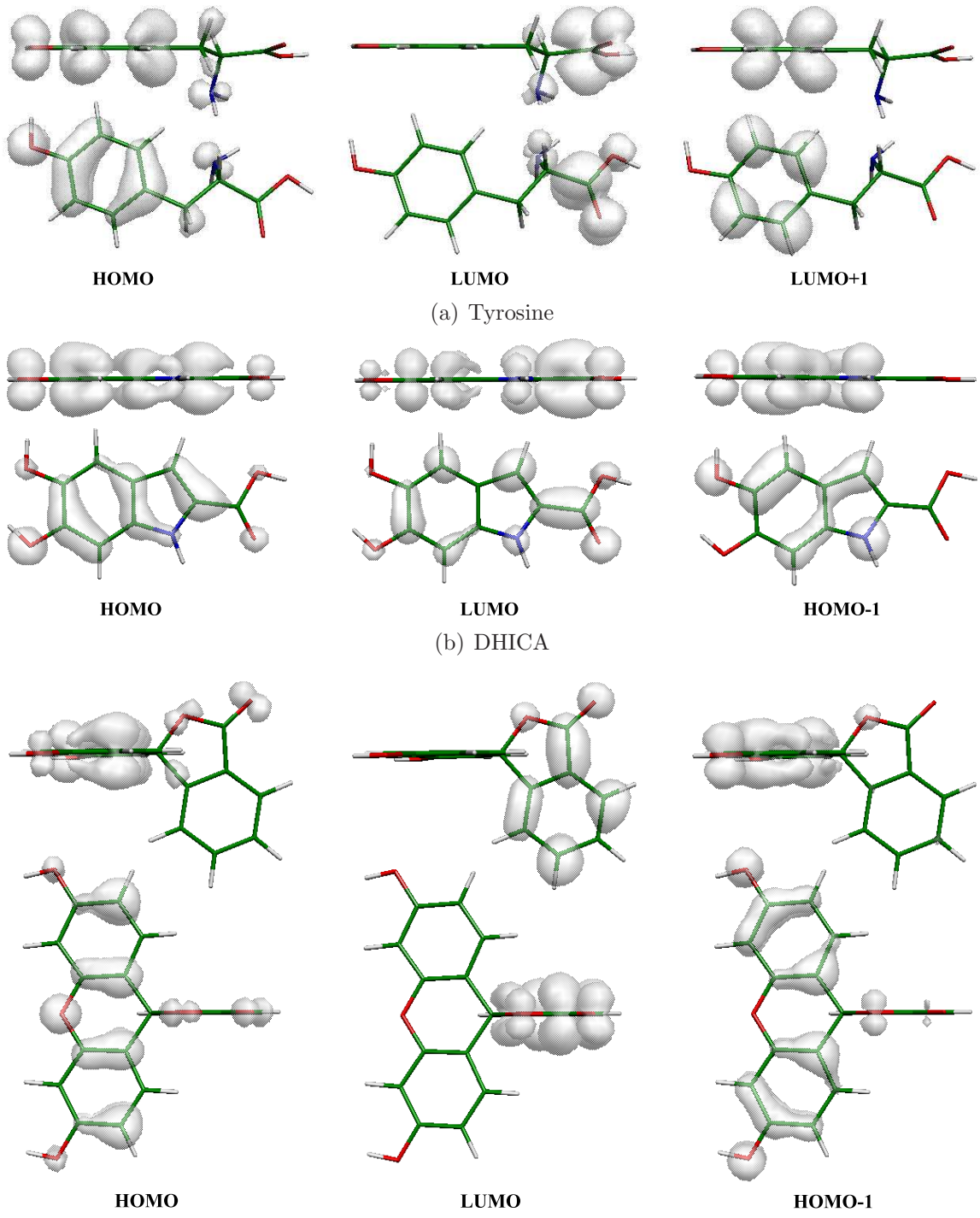

(a) Tyrosine

(b) DHICA

(c) Fluorescein

FIGURE 5.3: Electron densities of important molecular orbitals as calculated by NRLMOL. The HOMO to LUMO+1 transition is predicted to be that with substantial oscillator strength for tyrosine as shown in table 5.2; the tyrosine LUMO is also shown for comparison to DHICA and fluorescein. The HOMO to LUMO and HOMO-1 to LUMO transitions are predicted to be those with substantial oscillator strengths for fluorescein and DHICA, as shown in table 5.2. Red: oxygen, blue: nitrogen, green: carbon, white: hydrogen.

	Experiment				DFT		
	D_{exp} (debye^2)	$\nu_{av}(10^{15}$ Hz)	$\Delta\nu_{exp}(10^{15}$ Hz)		D_{DFT} (debye^2)	$\nu_{av}(10^{15}$ Hz)	Transitions used for D_{DFT}
Tyrosine	1.6	1.09	0.38 to 1.2		11	0.987	$\nu = 0.987$, HOMO to LUMO+1
DHICA	31	0.949	0.50 to 1.2		66	0.691	Total in experimental range
Fluorescein	140	0.611	0.44 to 0.75		112	0.454	Total in experimental range

Table 5.3: Dipole strengths, D, calculated using density functional theory (in vacuum, D_{DFT}) compared with experiment (in solution, D_{exp}). $\Delta\nu_{exp}$ are the frequency ranges over which the integrations of the experimental data were performed to determine the dipole strength. These ranges were also used to sum the DFT peaks for DHICA and fluorescein to obtain the values listed, whereas for tyrosine only the lowest energy DFT peak was considered to contribute, since it appears that the higher energy peaks in the DFT are not seen in the experimental spectrum (the transitions that were used for the calculation of the DFT dipole strengths are as shown in the final column). Essential trends are reproduced by the DFT results, although we do not achieve quantitative agreement as well as expected. The frequency where the main peak occurs experimentally (ν_{av}, experimental) can be compared to the frequencies for the main DFT predicted transitions (ν_{av}, DFT); as has been previously observed DFT consistently underestimates the magnitude of the energy gap but reproduces trends correctly [206].

We emphasise that DFT is a theory of the ground state, however it can reproduce trends in excited state behaviour (including transition energies and dipole strengths) [207, 208]. It is clear from table 5.3 that although DFT does not give strong quantitative agreement with the dipole strengths measured experimentally (particularly for tyrosine), it does reproduce the experimentally observed trends, giving the smallest dipole strength for tyrosine, and the largest for fluorescein. This shows that DFT is an appropriate tool for qualitatively modelling eumelanin and similar systems. The ability of DFT to reproduce the trends in the dipole strength also lends weight to our experimental results.

It is somewhat curious that better quantitative agreement is not observed between DFT results and experiment. As exemplified in reference [209] and references within that paper, it is well accepted that DFT delivers very accurate molecular polarizabilities (certainly better than 10%). The polarizability of a molecule depends quadratically upon the same dipole matrix elements that appear in the expression for absorptivity (equation 5.8) which also depends quadratically upon these elements. Therefore deviation between theoretical and experimental trends in table 5.3, particularily tyrosine, must be viewed as inexplicably large in comparison to $10-30\%$ deviations in energy gaps observed for these molecules and $\sim 5\%$ deviations in screened polarizabilities.

A number of theoretical techniques could provide more accurate values of the dipole strength. Time dependant DFT (TDDFT) has been shown to be effective for predicting excited state properties such as transition energies and optical absorption spectra [210]. Further, Yabana and Bertsch have shown that TDDFT reproduces dipole strengths of $\pi-\pi^*$ transitions for conjugated carbon molecules with a typical accuracy of $\sim 20\%$ [211]. The fact that TDDFT only reproduces dipole strengths in $\pi-\pi^*$ transitions for conjugated carbon molecules to 20% is indeed interesting given that a large body of results shows that DFT-based static polarizabilities lead to better agreement than this. It is also interesting to note in this context that Olsen *et al.* [50] have recently calculated the oscillator strengths for several oxidised forms of DHICA using state averaged complete active space calculations [SA3-CAS(4,3)] and multireference perturbation theory (MRPT2). These methods should be expected to provide higher accuracy than either DFT or TDDFT. However, Olsen *et al.* find oscillator strengths at least as large as the DFT results reported above for DHICA. This suggests that the disagreement between theory and experiment may not be soley due to the limitations of DFT. Understanding the origin of this deviation should be a future effort.

5.5.4 Prediction of radiative rates and lifetimes

Radiative rates and lifetimes were determined for eumelanin, tyrosine and fluorescein using previously measured emission spectra and quantum yield values [47, 182, 202] in addition to the extinction coefficients reported here, as outlined in the theory section. These are shown in table 5.4. The radiative quantum yield of eumelanin is known to vary with excitation wavelength [47] (this is an unusual property for an organic chromophore [212]). For calculations here, the value at $\lambda_{ex} = 380$ nm has been used (where λ_{ex} is the excitation wavelength). A and τ for fluorescein agree well with literature values which lends credibility to our values for eumelanin. Similarly, the lifetime predicted for tyrosine is consistent with the reported literature value.

	λ_{ex} (nm)	A (ns^{-1})		Φ	τ	
		(these results)	(literature)	(literature)	(these results)	(literature)
Eumelanin	380	$0.13N$	-	$(6.42 \pm 0.3) \times 10^{-4}$ [47]	$4.9N^{-1}$ ps	≤ 85 ps [47]
Fluorescein	490	0.38	0.221 [182]	0.92 ± 0.02 [182]	2.4ns	4.2ns [182]
Tyrosine	274	0.0082	-	0.13 [200]	16ns	3.4ns [200, 213]

Table 5.4: Radiative rates (A) and lifetimes (τ) calculated from emission and absorption spectra of eumelanin, tyrosine and fluorescein. λ_{ex} is the excitation wavelength, Φ is the radiative quantum yield. The extinction coefficient and fluorescence spectra for tyrosine used for these calculations are from reference [202]. The directly measured lifetimes agree to within an order of magnitude with those determined from the extinction coefficients, which is good considering that many parameters (such as the absorption coefficient, radiative quantum yield and the solution concentration), each with their own uncertainties, enter into determining this value. Also, we have used a first order theory that does not take higher order effects into account. Therefore, we are satisfied with this level of agreement with literature.

Lifetime (ns)	Relative Amplitude
≤ 0.085	51%
0.93	27%
3.5	17%
9.8	5.2%

Table 5.5: Multi-exponential fit parameters for the experimentally measured fluorescence excitation decay of eumelanin. The predominant excited state lifetime (85 ps) is relatively short, and may be shorter (this time is of the order of the instrument response function). The consistency between these measured lifetimes and that determined from the absorption and emission spectra is consistent with the broadband absorption spectrum being electronic in origin.

For a further comparison of the parameters determined from the extinction coefficient, the excited state lifetime of eumelanin was measured directly. The decay was found to be multiexponential, with lifetimes and relative amplitudes as shown in table 5.5. The predominant lifetime is the shortest: 85 ps. This is of the order of the instrument response, such that the actual predominant lifetime may be much shorter. These results are consistent with those reported by Forest [121] (predominant radiative lifetime of 59 ps at 420 nm). Note that this value is also likely to be an overestimate of the true radiative lifetime of eumelanin. Hence, we conclude that the excited state lifetime of eumelanin determined from the absorption and emission spectra is consistent with the directly measured lifetime. This agreement indicates that the absorption spectrum of eumelanin is genuinely electronic in origin, and not a result of scattering or some other non-electronic phenomenon (in agreement with our results in chapter 4).

The successful prediction of the lifetimes and radiative rates for eumelanin and the other compounds studied here indicates that the dipole strengths determined from this same data are reliable.

5.5.5 Time evolution of DHICA into eumelanin

So far we have considered the equilibrium properties of eumelanin and DHICA. It is now instructive to consider how these spectroscopic properties change in the reaction process as DHICA evolves to form eumelanin. DHICA was allowed to react and the absorbance monitored at intervals. The extinction coefficient as it evolves over time is shown in figure 5.4. The shape of the DHICA spectrum (measured at the initial time) is in good agreement with published spectra [188, 214], and, as it reacts, it shifts towards the eumelanin spectrum (both in shape and magnitude), as would be expected. Note that the extinction coefficient is plotted *per monomer*, since this is a more meaningful parameter for a macromolecule than the absolute extinction coefficient.

The dipole strength per monomer was determined at each time point, and is plotted in figure 5.5 for different choices of UV cut-off frequency. Note that, although the absolute magnitude of the eumelanin dipole strength is affected by the choice of integration range, the relative change in dipole strength over the course of the reaction is more robust. The dipole

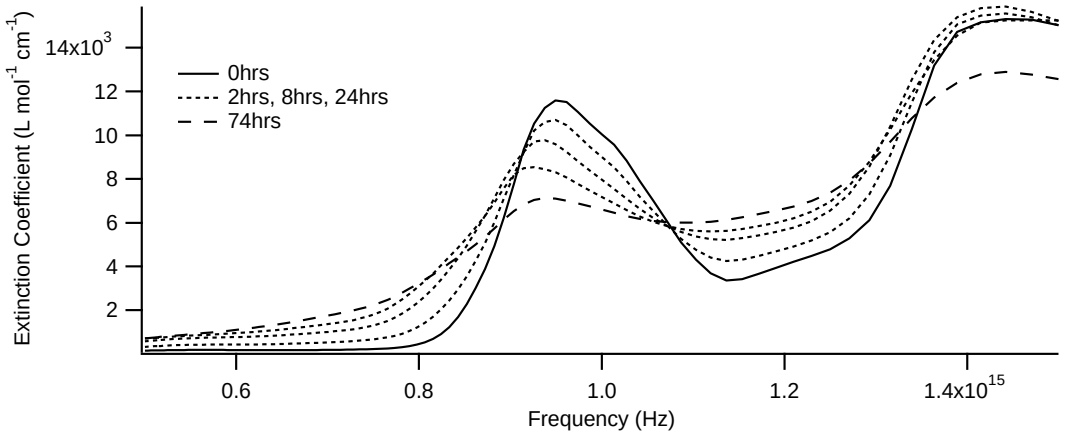

Figure 5.4: The extinction coefficient per monomer of DHICA as it undergoes oxidative polymerisation to form eumelanin. The initially peaked DHICA spectrum gradually shifts towards the broadband eumelanin spectrum, but does not change substantially in integration area. Dipole stengths determined from this data are shown in Fig. 5.5.

strength per monomer increases by approximately 20% over the course of the reaction (the increase is between between 12% and 26% for the UV cut-off frequencies we have considered). The dipole strength tends towards the value measured for eumelanin, as would be expected (when the same UV cut-off frequency is used for both).

This data indicates that eumelanin exhibits hyperchromism; the reaction process enhances absorption such that, after the reaction, the dipole strength of an oligomer is greater than the sum of the dipole strengths of the constituent monomers (for a discussion of hypochromism in biological molecules see reference [95]). The observed hyperchromism of eumelanin is interesting; bio-polymers often exhibit *hypo*chromism (*decrease* in UV/visible dipole strength per monomer upon polymerisation) of a similar magnitude to the hyperchromism we observe for eumelanin (5% to 10% for polystyrene [215, 216], 19% to 25% for poly(N-vinylcarbazole) [217] and 40% for DNA [95]). The hypochromism in these molecules is thought to be related to the formation of π-stacking interactions, which reduce the oscillator strength due to the parallel and adjacent arrangement of transition dipoles of the neighbouring molecules [218–221]. Hyperchromism, on the other hand, can occur when the dipoles of neighbouring molecules are arranged along the same axis and one behind the other. The hyperchromism observed for eumelanin might therefore be due to the edgewise association of DHICA molecules, forming planar oligomers. A slight hypochromism is also observed at later times, which may suggest subsequent π-stacking of planar oligomers. We wish to emphasise, however, that the magnitude of the observed hyperchromism (and especially the later hypochromism) is very small, and is of the order of the uncertainty due to the choice of UV cut-off frequency. We therefore caution that these results should not be over analysed without first measuring the extinction coefficient further into the UV.

Eumelanin's hyperchromism could be related to its role as a biological photoprotectant (an increase in absorption strength upon polymerisation enhances its ability to shield from incident photons). The fact that the magnitude of the hyperchromism is small, however, indicates that it is likely to be biologically less important than the evolution from a peaked

spectrum to a more broadband absorption spectrum. Most significantly, these results are consistent with the chemical disorder structural model for eumelanin [53]. In this model, the broadband absorption spectrum of eumelanin is produced by the summation of the (peaked) spectra of many distinct chemical species, as described in chapter 2. These species are suggested to be small oligomers of DHI and DHICA (figure 5.1) which would be expected to have dipole strengths per monomer similar to those of the monomer species (being similar in size). Since we observe only a small increase in the dipole strength per monomer over the course of the reaction, we conclude that these results are consistent with this model.

5.6 Chapter conclusions

We have shown that the dipole strength of eumelanin is not exceptional compared to other biologically relevant molecules. The dark colouring and photoprotection in the skin and hair of humans and other species must therefore be the result of a concentration effect. Our results also suggest that the highly unusual broadband absorption spectrum of eumelanin is electronic in origin, and not caused by scattering or other non-electronic processes, confirming the results presented in chapter 4. In addition, we found that the dipole strength per monomer of eumelanin increases by approximately 20% as it forms, indicating that eumelanin exhibits hyperchromism. Most significantly, the small magnitude of this hyperchromism is consistent with the currently favoured structural model of eumelanin (the chemical disorder model). It also suggests that the most important role of the reaction that forms eumelanin is to produce a broadband absorption spectrum, rather than an increased dipole strength. The resulting broadband absorption spectrum of eumelanin makes it capable of acting as an optical filter, protecting biological tissue from optical damage.

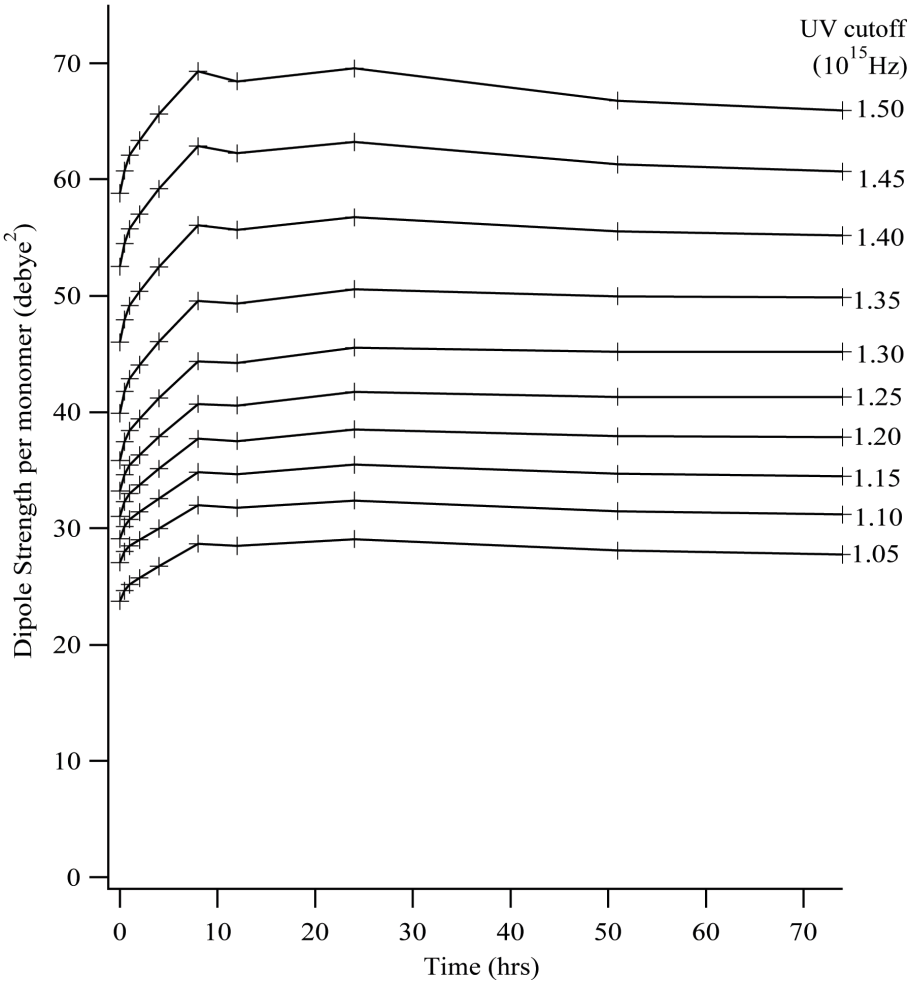

Figure 5.5: The dipole strength per monomer of DHICA over time, as it reacts to form eumelanin, determined using different UV cutoff frequencies. The variation between the curves indicates that the absolute value of the dipole strength at each time point is only accurate to within an order of magnitude. The overall increase in dipole strength is, however, more robust, showing that eumelanin exhibits between 12% and 26% hyperchromism (increase in dipole strength with polymerisation).

Part II

Energy dissipation in melanins

Energy dissipation in melanin

The accepted primary role of eumelanin is to function as a biological absorber, acting as a filter to shield us against damaging ultraviolet radiation. The broadband absorption spectrum ensures that we are protected against all wavelengths, and especially against the most damaging high energy photons. We have shown (in chapter 4) that this absorption is truly electronic in nature, rather than a scattering phenomenon, which raises the question of where the absorbed energy is ultimately channelled to. The processes by which eumelanin dissipates the energy it absorbs are not well characterised, and in many ways the dissipation processes are even more important than the absorption processes. A failure to dissipate energy properly in the skin may lead to chemical reactions and cell damage, and it is these energy dissipation processes that become critical when attempting to use eumelanin to harness energy in photovoltaic devices (for example).

Melanin may dissipate energy radiatively via fluorescence or phosphorescence. Fluorescence is due to spin allowed electronic transitions, giving rise to emission nanoseconds after absorption. Phosphorescence is due to the occurance of spin forbidden transitions (typically from a triplet state to a singlet state) which have very long excited state lifetimes; consequently the light may be emitted up to hours after absorption.

The absorbed energy may also be dissipated non-radiatively via a variety of mechanisms. Competing non-radiative dissipation pathways include

- Repopulation of the ground-state via electron-phonon coupling to vibrational modes of the molecule, converting energy to heat.
- Generation of non-emitting intermediates (such as semiquinones).
- Excited state chemical reactions. Biologically, in some highly specialised cases such as absorption by chlorophyll in photosynthesis, this may lead to beneficial conversion and storage of energy. However, photosynthesis is an extremely complex process that requires a great deal of cellular molecular machinery. Photoinduced chemical reactions therefore typically produce species that are harmful to bio-functionality. This is likely to be the case for melanins because there is no evidence of complex molecular processes of the type that are evident in the photosynthetic process. [3]

Understanding which of these processes contributes to energy dissipation in melanins is essential for understanding the functionality of the pigment.

[3]Interestingly, in a very recent publication, Dadachova et al. reported that allomelanin enhances the growth of fungi in the presence of ionizing radiation, and postulate that melanin might be involved in energy capture and utilization [222]. This suprising result is worthy of further investigation.

In the second part of this thesis we have focused largely on characterising and understanding the radiative dissipation processes in melanins. We report in chapter 6 an accurate characterisation of the radiative properties of eumelanin, including emission spectra and radiative quantum yields for a range of excitation wavelengths. The importance of re-absorption and inner filter effects is revealed, and a method to correct for these is presented and shown to be extremely effective. Chapter 7 reports a more in depth study of the radiative properties of eumelanin, with a detailed fluorescence map over the UV and visible range, and a map of the radiative quantum yield of eumelanin showing the dependance of this quantity upon excitation and emission wavelength over this range. This is the most detailed study of the emission properties of eumelanin to date. In chapter 8 we report the application of these methods to a synthetic analogue of pheomelanin so that the properties of this much less well studied form of the melanin pigment can be compared to those of eumelanin.

Chapter 9 reports a detailed study of the emission properties of DHICA, one of the eumelanin monomers. By accurately understanding the properties of this well characterised monomeric system we aim to work towards an understanding of the spectroscopic properties of the bulk eumelanin pigment. Chapter 10 provides a link between the two systems, reporting spectroscopic observation of DHICA as it polymerises to form eumelanin.

In chapter 11 we report a preliminary study into the non-radiative dissipation processes in eumelanin. In this chapter we outline the results of an inelastic neutron scattering study of melanin precursors to investigate in detail the vibrational properties of these molecules and their relation to the non-radiative dissipation processes in eumelanin.

6

The challenge of spectroscopy with melanin

6.1 Chapter abstract

We show that eumelanin emission spectra are strongly affected by re-absorption and inner-filter effects, and present a method to correct for these effects to achieve accurate emission spectra for eumelanin. These spectra show some interesting and atypical features, including a red-shift in the emission peak with decreasing excitation energy, and complete violation of the spectroscopic mirror image rule, both of which are consistent with the chemical disorder model. This method also allows for what we believe to be the first accurate measurement of the radiative quantum yield of eumelanin, which is shown to be very low (less than 0.1%), as is consistent with eumelanin's role as a photoprotectant. Atypically, the yield is also dependant upon excitation energy, which can again be explained by the chemical disorder model.

6.2 Chapter introduction

There are a variety of ways of measuring fluorescence and it is useful at this point to clarify our terminology. Firstly, emission spectra are measured by illuminating the sample with a single excitation wavelength (λ_{ex}) and by then measuring the intensity of fluorescence at each emission wavelength (λ_{em}) to produce a spectrum. This is the most intuitive way of measuring fluorescence.

Alternatively, if you are interested in the dependance of the fluorescence upon the excitation wavelength, you can measure an excitation spectrum. This is done by illuminating the sample with a range of excitation wavelengths (typically controlled by a monochromator) and by then detecting the intensity of fluorescence at a single emission wavelength. Excitation spectra can be less intuitive to interpret than emission spectra, but can be very useful for identifying atypical excitation properties.

A final parameter that is useful for characterising the fluorescence properties of a sample is the radiative quantum yield, $\Phi(\lambda_{ex})$. This is defined as the ratio of the number of photons emitted (integrated over all emission wavelengths) to the number of photons absorbed (at a particular excitation wavelength). The radiative quantum yield is an extremely useful parameter since it allows comparison of the intensity of fluorescence between samples. It is typically measured by comparison to a fluorescent standard with a known radiative yield.

6.2.1 Emission spectra

There are conflicting reports in the literature concerning eumelanin fluorescence. Several early reports state that eumelanin does not fluoresce [223, 224], and later studies report very weak fluorescence which was attributed to impurities or other chemicals [225–229]. There are several reasons why eumelanin was described as nonfluorescent, including

- Melanin has a very low radiative quantum yield ($< 0.1\%$, as shown in chapters 6 and 7), so the fluorescence is weak.
- Melanin is notoriously insoluble, so early fluorescence measurements were performed in the solid state (in KBr, for example). The process of solubilisation brings about a dramatic increase in the intensity of fluorescence, so early measurements performed in the solid state suffered from a further lowering of the measurable emission [230].
- The broadband absorbance spectrum of eumelanin causes re-absorption and inner filter effects at all wavelengths, significantly reducing the intensity of emission at all but the lowest concentrations.

Despite these difficulties, a variety of articles report emission spectra for eumelanin. These are summarised in table 6.1. It is clear that there is not a consistent agreement concerning the emission of eumelanin. A wide variety of peak positions are reported, and even the number of emission peaks is not consistent (most report one broad peak, but three studies report two). The differences between these spectra can be attributed to a variety of reasons, including variability in the source, excitation wavelengths, solvents and concentrations, all of which can affect emission spectra, as discussed below. The combination of these effects in past studies has obscured important subtle phenomena which are revealed by the results outlined in this chapter.

Melanin source

The emission spectra summarised in table 6.1 are for melanin from a variety of sources (synthetic, sepia ink, bovine and human) which have been shown to have different structural properties, and will likely exhibit different emission properties.

Excitation wavelength

Since melanin has a broadband absorbance spectrum there is no single wavelength that is logical for excitation of the pigment, which has led to a variety of excitation wavelengths

source	emission peaks (nm)	λ_{ex} (nm)	solvent	notes	reference
yellow mouse hair	425	320	NaOH solution	-	Ikejima and Takeuchi
black mouse hair	465	350			(1978) [231]
human hair	540	488	KBr (solid state)	strongly affected by	Kozikowski et al.
	540		alkaline H_2O_2	re-absorption	(1984) [230]
synthetic (from DHI)	560		NaOH solution		
	550		H_2O		
sepia ink	555		H_2O		
synthetic	420, 500	340	H_2O	small molecular fragments	Gallas and Eisner
(from DL-dopa)	420, 500	360		were removed. Only prior	(1987) [232]
	420, 500	380		study that includes	
	420, 500	400		re-absorption correction	
synthetic	440, 520	330	phosphate buffer	-	Mosca et al.
(from opioid peptides)					(1999) [233]
human foetal retina	465	364	saline	-	Boulton et al.
human retina 5-29yr	460, 590				(1990) [225]
human retina 30-49yr	455, 550				
human retina $>$ 50yr	465, 565				
bovine retina 1yr	460, 565				
synthetic	575	337	DMSO	-	Teuchner et al.
(from tyrosine)	575	400			(1999) [234]
sepia ink	450, 515	335	potassium phosphate buffer	450nm peak is narrow and possibly due to Raman scattering	Forest et al. (2000) [121]
synthetic	510	400	H_2O	-	Teuchner et al.
(from tyrosine)	520	400	EGE		(2000) [235]
	530	400	KOH		
	500	400	DMSO		
sepia ink	350	266	H_2O	size fractions	Simon (2000) [236]
sepia ink	450	300	H_2O	size fractions	Nofsinger and Simon
	450	325			(2001) [161]
	460	350			
	465	375			
synthetic	548	470	aqueous H_2O_2	deliberately oxidised	Kayatz et al.
bovine	543				(2001) [237]
sepia ink	490	unspecified	H_2O	size fractions	Birch et al. (2005) [238]

Table 6.1: Summary of melanin emission spectra as reported in the literature. λ_{ex} is the wavelength used for excitation.

selected by different authors. Emission spectra are independant of excitation wavelength for most organic chromophores above their minimum excitation energy, but the results presented in this chapter show that this is not the case for eumelanin. Therefore the variation in excitation wavelength leads to variation in the position of the emission peak. This effect is not well characterised, hence in this chapter we report an initial analysis of the effect of the excitation wavelength, with a much more detailed characterisation reported in chapter 7.

Solvent

Solubility is an issue when studying eumelanin, which has led to the use of a variety of solvents for emission studies. Solvent effects are known to be important for eumelanin, and specifically have been shown to affect emission spectra in non-trivial ways [235]. A variety of solvents used in the different studies therefore leads to a variety of emission spectra.

Re-absorption and inner filter effects

Re-absorption and inner filter effects have only been directly corrected for in one previous study (reference [232]). The other studies listed in table 6.1 rely upon sufficiently low concentrations to reduce (but not eliminate) the impact of these effects. We demonstrate in this chapter that re-absorption and inner filter effects affect eumelanin spectra in non-trivial ways, even at low concentrations, both decreasing peak height and shifting the wavelength where the peak occurs. These effects are concentration dependant, hence a variety of concentrations (not shown in table 6.1) will lead to apparent variation in emission spectra. We emphasise in this chapter the importance of correcting for these effects. The study by Kozikowski et al. in particular reports emission spectra that vary with concentration and other anomalous features; we believe these effects can be attributed to re-absorption by the eumelanin pigment [230].

Pigment degradation

It has been observed that oxidative degradation significantly increases the radiative quantum yield of eumelanin [225, 229, 233, 237, 239–241]. There is also evidence that increasing oxidation may also produce the appearance of a second peak in emission and excitation spectra [225], although this is not consistent throughout the literature and the reasons for it are not clear. Varying levels of degradation have been shown to be present in both natural and synthetic pigments [106, 118], and this is therefore a likely contributer to the variation in reports of eumelanin fluorescence. If oxidative degradation is associated with the breaking of covalent bonds this may be related to the observation that small eumelanin particles have higher radiative yields, and the observed differences between the emission spectra of size-separated eumelanin samples [161].

Aggregate size

It has been shown that eumelanin consists of particles of varying size, and that when these components are seperated into different fractions they have different emission properties (emission spectra, excitation spectra, and radiative yields) [161]. Synthetic samples have different aggregation properties to natural ones, and some studies on synthetic eumelanin have actively removed small molecular fragments via acid precipitation, whereas others have not. These factors will contribute to producing a variety of different emission spectra for different samples.

6.2.2 Excitation spectra

Excitation spectra give a first level indication of the dependance of emission spectra upon excitation wavelength, but unfortunately there is just as much variation in excitation spectra reported for melanins as there is in emission spectra, as demonstrated in table 6.2. Excitation spectra will be affected by all the same variables as emission spectra, leading to a great variation in the number and positions of excitation peaks that are reported (for all the same reasons). Re-absorption and inner filter affects also strongly affect exictation spectra, and

source	excitation peaks (nm)	λ_{em} (nm)	solvent	notes	reference
yellow mouse hair black mouse hair	308 376	unspecified	NaOH solution	-	Ikejima and Takeuchi (1978) [231]
human foetal retina human retina 5-29yr human retina 30-49yr human retina > 50yr bovine retina 1yr	355 380, 440 375, 440 360, 450 360, 460	570	saline	-	Boulton et al. (1990) [225]
synthetic (from opioid peptides)	310, 340, 450 340	440 520	phosphate buffer	-	Mosca et al. (1999) [233]
synthetic (from tyrosine)	530	620	DMSO	-	Teuchner et al. (1999) [234]
synthetic (from tyrosine)	375 375, 440 370, 450 360, 500 355, 530 350, 550	460 500 540 600 650 700	DMSO	-	Teuchner et al. (2000) [235]
sepia ink	280, 330 260, 385	400 500	H_2O	size fractions	Nofsinger and Simon (2001) [161]
synthetic bovine	471 469, 400, 420	540	aqueous H_2O_2	deliberately oxidised	Kayatz et al. (2001) [237]
synthetic (from tyrosine)	365 365 365, 490 365, 490	450 490 530 570	NaOH solution	Re-absorption corrected	Nighswander-Rempel et al. (2005) [242]

Table 6.2: Summary of melanin excitation spectra as reported in the literature. λ_{em} is the wavelength at which emission was measured.

these have only been taken into account in one recent study (by our group) that emphasises the significance of correcting for these effects [242].

6.2.3 Radiative quantum yield

Reports of the radiative quantum yield of eumelanin in the literature are summarised in table 6.3. Due to low emission levels, and re-absorption and inner filter effects, the radiative yield of this system is very difficult to measure. This has resulted in only four published reports of the radiative yield (as opposed to the many reported emission spectra listed in table 6.1). All reports agree that the yield is very low, but the exact estimates vary with source, solvent, and excitation wavelength. The radiative yield of eumelanin has also been shown to vary with aggregate size [161], which may contribute significantly to the variation between these reported results since some studies eliminate low molecular weight species through acid precipitation, whereas others do not (small species have a significantly larger radiative yield [161] and will therefore tend to dominate the radiative yield of the bulk system).

Photoacoustic calorimetry results for eumelanin show wavelength dependance in the energy dissipation processes in eumelanin, suggesting that electron-phonon coupling is less efficient at shorter wavelengths [162]. This is suggestive of wavelength dependance in the radiative quantum yield of eumelanin. To our knowledge, the excitation energy dependance of the radiative quantum yield has not been previously probed, which led us to initiate the study reported in this chapter (and the more in depth study reported in chapter 7).

It is essential for the measurement of quantum yields that optical scattering does not

source	radiative yield	λ_{ex} **(nm)**	**solvent**	**notes**	**reference**
synthetic (from tyrosine)	$< 10^{-3}$	unspecified	DMSO	-	Teuchner et al. (1999) [234]
synthetic (from tyrosine)	1×10^{-3} 1×10^{-3} 6×10^{-4} 2×10^{-4}	400	DMSO KOH H_2O EGE	-	Teuchner et al. (2000) [235]
sepia ink	1.9×10^{-3} 3.2×10^{-3} 5.2×10^{-3} 1.08×10^{-2}	350	H_2O	MW > 10000 $10000 >$ MW > 3000 $3000 >$ MW > 1000 MW < 1000	Nofsinger and Simon (2001) [161]
sepia ink	3×10^{-3}	350	H_2O	-	Nofsinger et al. (2001) [172]

Table 6.3: Summary of melanin radiative quantum yields as reported in the literature

make a significant contribution to the absorbance spectrum. This was shown to be the the case in Chapter 4, again highlighting the significance of that work. It is possible that scattering makes a very small contribution, which would lead to an under-estimation of the radiative yield (most notably at high energies where Rayleigh scattering becomes more significant).

6.2.4 Emission spectra as a probe

The variation between the published results listed in tables 6.1, 6.2 and 6.3 highlights how sensitive the emission properties of eumelanin are to environmental conditions and the exact preparation of the pigment. This makes it a challenging property to characterise accurately and repeatably, but it also makes the emission spectrum a highly sensitive non-invasive probe for the analysis of melanin (much more so than the relatively insensitive broadband absorption spectrum).

Eumelanin is known to consume oxygen and generate reactive free radicals upon UV excitation [150, 243, 244], which has been attributed to small molecular weight species (molecular weights < 1000 amu) since the eumelanin action spectra for photoinitiated free radical production and oxygen consumption are both very similar in shape to the absorption spectrum of these low molecular weight species [17, 173, 244]. The photogeneration of reactive oxygen species by eumelanin is the most likely cause of its paradoxical photosensitising properties, so it is worth investigating the low molecular weight species thought to be responsible. These small species in eumelanin have been shown to have a higher radiative quantum yield than their larger counterparts; the radiative yield of species with molecular weights less than 1000 amu was found to be $\sim 1\%$, whereas for larger species it ranges between $\sim 0.2\%$ and $\sim 0.5\%$ [161]. This suggests that the measurement of fluorescence spectra may be an effective non-invasive probe of the most interesting small molecular weight species that are likely to be most heavily involved in photochemical reactions.

Additionally, the measurements reported in this chapter identify several atypical features of eumelanin fluorescence that can be logically explained by the chemical disorder model. Hence spectroscopic examination of eumelanin pigment may provide us with a way to distinguish between the various models for the functionality of melanin. A first step towards this goal is presented here, with the accurate characterisation of emission spectra and radiative quantum yields for eumelanin, corrected reliably for re-absorption and inner filter effects.

Pheomelanin is treated in a similar manner in chapter 8.

6.3 Experimental

6.3.1 Sample preparation

Stock solutions of synthetic eumelanin were prepared in a manner identical to that described in section 4.3.1. From this, eumelanin solutions were prepared at a range of concentrations $(0.001 - 0.005\%)$. Under such conditions, pale brown, apparently continuous eumelanin dispersions were produced. Fluorescein ($\Phi_r = 0.92 \pm 0.02$) was purchased from Sigma Aldrich and used without further purification to prepare standard solutions at 10 different concentrations varying from $1.2 \times 10^{-4}\%$ to $5 \times 10^{-6}\%$ by weight in 0.1 M NaOH solution (18.2 Mohm MilliQ deionized water). Fluorescein and eumelanin concentrations were chosen so as to maintain absorbance levels within the range of the spectrometer whilst maximising emission.

6.3.2 Absorption spectrometry

Absorption spectra for the eumelanin and fluorescein solutions were measured as described in section 4.3.2.

6.3.3 Emission spectrometry

Emission spectra for eumelanin and fluorescein solutions were recorded for all concentrations using a Jobin Yvon (Paris, France) FluoroMax 4 Fluorimeter. Emission scans were performed between 400 and 700 nm using excitation wavelengths of between 350 and 410 nm for the eumelanin samples and 490 nm for the fluorescein samples. A band pass of 3 nm and an integration of 0.3 s were used. The emission spectra were corrected for attenuation of the probe beam and re-absorption of the emission according to the procedure outlined below. Background scans were performed under identical instrumental conditions using the relevant solvents. Spectra were corrected to account for differences in pump beam intensity at different excitation wavelengths via the use of an incident reference beam in the fluorimeter.

6.3.4 Emission correction procedure

We have developed a procedure to correct for probe beam attenuation and emission re-absorption which has been applied to all emission and excitation spectra reported in this thesis. This procedure is outlined in depth in reference [163]. Briefly, the measured emission intensity $I_m(\lambda_{em})$ at emission wavelength λ_{em} at any particular excitation wavelength λ_{ex} is related to the actual (corrected) emission intensity $I_c(\lambda_{em})$ via the relationship

$$I_c(\lambda_{em}) = I_m(\lambda_{em})k(\lambda_{em}) - I_{bg}(\lambda_{em}) \tag{6.1}$$

where $I_{bg}(\lambda_{em})$ is the background contribution to the measured intensity (solvent and impurity emission, and Raman scattering by the solvent), and $k(\lambda_{em})$ is a scaling factor defining

the probe beam attenuation and emission re-absorption. If we assume that only emission arising from a small volume at the waist of the excitation beam is collected by the spectrometer detection system, then $k(\lambda_{em})$ can be written as

$$k(\lambda_{em}) = \exp\left(\alpha_{ex} d_1 + \alpha_{em}(\lambda_{em}) d_2\right) \tag{6.2}$$

where α_{ex} is the absorption coefficient (cm^{-1}) at the excitation wavelength, d_1 (cm) is the effective path length responsible for attenuation of the excitation beam, $\alpha_{em}(\lambda_{em})$ is the absorption coefficient at the emission wavelength and d_2 is the path length for emission re-absorption. Equation 6.1 also holds for fluorescence excitation measurements, but in this case the scaling factor $k(\lambda_{ex})$ is dependant upon the excitation wavelength and is given by

$$k(\lambda_{ex}) = \exp\left(\alpha_{ex}(\lambda_{ex}) d_1 + \alpha_{em} d_2\right) \tag{6.3}$$

If the geometry of the measurement system is known, then the path lengths d_1 and d_2 can be found by inspection. For example, for a collimated excitation beam incident upon a square cross-section cuvette (sides of length x (cm)) with collection at 90° with respect to excitation (and in the same horizontal plane), then

$$d_1 = d_2 = \frac{x}{2} \tag{6.4}$$

However, if the geometry of the system is ill-defined, an estimate for the scaling factor can be found by analysing the relative attenuation of the Raman scattering of the probe beam in the sample with respect to the solvent. This technique is useful in the case of eumelanin emission and excitation studies because the relatively weak emission is of a similar magnitude to the intensity of the Raman scattering from the solvent (water). In this case, equations 6.2 and 6.3 (fluorescence emission and excitation respectively) can be rewritten as

$$k(\lambda_{em}) = \exp\left(\alpha_{em}(\lambda_{em}) d_{eff}\right) \tag{6.5}$$

$$k(\lambda_{ex}) = \exp\left(\alpha_{ex}(\lambda_{ex}) d_{eff}\right) \tag{6.6}$$

$$d_{eff} = \ln\left(\frac{I_{RB}}{I_R}\right)\frac{1}{\alpha_R} \tag{6.7}$$

where d_{eff} is an effective path length (reflecting both the pump beam attenuation and emission re-absorption), I_{RB} is the intensity of the Raman peak in the background (solvent) and I_R is the attenuated Raman peak intensity in the sample. These values can be found by fitting gaussian line shapes to the Raman and emission features in the emission spectrum. The absorption coefficient at the Raman peak (α_R) can be determined directly from the absorbance spectrum (figure 6.1(a)). This method is particularly useful in thin film emission experiments, where pump beam attenuation may be relatively weak but emission re-absorption may be significant. In the data presented in this thesis, all eumelanin and fluorescein spectra were corrected using equations 6.1, 6.2 and 6.4, although we have shown that approximately similar results are obtained using equation 6.5 to calculate $k(\lambda_{em})$ [163]. Absorption coefficients (α_{em} and α_{ex}) were determined from the absorbance spectra for each concentration. The errors associated with this correction procedure were estimated by considering the uncertainty in the scaling factor according to the equation

$$\Delta k = k\left[\left(\alpha_{ex}\Delta d_1\right)^2 + \left(\alpha_{em}(\lambda_{em})\Delta d_2\right)^2\right]^{1/2} \tag{6.8}$$

6.3.5 Quantum yield calculations

Radiative relaxation quantum yields at three excitation wavelengths (350, 380 and 410 nm) were calculated for synthetic eumelanin using the standard procedure outlined in reference [212]. Plotting the integrated emission vs absorbance for a range of concentrations allows the quantum yield (Φ_{mel}) to be determined according to the equation

$$\Phi_{mel} = \Phi_s \left(\frac{g_{mel}}{g_s}\right) \left(\frac{n_{mel}}{n_s}\right)^2 \tag{6.9}$$

where Φ_s (0.92 ± 0.02 for fluorescein) is the known quantum yield of the standard, n_{mel} and n_s are the refractive indicies of the eumelanin and standard solvents, respectively (in this case both 1.33) and g_{mel} and g_s are the gradients of the integrated emission vs absorbance plots. Given the dramatically different quantum yields of fluorescein and eumelanin, it was necessary to use neutral density filters (OD0.6 and OD1.0) to prevent detector saturation in the fluorescein emission measurements. These data were subsequently scaled with the seperately measured absorbance of the filters before the correction process. The errors associated with the quantum yield measurements were calculated according to the following equation (derived from equation 6.9)

$$\Delta\Phi_{mel} = \Phi_{mel} \left(\left(\frac{\Delta\Phi_s}{\Phi_s}\right)^2 + \left(\frac{\Delta g_{mel}}{g_{mel}}\right)^2 + \left(\frac{\Delta g_s}{g_s}\right)^2 \right)^2 \tag{6.10}$$

where Δg_{mel} and Δg_s are the uncertainties associated with the gradients determined from the integrated emission vs absorption plots. In this analysis we have assumed Δg_{mel}, Δg_s and $\Delta\Phi_s$ are uncorrelated.

6.4 Results and discussion

The well known broadband absorbance spectrum of eumelanin is shown in figure 6.1(a) for three different concentrations. As expected, the absorption coefficient scales linearly with concentration, confirmed by the linear regression shown in figure 6.1(b) (a plot of the absorption coefficient at 380 nm for each of these concentrations).

Emission spectra were measured for these three eumelanin solutions with excitation at 380 nm; the raw spectra (not corrected for re-absorption or inner filter effects) are shown in figure 6.2(a) with the solvent background spectrum included (dot-dash line). Note that the narrow peak at approximately 435 nm is due to Raman scattering from the solvent. Raman scattering is typically very weak in intensity and is often dwarfed by emission from the sample. This is not the case here, giving an indication of the weak intensity of the emission from eumelanin.

Note the following unusual features of these spectra:

- The emission intensity does not scale linearly with concentration.
- The emission peak shifts to longer wavelengths as the concentration increases (the intensity of the emission peak should vary as concentration changes, but the shape and position of the emission peak should be independant of concentration).

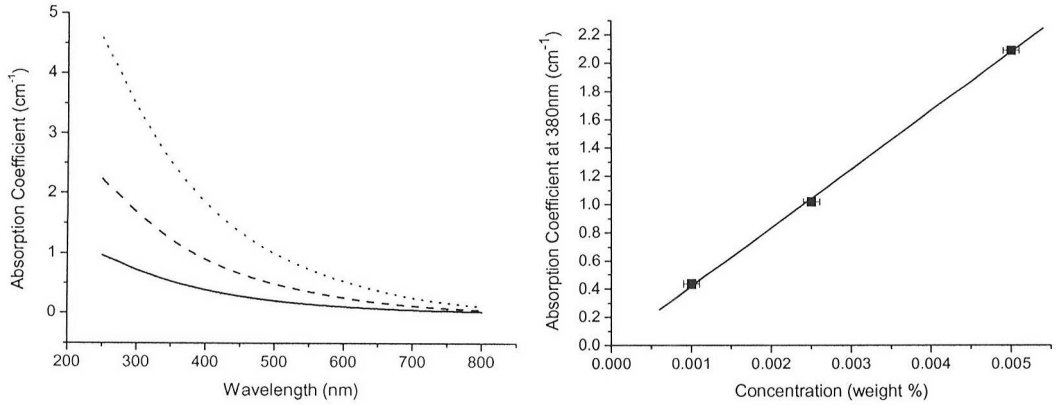

(a) Absorption spectra for three different concentrations

(b) Absorption coefficient at 380 nm vs concentration

FIGURE 6.1: (a) Absorption spectra for three synthetic eumelanin solutions (0.005% (dotted line), 0.0025% (dashed line) and 0.001% (solid line) by weight concentrations. (b) Absorption coefficient at 380 nm vs concentration for the three synthetic eumelanin solutions in (a) showing expected linear relationship.

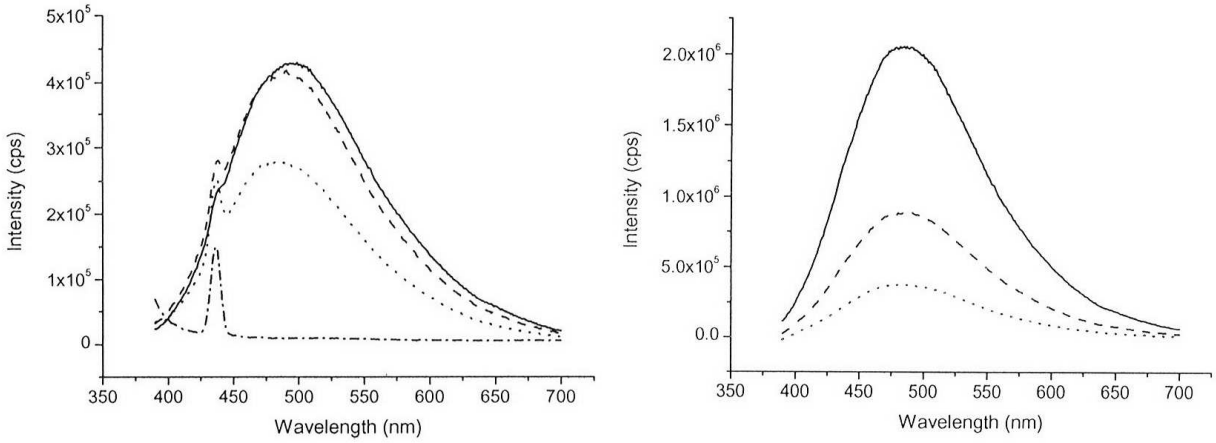

(a) Raw (uncorrected) spectra

(b) Spectra corrected for re-absorption and inner filter effects

FIGURE 6.2: Emission spectra (excitation at 380 nm) for three synthetic eumelanin solutions shown in figure 6.1(a). Concentration by weight: 0.005% (dotted line), 0.0025% (dashed line) and 0.001% (solid line), and solvent background (dot-dash line), showing Raman scattering peak at 435 nm (in (a) only).

- The Raman peak intensity decreases with increasing sample concentration (the Raman peak is a feature of the solvent, rather than the sample, and hence should be completely unrelated to the sample concentration).

All of these features can be attributed to re-absorption and inner-filter effects. The inner-filter effect is due to absorption of the excitation beam before it reaches the excitation volume at the centre of the cuvette (from which emission is detected). As concentration increases this effect becomes more significant, and manifests as an increasingly reduced intensity of emission spectra. Re-absorption occurs when the absorption coefficient is substantial at the wavelengths where emission is being measured. Emission from the excitation volume is re-absorbed before it reaches the outside of the cuvette. Since eumelanin has a broadband spectrum that increases exponentially towards higher energies, this manifests as a redshift in the eumelanin emission peak at higher concentrations (where re-absorption is more significant).

Re-absorption and inner-filter effects are typically avoided by the use of very low concentrations where the absorbance is sufficiently low that they do not significantly affect the emission spectra. This is not possible in the case of eumelanin where emission is extremely low and higher concentrations are required to maximise the emission signal. It was determined that a concentration of 0.0025% eumelanin by weight gives the maximum emission with minimum re-absorption and inner-filter distortions. At this concentration, however, it is necessary to apply a correction for these effects to recover accurate spectra.

Applying the correction to the raw emission spectra in figure 6.2(a) results in the corrected spectra shown in figure 6.2(b) (note that the solvent background spectrum included in figure 6.2(a) has been subtracted as a part of the correction procedure, and hence is no longer included in figure 6.2(b)). We find now that we have recovered the following important features:

- The spectra intensities scale linearly with concentration (as demonstrated by the linear regression in figure 6.3).
- The spectra are identical in shape and peak position.
- The Raman scattering peak from the solvent has been completely removed by the subtraction of the background without leaving spectral 'holes'.

The recovery of these features indicates that the correction procedure has worked properly to give us accurate emission spectra. The intensity of the corrected emission peak is plotted against concentration for these three solutions in figure 6.3 to show that the linear relationship with concentration is recovered.

The importance of this correction process is further highlighted in figure 6.4. Integrated emission is plotted against absorption coefficient for each concentration (which should be linear). Empty circles show uncorrected (raw) data, whereas filled squares show the data after the correction process is applied. For eumelanin, in figure 6.4(a), it is clear that the uncorrected values deviate significanty from linearity at all concentrations and the correction procedure is essential for recovery of the correct relationship. Upon application of the correction procedure, however, the linear relationship is completely recovered.

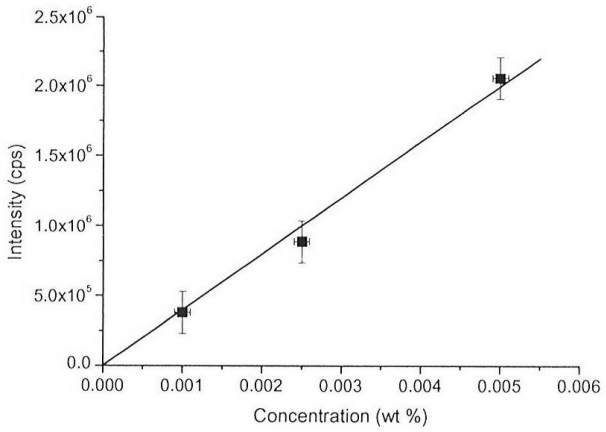

FIGURE 6.3: Corrected emission peak intensity vs concentration for three synthetic eumelanin solutions shown in figure 6.2(b).

To demonstrate that this procedure is not only applicable to eumelanin, figure 6.4(b) shows measurements for ten concentrations of fluorescein. The lower 5 concentrations (bottom left part of the graph) are in the regime usually used for measurements on fluorescein. It is clear that the correction process is unnecessary at these low concentrations. At higher concentrations, however, the uncorrected values deviate significanty from linearity and the correction procedure becomes important. Note that the intensity of emission is several orders of magnitude higher for fluorescein than that for eumelanin, meaning that lower concentrations of eumelanin could not be used in a similar way to remove the need for the correction procedure. For eumelanin the correction procedure is necessary for all five concentrations used, and at the highest concentration the deviation is very significant. By applying the correction procedure, however, we recover the expected linear relationship between emission and absorption to within the uncertainty of the correction.

Being able to accurately measure the emission spectra of eumelanin has allowed us to measure some previously unobserved features. The corrected emission spectra of eumelanin for a variety of excitation wavelengths are shown in figures 6.5(a) (vs wavelength), and 6.5(b) (vs energy). We see that the spectrum changes in shape and peak position as the excitation wavelength changes. This is in violation of Kasha's rule [245]; for most simple organic molecules emission will only vary in intensity as the excitation wavelength is varied. We also note that a low energy cut-off is evident; all curves share a common edge at low energy. All of these features suggest that multiple species are present in solution. As we excite at lower energies we cease to excite those species with larger excitation gaps. This means we no longer see emission from those species (which would presumably emit at the highest energies), so exciting at lower energies produces redshifting of the emission peak with a common cut-off at low energies.

The measured peak positions (after correction) are listed in table 6.4 for easy comparison to those previously reported in the literature summarised in table 6.1. The only other study to have applied a correction for re-absorption and inner filter effects [232] reports an emission spectrum with two gaussian peaks at 433 nm and 505 nm that vary in height as the excitation wavelength is varied (between 340 and 400 nm), exhibiting an isosbestic point

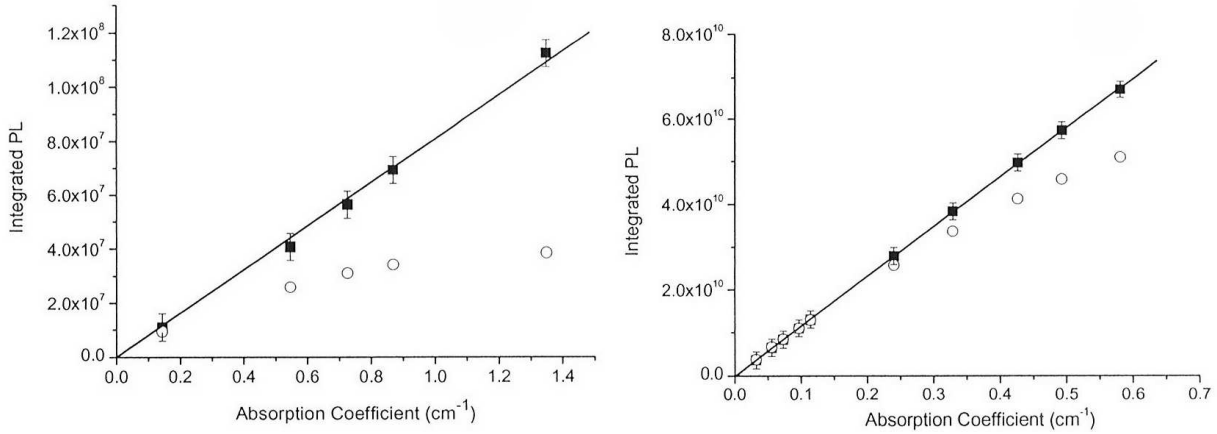

(a) Synthetic eumelanin (b) Fluorescein

Figure 6.4: Integrated emission vs absorption coefficient at the excitation wavelength for (a) eumelanin (excitation at 380 nm, five solutions of concentrations 0.001% to 0.005% by weight) and (b) fluorescein (excitation at 490 nm, ten solutions of concentrations 1.2×10^{-4}% to 5×10^{-6}% by weight). Open circles are raw data, filled squares are corrected data (with linear regression).

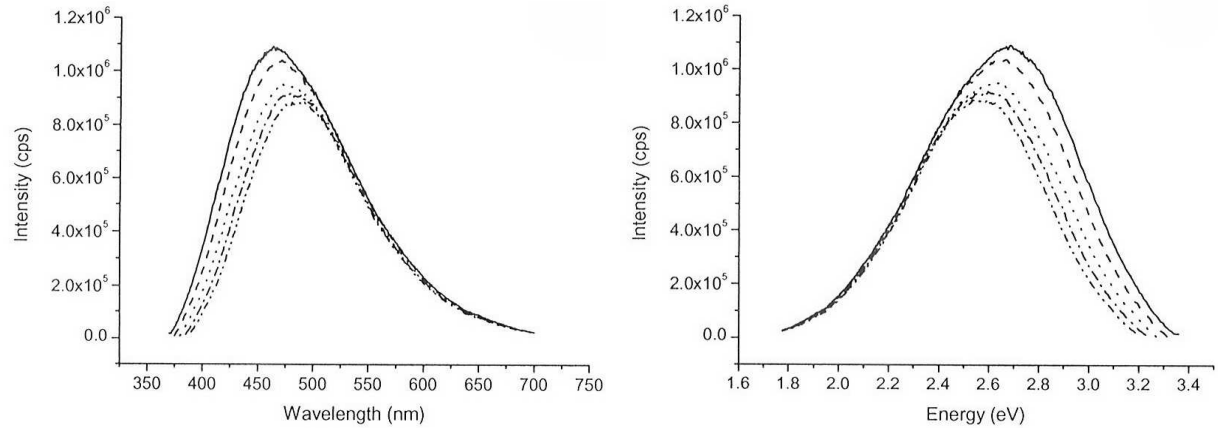

(a) Emission vs wavelength (b) Emission vs energy

Figure 6.5: Corrected emission spectra for a 0.0025% by weight synthetic eumelanin solution for five excitation wavelengths (360 nm, solid line, to 380 nm, inner dashed line) in 5 nm increments.

source	**emission peaks** (nm)	λ_{ex} (nm)	**solvent**	**notes**
synthetic	461	360	NaOH solution	Re-absorption correction
(from tyrosine)	467	365		applied.
	474	370		
	479	375		
	485	380		

Table 6.4: Summary of eumelanin emission spectra reported here, for comparison with table 6.1.

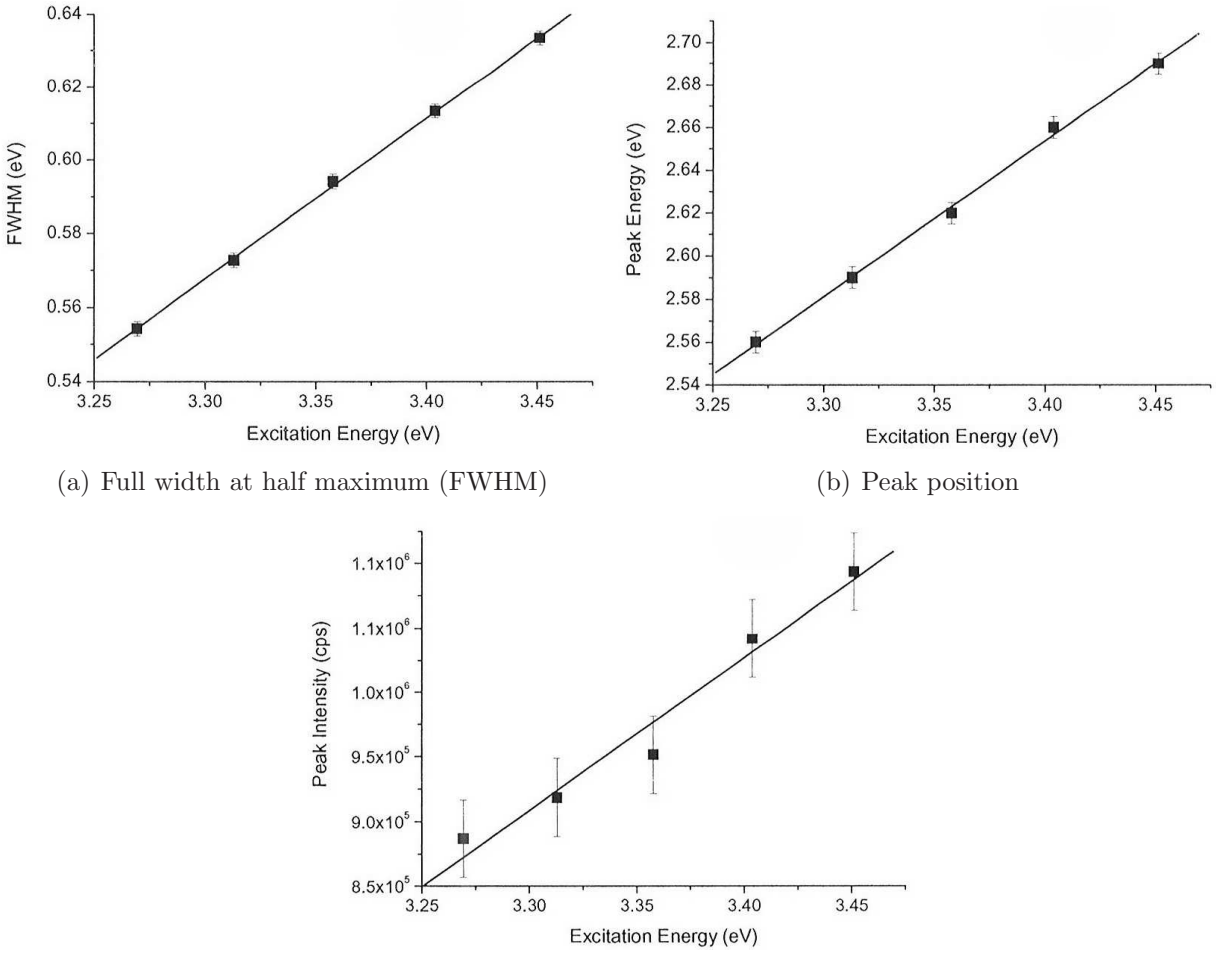

(a) Full width at half maximum (FWHM)

(b) Peak position

(c) Peak intensity

FIGURE 6.6: Analysis of corrected emission spectra with excitation energy for a 0.0025% by weight synthetic eumelanin solution.

at 470 nm. They attribute this to two distinct chemical species which interconvert as the pump wavelength is changed. This intriguing result has not been replicated in any later measurements (although several studies report two emission peaks, the isosbestic point has not been observed). The behaviour we observe here is also very different to that reported in that study.

Figure 6.6 plots the properties of the eumelanin emission peak as excitation energy is varied. As shown in figure 6.6(a) the full width at half maximum increases linearly with excitation energy, as does the energy where the peak occurs (6.6(b)), and the intensity of the peak (6.6(c)).

Another interesting feature of the emission spectrum of eumelanin is that it shows complete violation of the mirror image rule. This rule states that, due to the laws of quantum mechanics, the emission intensity divided by the energy cubed should be the mirror image of the absorption spectrum divided by energy (on an energy axis) [245], as illustrated in

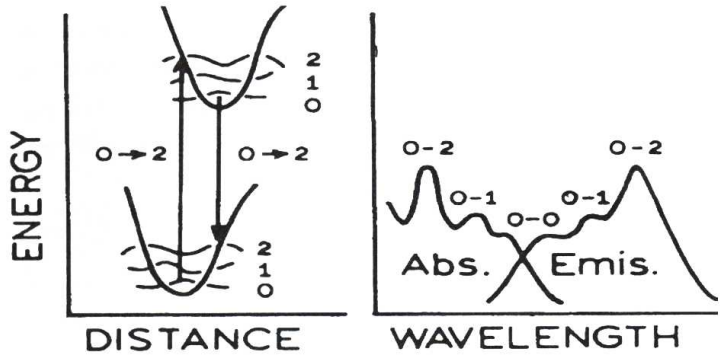

Figure 6.7: Because the same transitions are involved in both absorption and emission, and the S_0 and S_1 vibrational levels are typically similar, for simple molecules the emission spectrum will be the mirror image of the S_0 to S_1 transition in the absorption spectrum. Figure from reference [245].

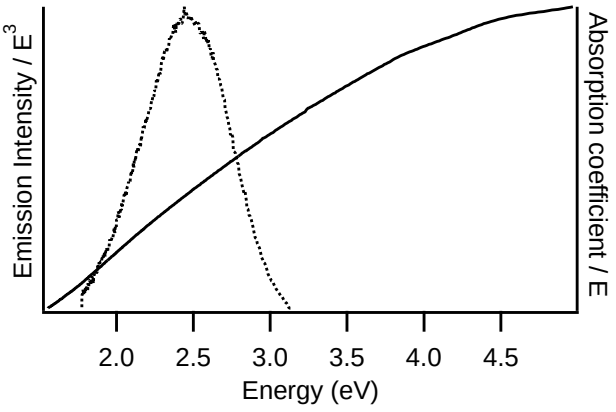

Figure 6.8: Emission / Energy^3 (broken line, left axis) and absorption coefficient / Energy (solid line, right axis) for synthetic eumelanin solution showing violation of the mirror image rule. For simple systems these quantities should mirror each other along the energy axis [245]. With a peaked emission spectrum and a broadband absorption spectrum, eumelanin completely violates this rule.

figure 6.7. This has been plotted for eumelanin in figure 6.8, which shows the clear violation. This can be explained by the presence of many chemically distinct species, which gives rise to a broadband absorption spectrum with a high energy cut-off in the far UV. Many of these species may be large oligomers which are expected to have strong electron phonon coupling and therefore dissipate absorbed energy largely by non-radiative processes so that they do not contribute to the emission spectrum. Only a small proportion of the species present have high enough radiative yields to contribute to emission; these are expected to be residual concentrations of monomers, or very small oligomers. Since only a small proportion of the species contribute to emission (whereas almost all contribute to absorption), it is reasonable to expect that the emission spectrum would no longer mirror the absorption spectrum.

These results show that emission spectra offer an extremely sensitive probe of the eumelanin system (far more so than absorption spectra, the broadband shape of which can

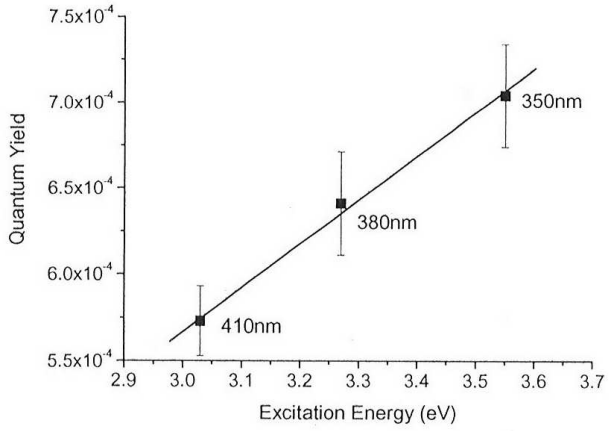

FIGURE 6.9: Radiative relaxation quantum yield for synthetic eumelanin excited at three wavelengths (350 nm, 380 nm and 410 nm). The solid line is a linear fit which is intended only as a guide to the eye.

source	radiative yield	λ_{ex} **(nm)**	**solvent**	**notes**
synthetic	7.0×10^{-4}	350	NaOH solution	Re-absorption
(from tyrosine)	6.4×10^{-4}	380		correction applied
	5.7×10^{-4}	410		

Table 6.5: Summary of melanin radiative quantum yields reported here, for comparison with table 6.3

be explained adequately by a variety of models). These emission measurements give much stronger evidence for distinguishing between various models for eumelanin.

6.4.1 Radiative quantum yield of eumelanin

The radiative quantum yield of eumelanin was determined at three different excitation wavelengths using equation 6.9 with gradients from linear regressions of plots like those shown in figure 6.4. The radiative yield of eumelanin is shown as a function of excitation energy in figure 6.9, where the linear regression is intended only as a guide to the eye. The measured radiative yields are also listed in table 6.5. Note that the yield for all excitation energies is very small, less than 0.1%. This confirms that eumelanin is capable of dissipating more than 99.9% of the absorbed UV and visible energy non-radiatively.

Most significantly, the radiative yield is dependant upon the excitation energy, which is atypical behaviour for an organic chromophore, and is indicative of chemical heterogeneity. This is investigated in depth in the following chapter.

6.5 Chapter conclusions

Eumelanin emission is strongly affected by re-absorption and inner filter effects which distort the intensity and shape of the measured emission spectrum. We apply a method to correct for these effects and recover accurate emission spectra for eumelanin. This accuracy

has allowed us to identify several features of eumelanin emission that are atypical for an organic chromophore, including excitation energy dependance in the emission spectrum, and violation of the mirror image rule. All of these atypical features are suggestive of chemical disorder. This method has also allowed us to make the first accurate measurement of the radiative yield of eumelanin, which is found to be very small (less than 0.1%), as is ideal for a photoprotectant. The radiative yield is also dependant upon excitation energy, which is unusual, and will be investigated in more depth in the following chapter.

7

Radiative quantum yield mapping

7.1 Chapter abstract

In this chapter we detail a complete fluorescence map for synthetic eumelanin over the UV/visible range and identify two different regimes of interest, $\lambda_{ex} > 310$ nm and $\lambda_{ex} < 310$ nm. For $\lambda_{ex} > 310$ nm eumelanin exhibits the previously observed properties indicative of the presence of multiple species; we report these features over a much wider range than previously measured. For $\lambda_{ex} < 310$ nm we report a previously unobserved regime which shows little dependance upon excitation energy which we attribute to emission from a single species. To further investigate the excitation energy dependance of the emission, we determine the radiative yield as a function of excitation energy, as well as a quantity which we call the 'specific quantum yield'; this gives the probability that a photon absorbed at a particular λ_{ex} will be emitted at a particular λ_{em}. Clear structure is observed, as is a non-trivial dependance upon the excitation wavelength, indicative of chemical disorder.

7.2 Chapter introduction

In chapter 6 we showed that the emission spectrum of eumelanin depends upon the excitation wavelength in a non-trivial way. In this chapter we extend upon the five discrete emission spectra that were reported in chapter 6, and give a complete fluorescence map over the entire ultra violet and visible range. This forms an extremely valuable tool for analysis of the energy dissipation processes of eumelanin.

We also showed in chapter 6 that the the radiative quantum yield of eumelanin is dependant upon excitation energy. This highlights the need to determine the radiative quantum yield as a function of excitation wavelength for a clearer understanding of eumelanin's de-excitation processes. We present in this chapter a method for measuring a quantum yield-like quantity that we call the 'specific quantum yield' - the fraction of photons absorbed at a

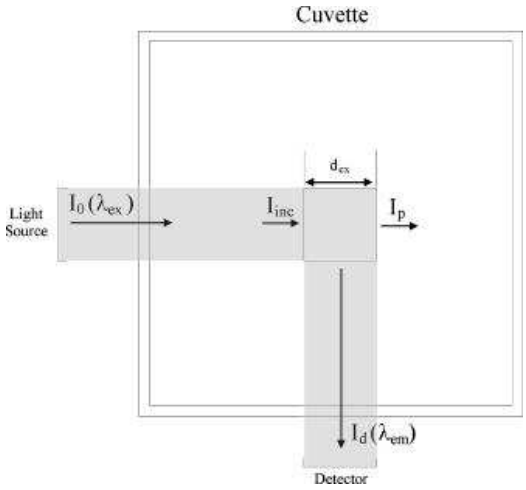

FIGURE 7.1: Cuvette and excitation volume with emission and excitation beam shown, viewed from above (figure from [48]).

wavelength λ_{ex} that are emitted at a specific wavelength λ_{em}. Integration of this quantity over λ_{em} yields the traditional quantum yield as a function of excitation energy. The specific quantum yield allows us to track the de-excitation path of each emitted photon. With the resulting specific quantum yield map we have a much more complete understanding of the spectroscopic properties of eumelanin. In addition to reporting the specific quantum yield for eumelanin, we present the general method for determination of the specific quantum yield for any compound.

7.3 Theory

We seek to determine an expression for the radiative quantum yield of a sample as a function of the excitation and emission wavelengths (λ_{ex} and λ_{em} respectively), in terms of measurable parameters, which we define as the 'specific' quantum yield ($Q(\lambda_{ex}, \lambda_{em})$, the percentage of photons absorbed at a particular excitation wavelength that are emitted at a particular emission wavelength).

In a typical spectroscopic measurement a small volume is defined in the centre of the cuvette by the slit widths for the incoming and outgoing beams, as shown in figure 7.1. This is the volume from which fluorescence is detected, given the instrumental design. We define $N_a(\lambda_{ex})$ to be the total number of photons absorbed in the central volume, and $N_e(\lambda_{ex}, \lambda_{em})$ to be the total number of photons emitted from the central volume. The specific quantum yield (as a function of λ_{ex} and λ_{em}) is then defined as

$$Q(\lambda_{ex}, \lambda_{em}) = \frac{N_e(\lambda_{ex}, \lambda_{em})}{N_a(\lambda_{ex})} \tag{7.1}$$

N_a is the difference between the number of photons incident on the central volume and the number of photons remaining after passing through the volume. Since the number of

photons is directly proportional to the light intensity with some proportionality constant K, we have

$$N_a(\lambda_{ex}) = K[I_{inc}(\lambda_{ex}) - I_p(\lambda_{ex})] \tag{7.2}$$

Moreover, by the Beer-Lambert law

$$I_p(\lambda_{ex}) = I_{inc}(\lambda_{ex})e^{-\alpha(\lambda_{ex})d_{ex}} \tag{7.3}$$

where $\alpha(\lambda_{ex})$ is the absorption coefficient of the sample at λ_{ex} and d_{ex} is the width of the central volume (as shown in figure 7.1). Combining equations 7.2 and 7.3 yields

$$N_a(\lambda_{ex}) = KI_{inc}(\lambda_{ex})[1 - e^{-\alpha(\lambda_{ex})d_{ex}}] \tag{7.4}$$

Consider now the photons that are emitted from the excitation volume. If we define I_e to be the total intensity emitted from the excitation volume (in all directions), then I_d (the fraction of I_e that is detected) will be proportional to I_e. The proportionality constant C (as defined in equation 7.5) will be less than one and dependant only on the system geometry and the detector sensitivity, not on λ_{ex} or λ_{em}. Thus,

$$N_e(\lambda_{ex}, \lambda_{em}) = \frac{KI_d(\lambda_{ex}, \lambda_{em})}{C} \tag{7.5}$$

The specific quantum yield is then given by (combining equations 7.1, 7.4 and 7.5)

$$Q\left(\lambda_{ex}, \lambda_{em}\right) = \frac{I_d^*\left(\lambda_{ex}, \lambda_{em}\right)}{C\left(1 - e^{-\alpha(\lambda_{ex})d_{ex}}\right)} \tag{7.6}$$

Here, I_d/I_{inc} has been replaced with I_d^*, reflecting the fact that raw emission intensity data recorded by the spectrometer will have been pre-corrected for variations in lamp intensity. Also, in order to account for probe attenuation and emission re-absorption within the sample, a correction has been applied to the raw spectra (as described in chapter 6) prior to the determination of the quantum yield. The value typically reported as the quantum yield (the'traditional' quantum yield, Φ) will then be the integral of equation 7.6 over all emission wavelengths,

$$\Phi\left(\lambda_{ex}\right) = \frac{1}{C}\frac{\int I_d^*\left(\lambda_{ex}, \lambda_{em}\right) d\lambda_{em}}{1 - e^{-\alpha(\lambda_{ex})d_{ex}}} \tag{7.7}$$

Note that the factor $1/C$ is a normalising parameter dependent only on the system geometry and the detector sensitivity. In order to determine this factor, we can measure the absorbance and emission spectra of a standard with a known quantum yield Φ_{st}. Then a simple rearrangement of equation 7.7 yields

$$\frac{1}{C} = \frac{\Phi_{st}\left(1 - e^{-\alpha_{st}(\lambda_{ex})d_{ex}}\right)\left(n_{sample}\right)^2}{\int I_{d,st}^*\left(\lambda_{ex}, \lambda_{em}\right) d\lambda_{em}\left(n_{st}\right)^2} \tag{7.8}$$

where n_{sample} and n_{st} are the refractive indices of the sample and reference standard, respectively. In our study, these values were the same. The above equations for the quantum yield are equivalent to standard methods provided in the literature [245]. Note that typically,

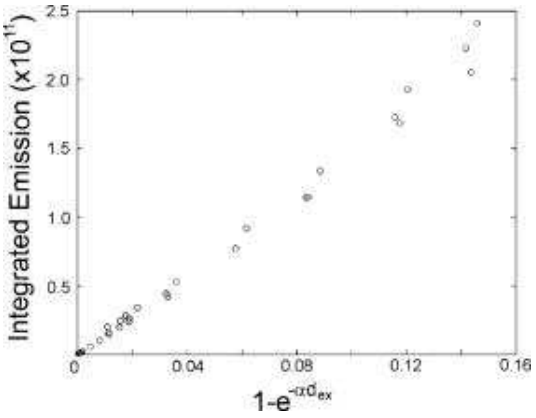

FIGURE 7.2: Integrated emission as a function of absorption coefficient (α) for 30 quinine sulphate solutions (concentrations 1×10^{-6} to 1×10^{-4}M in H_2SO_4). d_{ex} (length of excitation volume) assumed to be 0.1 cm (figure from [48]). Vertical axis is in counts per second.

the ratio of integrated emission to absorption coefficient is used for determining gradients to calculate the radiative yield, whereas the present discussion uses the ratio of integrated emission to $1 - e^{-\alpha d}$, as shown in figure 7.2. The former ratio is based upon the approximation $e^{-\alpha d} = 1 - \alpha d$, which is not valid for studies such as ours in which the sample (melanin) has large absorption coefficient values. For more precise results, we have measured the absorbance and emission of the standard solution for a wide variety of concentrations and plotted the expression in equation 7.8 (figure 7.2). $1/C$ is then given by the gradient of a linear regression.

7.4 Experimental

7.4.1 Sample preparation

Synthetic eumelanin derived by the non-enzymatic oxidation of tyrosine was purchased from Sigma-Aldrich (Sydney, Australia) and was treated by acid precipitation in order to remove small molecular weight components, following the method of Felix et al. [150]. Briefly, dopamelanin (0.0020 g) was mixed in 40 mL high-purity 18.2 MΩ milliQ de-ionized water and 0.5 M hydrochloric acid was added to bring the pH to 2. Solutions were centrifuged and the black precipitates were repeatedly washed in 0.01M hydrochloric acid and then de-ionized water. A 0.0050% solution (by weight) of the remaining precipitate was prepared in de-ionized water. To aid solubility, the solution was adjusted to pH 10 using NaOH (as in previous chapters). Given that high pH also enhances polymerization [246], this adjustment also ensured that the presence of any residual monomers or small oligomers in the solution was minimized. A pale brown, apparently continuous solution was produced. Quinine sulphate (Sigma-Aldrich) was used without further purification at 30 different concentrations (1×10^{-6} to 1×10^{-4}M in 1 N H_2SO_4 solution) as a standard for the determination of the radiative quantum yield.

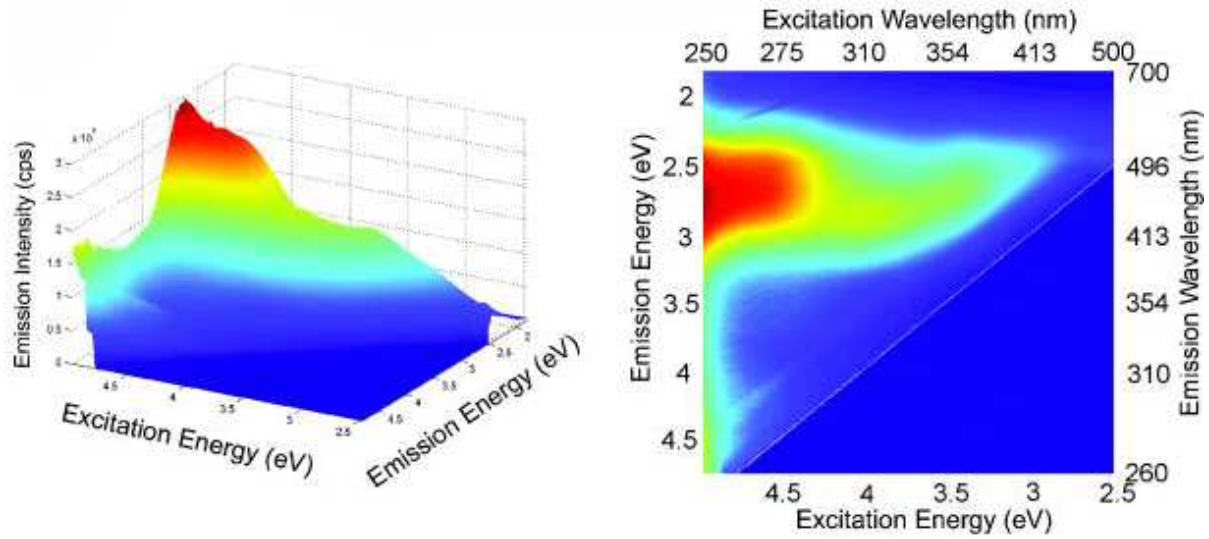

Figure 7.3: Re-absorption corrected fluorescence map for synthetic eumelanin (high emission in red, low emission in blue). From [48].

7.4.2 Absorption and emission spectrometry

Absorbance spectra for each solution were measured as described in section 4.3.2. Fluorescence emission spectra for eumelanin and quinine sulphate were recorded in a very similar manner to that described in section 6.3.3 with an integration time of 0.5 s. Matrix scanning software allowed excitation and emission intervals of 1 nm. All emission spectra were corrected for re-absorption and inner filter effects using the method outlined in chapter 6. Quantum yields were calculated using the method outlined above with standard values [247]. Since the quantum yield of quinine is temperature dependent, the ambient temperature surrounding the cuvette was measured to be 35°C, resulting in a 2.5% shift from the published value of 0.546.

7.5 Results and discussion

Figure 7.3 shows the measured fluorescence map for synthetic eumelanin as a three dimensional projection, and as a contour map. As was reported for the emission spectra in chapter 6, a narrow peak was observed in the raw emission spectra due to Raman scattering from the solvent (water). This peak was completely removed by the re-absorption and inner filter correction process (which includes subtraction of background emission from the solvent), showing again that the correction process described in chapter 6 was accurate. First and second order Rayleigh scattering peaks were also observed in the emission spectra, and were removed manually (due to their high intensity relative to eumelanin emission these peaks saturated the detectors and hence could not be removed by background subtraction).

The maximum emission was observed for $\lambda_{ex} = 295$ nm (4.2 eV) at $\lambda_{em} = 460$ nm (2.7 eV), although from the shape of the peak it is likely that there is even greater emission at higher excitation energies. Higher energies were not probed in this study since all measurements

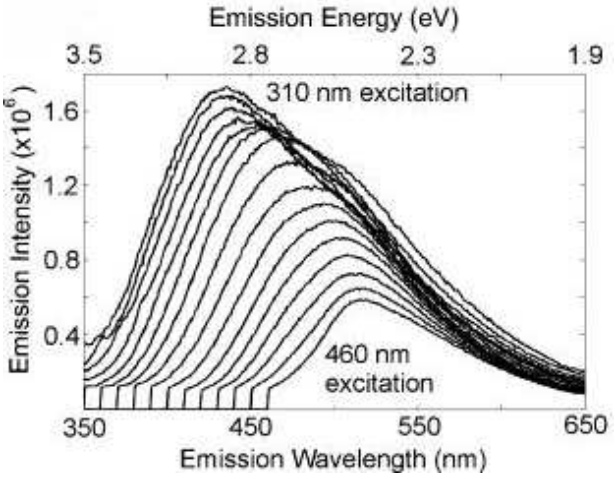

FIGURE 7.4: Emission spectra for synthetic eumelanin solution, extracted as vertical cross sections from fluorescence map in figure 7.3. We observe a broad band that shifts with excitation wavelength. Vertical axis is in counts per second.

were performed in water, which has strong absorbance outside of this range.

We can identify two distinct regimes in figure 7.3. Firstly, for $\lambda_{ex} > 310$ nm the emission peak position shows a dependance upon the excitation energy (there is a gradual diagonal shift in peak position with excitation wavelength). This dependance of the emission spectra upon the excitation energy was observed previously in chapter 6 for 360 nm $< \lambda_{ex} <$ 380 nm; we observe it here over a much larger range of excitation energies (310 nm $< \lambda_{ex} <$ 460 nm). This is depicted as discrete emission spectra in figure 7.4 for comparison to earlier results (emission spectra can be easily extracted from the fluorescence map as vertical cross sections). We observe the same decrease in peak height and redshifting of the emission with decreasing excitation wavelength with a low energy cut-off as was observed in chapter 6. As discussed earlier, emission spectra are usually independant of excitation energy, and the violation of this in this case is indicative of the presence of multiple chemical species. The emission peak position shifts from $\lambda_{em} = 435$ nm (2.9 eV) to 517 nm (2.4 eV) with excitation energy change from $\lambda_{ex} = 310$ nm (4.0 eV) to 460 nm (2.7 eV).

Figure 7.3 also reveals the presence of a previously unobserved regime for $\lambda_{ex} < 310$ nm, where emission is independant of excitation energy. At these higher energy excitation wavelengths the emission peak occurs at $\lambda_{em} = 460$ nm (2.7 eV) independant of excitation energy, and merely increases in intensity with increasing energy (with cut-offs on both the low and high energy side of the peak). This suggests that emission in this part of the spectrum is due to a single species, whereas multiple chemical species contribute at lower energies.

Note that we do not observe a dual peaked emission spectrum at any excitation energy, as has been observed in some previous studies [121, 225, 232, 233].

Excitation spectra extracted as horizontal cross sections from the fluorescence map are shown in figure 7.5. These spectra are in good agreement with those previously reported in reference [164]. They are multi-peaked, with a main peak at $\lambda_{ex} = 365$ nm (3.40 eV) that

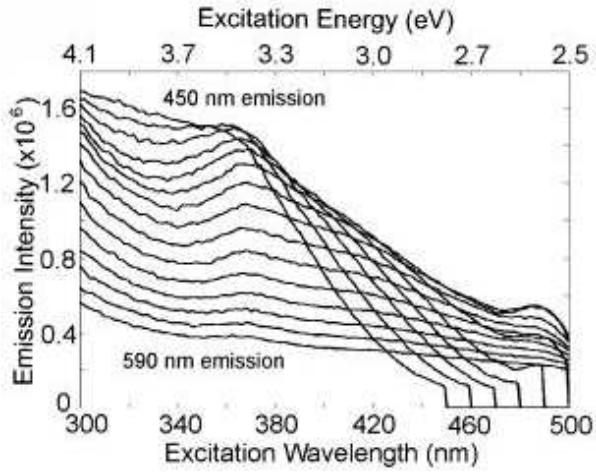

Figure 7.5: Excitation spectra for synthetic eumelanin solution, extracted as horizontal cross sections from fluorescence map in figure 7.3. We observe a peak constant in position at 365 nm that varies in intensity with emission wavelength (from [48]). Vertical axis is in counts per second.

varies in intensity with λ_{em}, but not in position (observed for 450 nm (2.8 eV) $< \lambda_{em} <$ 590 nm (2.1 eV)). This could suggest the presence of a species that absorbs strongly at 365 nm and transfers energy to multiple other species which then give rise to emission at a range of wavelengths. A secondary peak is also observed at $\lambda_{ex} = 490$ nm for the emission wavelength range 500 nm (2.5 eV) $< \lambda_{em} <$ 540 nm (2.3 eV).

Typically, excitation spectra (such as those presented in figure 7.5) will be close to the shape of the absorbance spectrum (higher absorbance at a particular excitation wavelength typically leads to increased emission). The excitation spectra in figure 7.5 show an increase towards higher energies in a similar manner to the absorption spectrum (shown in figure 2.3), but it is clear that there is much more structure in these excitation spectra. This is an indication that the radiative quantum yield is dependant on excitation energy. We showed in chapter 6 that the radiative quantum yield does vary with excitation wavelength, at just three points, in agreement with the data shown here. To probe this further, we measured the radiative yield of eumelanin as a function of excitation wavelength, as shown in figure 7.6. The solid line shows the traditional quantum yield, here measured as a function of λ_{ex}, with values reported previously shown as discrete points for comparison. We show excellent agreement with the results reported in chapter 6, confirming the validity of our method. We emphasise the very low magnitude of the radiative yield of eumelanin which is of the order of 10^{-4} throughout the wavelength range measured. It can be seen that the yield is very clearly dependant upon the excitation wavelength in a non-trivial way, (it varies by a factor of 4 over the measured range, 250 nm to 500 nm) which is another indication of the presence of multiple species in our sample. Peaks in the yield are evident at 3.4 eV and 4.6 eV.

The specific quantum yield map for eumelanin is shown in figure 7.7. This quantity gives the radiative yield as a function of λ_{ex} and λ_{em}, as outlined in the theory section of this chapter. It is similar in shape to the fluorescence map, but is now scaled with the absorbance spectrum such that it gives the probability that a photon absorbed at a particular λ_{ex} will

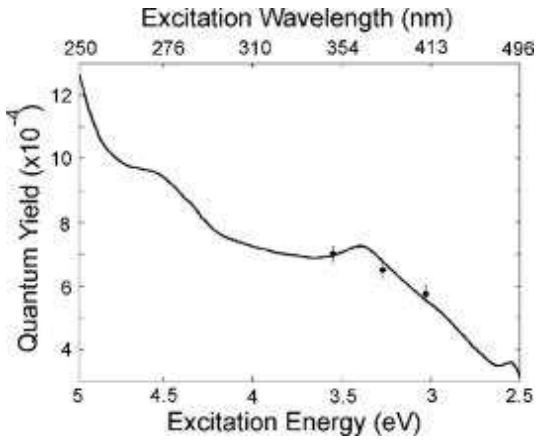

FIGURE 7.6: The traditional radiative quantum yield as a function of excitation energy across UV and visible wavelengths (solid line). Circles and error bars show previously measured quantum yield values from chapter 6 (figure from [48]).

be emitted at each λ_{em}. Three peaks are evident at excitation energies of 3.4 eV, 4.6 eV and > 5 eV. Note that the values are very small, the maximum being 5.2×10^{-6} (0.00052%), which is in keeping with the previously measured low radiative yields of eumelanin.

Acid precipitation makes the presence of monomers and small oligomers unlikely, but it is possible that residual concentrations remain in solution. Monomeric species have been shown to have significant radiative yields ($\sim$ 60%), whereas the yield of dimers is significantly reduced [248]. Increasing covalent bonding is thought to further reduce the radiative yield through increased electron-phonon coupling. Since the yield of eumelanin is very small is it possible that it is due to emission from a residual concentration of a monomeric species or other small molecule, or a collection of dimers and small oligomers with higher concentrations, but low radiative yields. We suggest that the $\lambda_{ex} < 310$ nm regime is due to a residual concentration of a single monomeric species (as suggested by the λ_{em} peak being independant of λ_{ex} and the relative insensitivity of the radiative yield to λ_{ex}). The $\lambda_{ex} > 310$ nm regime is more likely due to emission from multiple species (higher concentrations of low yield dimers and small oligomers).

7.6 Chapter conclusions

We have fully characterised the equilibrium spectroscopic properties of synthetic eumelanin over the UV/visible range, taking re-absorption and inner filter effects into careful account. Two distinct regimes are observed in the fluorescence map: $\lambda_{ex} > 310$ nm (likely due to a collection of low yield oligomers) and $\lambda_{ex} < 310$ nm (possibly due to a residual concentration of a single monomeric species with a substantial radiative yield). Clear structure and excitation energy dependance is revealed in both the specific radiative yield and the traditional radiative yield, indicative of the presence of multiple chemical species in eumelanin.

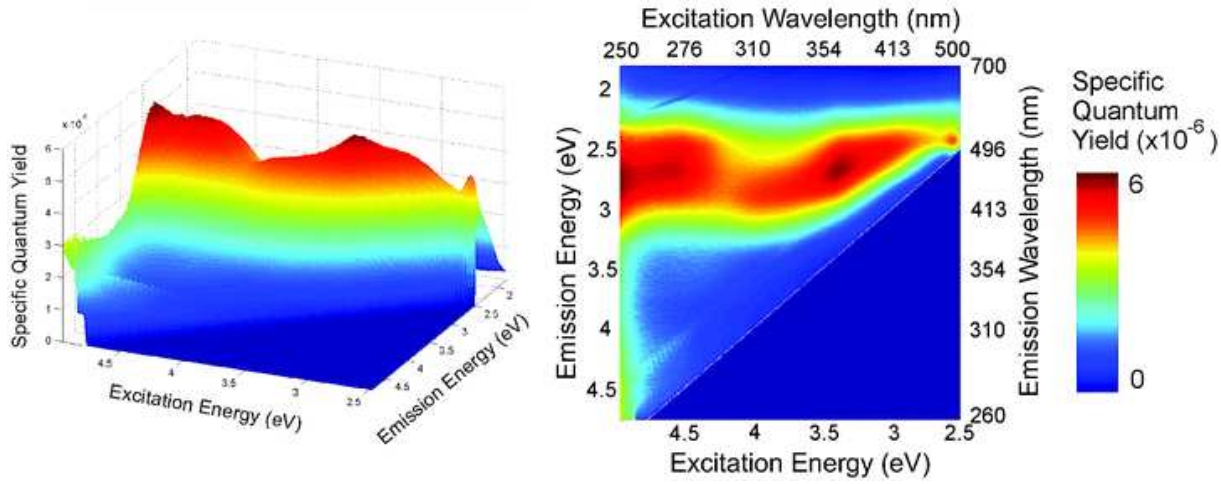

Figure 7.7: Specific quantum yield map for synthetic eumelanin (the fraction of photons absorbed at each excitation wavelength that are emitted at each emission wavelength). Two peaks are evident, with limiting values at high and low emissions (figure from [48]).

8

Radiative relaxation in synthetic pheomelanin

8.1 Chapter abstract

We report a detailed spectroscopic study of cysteinyldopa-melanin (CDM), a synthetic analogue of pheomelanin. Although CDM and dopa-melanin (DM, the synthetic analogue of eumelanin) have very similar absorption spectra, we find that they have very different excitation and emission characteristics; CDM has two distinct fluorescence peaks that do not shift with excitation wavelength. Additionally, our data suggests that the radiative quantum yield of CDM is excitation energy dependant (alike to eumelanin). Finally, we find that the radiative quantum yield for CDM is $\sim 0.2\%$, twice that of eumelanin, although still extremely low.

8.2 Chapter introduction

Pheomelanin is the red to yellow type of melanin found in human skin, hair and eyes. Although it is less predominant than eumelanin, pheomelanin is of significant interest since is more closely linked to melanoma skin cancer. 5-*S*-cysteinyldopa, a precursor of pheomelanin, is one of the best markers of malignant melanoma, being found in plasma and urine of melanoma patients in significant quantities [249]. It has also been shown that pheomelanin becomes mutagenic after exposure to UV light [250, 251], and is more photolabile than eumelanin [252–255]. Pheomelanin is known to produce a variety of photoproducts that trigger oxidative stress and can cause DNA damage (hydrogen peroxide, superoxide and hydroxyl radicals) [19, 256] and it has been suggested that this is why people with red hair (who have high pheomelanin levels) are more susceptible to skin cancer than those with dark colouring [16, 257, 258]. Other studies suggest that the ratio of pheomelanin to eumelanin is the important parameter, those with a higher ratio having a higher risk of melanoma, regardless of the overall amount of pigment [259, 260]. Still other studies suggest that

pheomelanin may be photoprotective or photosensitising depending upon the concentration of the pigment, and the wavelength of irradiation [251]. There remains great uncertainty as to the biological functioning of pheomelanin vs eumelanin, making it extremely challenging to determine their respective roles in photoprotection and the development of melanoma skin cancer [19].

It should not be assumed that pheomelanin behaves in the same way as eumelanin. Firstly, pheomelanin has a distinctly different colour to eumelanin, suggesting different spectroscopic properties. Additionally, although both types of melanin have been shown to quench the fluorescence of porphyrin compounds, there are significant differences in their behaviour that suggest the mechanism of interaction is quite different for the two pigments [261]. Hence we believe that pheomelanin deserves substantial independant study (although it represents a relatively small component of this thesis).

Biologically, it appears that melanogenesis occurs in three stages, with the first two involving the production of cysteinyldopa and pheomelanin respectively. Eumelanins are only produced in the third stage, when all cysteinyldopa is depleted. This suggests that eumelanin may be deposited onto preformed pheomelanin particles [39, 262]. Advanced chemical methods have been developed to accurately determine the relative amounts of eumelanin and pheomelanin in natural samples [204, 263], but the way in which the two pigments are structurally arranged is not well understood.

We have discussed structural models for eumelanins (in chapter 3), but pheomelanins have been studied far less extensively and their structure should not be assumed to be identical. The pheomelanin monomers, benzothiazines, are structurally different to DHI and DHICA [39], and follow a different synthetic pathway to form pheomelanins, as shown in figure 1.2. Several benzothiazine dimers have been isolated from natural pheomelanins, confirming the fact that 1,4-benzothiazines are the monomeric species that form pheomelanin biologically, and suggesting likely binding sites for the formation of the pheomelanin macromolecule [264]. These benzothiazine dimers are termed 'trichochromes', structures of which are shown in figure 8.1. Small benzothiazine oligomers have also been obtained from oxidation of cysteinyldopa under a variety of conditions [265, 266], with structures as shown in figure 8.2. Which oligomers are formed sheds light on the way that the benzothiazine monomers might bind to form the macromolecular structure of pheomelanin [267].

MALDI (matrix assisted laser desorption ionization) mass spectrometry measurements on hair pheomelanin suggests that it consists mostly of small oligomeric species, rather than large polymeric structures [268]. As in the case of eumelanin, however, it is possible that large species escaped detection due to the limitations of this method. A variety of other studies of the chemical structure of pheomelanin have been conducted, including radiotracer studies and NMR spectroscopy [269–271], and atomic force microscopy imaging of whole melanosomes (showing the spherical and fragile nature of pheomelanosomes, as described in an earlier chapter) [85]. Despite these studies, a clear and accurate picture of the primary and secondary structure of pheomelanin remains even more elusive than for eumelanin. This adds substantial difficulty to the identification of features in spectroscopic analysis [261].

As stated earlier, pheomelanins have been studied far less extensively than eumelanins in almost all respects, and spectroscopic analysis is no exception. The absorption spectrum of pheomelanin is well known to be broadband and exponential (as shown in figure 8.3),

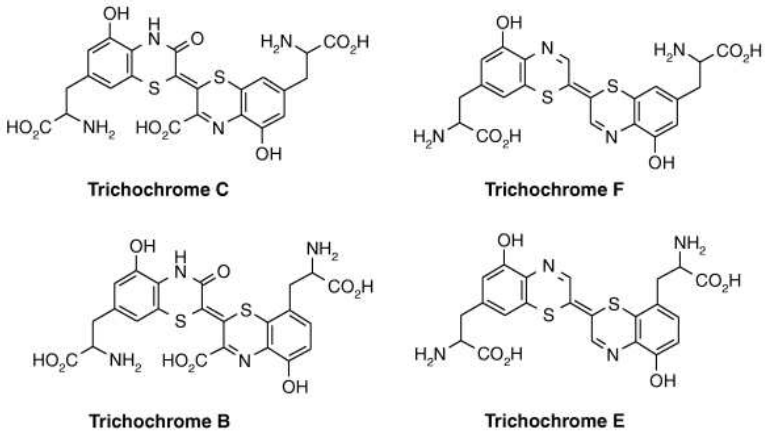

Figure 8.1: Structures of trichochromes (benzothiazine dimers) isolated from natural pheomelanin (from [267]).

similar to eumelanin. Also similar to eumelanin, pheomelanin fluorescence is reported to be extremely weak, and significantly enhanced by oxidative degradation [272]. Emission and excitation spectra for melanin extracted from the hair of yellow mice were reported in 1978 by Ikejima and Takeuchi; the yellow pigment is believed to be predominantly pheomelanin. They measured a multipeaked excitation spectrum with a maximum at 308 nm, and a single peaked emission spectrum with a maximum at 425 nm (λ_{ex} = 320 nm). The spectra are notably different from those measured for melanin extracted from the hair of black mice in the same manner, suggesting definite differences between the spectroscopic properties of the two pigments. Additionally, Olivecrona and Rorsman observed in 1966 that melanocytes from red hair fluoresce more strongly than those from black hair [273], perhaps suggesting that pheomelanin has a greater radiative yield than eumelanin (which we confirm in this chapter).

There have been several studies of the ultrafast absorption dynamics and energy transfer of pheomelanins, revealing that they have very short decay lifetimes [274–277]. Similar to eumelanin, it has been shown that pheomelanin does not exhibit complete ground state recovery after photoexcitation, suggesting that it might form long-lived intermediates [276]. It has also been proposed that the ratio of absorbances at 650 nm and 500 nm can be used as a non-invasive indicator of the relative amounts of eumelanin and pheomelanin in solution, due to the distinct differences in their spectra [278]. Otherwise, the bulk of the spectroscopic literature has focused on eumelanins, rather than their more photoactive counterpart, the pheomelanins.

In this chapter we present accurate fluorescence spectra for pheomelanin that have been corrected for re-absorption and inner filter effects using the method outlined in chapter 6. The use of this method has also allowed us to accurately measure the radiative quantum yield of pheomelanin, we believe for the first time. We have used cysteinyldopa-melanin (CDM) and dopa-melanin (synthetic eumelanin) as synthetic analogues for pheomelanin and eumelanin respectively [279].

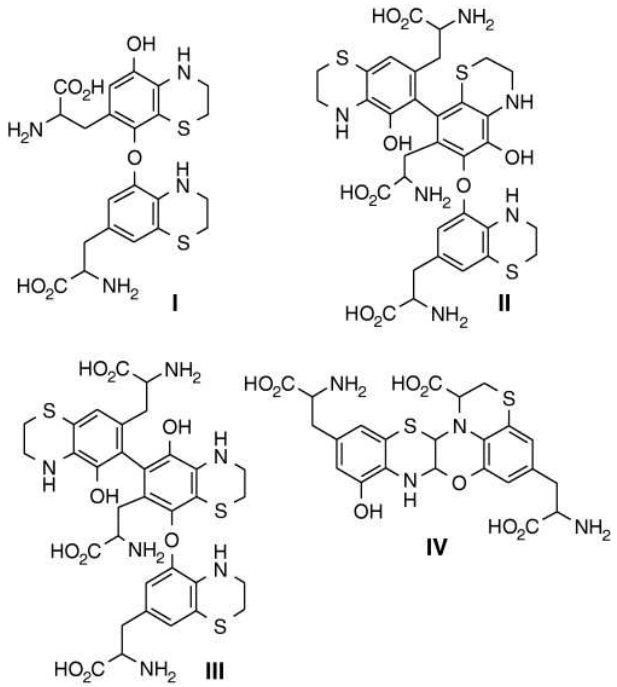

FIGURE 8.2: Oligomers of 1,4-benzothiazine obtained from oxidation of cysteinyldopa under a variety of conditions (from [267]).

8.3 Experimental

8.3.1 Sample preparation

CDM was derived from the tyrosinase-catalyzed oxidation of a mixture of L-dopa and L-cysteine in the ratio 1 : 1.5, as described fully in reference [280]. The powder was diluted to a range of concentrations (0.001% to 0.005% by weight macromolecule) in high purity 18.2MΩ MilliQ de-ionised water. To aid solubility, the solutions were adjusted using NaOH to $\sim$ pH10, and gently heated with sonication. Pale brown, apparently continuous dispersions were produced. Between measurements solutions were stored in darkness at 4°C. Synthetic eumelanin solutions were prepared as described in section 4.3.1. Fluorescein solutions (for use as a radiative quantum yield standard) were prepared as described in section 6.3.1 at five different concentrations (1×10^{-5}% to 4×10^{-5}% by weight).

8.3.2 Absorption spectrometry

Absorption spectra were measured as described in section 4.3.2.

8.3.3 Fluorescence emission and excitation spectrometry

Fluorescence emission and excitation spectra were measured as described in section 6.3.3 with an integration time of 0.5 s. All spectra were corrected for re-absorption and inner-filter effects using the method outlined in chapter 6. Quantum yields were calculated as

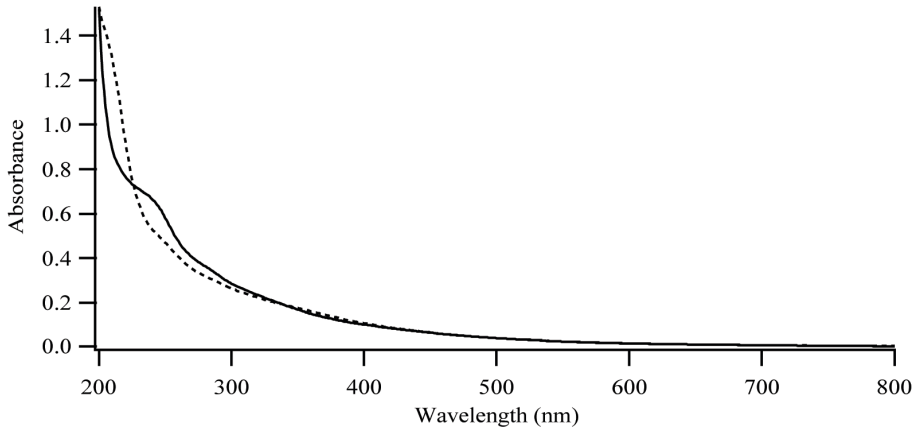

Figure 8.3: Absorbance of CDM solution (0.001% by weight), (solid line: 0 days, dotted line: 10 days). The absorbance spectrum stabilised completely after approximately 10 days, and very little further change was observed.

described in section 6.3.5.

8.4 Results and discussion

8.4.1 Absorption

The absorbance spectrum of CDM was monitored over a period of 24 days; initial and final absorption spectra are shown in figure 8.3. Initially, small peaks were observed at approximately 240 nm and 330 nm; these decreased gradually over a period of 10 days, after which time very little change in the spectrum was observed. At the final time-point the CDM absorbance spectrum was characteristically broadband, like eumelanin, increasing monotonically towards higher energies. The peaks found in the initial spectrum were attributed to small amounts of precursors (potentially benzothiazine or cysteinyldopa units) which eventually polymerised.

Figure 8.4 compares the absorption spectra of CDM and eumelanin. Both increase monotonically towards higher energies, although CDM does so more steeply. Since the cysteinyldopa monomer has fewer crosslinking sites than either DHI or DHICA (the eumelanin monomers) it might be expected that CDM is structurally less disordered than eumelanin. Possibly, then, there are fewer oligomers with absorbances in the visible range, giving a steeper absorbance curve. Both spectra are extremely close to exponential in shape in wavelength space. Fit parameters are shown in table 8.1, with fitting to the expression

$$A = k_0 + k_1 e^{-k_2 \lambda} \tag{8.1}$$

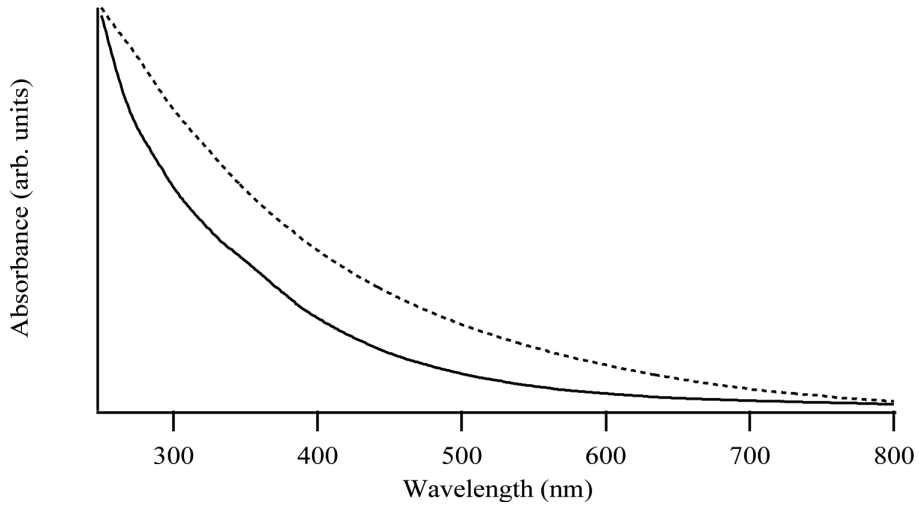

FIGURE 8.4: Comparison of the absorbance spectrum for CDM (at 10 days) (solid line) and eumelanin (dotted line). The curves show signficantly different shapes, although both are broad-band and almost entirely featureless. Spectra have been scaled for shape comparison. Both are exponential, fitting parameters of which are shown in table 8.1.

	k_0 (dimensionless)	k_1 (dimensionless)	k_2 (nm^{-1})
CDM	0.0013	4.19	0.0092
eumelanin	-0.0073	1.98	0.0061

Table 8.1: Fit parameters for melanin absorbance spectra (shown in figure 8.4), as defined in equation 8.1. Both solutions were at a concentration of 0.001% by weight, with a 1 cm absorption path length. CDM values are taken at 10 days, when the solution had stabilised.

8.4.2 Emission

The CDM emission spectrum exhibits two clearly resolved gaussian peaks that do not shift over time, or with changes in excitation wavelength, as shown in figure 8.5. The two peaks, occuring consistently at 2.27 ± 0.08 eV (548 nm) and 2.72 ± 0.08 eV (458 nm) are evident at all time-points and excitation wavelengths, and only vary in relative heights. Gaussian fittings were performed for all spectra[1] according to the equation

$$I = N_1 e^{-[(E-E_1)/D_1]^2} + N_2 e^{-[(E-E_2)/D_2]^2} + A \tag{8.2}$$

All fits to a simple two gaussian model were excellent; a representative example is shown in figure 8.6. The resulting fit parameters are given in table 8.2.

The fact that the emission peaks do not shift with excitation wavelength is a significant difference between pheomelanin and eumelanin; recall from chapter 6 that the eumelanin emission spectrum consisted of a single peak that showed a consistent migration to lower

[1]As stated in an earlier section, all fitting has been performed in energy space (E) since line broadening is characteristically gaussian in energy (not in wavelength).

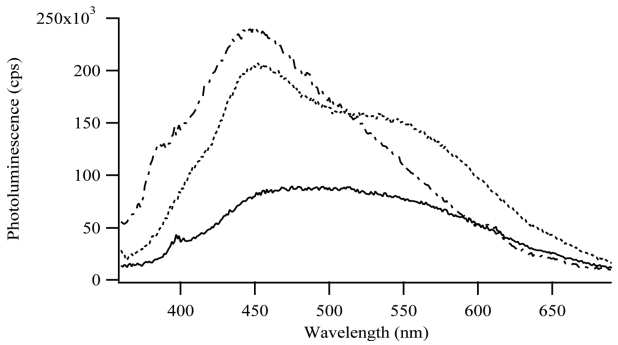

(a) Excitation at 350 nm

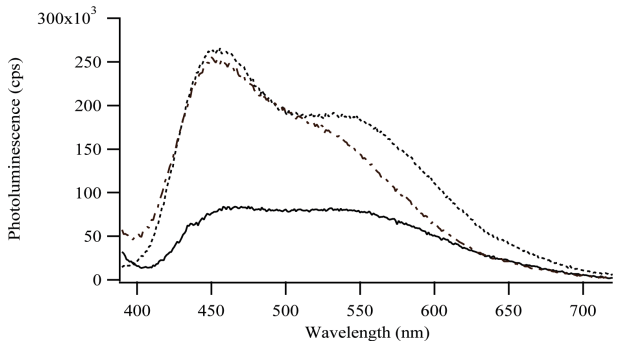

(b) Excitation at 380 nm

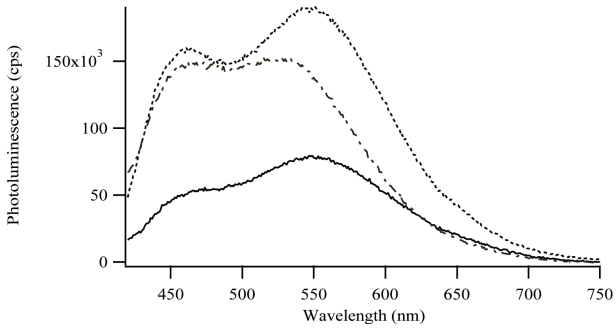

(c) Excitation at 410 nm

Figure 8.5: Fluorescence of CDM solution (0.001% by weight). Only key time points are shown for clarity (solid: 0 days, dotted: 6 days, dot-dash: 10 days). The spectrum stabilised after approximately 10 days, and little further change was observed. The small peak evident at approximately 400 nm in some spectra is a remnant of the Raman scattering peak that was not completely removed by background subtraction due to lamp intensity fluctuations.

time	$\lambda_{excitation}$	E_1 (eV)	E_2 (eV)	N_1 (cps)	N_2 (cps)	D_1 (eV^{-1})	D_2 (eV^{-1})	A (cps)
0 days	350 nm	2.17	2.59	24800	80600	0.227	0.483	7110
	380 nm	2.24	2.69	69200	74100	0.286	0.287	2100
	410 nm	2.26	2.72	78100	43900	0.301	0.235	-1350
6 days	350 nm	2.21	2.73	103000	183000	0.248	0.369	15500
	380 nm	2.31	2.76	188000	236000	0.329	0.222	-1690
	410 nm	2.27	2.73	187000	143000	0.270	0.228	-383
10 days	350 nm	2.22	2.76	15200	227000	0.181	0.540	1150
	380 nm	2.34	2.75	146000	226000	0.280	0.257	4790
	410 nm	2.33	2.75	143000	126000	0.284	0.245	-258

Table 8.2: Gaussian fit parameters to CDM fluorescence spectra. Parameters are as defined in equation 8.2.

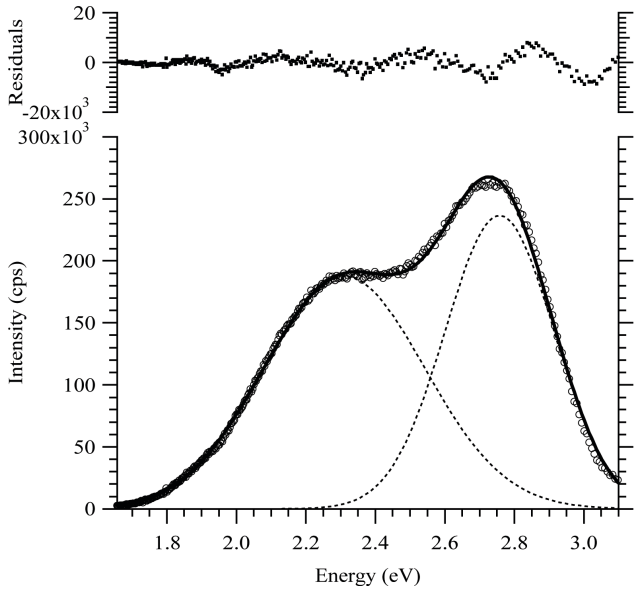

FIGURE 8.6: Fluorescence of CDM (6 days, 380 nm excitation) with double gaussian fit (as per equation 8.2). The excellent fit of the double gaussian is representative of all spectra. Open circles: experimental data, solid line: fit, dotted line: peaks 1 and 2.

energies as the excitation energy was reduced. This suggests that while eumelanin is dominated by chemical disorder, CDM may have fewer species contributing to radiative emission, giving rise to only two peaks that do not shift with varying excitation wavelength. The two peaks could be representative of two distinct chemical species, or two collections of chemical species with very similar excitation energies.

It is possible that the synthetic method for the CDM used here could produce a sample that is a mixture of CDM and eumelanin (dopa-melanin). This would produce two peaks in the CDM spectrum (one due to pure CDM, the other due to eumelanin). We believe that this is not the case, however, since neither of the peaks coincide with the seperately measured eumelanin peak when excited at the same energy (as shown in figure 8.7), and

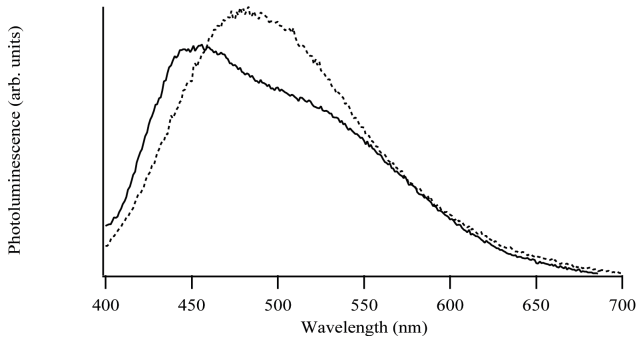

FIGURE 8.7: Fluorescence of CDM (stabilised at 10 days, solid line) and eumelanin (dotted line) with excitation at 380 nm.

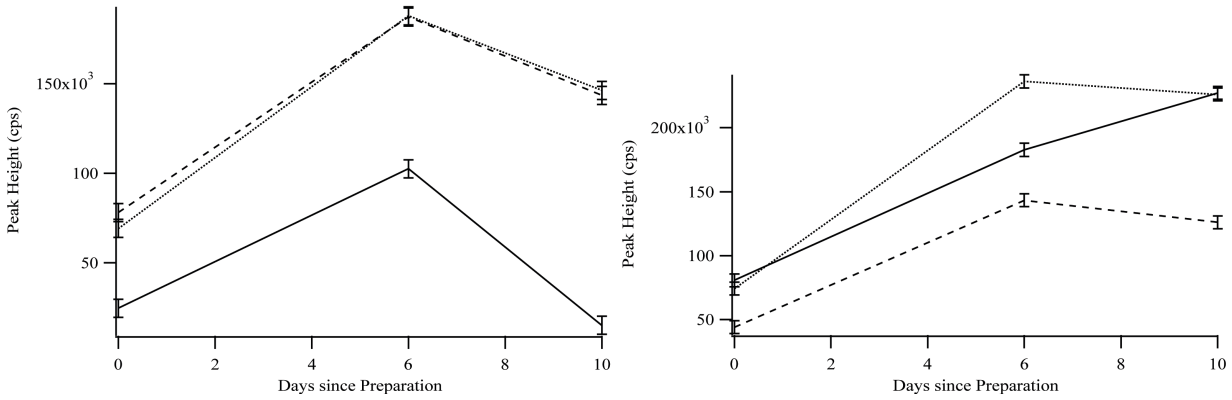

(a) Height of low energy peak ($\lambda_{em} = 548$ nm) (b) Height of high energy peak ($\lambda_{em} = 458$ nm)

Figure 8.8: Relative heights of the two gaussian CDM emission peaks over time (parameters N_1 and N_2 as defined in equation 8.2, and listed in table 8.2). Solid line: $\lambda_{ex} = 350$ nm, dotted line: $\lambda_{ex} = 380$ nm, dashed line: $\lambda_{ex} = 410$ nm.

neither peak shifts with excitation energy in the same way. Interestingly, Gallas and Eisner [232] observed a double peaked eumelanin spectrum (not CDM), although their spectra showed an isosbestic point at 470 nm which we do not observe in our spectra.

As for the absorbance spectrum, we believe that the changes observed in the emission spectrum over time are due to a combination of high pH-induced polymerisation of remnant low molecular weight precursors and pheomelanin autooxidation (which is known to increase fluorescence [237]). However, we do not believe this process to be dominated by oxidation, since this would also result in increased absorbance at long wavelengths (which is not observed). This suggests that we are mainly observing a polymerisation reaction. The relative heights of the two peaks determined from the gaussian fitting (N_1 and N_2, listed in table 8.2) have been plotted in figure 8.8. Over time we see that the higher energy peak (at 458 nm) increases in intensity, and then appears to stabilise (except when excited at 350 nm), whereas the lower energy peak (at 548 nm) increases initially, then decreases. This suggests that the concentrations of the two sub-populations of oligomers responsible for these peaks are changing over time as the CDM polymerises. Possibly, the lower energy peak is due to a small oligomeric species that increases in concentration initially, then gradually polymerises into larger units (which potentially give rise to the higher energy peak).

8.4.3 Excitation

Figure 8.9 shows fluorescence excitation data for CDM. These spectra were measured after the CDM had stabilised (at 10 days), and have been fully corrected for re-absorption and inner filter effects. The detection wavelengths (465 nm and 550 nm) were selected since they are close to the positions of the two peaks observed in the fluorescence spectra. We can see that the higher energy peak (at 458 nm) will show maximum emission when excited at approximately 380 nm. The lower energy peak (at 548 nm) will show maximum emission when excited at approximately 395 nm. As discussed in the previous chapter, the fluorescence

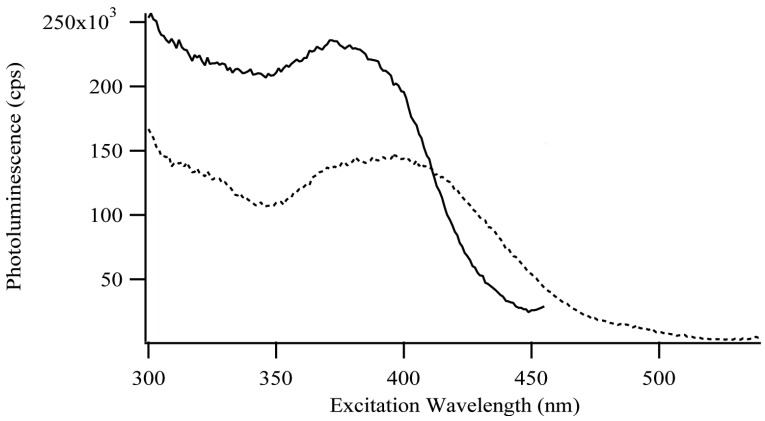

FIGURE 8.9: Fluorescence excitation of CDM solution (0.001% by weight) after 10 days. Solid line: $\lambda_{em} = 465$ nm, dashed line: $\lambda_{em} = 550$ nm.

excitation spectrum typically has the same shape as the absorption spectrum, but this is clearly not the case for CDM. This suggests that the processes of photon absorption and photon emission are not closely linked in CDM (they are likely separated by a great deal of coupling to phonon modes of the system, or other non-radiative relaxation processes). This result highlights the need for accurate radiative relaxation quantum yield data for CDM, to better understand the relationship between photon absorption and emission.

8.4.4 Radiative quantum yield

The use of the re-absorption correction method outlined in chapter 6 allowed accurate measurement of the radiative quantum yield of CDM, shown in figure 8.10. The yield was monitored for a period of 24 days. Note that as for eumelanin the yield is extremely small, approximately 0.2%. This means that 99.8% of the energy absorbed by CDM is dissipated via non-radiative pathways. Calorimetry measurements for pheomelanins would allow a distinction between the various non-radiative pathways. We see that over time the yield initially increased, and appears to have stabilised after the first 10 days, with some minor fluctuations. The stabilised quantum yield values at each excitation wavelength are shown in table 8.3. It is surprising that the yield increased over time, since we suspect that the concentration of small monomeric and oligomeric species was reducing over this time, and these species are known to have higher radiative yields [161]. Additionally, this result is inconsistent with the results reported in chapter 10 (as DHICA polymerises to form eumelanin the yield decreases substantially). This finding should be explored further.

It is clear that like eumelanin, the radiative quantum yield of CDM is dependant upon the excitation wavelength [245], suggestive of chemical heterogeneity. It is interesting to note that the yields when excited at 380 nm and 410 nm are very similar at all time points, but the yield at 350 nm is always significantly lower. This is because the consistently higher absorption at 350 nm is not reflected in an increase in fluorescence when excited at that wavelength (the integrated intensity is very similar to that when excited at 380 nm). This, combined with the fact that the peak height results (figure 8.8) showed differing behaviour

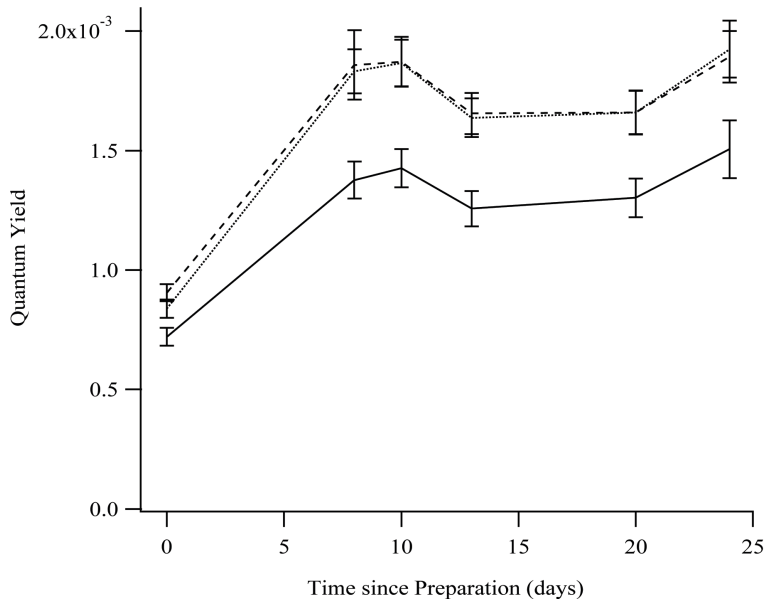

Figure 8.10: The quantum yield of CDM over time. Solid line: $\lambda_{ex} = 350$ nm, dotted line: $\lambda_{ex} = 380$ nm, dashed line: $\lambda_{ex} = 410$ nm.

λ_{ex} (nm)	radiative quantum yield (%)
350	0.143 ± 0.008
380	0.19 ± 0.01
410	0.19 ± 0.01

Table 8.3: Radiative quantum yield values for CDM (at 10 days).

for excitation at 350 nm suggests that the relaxation process at this wavelength is different to that at 380 nm and 410 nm. Interestingly, there is a trough centered around 350 nm in the fluorescence excitation spectra (figure 8.9) for both detection wavelengths. Further spectroscopic studies should take this into account by observing behaviour when excited at 350 nm, in addition to other wavelengths.

Figure 8.11 compares the radiative yield of CDM to that previously measured for eumelanin. Most significantly, the radiative quantum yield of CDM, although very small, is approximately twice that of eumelanin. This perhaps reflects the fact that eumelanin is known to be a better photoprotectant than pheomelanin. Since relaxation via phonon modes occurs on a significantly shorter timescale than fluorescence (picoseconds, rather than nanoseconds [245]), a larger number of CDM oligomers will remain excited until relaxing radiatively, potentially related to pheomelanin's higher photoreactivity. We also see that the yield for CDM follows a different trend with excitation wavelength to that for eumelanin, indicating that although these two molecules are very similar in many ways, they do have different energy dissipation behaviour.

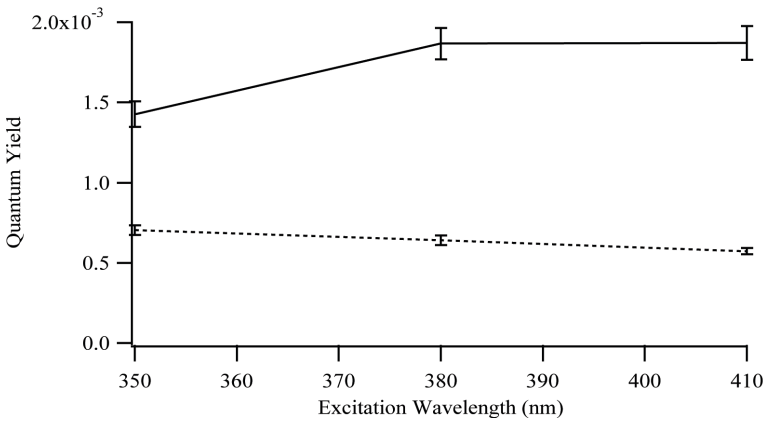

FIGURE 8.11: The quantum yield of CDM (at 10 days, solid line) and eumelanin (from chapter 6, dashed line).

8.5 Chapter conclusions

In this chapter we present a quantitative study of the emission and excitation properties of CDM, a synthetic analogue of pheomelanin. We find that the spectra are fundamentally different to those for eumelanin, having two distinct broad peaks which do not shift with excitation wavelength. We have also accurately measured radiative quantum yields for CDM, showing that although the yield is twice that of eumelanin, it is extremely low (0.2%), consistent with pheomelanin's role as a primary photoprotectant.

9

Quantitative spectroscopy of 5,6-dihydroxyindole-2-carboxylic acid (DHICA), a key eumelanin monomer

9.1 Chapter abstract

We report accurate, quantitative spectroscopic measurements for 5,6-dihydroxyindole-2-carboxylic acid (DHICA), a key eumelanin monomer. The DHICA extinction coefficient shows two peaks at 3.8 eV and 4.2 eV, consistent with previous studies. The excitation spectrum shows peaks in identical locations but with different relative heights, suggesting unusual excitation energy dependance in the radiative quantum yield. Emission spectra have a single gaussian peak at 3.1eV that is independant of excitation energy which suggests radiative emission occurs from a single electronic state in this system. The absence of a second peak in the emission spectrum causes violation of the mirror-image symmetry rule, which we propose is due to convergent adiabatic and nonadiabatic excited-state intramolecular proton-transfer (ESIPT) processes. This suggests that intramonomer proton transfer may contribute to energy dissipation in eumelanin.

9.2 Chapter introduction

Interest in DHICA has predominantly stemmed from its role as a monomer in the macromolecular eumelanin pigment. Eumelanin is difficult to study and model accurately due to its extreme heterogeneity, but the eumelanin monomers (DHI and DHICA) offer a much more controlled and easily characterised system. It is hoped that by studying and understanding the electronic, structural and physical properties of the monomers we may extrapolate to

dimers and larger oligomers, and eventually to the eumelanin macromolecule.

It has also been suggested that the monomers may actually have biological functionality themselves, apart from their involvement in eumelanin pigment. DHI and DHICA are found in significant amounts in epidermal tissue and body fluids [105], and DHI, DHICA and the eumelanin macromolecule have all been shown to have excellent hydrogen donor activity (and therefore antioxidant activity), with both precursors being more efficient than eumelanin [188]. This suggests that photoprotection by eumelanin may also involve scavenging of free radicals (produced by UV exposure) by the monomeric precursors [105, 158, 281–283]. Conversely, it has also been proposed that the eumelanin precursors may be involved in the paradoxical cytotoxic effects of melanin [214, 281, 282, 284, 285]; DHI in particular is known to exhibit potent cytotoxicity [286], and it has been shown that DHICA can induce DNA strand breaks with UVA irradiation via a mechanism involving reactive oxygen species [287]. The paradoxical 'photosensitising vs photoprotecting' action of DHICA is a fascinating property of this system [288]. Additionally, it has even been suggested that DHICA functions as a chemical messenger mediating interaction between active melanocytes and macrophages in epidermal inflammatory and immune responses [289]. Hence the eumelanin precursors (DHI and DHICA) are themselves interesting subjects of study.

There is a limited amount of spectroscopic data available for DHI and DHICA. DHI absorbance is double peaked with maximum absorbance at 296 nm and a shoulder at 270 nm (in deaerated water) [188, 214, 290, 291]. DHICA also has a double peaked spectrum with a main peak at 323 nm and a shoulder at 300 nm (in pH 9 water) [76, 188, 214, 287, 291]. The red-shifting of the DHICA peaks relative to DHI is thought to be due to increased delocalisation over the carboxyl group [188]. Both species are known to exhibit blue fluorescence [188, 291] and Zhang et al. report excitation maxima at 330 nm for DHI and 345 nm for DHICA (monitoring fluorescence at 420 nm). We were unable to find published emission maxima, emission or excitation spectra or radiative quantum yield values. Radiative emission is known to be a significant de-excitation pathway for DHICA, so it is surprising that there is not more literature about its emission properties. This highlights the need for an accurate quantitative study of the spectroscopic properties of the eumelanin precursors.

An accurate knowledge of the pK_a's of these monomers is essential for understanding the polymerisation processes that occur in eumelanin formation, and the interesting pH dependant behaviour of these molecules. The best estimates come from Charkoudian and Franz [292], who measure the pK_a's of DHI to be 9.54 and 13.09, and the pK_a's of DHICA to be slightly higher at 9.76 and 13.2, with a third pK_a for DHICA discernable at 4.25. Murphy et al. assign the pK_a's of DHI to the 5-hydroxyl group dissociation (pK_a = 8.9) and the 6-hydroxyl group dissociation (pK_a > 10.2) [290]. We could not find similar assignments for DHICA, although it seems likely that the pK_a for DHICA discernable at 4.25 is due to dissociation of the carboxylic acid proton, with the two higher pK_a's attributable to the 5- and 6-hydroxyl group dissociations. The work presented in this chapter is all performed in a pH 9 buffer; considering the pK_a's for DHICA we might expect the molecule to be monoanionic state **CA** shown in figure 9.1. However, macroscopic pK_a's of multiprotic acids with interacting sites do not correspond to individual site pK_a's, but rather represent averages over all pathways connecting the ensembles with n and $n-1$ protons [50, 293]. Since the pH of this study is close to the pK_a's of the catecholate groups we must consider

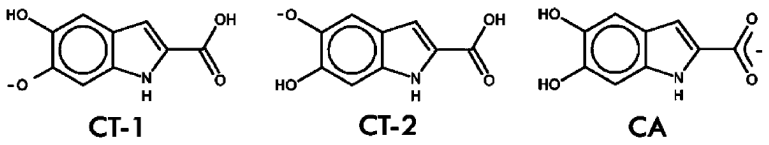

Figure 9.1: Three possible DHICA monoanions present at pH9 with nomenclature (from [50])

all the possible DHICA monoanions shown in figure 9.1 to be possibly present in solution (consideration of dianions is not necessary since we are below the second macroscopic pK_a, so the ratio of dianions to monoanions should be small) [50].

Quantum chemical study of eumelanin precursors has focused more on DHI than DHICA since it is a smaller and simpler molecule which favours computational analysis. Density functional theory (DFT) has been used extensively to model DHI [64, 78, 79], and recently also the approximated singles-and-doubles coupled-cluster method [294]. Where larger eumelanin oligomers are concerned, almost all calculations have involved oligomers of DHI only (DHICA has not been considered); Galvao and Caldas considered only DHI in their landmark Huckel analysis of eumelanin [61–63], as have authors of DFT studies of eumelanin oligomers [73–75, 80, 82]. While these studies form an excellent first level of modelling, we believe that it is important to consider the unique characteristics of DHICA in this system. The two eumelanin precursors are known to have different properties, so conclusions about the electronic properties of DHI should not be extended necessarily to DHICA, and this important species should be considered seperately. DHICA should also be considered in any modelling of the whole pigment system; DHICA is known to form an important part of natural eumelanin, and in some cases fulfills an integral role. For example, the proportion of DHICA-derived units in the pigment of some rodents is as high as 98%, and eumelanin found in the eye of the catfish is known to consist of pure DHICA-melanin [83] (care is required in this interpretation however, since degradation processes are known to produce carboxylic acid units even in pure DHI-melanin which may confuse some experimental results [295]). The DHICA carboxyl groups are believed to significantly alter the properties of the pigment [296]; pure DHI and DHICA pigments have been shown to have measurably different properties, including different colours (DHICA eumelanin is brown whereas DHI eumelanin is black) [104]. Therefore we believe that it is important to consider the role of DHICA in eumelanin.

To our knowledge, there are only two pre-existing quantum chemical studies of DHICA. The properties of isolated DHICA in vacuo were studied via DFT in 2005 by Powell [77]; this study confirmed that the carboxylation has a significant effect on the molecular properties such as the excitation energy. This study was later extended to DHICA dimers, showing that dimerisation red-shifts excitation energies [76]. The vibrational properties of DHICA have also been studied via DFT by Okuda et al. in a very recent publication; this shall be discussed in detail in chapter 11 [297].

We report here a comprehensive analysis of the spectroscopic properties of DHICA for two reasons; firstly because DHICA is much less well studied than DHI and we seek to investigate the properties of this second monomer, and secondly because DHICA is much more stable than DHI in solution. Several studies agree that while DHI is very susceptible to air oxidation and rapidly reacts to form eumelanin pigment, DHICA is more stable in solution

(at alkaline pHs it may take minutes or hours to oxidise, and at acidic pHs it is entirely stable) [214, 292, 298]. The relative stability of DHICA in solution allows measurements that may take some time to be performed accurately on the pure system (such as the determination of the radiative quantum yield). These accurate spectroscopic results, available for the first time, have led to very comprehensive and sophisticated quantum theory calculations for DHICA, which identify characteristic de-excitation pathways for DHICA, as shall be outlined at the end of this chapter.

9.3 Experimental

9.3.1 Sample preparation

To synthesise DHICA, the procedure of Wakamatsu and Ito was followed [299]. DL-DOPA was purchased from Sigma, and all the other reagents were commercially available and used as such. DL-DOPA (1 g, 5 mmol) was stirred in water (500 mL). In five minutes, a solution of $K_3[Fe(CN)_6]$ (6.6 g, 20 mmol) in 60 mL water was added. A wine-red solution was obtained which was mixed with 70 mL of 1 M NaOH solution to raise the pH to 13. The solution was stirred under argon for 20 mins, acidified to pH2 with 6 M HCl (∼17 mL), and extracted with ethyl acetate (3×100 mL). The combined organic extracts were filtered, and the pale brown filtrate was washed first with brine (100 mL) containing 0.19 g (1 mmol) $Na_2S_2O_5$, then with brine (2×200 mL), and dried (anhy. Na_2SO_4). Evaporation of solvent resulted in 1 g of pale brown solid, which was dissolved in a minimum amount of acetone by warming. Addition of hexane gave initially a brown oil which was discarded. The supernatant solution was transferred into a clean beaker and the addition of hexane continued when 5,6-DHICA separated as a white material. Filtration provided 264 mg (27%) of the compound compound which was pure by TLC (5% EtOH - $CHCl_3$) and NMR spectroscopy, as described below.

9.3.2 Sample characterisation

^{1}H NMR and ^{1}3C NMR (500 and 125.758 MHz respectively) spectra were recorded on a Bruker Digital NMR, Avance - 500 spectrometer in d_6-DMSO. Splitting patterns are designated as: s, singlet, br, broad, m, multiplet. Results were as follows:

^{1}H NMR (d_6-DMSO):δ = 11.08 (s, 1H, NH); 9.02 (br, OH), 8.55 (br, OH), 6.85 (s, 1H, H-3); 6.81 (m, 1H, H-4), 6.76 (s, 1H, H-7). Lit[2] (d_6-DMSO) δ = 12.3 (br, COOH), 11.09 (NH); 9.08 (br, OH), 8.57 (br, OH), 6.87 (s, H-3); 6.80 (m; H-4); 6.76 (s, H-7).

^{13}C NMR: (d_6-DMSO): δ = 162.8 (COOH), 146.1 (C-5), 142.0 (C-6), 132.6 (C-8), 125.8 (C-2), 119.9 (C-9), 107.1 (C-4), 104.9 (C-3), 97.0 (C-7). Lit[2]: (d_6-DMSO) δ = 162.9 (COOH), 146.3(C-5), 142.2 (C-6), 132.8 (C-8), 125.9 (C-2), 120.1 (C-9), 107.3 (C-4), 105.1 (C-3), 97.1 (C-7).

An EI Mass Spectrum was recorded on a Kratos MS25 RFA via direct insertion probe at 70 eV and source temperature of 200°C. Results were as follows: m/z (%): 193 (M^+, 34), 175 (M^+ - H_2O, 33), 149 (M^+ - CO_2, 48), 121 (5), 103 (15), 44 (CO_2, 100). Lit[2]: m/z (%) = 193 (99), 175 (100), 149 (12), 148 (5), 147 (45), 146 (5), 121 (9), 119 (8), 101 (5), 63 (8), 43 (12).

An infrared spectrum (IR) was recorded on a Perkin Elmer Spectrum 2000 FT-IR spectrometer. Group frequencies in cm^{-1} were as follows: 3411 (s, NH), 3244 (s, broad, OH), 1658 (ss, C=O), 1525 (s), 1437 (w) 1339 (w), 1221 (ss), 1161(ss), 871 (s), 770 (s), 609 (s).

9.3.3 Optical spectroscopy

For optical spectroscopy measurements the DHICA was solubilised in a pH 9 borax buffer solution (80 ml of 0.05 M borax with 20 ml of 0.2 M boric acid [300]). Sonication for ten minutes ensured complete solubilisation. Five DHICA concentrations between 0.7×10^{-5} mol L^{-1} and 2.2×10^{-5} mol L^{-1} were used (for the purpose of determining the radiative quantum yield).

Absorbance spectra were recorded as described in section 4.3.2 with 2 nm bandpass slit widths. Emission spectra were recorded as described in section 6.3.3 with excitation wavelengths of 323 nm, 350 nm and 380 nm, excitation and emission slits set to 2 nm bandpass, and an integration time of 0.5 s. Excitation spectra were recorded with identical instrument parameters and a detection wavelength of 400 nm. Solvent backgrounds were recorded and subtracted after a re-absorption correction was applied, as described in chapter 6.

Radiative relaxation quantum yields at three excitation wavelengths (323 nm, 350 nm and 380 nm) were calculated using the standard procedure outlined in section 6.3.5. Quinine sulfate was used as a standard, in 0.1 M H_2SO_4, at five concentrations between 1×10^{-5} and 5×10^{-5} mol L^{-1} (literature quantum yield of 0.54 [301]). Corrections for re-absorption and inner filter effects were applied throughout.

9.4 Results and discussion

9.4.1 Extinction coefficient

The measured absorbance peaks of DHICA shown in figure 9.2 fit well to gaussians (in energy space[1]) with peaks at 3.8 eV (323 nm), 4.2 eV (300 nm) and 6.2 eV (200 nm). The extinction coefficient agrees well with that previously published by Zhang et al. [188], both in shape and intensity. Differences may be attributed to the different solvents used (borax buffer, compared with wet acetonitrile as used by Zhang et al.). The peaks are notably more clearly resolved in this study, which highlights the significant effect that the solvent can have upon the spectroscopic properties of DHICA. Very recent experiments within our group suggest that the borax buffer may form a complex with the DHICA catecholate groups which inhibits polymerisation and causes the observed differences in absorbance between this study and the results published by Zhang et al. This intriguing possibility is under current investigation and has very significant implications for the interpretation of the results reported in this chapter. We have included the most up to date information that was available at the time of submission of this thesis, but we direct the interested reader to subsequent publications for further results.

[1] As stated earlier, all curve fitting has been performed against energy, rather than wavelength, since solvent broadening is expected to by symmetric in energy.

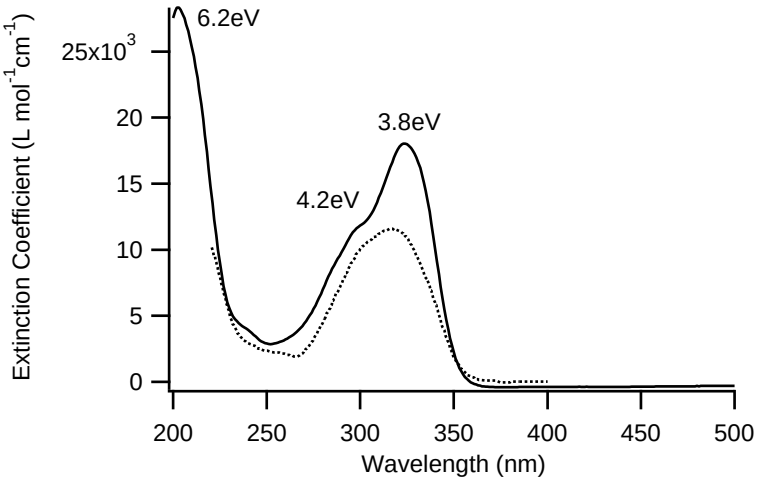

FIGURE 9.2: Extinction coefficient of DHICA, as measured in this study (solid line), compared with that previously published by Zhang et al. (dotted line) [188]. The peak positions and relative heights are in good agreement; differences may be attributed to the different solvents (borax buffer, compared with wet acetonitrile).

.

	λ_{ex} (nm)	FWHM (eV)	emission peak (eV)
DHICA	323	0.6	3.1
	350	0.6	3.1
	380	0.6	3.1
eumelanin	380	0.7	2.6
quinine	250	0.5	2.8
fluorescein	490	0.2	2.4

Table 9.1: Properties of single gaussian emission spectra for DHICA, eumelanin, and other organic molecules for comparison.

9.4.2 Emission spectra

Emission spectra of DHICA are a single gaussian (in energy), centered at 3.1 eV (400 nm), regardless of excitation energy (figure 9.3). Table 9.1 compares the properties of the emission peak of DHICA with that of other molecules that show a single peaked emission spectrum. The DHICA spectrum is broad, although not unusually so. DHICA has a similarly shaped emission spectrum to eumelanin (reflected in the similar FWHM), the main differences being a significantly greater intensity, and a smaller Stokes shift (the emission of DHICA is blue-shifted from that of eumelanin by 0.5 eV). The fact that the shape and position of the emission spectrum of DHICA is independant of excitation energy strongly suggests that all emission occurs from one energy level, higher energy absorption being dissipated via non-radiative processes to that state. This is a very significant finding, and should be investigated over a larger range of excitation energies.

As seen from figure 9.4, DHICA exhibits a typical Stokes shift of 0.72 eV. More unusually, DHICA also exhibits violation of the mirror image rule. It is predicted for simple organic

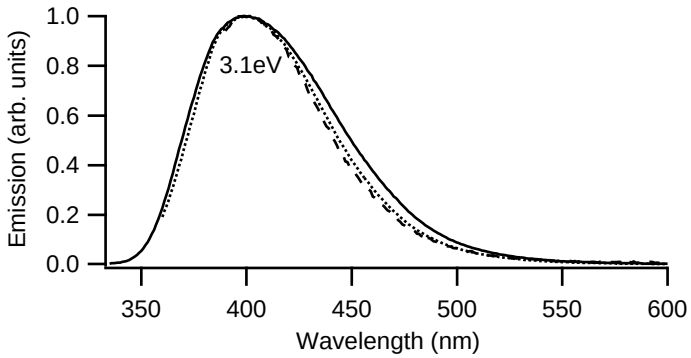

Figure 9.3: Emission spectra of DHICA for various excitation wavelengths, scaled for qualitative comparison (note that the emission intensities varied by a factor of 100 due to the variation in absorbance at each excitation wavelength). Solid line: $\lambda_{ex} = 323$ nm, dotted line: $\lambda_{ex} = 350$ nm, dashed line: $\lambda_{ex} = 380$ nm.

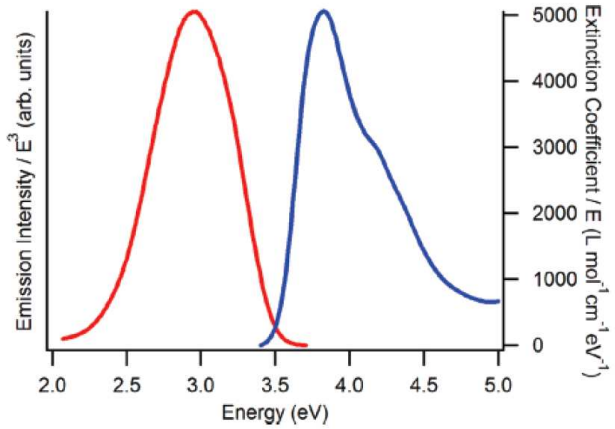

Figure 9.4: Scaled absorption / energy (blue, right peak) and emission / energy^3 (red, left peak, $\lambda_{ex} = 323$ nm) spectra of DHICA. These peaks typically form a mirror image. The symmetry here is clearly broken by the absence of a shoulder in the emission spectrum and the larger FWHM of the emission.

molecules that the emission spectrum should be a mirror image of the absorption spectrum when plotted as shown in figure 9.4 due to the laws of quantum mechanics [245]. This is clearly not the case for DHICA, since the shoulder evident in the absorption spectrum is absent in emission, and the emission peak is significantly broader. These observations suggest that the de-excitation pathways in DHICA are non-trivial and worthy of further investigation.

9.4.3 Theoretical calculations

These accurate quantitative spectroscopic measurements have allowed comparison to sophisticated quantum chemical calculations [50] which are outlined briefly here. As discussed in the introduction to this chapter, the monoanions shown in figure 9.1 are the most likely

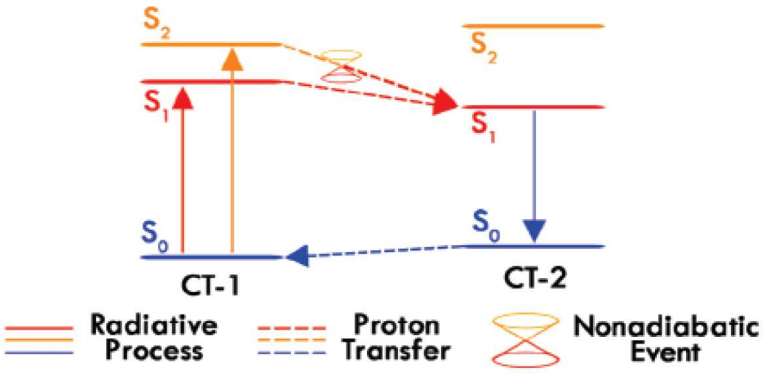

FIGURE 9.5: The proposed excitation and de-excitation pathways of DHICA, based on quantum chemical calculations and these experimental obervations (from [50])

structures to be present in solution at pH 9 (based on the known pK_a's of this system). Calculations universally suggest that **CT-1** is energetically favoured in the ground state, and hence is likely to be the prevalent species in solution in the absence of excitation. $S_0 \rightarrow S_1$ and $S_0 \rightarrow S_2$ transition energies in the ground and excited states were calculated for all three monoanions via sophisticated quantum chemical methods. These values and the known tendancies of each quantum chemical method to underestimate or overestimate energies by various amounts were then compared to the experimental excitation and emission energies. Based on these results, it was proposed that the scenario outlined in figure 9.5 is the most consistent with our experimental measurements and quantum chemical calculations on this system. Within this model, **CT-1** is the main absorbing species, with an $S_0 \rightarrow S_1$ absorbance at 3.8 eV and an $S_0 \rightarrow S_2$ absorbance at 4.2 eV. These states then decay via excited state intramolecular proton transfer (ESIPT) processes to the S_1 state of **CT-2** (adiabatically from S_1 and non-adiabatically from S_2). The S_1 state of **CT-2** then decays via radiative emission to its S_0 state (3.1 eV), which then undergoes the reverse reaction to form ground state **CT-1** once again.

This model explains the mirror image violation of DHICA spectra, and gives a novel insight into possible non-radiative de-excitation pathways for eumelanin (which are known to be of critical significance). For more details of the calculations, please refer to the publication (reference [50]). Further work is underway to confirm the validity of this model, including further quantum chemical calculations, titration studies of DHICA, and investigation of the effect of the borax buffer (through possible chelating interactions with the DHICA catecholate group).

9.4.4 Excitation spectra

The excitation spectrum of DHICA, as shown in figure 9.6, reveals two gaussian peaks (in energy space), centered at 3.8 eV (323 nm) and 4.2 eV (300 nm). Interestingly, Zhang et al. report the excitation maximum for DHICA to be at 345 nm, when monitoring emission at 420 nm [188], which is quite different to our result. We believe this is likely due to differences in solvent (Zhang et al. used wet acetonitrile), highlighting again the significance of the solvent effects upon absorption and emission properties. An alternative explanation

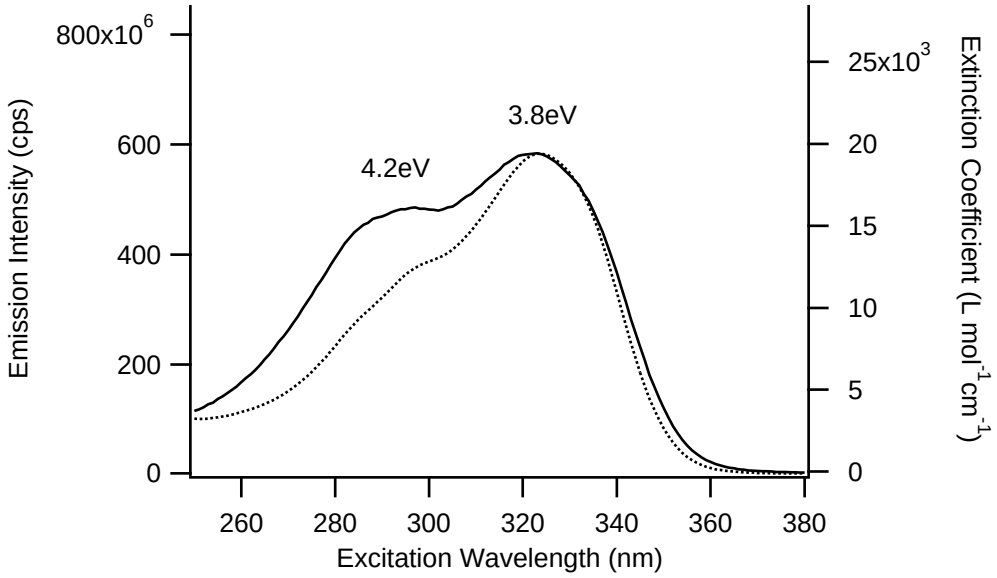

Figure 9.6: Comparison of the DHICA absorbance spectrum (right axis, dotted line) and excitation spectrum (left axis, solid line). Note that the relative scale of the two graphs is arbitrary, and has been chosen for ease of comparison of their relative shapes. $\lambda_{em} = 400$ nm.

is that this discrepancy is due to the different probe wavelengths used (420 nm rather than 400 nm as used here); emission from multiple species may mean we are measuring a different emission peak. Our emission spectra results (figure 9.3) make this seem unlikely, however, since we observe the identical emission spectrum shape regardless of excitation wavelength. This suggests that we are observing emission from a single electronic level of a single species. To resolve this issue we recommend as future work the measurement of a full fluorescence map for DHICA (in a manner similar to that outlined in chapter 7) with a variety of solvents and pHs.

The excitation spectrum corresponds qualitatively with the absorbance spectrum (also shown in figure 9.6), which also has two peaks of similar relative heights occuring at the same energies. The peak at 4.2 eV shows an increased intensity (relative to the 3.8 eV peak) in the excitation spectrum. Because the emission peak appears to be at 400 nm regardless of excitation wavelength, this difference between the absorbance and excitation spectra suggests an excitation energy dependance in the radiative quantum yield of DHICA. Based on these spectra, we propose that the radiative quantum yield for excitation at 4.2 eV (300 nm) is greater than that at 3.8 eV (330 nm).

9.4.5 Radiative quantum yield

The quantum yield of DHICA was measured at three wavelengths: 323 nm (maximum absorbance), 350 nm (absorbance is small) and 380 nm (absorbance is negligible). Figure 9.7 shows the linear regression that was used for determination of the quantum yield at 323 nm. Note that it was necessary to correct for reabsorption and inner filter effects to recover the linear relationship of the data [47, 163]. After correction the points are linear and the regression passes through the origin, confirming the good quality of our data.

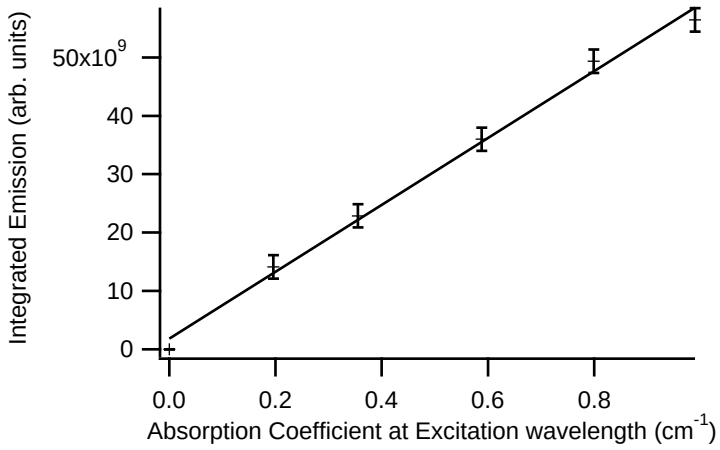

FIGURE 9.7: Integrated emission vs absorption coefficient for five concentrations of DHICA excited at 323 nm. The gradient of the linear regression shown was compared with that of a standard solution for determination of the DHICA quantum yield at 323 nm.

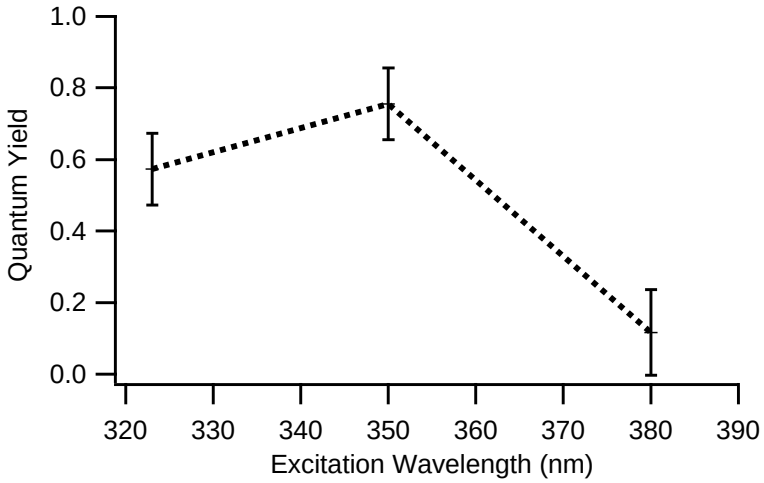

FIGURE 9.8: Radiative quantum yield of DHICA for various excitation wavelengths.

The quantum yield of DHICA was found to depend upon the excitation wavelength, as shown in figure 9.8. This is highly unusual for a simple well behaved molecule such as DHICA. We believe that in this case it is due to uncertainty in the absorbance measurement at 380 nm. With the very low absorbance at this wavelength effects such as minor scattering and initial polymerisation of the pigment have become significant and have caused an overestimate of the absorbance. This has led to a significant underestimation of the radiative yield at that wavelength. We caution that future measurements of the radiative yield of these systems should be performed where absorbance is substantial.

The yield measurements at 323 nm and 350 nm are thought to be reliable, and these are within error of each other, giving the yield of DHICA to be approximately 60%. Examination of the excitation spectrum indicates that both of these measurements are probing the adiabatic **CT-1** $S_1 \rightarrow$ **CT-2** S_1 transition, and hence would be expected to have the same radiative yield (since they probe the same process). A measurement of the yield at 4.2 eV

would be instructive to determine whether the discrepancy between the excitation spectrum and the absorption spectrum is in fact due to energy dependance in the radiative yield, and to probe the non-adiabatic **CT-1** $S_2 \rightarrow$ **CT-2** S_1 transition.

A radiative quantum yield of 60% for DHICA is typical of a molecule of this nature, and is consistent with our expectations. Note that the yield of DHICA is much higher than that of eumelanin, which has been determined to be less than 0.1% (see chapter 6). This suggests that covalent bonding of the eumelanin monomers significantly lowers the radiative yield of these species; this is consistent with other experimental observations within our group, and further work measuring the spectroscopic properties of eumelanin dimers and larger oligomers is underway to confirm this hypothesis. The following chapter reports how the radiative yield changes as DHICA polymerises to form eumelanin, to probe this process further.

9.5 Chapter conclusions

We have made the first comprehensive quantitative study of the UV/vis spectroscopic properties of DHICA, and based on these observations and sophisticated quantum chemical calculations proposed a scheme for the radiative and non-radiative processes in DHICA. This study forms an essential basis for further study comparing the properties of eumelanin monomers, dimers and oligomers, leading towards an understanding of how they contribute to the structure and energetics of eumelanin. These accurate, quantitative spectroscopic measurements of this fundamental component of eumelanin highlight the importance of this spectroscopic study and lead the way for more substantial studies. Specifically, we propose that more work to characterise the pH dependant properties of DHICA would be worthwhile, and would allow confirmation of the theoretical model proposed. Additionally, an accurate radiative quantum yield measurement at the 4.2 eV DHICA absorbance peak should be performed.

10

Spectroscopic observation of eumelanin formation

10.1 Chapter abstract

A solution of DHICA was observed spectroscopically as it evolved to form eumelanin. The extinction coefficient was observed to form the broadband eumelanin spectrum, and the radiative emission decreased gradually to the very low values previously measured for eumelanin. Significantly, the shape of the emission spectrum did not change over time, indicating that DHICA was the only fluorescencent species in the solution with an appreciable radiative quantum yield. This allowed us to determine the percentage of DHICA remaining in solution at each timepoint. It also indicates that DHICA dimers and larger oligomers have very low radiative quantum yields. Emission and excitation spectra at the final timepoint were in good agreement with those previously measured for eumelanin, and show the same dependance upon excitation energy. The radiative quantum yield was measured over time, and observed to decrease gradually until it reached the very low value characteristic of eumelanin. These results are consistent with the chemical disorder structural model of eumelanin.

10.2 Chapter introduction

It has long been known that UV illumination of early melanin precursors in the presence of oxygen causes chemical reactions that lead to the formation of melanin. In 1937 Arnow showed that UV illumination stimulates the formation of dopa from tyrosine [302], and Chedekel et al. later showed that both UV light and ionizing radiation cause dopa to polymerise into melanin [303].

Both DHI and DHICA are also known to be photolabile. DHI is more reactive to UV

illumination than DHICA; the quantum yields for photodestruction by 300 nm photons has been shown to be $\Phi = 4.9 \pm 0.8\%$ for DHI and $\Phi = 3.3 \pm 0.3\%$ for DHICA [214]. One could argue that photoinitiation of polymerisation is not biologically relevant since melanin synthesis occurs in melanocytes which are relatively deep in the skin and hence would not be expected to be exposed to substantial levels of UV radiation. It is believed, however, that *in vivo* only the initial oxidation of dopa is under enzymatic control, so the initiation of later steps via other means (such as chemical stimulation of later intermediates) should be biologically relevant [303]. The use of enzymatic polymerisation *in vitro* is prohibited by the extremely slow rate-determining steps involved. Note also that dopaquinone (in addition to cyclodopa and cysteinyldopa) plays an important role in promoting oxidation of DHI [84].

Several recent studies report absorption spectra as DHI and DHICA polymerise to form eumelanin. Charkoudian and Franz observed the oxidation of DHI in air at pH 9 and showed a substantial increase in oscillator strength over time [292]. This is a surprising result, completely at odds with our findings in chapter 5. They also described the formation of a precipitate over time, so we suspect that they were instead simply observing an increase in scattering from their solutions. Scattering intensity is dependant upon the particle radius to the sixth power (as described in chapter 4), so even a small increase in aggregation will lead to a substantial increase in optical density. A similar study by Tran et al. on the absorption spectrum of DHICA as it polymerises to form eumelanin is more consistent with our findings in chapter 5. These authors do not calculate oscillator strengths, but it is clear from the reported spectra that it does not increase substantially over time [76].

UV-visible difference spectra for DHI and DHICA have both been shown to exhibit isosbestic points, suggesting initial photoconversion into a single photoproduct [214]. For DHICA, these intermediates were stable for minutes to hours, whereas for DHI they polymerised further much more rapidly. This intermediate is likely to be a particular dimer, although it has not been isolated or characterised thus far. The work reported in this chapter aims to quantitatively observe the spectroscopic changes that occur as DHICA forms macromolecular eumelanin[1], to perhaps find clues as to the intermediates that are formed during this process and therefore better understand the molecular structure of eumelanin.

10.3 Experimental

10.3.1 Sample preparation and characterisation

DHICA (5,6-dihydroxyindole-2-carboxylic acid) was prepared and fully characterised as described in section 9.3.1. For spectroscopy measurements it was solubilised in a pH 9 borax buffer solution as described in section 9.3.3.

[1]It is important to note that natural melanin is thought to contain a combination of DHI and DHICA, intimately copolymerised, in varying ratios depending upon the source of the melanin. The results discussed in this chapter should be interpreted with the understanding that this is a simplified model system consisting of only DHICA.

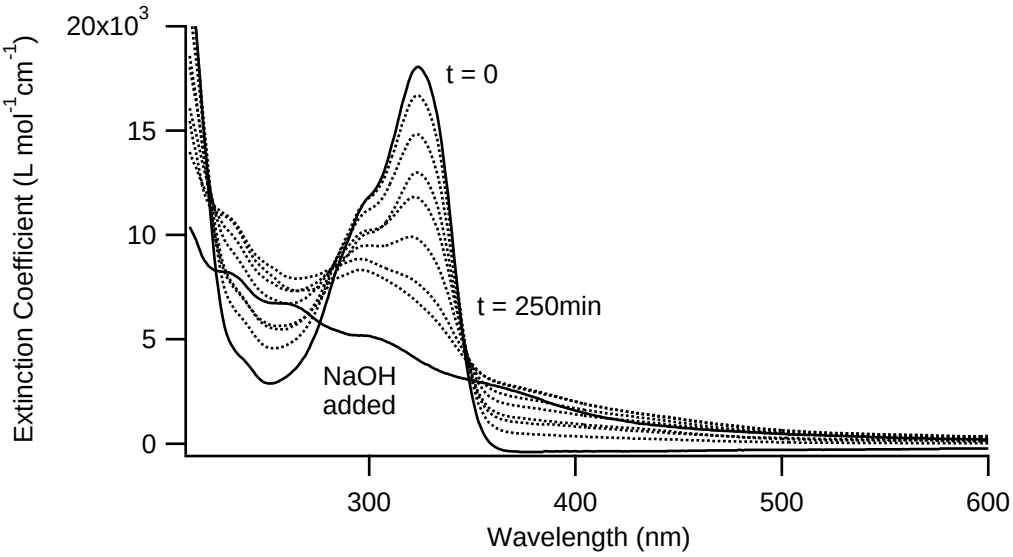

Figure 10.1: The extinction coefficient as DHICA evolves to form eumelanin.

10.3.2 Optical spectroscopy

DHICA was found to be very stable in the pH 9 buffer solution, as opposed to previous evolution studies, where a more alkaline pH was used. Therefore a low intensity hand-held ultra-violet lamp was used to induce polymerisation for time periods as indicated. This provided a method of accurately controlling the degree of polymerisation as desired. The following (cumulative) illumination times were used: For excitation at 323 nm: 0, 10, 20, 30, 40, 50, 60, 70, 80, 90, 100, 120, 240 minutes. For excitation at 350 nm and 380 nm, and for excitation spectrum of emission at 400 nm: 0, 20, 40, 60, 80, 120, 200, 240 minutes. For the final time-point, a sufficient quantity of very strong NaOH was added to overcome the buffer solution and increase the pH to approximately 12. The solutions were allowed to stand for one hour, then measured for the final time.

Absorbance spectra, emission spectra and radiative quantum yields were recorded at each timepoint as described in section 9.3.3.

10.4 Results and discussion

The extinction coefficient was measured as DHICA evolved to form eumelanin, as shown in figure 10.1. The main peaks at 3.8 eV, 4.2 eV and 6.2 eV reduced in height, and peaks at other wavelengths appeared until the (mostly) broadband spectrum of eumelanin was reached. As DHICA polymerises to form other species (dimers, trimers and larger oligomers), the concentration of DHICA decreases (causing the decrease in height of the initial peaks characteristic of the monomer). The newly formed species are expected to have different excitation energies to DHICA [76], and hence show absorption peaks at different positions. The spectrum thus broadens and flattens into the eumelanin spectrum.

The emission spectra for excitation at 323 nm (the DHICA absorption peak), 380 nm (where DHICA has negligible absorption) and 350 nm (where DHICA has intermediate

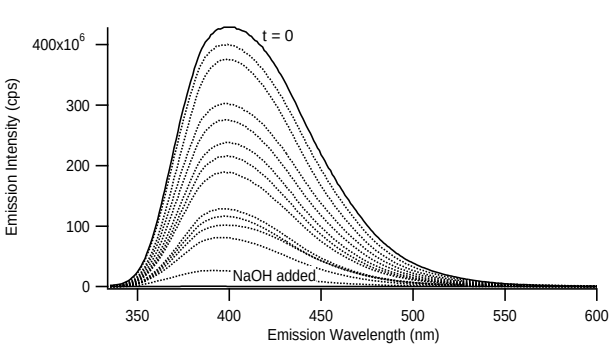

(a) λ_{ex} = 323nm

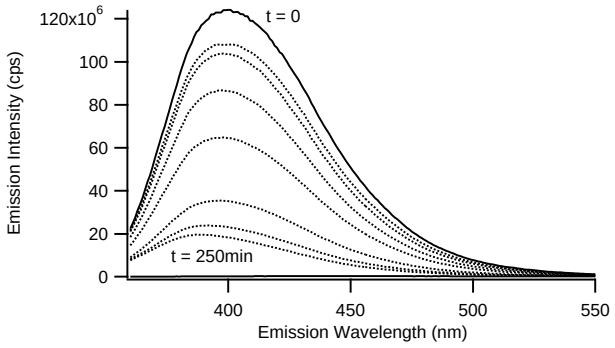

(b) λ_{ex} = 350nm

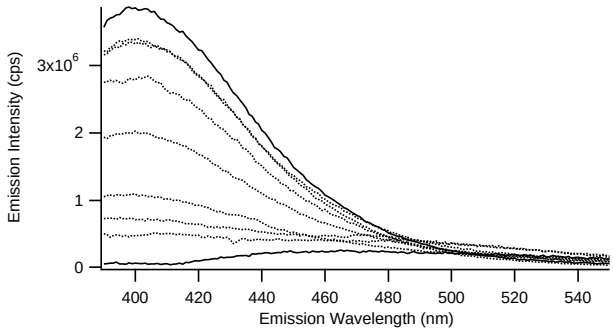

(c) λ_{ex} = 380nm

FIGURE 10.2: Emission spectra as DHICA evolves to form eumelanin, for three different excitation wavelengths.

absorption) as DHICA evolves to form eumelanin are shown in figure 10.2. The emission gradually decreases in intensity at each wavelength until it reaches the very low emission levels characteristic of eumelanin [47, 163]. Most significantly, the shape of the emission spectrum does not change (until the last few time-points), only the intensity. This indicates that none of the dimers, trimers and larger oligomers formed from DHICA have significant radiative quantum yields, so the only fluorescencent species in the solution is DHICA itself. This feature allows the estimation of the amount of DHICA remaining in solution at each time as the polymerisation occurs, simply by taking the ratio of the emission curve area at each time to that at the initial time-point (when the solution is 100% DHICA). This was done for the λ_{ex} = 323 nm data (since it is the most intense, and therefore has the best signal to noise ratio), and is shown in figure 10.3. The concentration appears to follow an exponential relationship, as is shown on the plot.

Tran et al. reported that the main absorption peak in the DHICA spectrum decreases linearly over time as it polymerises, suggesting that DHICA molecules are consumed at a constant rate [76]. We propose, however, that the species being formed will have overlapping absorption spectra with the inital DHICA spectrum, making this an unreliable probe of DHICA concentration. Based on the results presented here, we propose that the emission spectrum provides a much more reliable probe.

Since the shape of the emission spectrum does not change until the very last few time-points, we postulate that all DHICA dimers and oligomers have significantly lower radiative

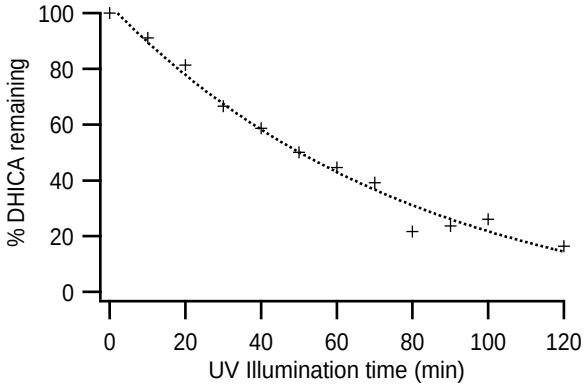

Figure 10.3: The percentage of DHICA remaining in the solution over the course of the polymerisation, as determined from emission spectra ($\lambda_{ex} = 323$nm). Dotted line - exponential fitting: $k_0 + k_1 exp(-k_2 T)$ where $k_0 = 11.4$, $k_1 = 114$, $k_2 = 0.0124$.

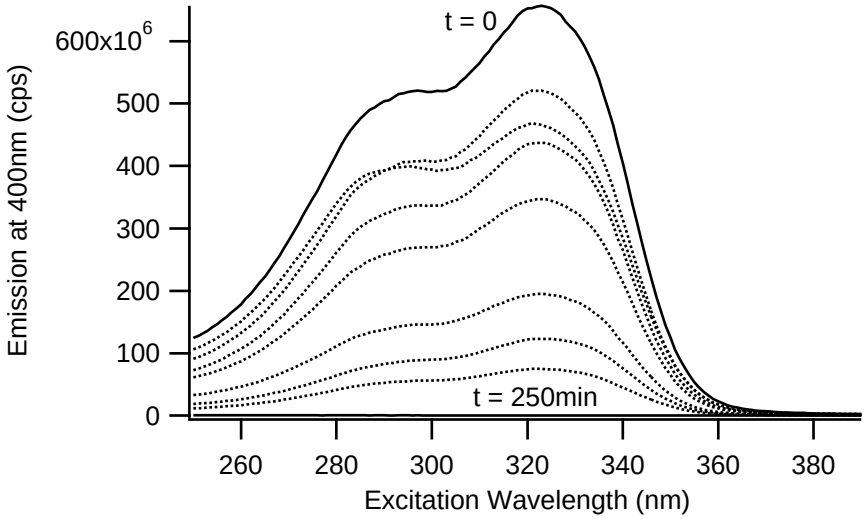

Figure 10.4: Excitation spectrum as DHICA evolves to form eumelanin ($\lambda_{em} = 400$ nm).

quantum yields than the DHICA monomer (otherwise they would influence the shape of the emission spectrum). The shape is only affected when the DHICA concentration becomes extremely low. Experiments to test this hypothesis are currently underway.

The polymerisation of the excitation spectrum as DHICA forms eumelanin is shown in figure 10.4. Similar to the emission spectra, it does not change shape over time but merely decreases in intensity (until the very final time-points). This supports our supposition that DHICA is the only species in solution with substantial emission.

At the last few time-points the concentration of DHICA is so low that even very low quantum yield species begin to have comparable emission, so the shape of the emission spectrum begins to change. This is demonstrated in figure 10.5. In each graph, A is the initial spectrum (pure DHICA), and B, C and D show the spectra at the final few time-points. It is interesting that for excitation at both 323 nm and 350 nm the spectrum first shifts to slightly higher energies, then broadens, showing multiple peaks. Excitation at 380 nm is

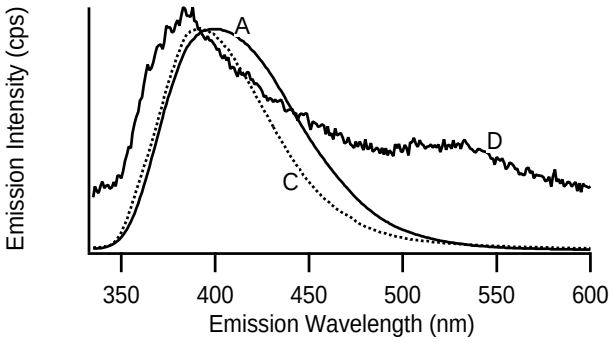

(a) $\lambda_{ex} = 323$nm

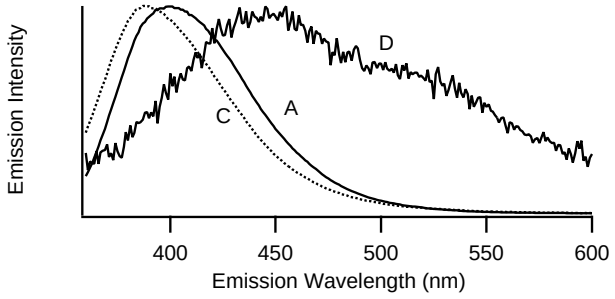

(b) $\lambda_{ex} = 350$nm

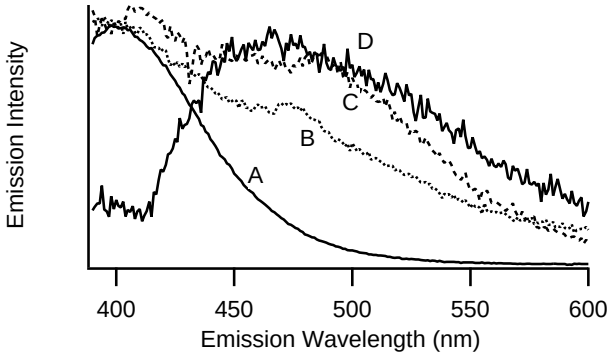

(c) $\lambda_{ex} = 380$nm

FIGURE 10.5: Emission spectra as DHICA evolves to form eumelanin, for three different excitation wavelengths. Spectra are scaled to show relative shapes (note that intensity at final time is significantly lower than the initial intensity). A: Initial DHICA spectrum, B: 200 minutes of cumulative UV illumination , C: 240 minutes of cumulative UV illumination , D: After NaOH was added.

slightly different because this is far away from the DHICA absorption peak. This means that for even quite early time-points the emission from other species in solution becomes comparable to that from DHICA, and hence influence the shape of the spectrum.

The excitation spectrum at the final timepoint is shown in figure 10.6. It is similar in shape to that previously measured for eumelanin [163, 164], and loosely follows the shape of the absorption spectrum at the final timepoint (dotted line), as would be expected.

An analysis of the spectra at the final time-point can give an indication of the energy structure of the fluorescent species produced as DHICA evolves into eumelanin. An emission peak at 2.3 eV is evident in all the final time-point spectra (figure 10.5). The excitation spectrum (figure 10.6) shows peaks at 3.7 eV and 5.0 eV. Large amounts of broadening (believed to be due to chemical disorder) and low radiative yields make quantitative analysis challenging, however. Experiments using directed chemical synthesis combined with density functional theory analysis are currently underway to identify possible species that may contribute to these spectra.

The emission spectra for excitation at 350 nm and 380 nm at the final time-point agree well with those measured previously for eumelanin, as shown in figure 10.7. Note that shorter instrument integration times were used in this experiment due to the necessity of keeping

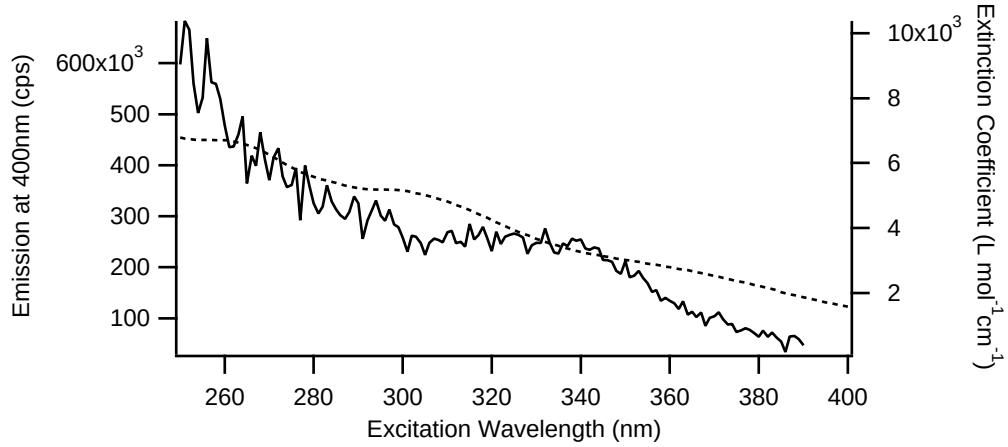

Figure 10.6: Excitation spectrum at the final timepoint (after addition of NaOH, solid line), compared with the extinction coefficient at the same timepoint (dotted line) ($\lambda_{em} = 400$ nm).

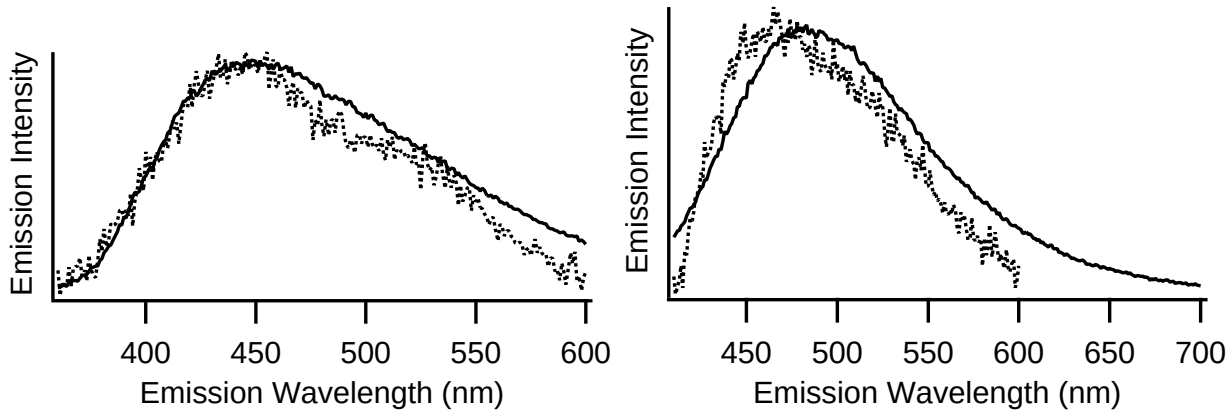

(a) $\lambda_{ex} = 350$nm (b) $\lambda_{ex} = 380$nm

Figure 10.7: Emission spectra at the final time-point (dotted line) compared with emission spectra for eumelanin at the same excitation wavelength (solid line). Eumelanin spectra from chapter 6.

instrument parameters the same throughout the experiment. This has resulted in a lower signal to noise ratio in the data reported here. Regardless, the good agreement between these final time-point spectra and the eumelanin spectra is evident. The final time-point emission spectra show the same shifting of the peak with excitation energy that has been previously observed for eumelanin [47], as shown in figure 10.8, suggestive of chemical heterogeneity in the final eumelanin product.

The radiative quantum yield of the solution was observed to decrease over time for all three excitation wavelengths (figure 10.9), and at the final time-point reached the very low value previously observed for eumelanin ($\sim 0.1\%$). Dimers and larger oligomers of DHICA could be expected to have a larger number of vibrational modes available for non-radiative dissipation of energy, and hence may be expected to have lower radiative quantum yields than the DHICA monomer. As DHICA polymerises to form these larger species, the quantum

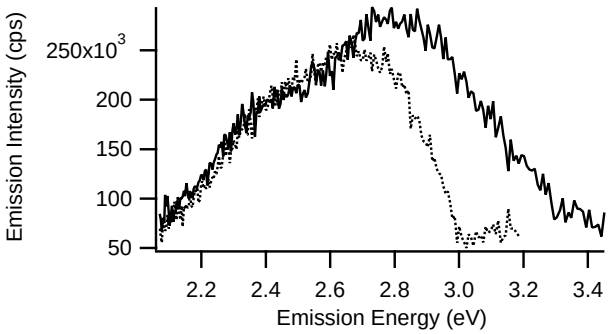

FIGURE 10.8: Emission spectra at the final time-point shown the same dependance upon excitation energy as eumelanin spectra (chapter 6). Solid line: $\lambda_{ex} = 350$nm, dotted line: $\lambda_{ex} = 380$nm

yield of the solution therefore decreases.

10.5 Chapter conclusions

We have shown that as DHICA polymerises to form DHICA eumelanin, the emission decreases in intensity, but the emission spectrum does not change in shape. This suggests that all dimers, trimers and oligomers formed from DHICA have very low radiative yields, and therefore do not contribute to the emission spectrum until the concentration of DHICA reaches an extremely small value. Experiments are currently underway to probe this hypothesis; we are synthesising likely DHICA dimers for the accurate measurement of their radiative yields and emission spectra. Comparison to the final timepoint spectra presented here may allow for identification of the oligomer species present in the final eumelanin product.

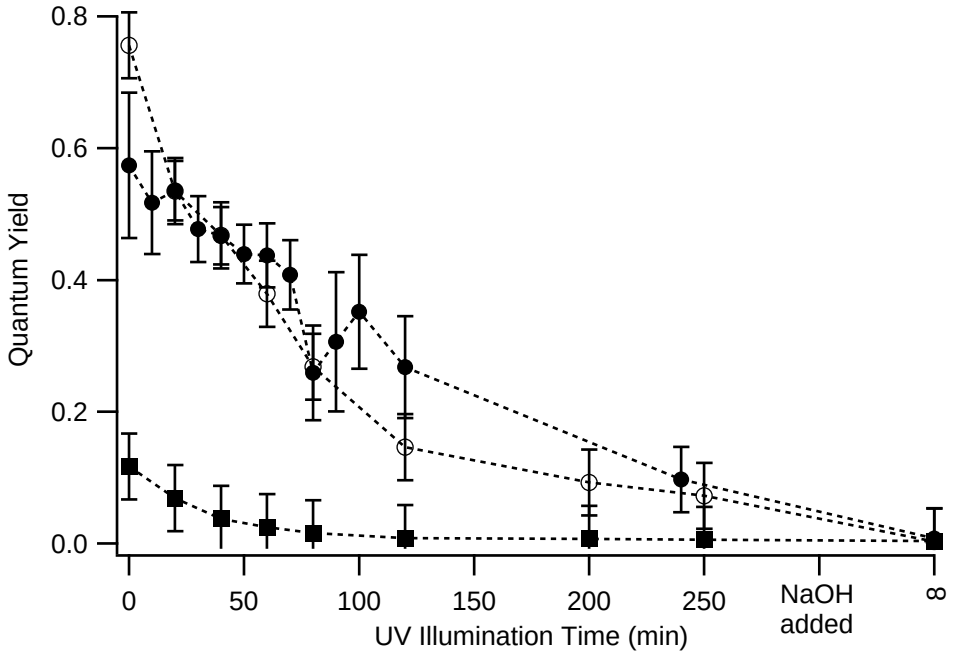

Figure 10.9: The radiative quantum yield as DHICA evolves to form eumelanin. (filled squares: $\lambda_{ex} = 380$nm, empty circles: $\lambda_{ex} = 350$nm, filled circles: $\lambda_{ex} = 323$nm.

11

Inelastic neutron scattering spectroscopy

11.1 Chapter abstract

We have obtained inelastic neutron scattering (INS) spectra of indole-2-carboxylic (ICA) acid and 5,6-dihydroxyindole-2-carboxylic acid (DHICA), a key melanin monomer. To our knowledge this is the first study of its kind on eumelanin precursors. We have assigned these spectra to vibrational modes based on density functional theory calculations and comparison to the previously measured modes of indole. These assignments form the foundation for accurate interpretation of spectra of larger related species leading towards an understanding of the vibrational energy dissipation pathways of eumelanin.

11.2 Chapter introduction

McGinness and Proctor suggested in 1973 that the black appearance of melanin indicates that electron-phonon coupling may be particularly efficient in this material [304]. They postulated that a significant biological function of melanin may therefore be to convert the energy of excited states into heat by means of photon-phonon conversion processes. Dissipation of energy via electron-phonon coupling occurs over picosecond timescales, and is the most rapid form of energy dissipation (radiative emission, for example, occurs over nanoseconds). Rapid energy dissipation via vibrational states is the best way of reducing the possibility of excited state chemistry (which is almost always harmful in a biological environment), and hence as a photoprotectant, eumelanin could reasonably be expected to dissipate energy mainly through conversion of photoexcitations to heat.

A variety of studies show that the majority of energy dissipation in eumelanin is non-radiative [243, 261, 305, 306]. Forest and Simon used photoacoustic calorimetry to show that essentially all the absorbed energy is released as heat when excited at 527 nm (visible green light) and 400 nm (violet/near UVA-I light) [162]. With higher energy excitation some

of the energy is dissipated via other means; with excitation at 351 nm (UVA-I), 95% of the absorbed energy is converted to heat, and with excitation at 264 nm (UVC) only 70% is released as heat. This wavelength dependance is consistent with chemical heterogeneity, since exciting at different wavelengths probes different species, which may easily have different electron-phonon coupling properties. Nofsinger et al. later confirmed that the dominant non-radiative process in eumelanin is repopulation of the ground electronic state [172]. As shown in chapters 6 and 7, eumelanin has an extremely low radiative quantum yield [47], again suggesting that the majority of energy dissipation occurs by non-radiative relaxation. Hence the vibrational modes of eumelanin are of considerable interest.

Raman and infrared (IR) spectroscopies have been applied to melanins from various sources in a number of studies; we have summarised those relevant to eumelanin in table 11.1. Many studies only identified one or two broad peaks, and none were able to give accurate vibrational mode assignments. These results show that due to chemical heterogeneity, eumelanin has a complex vibrational spectrum with many overlapping modes, making it very difficult to draw any firm conclusions from vibrational spectra. Studies on small oligomers extracted from melanin are more promising, showing clearer peaks that potentially allow for a more informative analysis [83], and IR study of the monomer DHICA has been extremely successful, as outlined later in this introduction [297]. We have therefore chosen to first study the vibrational modes of DHICA using inelastic neutron scattering (INS) spectroscopy, with an aim to accurately assigning the spectra of the eumelanin monomers and then larger species until the vibrational properties of the eumelanin system as a whole can be elucidated.

Table 11.1: Summary of previous IR and Raman studies on melanins. Studies of neuromelanin [307] and fungal melanins [308–312] have not been included since these are chemically different and have not been dealt with in this thesis. Abbreviations: s - strong, w - weak, b - broad, sh - shoulder, ν - in plane stretching, ben. - benzene, skel. - skeletal, def. - deformation.

ref	**method**	**source**	λ_{ex} **(nm)**	**freq (cm^{-1})**	**assignments**
Cooper et al. 1986 [313]	raman	synthetic tyrosine	363.8	1300(b)	
			488	1385(b)	
				1590-1615(b)	
				2930(b)	
Panina et al. 1998 [314]	raman	synthetic and fungal	514.5	1337-1380(b)	
				1580-1620(b)	
Wegmann et al. 1999 [315]	IR	hair	-	854	
				1032	
				1070	
				1208	CO-
				1388	CH def.
				1530	
				1622	
				1700	
Bilinska 2001 [316]	IR	red hair	-	810	
				1100	
				1200	
				1380	
				1465	
				1630	
				1710	
				1740	
				2855	
				2930	aliphatic CH
				2960	aliphatic CH
				3280-3500	

Continued on next page

Table 11.1 – continued from previous page

ref	method	source	λ_{ex} (nm)	freq (cm^{-1})	assignments
		dark hair	-	800	
				1100	
				1210	
				1350	
				1615	
				1710	
				2850	
				2920	
				3050-3400	
Samokhvalov et al. 2004 [31]	raman	sepia ink	632.8/779.6	460(w)	
				950-980(b)	
				1210(sh)	ben. def., νC-O
				1330(sh)	ben. def.
				1400(s)	aromatic C-N
				1550(sh)	
				1600(s)	aromatic C-C
Liu et al. 2004 [156]	raman	synthetic		1400(s, b)	aromatic
				1600(s, b)	aromatic
Huang et al. 2004 [317]	raman	sepia	457.9	1399	
				1585	
			514.5	1405	
				1585	
			632.8	1408	
				1581	
			785	1400	
				1583	
		synthetic dopa	457.9	1384	
				1595	
			514.5	1387	
				1592	
			632.8	1374	
				1588	
			785	1378	
				1589	
		human black hair	632.8	1355	
				1584	
			785	1386	
				1578	
		feline black hair	632.8	1355	
				1584	
			785	1395	
				1585	
		human skin in vivo			
		normal	785	1362	
				1566	
		nevus	785	1372	
				1578	
		melanoma	785	1378	
				1572	
		summary	many	1580	νskel. def
		of above		1380	νC-C

INS is a well established technique that makes use of modern spallation neutron sources to obtain spectral bandwidths similar to those obtained from the optical spectroscopy of solids [318]. INS has the advantage that its observed intensities can be simply and immediately compared to calculations of the mean square vibrational atomic displacements that appear as output from standard *ab-initio* programs. Moreover, the technique emphasises those vibrational modes involving hydrogen motions and is ideal for the study of organic molecular crystals, as is described in detail elsewhere [318]. INS spectroscopy does not have forbidden

modes as do both IR and Raman spectroscopy, and it is particularly sensitive to low energy vibrations. High energy vibrations (such as those most easily probed by IR and Raman spectroscopy) are typically due to the motions of isolated functional groups and single atoms in the molecule, and hence are particularly useful for chemical characterisation. In this study, we are more interested in the low energy vibrations (that are probed by INS), since these are typically due to whole molecular motions. These whole molecular motions will tend to be the ones most affected by variations in primary and secondary structure, and so can give extremely useful information about intermolecular bonding and motions on a larger scale.

To accurately assign the spectrum of DHICA, it was necessary to initially make INS measurements of indole. Indole is a very well studied system, and its vibrational frequencies over a wide range of energies have been determined from IR and Raman spectroscopy. The assignments of these vibrational frequencies to particular vibrational modes has been reported in a variety of publications and is well agreed upon. Our group measured the INS spectrum of indole and assigned the observed modes with confidence based upon these previous IR and Raman assignments [319]. The INS assignments of indole from that previous study are summarised in table 11.2 (since we later refer to these mode numbers in our assignments).

Table 11.2: The *ab-initio* calculated frequencies (cm^{-1}) of indole compared with observations, from reference [319]. This publication did not include higher energy modes since these were not within the range accessed by INS, but we include here all modes calculated by GAUSSIAN98 since we use several of these higher energy modes in the assignment of our spectra. A" - out of plane vibrations, A' - in plane vibrations, ν - assigned mode numbers (consistent with general literature on indole), Obs - observed INS frequencies, G98 - calculated frequencies.

A"			**A'**		
ν	**Obs** (cm^{-1})	**G98** (cm^{-1})	ν	**Obs** (cm^{-1})	**G98** (cm^{-1})
42	239	222			
41	265	256			
			29	397	410
40	429	445			
39	516	543			
			28	542	562
38	578	597			
37	608	625			
			27	619	630
36	730	748			
35	758	777			
			26	758	781
34	-	819			
33	854	888			
			25	867	903
32	-	911			
			24	896	925
31	937	972			
30	971	1020			
			23	1006	1043
			22	-	1098
			21	-	1126
			20	-	1163
			19	-	1207
			18	-	1245
			17	-	1298
			16	-	1311
			15	-	1384
			14	-	1407
			13	-	1457
			12	-	1494

Continued on next page

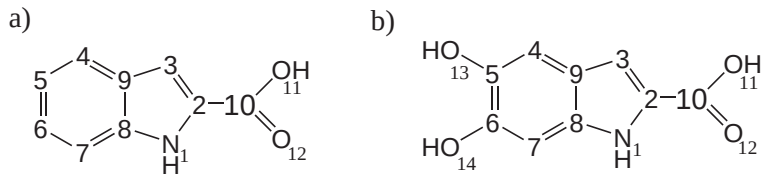

Figure 11.1: Chemical structures with atom numbering used in tables following. a) indole-2-carboxylic acid (ICA), b) 5,6-dihydroxyindole-2-carboxylic acid (DHICA).

Table 11.2 – continued from previous page

A"			A'		
ν	**Obs** (cm^{-1})	**G98** (cm^{-1})	ν	**Obs** (cm^{-1})	**G98** (cm^{-1})
			11	-	1540
			10	-	1559
			9	-	1627
			8	-	1669
			7	-	3185
			6	-	3192
			5	-	3204
			4	-	3218
			3	-	3273
			2	-	3298
			1	-	3694

Having achieved this careful assignment of the modes of indole we are in an excellent position to analyse the INS spectrum of indole-2-carboxylic acid (ICA). The structure of ICA is shown in figure 11.1(a) with standard atom numbering. ICA provides a critical link between indole and DHICA (figure 11.1(b)), allowing us to determine the effect of the addition of a carboxylic acid group to indole, and then deal seperately with the addition of the hydroxyl groups to ICA in the analysis of the INS spectrum of DHICA.

We therefore report in the first part of this chapter the measurement of the INS spectrum of ICA, the calculation of its vibrational modes using density functional theory, and the assignment of the observed vibrational modes via comparison to the modes of indole reported in reference [319]. We then report in the second part of this chapter the assignment of the INS modes of DHICA based upon the ICA assignments. The structure of DHICA with standard atom numbering is shown in figure 11.1(b)).

Several vibrational studies have been performed for ICA, which assist with the assignment of INS spectra. In 1977 Singh and Prakash reported very rough assignments of the IR spectra of ICA, [320], as did Viossat et al. in 2005 [321] and Rele et. al in 2006 [322]. Additionally, Ahmed reported IR frequencies for divalent transition metal complexes with ICA [323, 324]. We have listed the frequencies reported in these publications in table 11.3. Complete IR spectra for ICA were published by Tine et al (500 cm^{-1} to 2000 cm^{-1}) [325] and Morzyk-Ociepa et al. (500 cm^{-1} to 4000 cm^{-1}) [326] in good agreement with each other and we have extracted the positions of peaks from those graphs for inclusion in table 11.3. Only the most significant peaks in those publications were roughly assigned. The INS frequencies observed in this study are also included for ease of comparison.

Table 11.3: Table of the band positions (cm^{-1}) in the INS spectrum of ICA as compared to results of previous optical (IR) studies. Abbreviations: s = sharp, b = broad, sh = shoulder, v = very strong, st = strong, m = medium, w = weak.

INS (this work)	**[326]**	**[325]**	**[321]**	**[322]**	**[320]**
204					
262					
274					
283					
365					
383					
437					
		416			
539	526	506			
567	574	554			
	584	566			
609					
	623	600			
744	739	723			
	754	742(v)			
769	778	767			
813					
830	826	811			
853	855	835			
890	904	884			
939	934	924			
	938				
964	962				
	971	954			
1009	1010				
1116	1112	1108			
1150	1146	1150			
1209	1194	1195(v)	1196(st)	1105(v)	1203(m)
1237	1233	1234			
	1296	1292			1295
	1339	1336			
	1359	1351			
	1407	1408	1418(m)		1415(w)
	1436	1440(s)	1439(m)		1445(w)
	1484	1500(w)			
	1509	1520	1520(m)	1538(m)	1570(w)
	1571	1561			
	1610	1610	1622(w)		1615(w)
	1707	1704	1714(m,b)	1699(s)	1700(s)
	3052(b)		3036		
			3064		
				3298(s)	
	3350(v)	3350(st)	3352(m)	3368(m)	3395(s)
	3453	3453(w)	3454(w)	3416(m)	

Due to its role as a monomer in the eumelanin macromolecule, DHICA has received a more thorough treatment in a very recent publication by Okuda et al. [297]. The authors reported the mid-infrared (1000 cm^{-1} to 4000 cm^{-1}) absorption spectrum of DHICA with detailed assignments based on density functional theory calculations. They determined that hydrogen bonds play an important role in the vibrational properties of DHICA [297]. This IR study forms an excellent comparison for our INS spectrum and has assisted with our assignment process. The IR frequencies and intensities reported in that study are included in table 11.4 with a comparison to the INS frequencies observed in our study, and those we have calculated using density functional theory.

Table 11.4: Table of the IR observed frequencies (cm^{-1}) for DHICA as reported in reference [297], with the authors' assignments to band frequencies, IR intensities and mode descriptions calculated using GAUSSIAN03. We include for comparison the *ab-initio* calculated results reported here, calculated using GAUSSIAN98 (G98) and NRLMOL. Mode descriptions were matched with our calculated displacement vectors for each vibration to ensure accurate matching between these studies. τ - torsion (out of plane twisting), γ - out of plane bending, δ - in plane bending, ν - stretching, Skel. - skeleton, Ben. - benzene, Pyr. - pyrrole, def. - deformation, br. - breathing. Atom numbering as shown in figure 11.1. A" - out of plane vibrations, A' - in plane vibrations.

	G98			**NRLMOL**			**G03 [297]**			
ν	**Freq (cm^{-1})**		**IR**	**Freq (cm^{-1})**		**IR**	**Freq**	**IR**	**Description**	**IR Obs [297]**
	A"	**A'**	**Int**	**A"**	**A'**	**Int**	**(cm^{-1})**	**Int**		**(cm^{-1})**
57	76		0	65.7		0.0	-	-	-	-
56	86		0	78.1		0.0	-	-	-	-
39		127	0		119	0.0	-	-	-	-
55	167		0	151		0.0	-	-	-	-
54	214		0	195		0.1	-	-	-	-
53	280		173	236		2.6	-	-	-	-
38		307	3		304	0.1	-	-	-	-
37		314	12		306	0.2	-	-	-	-
36		328	7		317	0.1	-	-	-	-
52	348		1	322		0.1	-	-	-	-
51	392		1	376		0.0	-	-	-	-
50	439		11	409		0.1	-	-	-	-
35		440	12		423	0.2	-	-	-	-
49	506		140	481		1.3	-	-	-	-
34		527	79		509	1.4	-	-	-	-
33		551	5		529	0.2	-	-	-	-
48	568		114	501		2.9	-	-	-	-
47	621		82	448		0.6	-	-	-	-
46	638		69	600		0.0	-	-	-	-
32		647	17		627	0.3	-	-	-	-
31		686	7		668	0.3	-	-	-	-
45	700		5	674		0.0	-	-	-	-
44	746		34	696		0.2	-	-	-	-
30		768	15		748	0.2	-	-	-	-
43	788		14	738		0.8	-	-	-	-
29		795	6		765	0.1	-	-	-	-
42	866		1	781		0.0	-	-	-	-
41	879		16	798		0.0	-	-	-	-
28		880	13		860	0.2	-	-	-	-
40	907		82	815		1.4	-	-	-	-
27		984	35		956	0.3	-	-	-	-
26		1085	346		1068	3.3	1093	19.8	δC3H, δN1H, νC10O11	1095(w)
25		1110	142		1102	3.5	1122	274	δO11H, δN1H, νC5O11	1120(w)
24		1160	441		1114	10.4	1137	424	δO11H, δC3H, νC10O11	1138
23		1182	42		1143	0.7	1176	198	δC7H, δO11H, δO12H, δO11H	1172
22		1196	221		1163	2.7	1210	54.5	δO12H, δO11H, νC6O12, Skel, def.	-

Continued on next page

Table 11.4 – continued from previous page

ν	G98			NRLMOL			G03 [297]			IR Obs [297] (cm^{-1})
	Freq (cm^{-1})		IR	Freq (cm^{-1})		IR	Freq (cm^{-1})	IR	Description	
	A"	A'	Int	A"	A'	Int		Int		
21		1234	16		1201	3.5	1407	2.7	Skel. def., νC10O11, δO12H	-
20		1269	40		1215	0.6	1226	92.7	δC4H	-
19		1287	95		1228	4.0	1243	196	δN1H, δC3H, νC6O12	1230
18		1325	312		1295	8.2	1320	436	δO11H, νC6O12, νC10O11, Skel. br.	1255
17		1376	37		1334	0.1	1349	9.3	δO11H, δO12H	-
16		1391	30		1360	0.7	1371	15.4	Pyr. def., Ben. br., νC5O11, νC6O12	1339(m)
15		1435	9		1401	0.2	1428	124	νN1C2	1439(m)
14		1452	44		1412	2.3	1158	18.7	δN1H, νC7H	-
13		1513	15		1469	0.3	1486	11.1	Skel. def., νC5O11	1474(w)
12		1563	34		1513	2.2	1529	68.2	Skel. def., νC6O12	1531(st)
11		1575	143		1527	4.6	1657	23.4	Benzene def.	-
10		1639	48		1583	0.4	1549	279	Pyr. br., Ben. def.	1541(st)
9		1688	731		1701	15.4	1750	517	νC10O12	1684(st)
8		1693	79		1633	0.7	1600	9.5	Skel. def.	1597(w)
7		3197	13		3094	0.3	3097	15	νC4H	-
6		3237	2		3126	0.0	3138	3	νC7H	-
5		3297	0		3191	0.0	3192	0.7	νC3H	-
4		3618	163		3634	3.5	3681	129	νO12H	3273(b)
3		3628	91		3657	2.5	3675	117	νO11H	3273(b)
2		3674	94		3569	2.1	3598	101	νN1H	3433(st)
1		3712	66		3721	1.8	3751	68	νO11H	3273(b)

In summary, we report in this chapter the measured INS spectra of ICA and DHICA with detailed assignments based upon *ab-initio* density functional theory calculations, previous detailed assignments of indole spectra, and previous assignments of IR spectra for these molecules. The assignment of the vibrational modes of DHICA will allow us to make firm and detailed conclusions about the spectra of eumelanin related molecules.

11.3 Experimental

11.3.1 Sample preparation

Indole-2-carboxylic acid, > 99%, was obtained from the Aldrich Chemical company and used without further treatment. DHICA was synthesised as reported by Tran et al. [76].

11.3.2 Spectrometer

The powdered samples were wrapped in aluminium foil (5 g of ICA and 1 g of DHICA) and held in flat sample cells. These were maintained at 20 K in the neutron beam of the TOSCA spectrometer [327], at the ISIS Facility, The Rutherford Appleton Laboratory, Chilton, OX11 0QX, UK. TOSCA is a pulsed neutron, indirect geometry, low band-pass spectrometer with good spectral resolution (ΔEt/Et $\approx 2\%$). On these types of spectrometer each energy, E_t, is associated with a specific momentum transfer value, Q, as such mode dispersion cannot be tracked on these spectrometers. Also, the momentum transfer vector, Q, is perpendicular to the face of the sample cell [318]. Data were collected for about 6 to 12 hours and transformed into the conventional scattering law vs energy transfer (where E_t is given in cm^{-1}), using standard programs.

11.4 Calculations

11.4.1 Ab-initio calculations

Our calculations were performed in GAUSSIAN98 (G98) [328] and the Naval Research Laboratory Molecular Orbital Library (NRLMOL) [191–197] for the isolated molecules. In GAUSSIAN98 the molecular geometry was constrained planar and optimised at the B3LYP level. The DFT calculation (with the 6-31G** basis set) produced harmonic vibrational frequencies.

NRLMOL performs massively parallel electronic structure calculations using gaussian orbital methods. We fully relaxed the geometry with no symmetry constraints using the Perdew, Burke and Ernzerhof (PBE) [198] exchange correlation functional, which is a generalized gradient approximation (GGA) containing no free parameters. In the calculations presented in this paper we use Porezag-Pederson (PP) basis sets [329], which, in contrast to standard approaches, are not a fixed set of basis functions, but are adjusted on a total-energy criterion. PP basis sets have been proven to satisfy the $Z^{10/3}$ theorem and, for weakly interacting atoms, it has been shown that PP basis sets have no superposition error [330].

Our basis sets are available on request. For a discussion of the calculation of vibrational modes see references [195–197].

The atomic displacement vectors appearing in the output files from GAUSSIAN98 ('.LOG' file) were used as input to the aCLIMAX program [331] to determine INS intensities.

11.4.2 Data visualisation

aCLIMAX [331] is a program that displays the INS spectra taken on any low-bandpass spectrometer for comparison with the results of *ab-initio* calculations [318]. The program accepts input from GAUSSIAN98 and NRLMOL, and, in principle, any eigenvalue and eigenvector data (in the correct units) and calculates INS intensities. Unlike optical spectroscopy, the INS technique expresses not only fundamentals but also all combination bands and overtones. The aCLIMAX program calculates these intensities (combinations and overtones are treated harmonically out to the tenth order) and adds the contributions from all sources of intensity to determine the total INS spectrum [318]. Most of the calculated contributions from combination bands and overtones add only weak and very broad features to the region above 1500 cm^{-1}, but in the mid frequency range sharp overtones and combinations (arising from intense bands at low energies) are sometimes found. Hence every observed INS peak does not necessarily correspond to a new vibrational motion of the molecule. The aCLIMAX program generates all the transition bands as gaussian profiles according to a set of fixed parameters and, as such, bands of dramatically different widths in the same spectrum are not readily accommodated.

11.4.3 Specific data treatment

ICA

The following process was used to obtain initial estimates of the assignments of ICA INS peaks. The GAUSSIAN98 displacement eigenvectors for each vibrational mode determined computationally were examined and sorted into in plane (A') and out of plane (A") modes. The displacement eigenvectors from NRLMOL were then compared to those from GAUSSIAN98 to match the vibrational frequencies, as listed in the first six columns of table 11.7. The nature of the ICA vibrations was then compared, using the program ViPA [332], with those of indole [319]. The results of this exercise are the mode descriptions given in the 7th column of table 11.7. This indicated which of the vibrations are very similar in nature to those of indole. The vibrational modes of indole have been measured using INS and carefully assigned as reported in reference [319]; the details of these modes were extracted and are listed in columns 8-11 of table 11.7, including calculated and observed wavenumbers, and shifts (the difference between the observed and calculated wavenumbers). The ICA observed INS modes were then matched with the ICA calculated modes to produce similar shifts to those seen for the equivalent indole modes. The GAUSSIAN98 calculated frequencies were then given small shifts to match with the observed values, the new frequencies being listed in the 'Final Freqs' column of table 11.7. These are the frequencies that were used with aCLIMAX determined intensities to produce figure 11.3. The IR frequencies for ICA measured by Morzyk-Ociepa et al [326] were also taken into consideration by comparison to the

IR calculated intensities from GAUSSIAN98 (listed in the final two columns of table 11.7).

Further small refinements were then made to certain peaks to produce a more faithful match between the aCLIMAX calculated INS spectrum and the experimental spectrum, as described in the discussion. Due to the known rigid nature of ICA (similar in nature to indole), a non-default wing shape that was narrow in frequency was used (rigid molecules tend to give sharp, high intensity peaks, as we have observed in the ICA spectrum). Also due to this rigidity, the wing status A external isotropic generation value was reduced from the default value to small 0.015. The 'Auto generate Sachs-Teller' option was utilized to distribute the isotropic A external value in an anisotropic manner (allowing the in plane and out of plane modes to be different).

DHICA

A very similar process was used for the assignment of DHICA vibrational modes, based upon the previous assignments for ICA (rather than indole). The results of this process are outlined in table 11.9. IR frequencies with assignments from reference [297] in the range 1000cm^{-1} to 4000cm^{-1} were taken into consideration (listed in table 11.4).

The DHICA spectrum is more challenging to replicate computationally than that for ICA since DHICA has a rigid main body, combined with much 'softer' hydroxyl groups. The hydroxyl groups give rise to very broad, low intensity phonon wing bands that are barely visible whereas the rigid body gives rise to sharp peaks of significant intensity (as was observed for ICA). The aCLIMAX program is unfortunately unable to deal with systems of this nature, being able to only accommodate one type of wing shape per spectrum. For modelling DHICA we have therefore chosen to use the same non-default narrow wing shape that was used for ICA (to give an accurate representation of the peaks arising from the rigid main body of the molecule), and to then manually reduce the intensity of the overtones of peaks we assign to be the hydroxyl vibrations. The assignment of these peaks is non-trivial (as discussed below), and would be aided by the measurement of a deuterated DHICA spectrum for comparison. We recommend this for future work, and caution that the assignment scheme given here for DHICA is tentative only.

11.5 Discussion

11.5.1 Calculated structural results

The lowest energy structures of both ICA and DHICA were found to be planar, and are shown in figures 11.2(a) and 11.2(b) respectively. The structure of DHICA was consistent with that from Powell's previous study [77]. Energies calculated using both GAUSSIAN98 and NRLMOL for each molecule are listed in table 11.5, and it can be seen that they agree closely. Dipoles and rotational constants calculated using GAUSSIAN98 for each molecule are also included in table 11.5.

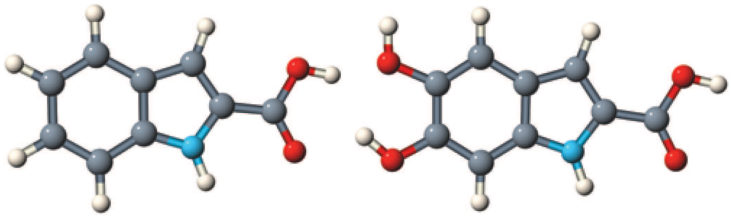

(a) ICA (b) DHICA

FIGURE 11.2: The lowest energy structures for ICA and DHICA as calculated by GAUSSIAN98. Red: oxygen, blue: nitrogen, white: hydrogen, grey: carbon.

Table 11.5: Properties of ICA and DHICA calculated using density functional theory (G98 and NRLMOL).

		Energy		Dipole	Rotational constants		
		(kJ mole^{-1})	(Ha)	(D)	(MHz)		
ICA	**G98**	-1449932.102	-552.2175697	3.3679	2918.41	534.07	451.45
	NRLMOL	-1449349.553	-551.9957015				
DHICA	**G98**	-1844868.312	-702.6320022	2.8669	2129.52	339.13	292.55
	NRLMOL	-1844198.597	-702.3769361				

Structural lengths of interest for each molecule are listed in table 11.6, with atom numbering as shown in figure 11.1. The lengths from GAUSSIAN98 and NRLMOL all agree to within 1%. The N-H bond length is identical for ICA and DHICA, so we expect that the vibrational frequencies relating to this group might be very similar for the two molecules. The addition of the hydroxyl groups has had more influence over the skeletal lengths (as would be expected), so we expect to see more variation between the vibrational frequencies involving skeletal deformations.

11.5.2 Assignment of the INS modes of ICA

The experimental INS spectrum of ICA is shown as the solid line in figure 11.3. The final calculated spectrum for this molecule generated from GAUSSIAN98 frequencies and aCLIMAX intensities is shown as the dotted line. Note that the calculated vibrational peaks have undergone small shifts to produce better matching with the experimental spectrum, with initial and final calculated frequencies listed in table 11.7. The aim of this process is not to

Table 11.6: Significant structural distances and bond lengths of ICA and DHICA calculated using density functional theory (G98 and NRLMOL).

		Structural lengths (Å)			
		N-H	**Ring fused C-C**	**C2 to H5**	**C2 to H6**
ICA	**G98**	1.009	1.434	7.088	6.999
	NRLMOL	1.013	1.432	7.087	6.994
				C2 to O13	**C2 to O14**
DHICA	**G98**	1.009	1.434	5.970	5.910
	NRLMOL	1.013	1.431	5.940	5.885

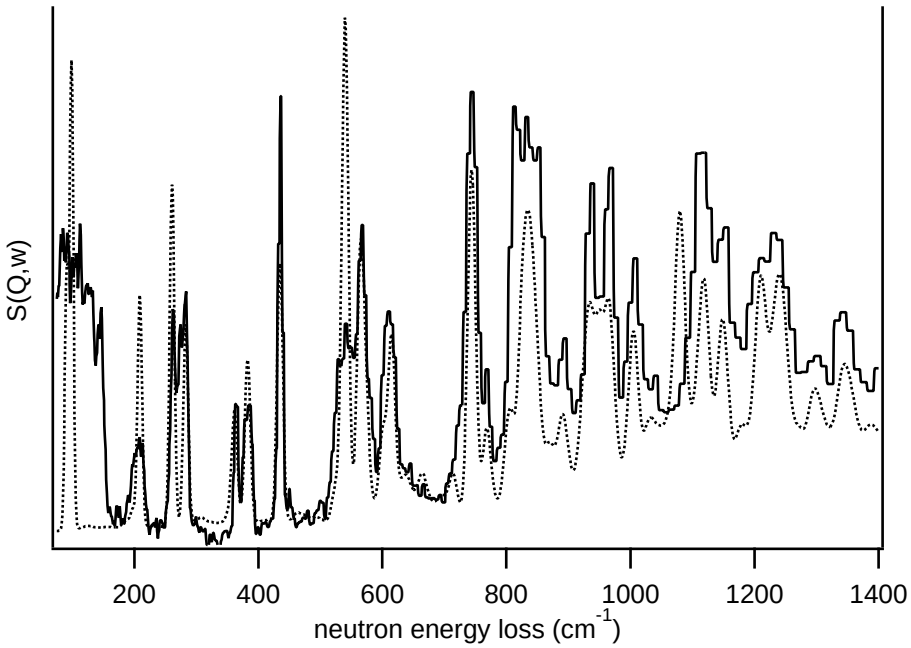

Figure 11.3: The INS spectra of ICA, as observed (continuous line) and as calculated (discontinuous line). Peak positions are listed in tables 11.8 and 11.7.

test the ability of the computational methods used, but rather to obtain mode assignments for the observed frequencies. Based on the earlier indole study we know the amount and direction that each observed band moved from the initial calculated frequency, so we have allowed shifting of calculated bands of similar magnitudes to attempt to obtain the ideal fit between experiment and theory. This allows us to identify the vibrational motions associated with each INS peak.

The region $200 - 800$ cm^{-1} fitted reasonably well from the original assignments (made by comparison with previously measured and assigned indole spectra [319], as described in the section on the specific data treatment). This region required only minor adjustments to improve the fitting, where the comparison with indole had been ambiguous. However, the region $800 - 1100$ cm^{-1} is quite different from that of indole, meaning that the assignments based on the indole spectrum were not as successful. It appears that the carboxylic acid group has modified the indole vibrations involving the pyrrole ring, and suppressed the frequencies of those indole modes about 1050 cm^{-1}. A shift in these modes was observed in indole that was deuterated at the 3 position (to about 850 cm^{-1}); we believe that the carboxylic acid has acted here like the deuteration of the pyrrole [319].

It is also important to consider that the calculations were done for isolated molecules, whereas experimentally we are observing a solid state system which will include hydrogen bonding between molecules. To take this into consideration, it was necessary to move the γ(OH) mode ($\nu = 46$) from the isolated molecule calculated position of 572 cm^{-1} to a more realistic 826 cm^{-1} (we believe this is consistent with the IR data). The intensity of this mode was also suppressed by dividing the displacement by 2 (this suppressed the (0-2) transition intensity, and suggests anharmonicity). Note that the γ(OH) shows significant broadening.

In melanin this could be assumed to be due to chemical disorder, but it cannot be due to disorder in this pure ICA system (many of the observed bands have full-widths at half-height similar to the spectrometer's resolution, suggesting that chemical disorder does not dominate the properties of ICA (or DHICA) as we believe it does in eumelanin). The origin of the broadening of this peak is not well understood at this stage.

The resulting final spectral fitting (shown in figure 11.3) is of reasonable quality, suggesting that we have accurately assigned the ICA modes in the order listed in table 11.7. These results are summarised in table 11.8 with basic descriptions of the types of vibrational motions that each represents.

Table 11.7: Table of the *ab-initio* calculated frequencies (cm^{-1}) of ICA compared with INS observations, as discussed in the text. The list of frequencies used to produce figure 11.3 is included in column Final Freq. Indole modes shown are from reference [319] and are summarised here in table 11.2. GAUSSIAN98 results are in the columns headed G98, and the results from NRLMOL are under NL. Our mode descriptions are taken from the GAUSSIAN98 output and given with respect to the modes of indole (after [332]); x(y) implies that this ICA mode has x% of the indole mode number y (only contributions greater than 10% are shown). IR observed results are from reference [326]. A" - out of plane vibrations, A' - in plane vibrations, ν - mode number.

ICA							**INDOLE**				**ICA**				
A"			**A'**											**IR**	
ν	**G98 (cm^{-1})**	**NL (cm^{-1})**	ν	**G98 (cm^{-1})**	**NL (cm^{-1})**	**ViPA description**	**Compare to indole ν**	**Obs (cm^{-1})**	**Calc (cm^{-1})**	**Shift (obs-calc) (cm^{-1})**	**Obs (cm^{-1})**	**Final Freq (cm^{-1})**	**Shift (obs-calc) (cm^{-1})**	**Obs [326] (cm^{-1})**	**G98 Int**
51	92	83				-	-	-	-	-	-	92	-	-	1
50	99	89				11(42)	-	-	-	-	-	99	-	-	1
			35	142	137	-	-	-	-	-	204	209	62	-	2
49	266	242				98(41)	41	265	256	9	262	261	-4	-	0
48	284	259				85(42)	42	239	222	17	274	283	-10	-	0
						-	-	-	-	-	283	-	-	-	-
			34	350	342	-	-	-	-	-	365	362	15	-	8
			33	377	361	56(29)	29	397	410	-13	383	383	6	-	2
47	459	418				96(40)	40	429	445	-16	437	435	-22	-	3
			32	563	537	33(29)	-	-	-	-	567	563	4	574	19
46	572	541				29(37)	-	-	-	-	830	826	258	826	121
			31	586	561	63(28)	28	542	562	-20	-	574	-	584	34
45	593	562				97(38)	38	578	597	-19	-	566	-	-	0
44	626	474				87(39),12(37)	39	516	543	-27	539	540	-87	526	76
			30	633	601	98(27)	27	619	630	-11	609	601	-24	-	3
43	643	614				51(37)	37	608	625	-17	-	615	-	623	61
			29	686	667	21(26),13(28)	-	-	-	-	769	768	83	778	12
42	766	719				82(36)	36	730	748	-18	744	744	-22	739	0
41	780	728				91(35)	35	758	777	-19	-	744	-	754	135
40	809	750				85(34)	34	-	-	-	813	809	4	-	5
			28	820	799	70(26),17(24)	26	758	781	-23	-	849	-	-	0
39	882	800				91(33)	33	854	888	-34	853	837	-29	855	16
38	905	824				91(32)	32	-	-	-	939	935	34	934	20
						-	-	-	-	-	-	-	-	938	-
			27	925	879	89(25)	25	867	903	-36	890	890	-35	904	1
37	983	913				100(31)	31	937	972	-35	-	950	-	-	5
			26	983	954	59(24),15(22)	24	896	925	-29	964	967	-19	962	33
36	1025	948				100(30)	30	971	1020	-49	-	966	-	971	0
			25	1041	1006	97(23)	23	1006	1043	-37	1009	1005	-32	1010	3
			24	1095	1079	32(22),12(21)	-	-	-	-	1116	1116	21	1112	292
			23	1162	1108	66(20),19(21)	20	-	1163	-	1150	1120	-12	1146	14
			22	1170	1119	32(22),16(20)	-	-	-	-	1209	1149	39	1194	227
			21	1210	1141	93(19)	19	-	1207	-	1237	1210	27	1233	2
			20	1264	1186	76(18)	18	-	1245	-	-	1235	-	1296	9
			19	1281	1220	63(17)	17	-	1298	-	-	1247	-	1339	15

Continued on next page

Table 11.7 – continued from previous page

ICA							INDOLE				ICA				
A"			A'											IR	
ν	G98 (cm^{-1})	NL (cm^{-1})	ν	G98 (cm^{-1})	NL (cm^{-1})	ViPA description	Compare to indole ν	Obs (cm^{-1})	Calc (cm^{-1})	Shift (obs-calc) (cm^{-1})	Obs (cm^{-1})	Final Freq (cm^{-1})	Shift (obs-calc) (cm^{-1})	Obs [326] (cm^{-1})	G98 Int
			18	1315	1276	42(16), 24(17)	16	-	1311	-	-	1295	-	1359	21
			17	1359	1317	35(16), 31(15)	-	-	-	-	-	1359	-	1407	84
			16	1395	1340	82(14)	14	-	1407	-	-	1345	-	1436	69
						-	-	-	-	-	-	-	-	1484	-
			15	1426	1388	46(15), 16(10)	15	-	1384	-	-	1426	-	-	28
			14	1454	1412	90(13)	13	-	1457	-	-	1454	-	-	16
			13	1487	1433	81(12)	12	-	1494	-	-	1487	-	-	29
			12	1547	1488	96(11)	11	-	1540	-	-	1547	-	-	2
			11	1576	1524	56(10)	10	-	1559	-	-	1576	-	1509	76
						-	-	-	-	-	-	-	-	1571	-
						-	-	-	-	-	-	-	-	1601	-
			10	1623	1567	95(9)	9	-	1627	-	-	1623	-	-	1
			9	1671	1613	99(8)	8	-	1669	-	-	1671	-	-	10
			8	1690	1700	33(2)	-	-	-	-	-	1690	-	1707	694
			7	3193	3093	98(7)	7	-	3185	-	-	3193	-	-	0
			6	3201	3103	96(6)	6	-	3192	-	-	3201	-	-	3
			5	3212	3116	97(5)	5	-	3204	-	-	3212	-	-	31
			4	3224	3121	99(4)	4	-	3218	-	-	3224	-	-	26
			3	3298	3188	74(3), 26(2)	3	-	3273	-	-	3298	-	-	0
			2	3629	3645	-	-	-	-	-	-	3629	-	-	93
			1	3673	3559	100(1)	1	-	3694	-	-	3673	-	3350	92

Table 11.8: Descriptions of the vibrational modes of ICA. τ - torsion (out of plane twisting), γ - out of plane bending, δ - in plane bending, ν - stretching, Skel. - skeleton, Ben. - benzene, Pyr. - pyrrole, def. - deformation, br. - breathing. Atom numbering as shown in figure 11.1. A" - out of plane vibrations, A' - in plane vibrations.

A"		**A'**				
ν	**G98 (cm^{-1})**	ν	**G98 (cm^{-1})**	**Obs (cm^{-1})**	**Final Freq (cm^{-1})**	**Description**
51	92			-	92	τC2C10
50	99			-	99	γSkel. def. (butterfly)
		35	142	204	209	δC2C10
49	266			262	261	τSkel. def.
48	284			274	283	γSkel. def. (standing wave)
		34	350	365	362	νSkel. def., νC2C10, δO11H
		33	377	383	383	δSkel. def., δC2C10
47	459			437	435	γC4H, γC7H
		32	563	567	563	δBen. def., δC3H, δN1H, δO11H
46	572			830	826	γO11H
		31	586	-	574	νBen. def., δO11H
45	593			-	566	γC5H, -γC6H, τSkel. def.
44	626			539	540	γN1H
		30	633	609	601	νSkel. def.,
43	643			-	615	γO11H, -γC3H
		29	686	769	768	δO11H, νSkel. def.
42	766			744	744	γC3H, -γC7H, -γC5H, -γC6H
41	780			-	744	γC5H, γC6H, γC4H
40	809			813	809	γC7H, -γC4H, τSkel. def.
		28	820	-	849	νSkel. br., νC8C9, νC3C9, νN1C8, γC3H
39	882			853	837	γC3H, γC7H, -γC4H, γC6H, -γC5H
38	905			939	935	γC3H, γC5H, -γC7H, γC4H
		27	925	890	890	νSkel. def., νC3C9, -νC8N1
37	983			-	950	γC4H, γC7H, -γC6H, -γC5H
		26	983	964	967	νPyr. def., νC9C8, νC2C10, νC10O11
36	1025			-	966	γC6H, -γC5H, γC4H, -γC7H
		25	1041	1009	1005	δC4H, -δC7H, νBen. br., δC5H, -δC6H
		24	1095	1116	1116	δO11H, δC3H, -δN1H, νPyr. br., νC10O11H
		23	1162	1150	1120	δC5H, δC6H, -δC4H, -δC7H
		22	1170	1209	1149	δC3H, -δO11H, δC4H, νC2C10
		21	1210	1237	1210	δC5H, -δC6H, δC7H, -δC4H
		20	1264	-	1235	δN1H, δC3H, δO11H
		19	1281	-	1247	δC4H, δC7H, δN1H
		18	1315	-	1295	δO11H, -δN1H, -δC6H
		17	1359	-	1359	δO11H, δC3H, -δC4H, νSkel. def., νC8C9, -νC9C3
		16	1395	-	1345	δC5H, δC4H, δC7H, -δC3H, -δN1H, δC6H
		15	1426	-	1426	νPyr. br., νBen. Def., δC5H, -δC6H
		14	1454	-	1454	δN1H, -δC6H, νC2N1, -νC7C6
		13	1487	-	1487	δC4H, -δC7H, νC9C8
		12	1547	-	1547	δC5H, δN1H, νSkel. def., νC9C4, νC5C4
		11	1576	-	1576	νSkel. def, νPyr. br., νC2C3, -νC10O12, δC6H, δC3H, -δN1H

Continued on next page

Table 11.8 – continued from previous page

A”		A’		Obs	Final Freq	Description
ν	G98 (cm^{-1})	ν	G98 (cm^{-1})	(cm^{-1})	(cm^{-1})	
		10	1623	-	1623	νSkel. def, νC6C5, νC8C9, δN1H, δC6H
		9	1671	-	1671	νSkel. def, νC7C8, νC5C4, δN1H, δC4H
		8	1690	-	1690	νC2C10, -νC10O12, δO11H, νPyr. br.
		7	3193	-	3193	νC6H, -νC5H, νC4H, -νC7H
		6	3201	-	3201	νC7H, νC4H, -νC6H, -νC5H
		5	3212	-	3212	νC7H, -νC4H, νC6H, -νC5H
		4	3224	-	3224	νC6H, νC5H, νC7H, νC4H
		3	3298	-	3298	νC3H
		2	3629	-	3629	νO11H
		1	3673	-	3673	νN1H

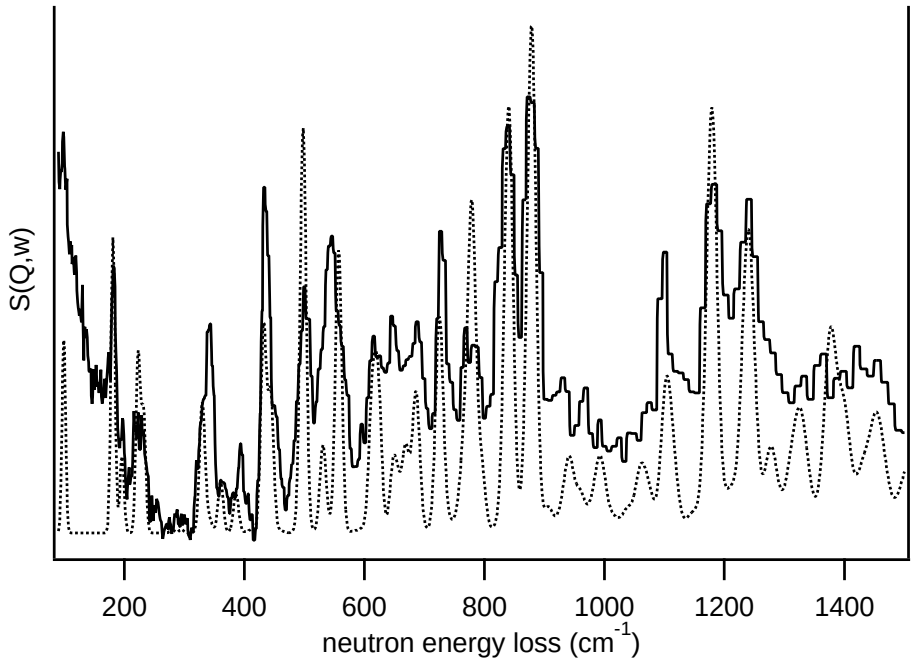

FIGURE 11.4: The INS spectra of DHICA, as observed (continuous line) and as calculated (discontinuous line). Peak positions are listed in tables 11.10 and 11.9.

11.5.3 Assignment of the INS modes of DHICA

The experimental INS spectrum of DHICA is shown as the solid line in figure 11.4, with the final calculated spectrum for this molecule from GAUSSIAN98 and aCLIMAX included as the dotted line. As for ICA, small peak shifts were permitted to produce the ideal spectral fit; initial and final calculated frequencies are outlined in table 11.9. Shifts were selected to obtain similarity to the shifts observed for ICA for the corresponding mode.

As suggested by Okuda et al. [297] hydrogen bonding is significant in DHICA in the solid state and has a strong effect on the vibrational modes involving the motion of hydroxyl groups. This was confirmed by our assignments for ICA, where we showed that the γOH mode ($\nu = 46$) shifted substantially from the vacuum calculated position of 572 cm^{-1} to a much higher energy 826 cm^{-1}. We have therefore made a similar shift in our assignment of the DHICA γOH mode (for the carboxylic acid OH group, $\nu = 48$), moving it from the vacuum calculated position of 568 cm^{-1} to a substantially higher energy 842 cm^{-1} (where a similar peak is observed in the experimental spectrum).

DHICA also has two additional hydroxyl groups which are not present in ICA, and we expect that the modes involving these groups will also be substantially affected by hydrogen bonding. Modes 53 and 49, calculated to be at 280 cm^{-1} and 506 cm^{-1} respectively are strongly γOH in character, so we expect these to occur at substantially higher energies. They have been shifted to 343 cm^{-1} and 544 cm^{-1} respectively, although larger shifts are possible. Mode 46 also involves γOH motion (although it is mixed with other molecular motions), and modes 26, 25, 22, 21 and 18 all have δOH character (also mixed with other molecular motions to various degrees). The mixing of these modes is likely to reduce the

impact due to hydrogen bonding. We have taken these effects into account in the assignment of these modes, although unfortunately it is not possible to assign them with complete certainty based upon this information. The detailed analysis of this spectrum has revealed that an INS measurement of the deuterated system would allow a much clearer assignment of the modes of DHICA, particularly allowing identification of modes involving the hydroxyl groups. We recommend this for future research before the mode assignments for DHICA listed here are used further.

The measurement of a deuterated spectrum would also allow a clearer analysis of the effect of overtones in this spectrum for a more accurate assignment. The aCLIMAX calculated spectrum initially had a strong peak at 1026 cm^{-1} that did not appear at all in the experimental spectrum. This peak was due to a 0-3 transition overtone from the calculated γO13H mode ($\nu = 53$) at 343 cm^{-1}. The overtones due to the other γOH modes were also unrealistically dominant, for the reasons discussed above in section 11.4.3. The intensities of all overtones involving γOH motions were therefore set to zero to produce a more faithful fit to the experimental data. Also, the intensity of the γNH mode ($\nu = 47$) was reduced to lessen the intensity of the overtone due to that peak. The remaining overtones around the region 1600 cm^{-1} appear to be more reliable and have been left as calculated.

After these minor adjustments the fit to the experimental data appears to be satisfactory (figure 11.4) indicating that most modes are assigned correctly. We wish to empahsise again, however, that these mode assignments are not as reliable as those for ICA reported above, and should be confirmed with experiments on the deuterated system.

Table 11.9: Table of the *ab-initio* calculated frequencies (cm^{-1}) of DHICA compared with INS observed frequencies, as discussed in the text. The list of frequencies used to produce figure 11.4 is given in column Final Freq. G98: calculated frequencies from GAUSSIAN98. NL: calculated frequencies from NRLMOL. ViPA mode descriptions were determined from the GAUSSIAN98 data with respect to the modes of ICA after reference [332]; x(y) implies that this DHICA mode has x% of the ICA mode number y (only contributions greater than 10% are included). A" - out of plane vibrations, A' - in plane vibrations.

DHICA							**ICA**				**DHICA**			
A"			**A'**											
ν	**G98 Freq (cm^{-1})**	**NL Freq (cm^{-1})**	ν	**G98 Freq (cm^{-1})**	**NL Freq (cm^{-1})**	**ViPA description (% of ICA modes)**	**Compare to ICA ν**	**Obs (cm^{-1})**	**Calc (cm^{-1})**	**Shift (obs-calc) (cm^{-1})**	**IR Obs [297] (cm^{-1})**	**INS Obs (cm^{-1})**	**Final Freq (cm^{-1})**	**Shift (obs-calc) (cm^{-1})**
57	76	65				65(50),6(41)	50	-	99	-	-	99	99	23
58	86	79				79(51),5(50),5(36)	51	-	92	-	-	196	196	110
			39	127	117	84(35)	35	204	142	62	-	223	223	96
55	167	151				35(49), 17(36), 14(51), 13(45)	-	-	-	-	-	181	181	14
54	214	195				56(48), 19(50)	48	274	284	-10	-	232	232	18
53	280	244				-	-	-	-	-	-	343	343	63
			38	307	304	37(21), 23(34)	21	1237	1210	27	-	334	334	27
			37	314	306	42(33)	33	383	377	6	-	329	329	15
			36	328	317	55(34), 12(33)	34	365	350	15	-	360	360	32
52	348	322				58(49), 24(45)	49	262	266	-4	-	432	432	84
51	392	376				34(48), 26(41)	41	-	780	-	-	386	386	-6
50	439	409				92(47)	47	437	459	-22	-	498	498	59
							-	-	-	-	-	392	-	-
			35	440	423	31(33), 29(30)	30	609	633	-24	-	-	498	-
49	506	481				-	-	-	-	-	-	544	544	38
			34	527	509	43(45), 31(31)	-	-	-	-	-	453	444	-74
			33	551	529	42(31), 36(32)	31	-	586	-	-	531	531	-20
48	568	501				98(46)	46	830	572	258	-	842	842	274
47	621	448				98(44)	44	539	626	-87	-	725	725	104
46	638	600				98(43)	43	-	643	-	-	557	557	-81
			32	647	627	22(30), 15(32), 14(23)	32	567	563	4	-	613	613	-34
			31	686	668	92(29)	29	769	686	83	-	623	623	-63
45	700	674				48(45), 15(39)	45	-	593	-	-	648	648	-52
44	746	697				60(42), 23(41), 14(40)	42	744	766	-22	-	686	686	-60
			30	768	748	39(28), 20(25), 11(31), 11(4)	25	1009	1040	-31	-	669	669	-99
43	788	738				79(40), 12(42)	40	813	809	4	-	766	766	-22
			29	795	765	47(27), 33(30)	27	890	925	-35	-	795	795	0
42	866	781				47(39), 15(38), 14(36), 13(26)	39	853	882	-29	-	779	779	-87
41	879	798				29(38), 20(36), 19(39), 19(26)	26	964	983	-19	-	880	880	1
			28	880	860	53(28), 19(25)	28	-	820	-	-	838	838	-42
40	907	815				43(26), 40(38)	38	939	905	34	-	877	877	-30
							-	-	-	-	-	928	-	-
							-	-	-	-	-	966	-	-
			27	984	956	94(26)	26	964	983	-19	-	989	989	5
			26	1085	1068	73(24)	24	1116	1095	21	1095(w)	1102	1102	17
			25	1110	1102	26(24), 13(27), 11(7)	-	-	-	-	1120(w)	-	1102	-
			24	1160	1114	66(22)	22	1209	1170	39	1138	-	1179	-

Continued on next page

Table 11.9 – continued from previous page

DHICA							ICA				DHICA			
A”			A’											
ν	G98 Freq (cm^{-1})	NL Freq (cm^{-1})	ν	G98 Freq (cm^{-1})	NL Freq (cm^{-1})	ViPA description (% of ICA modes)	Compare to ICA ν	Obs (cm^{-1})	Calc (cm^{-1})	Shift (obs-calc) (cm^{-1})	IR Obs [297] (cm^{-1})	INS Obs (cm^{-1})	Final Freq (cm^{-1})	Shift (obs-calc) (cm^{-1})
			23	1182	1143	20(22), 13(23)	-	-	-	-	1172	1179	1179	-3
			22	1196	1163	25(21), 11(22)	-	-	-	-	-	1179	1179	-17
			21	1234	1201	23(23), 13(20), 11(18)	23	1150	1162	-12	-	1236	1236	2
			20	1269	1215	84(19)	19	-	1281	-	-	1236	1236	-33
			19	1287	1228	61(20)	20	-	1264	-	1230	1245	1245	-42
			18	1325	1295	53(18), 20(17)	18	-	1315	-	1255	-	-	-
			17	1376	1334	61(16)	16	-	1595	-	-	-	-	-
			16	1391	1360	53(17)	17	-	1359	-	1339(m)	-	-	-
			15	1435	1401	82(15), 11(14)	15	-	1426	-	1439(m)	-	-	-
			14	1452	1412	56(14), 16(13), 11(16)	14	-	1454	-	-	-	-	-
			13	1513	1469	62(13)	13	-	1487	-	1474(w)	-	-	-
			12	1563	1513	67(12)	12	-	1547	-	1531(st)	-	-	-
			11	1575	1527	89(11)	11	-	1576	-	-	-	-	-
			10	1639	1583	90(10)	10	-	1623	-	1541(st)	-	-	-
			9	1688	1700	87(8), 11(9)	8	-	1690	-	1684(st)	-	-	-
			8	1693	1633	83(9), 12(8)	9	-	1671	-	1597(w)	-	-	-
			7	3197	3094	37(6), 32(5), 18(7), 14(4)	-	-	-	-	-	-	-	-
			6	3237	3126	36(5), 35(6), 15(7), 14(4)	-	-	-	-	-	-	-	-
			5	3297	3191	100(3)	3	-	3298	-	-	-	-	-
			4	3618	3634	-	-	-	-	-	3273(b)	-	-	-
			3	3628	3657	100(2)	2	-	3629	-	3273(b)	-	-	-
			2	3674	3569	100(1)	1	-	3673	-	3433(st)	-	-	-
			1	3712	3721	-	-	-	-	-	3273(b)	-	-	-

Table 11.10: Descriptions of the vibrational modes of DHICA. τ - torsion (out of plane twisting), γ - out of plane bending, δ - in plane bending, ν - stretching, Skel. - skeleton, Ben. - benzene, Pyr. - pyrrole, def. - deformation, br. - breathing. Atom numbering as shown in figure 11.1. A" - out of plane vibrations, A' - in plane vibrations.

A"		**A'**				
ν	**G98 (cm^{-1})**	ν	**G98 (cm^{-1})**	**Obs (cm^{-1})**	**Final Freq (cm^{-1})**	**Description**
57	76			99	99	γSkel. def. (butterfly)
56	86			196	196	τC2C10
		39	127	223	223	δC2C10
55	167			181	181	τSkel. def.
54	214			232	232	γSkel. def. (standing wave)
53	280			343	343	γO13H
		38	307	334	334	γC2C10, δO13H, -δO14H
		37	314	329	329	δSkel. def., δC2C10, δC5O13
		36	328	360	360	νBen. br., νC6O14
52	348			432	432	τSkel. def., δC4H, -δC7H, -δC3H
51	392			386	386	γSkel. def. (standing wave)
50	439			498	498	γC7H, γC4H
				392	-	
		35	440	-	498	νBen. def., δC5O13
49	506			544	544	γO14H
		34	527	453	444	νBen. def., δO11H, δN1H
		33	551	531	531	νBen. def., δC3H
48	568			842	842	γO11H
47	621			725	725	γN1H
46	638			557	557	γO11H, γPyr. def., -γC3H
		32	647	613	613	νSkel. def., δC7H, δC4H, -δO13H, -δO14H
		31	686	623	623	δC10O11, δO11H, νSkel. def.
45	700			648	648	τBen. def., γC4H, -γC7H
44	746			686	686	τSkel. def., γC3H γC4H, -γC7H
		30	768	669	669	νBen. br., νC5C6, νC9C8
43	788			766	766	τPyr. def., γC2C10, γC3H, -γC4H, γC7H
		29	795	795	795	νSkel. def.
42	866			779	779	γC3H, -γC4H
41	879			880	880	γC7H
		28	880	838	838	νSkel. br, δC4H, -δC7H
40	907			877	877	γC3H, γC4H
				928	-	
				966	-	
		27	984	989	989	νPyr. br, νC3C2, νC2N1, νC10O11
		26	1085	1102	1102	δO11H, δC3H, -δO13H, νPyr. br.
		25	1110	-	1102	δO13H, δO11H, νBen. def., νC5O13
		24	1160	-	1179	δC3H, δC4H, δO13H, -δO11H
		23	1182	1179	1179	δC7H, δN1H, δO13H
		22	1196	1179	1179	δO14H, δC7H, δO13H
		21	1234	1236	1236	δO14H, δC4H, δO11H
		20	1269	1236	1236	δC4H, δC7H
		19	1287	1245	1245	δC3H, δN1H
		18	1325	-	-	δO11H, νBen. br., -νPyr. br.
		17	1376	-	-	δN1H, δO13H, δO14H, -δC4H, -δC7H, -δO11H
		16	1391	-	-	νBen. br., νC9C3, νN1C8, δO14H
		15	1435	-	-	νSkel. def, νN1C2, -νC6C5, νC9C8
		14	1452	-	-	νBen. def, νPyr. br., δC7H, -δN1H
		13	1513	-	-	νSkel. def., δC4H, -δN1H, -δC7H, νC4C5
		12	1563	-	-	νSkel. def., δC4H, δN1H, -δC7H, νC4C9
		11	1575	-	-	νSkel. def., δC3H, νC3C2, νC10O12
		10	1639	-	-	νSkel. def., δN1H, νC5C6, νC9C8
		9	1688	-	-	νSkel. def., νC2C10, νC10O12, δO11H
		8	1693	-	-	νSkel. def., νC4C5, νC7C8, νC10O12
		7	3197	-	-	νC4H
		6	3237	-	-	νC7H
		5	3297	-	-	νC3H
		4	3618	-	-	νO14H
		3	3628	-	-	νO11H
		2	3674	-	-	νN1H

Continued on next page

Table 11.10 – continued from previous page

A”		A’		Obs (cm^{-1})	Final Freq (cm^{-1})	Description
ν	G98 (cm^{-1})	ν	G98 (cm^{-1})			
		1	3712	-	-	νO13H

11.6 Chapter conclusions

The inelastic neutron scattering spectra of ICA and DHICA powders have been compared to their spectra derived from *ab-initio* calculations. These formed the basis for the detailed assignment schemes given in tables 11.8 and 11.10 . The careful and reliable assignment of these vibrational spectra forms a solid basis for study of the vibrational properties of the eumelanin macromolecule. Further work is underway with the objective of understanding non-radiative decay pathways in model eumelanin components, particularly melanin dimers and larger oligomers.

12
Future research directions

There still remain many unknowns concerning the melanin system, and many possible experiments that could shed light on its function and properties. We have already mentioned several pertinent specific experiments in earlier chapters, including:

- Further use of high resolution transmission electron microscopy for structural measurements of melanins from various sources (section 3.4.4). This is discussed in more detail below.

- Determination of the particle size distribution for melanin solutions of the type used for spectroscopic analysis throughout this thesis via dynamic light scattering or other methods (section 4.5.1). This is also discussed in more detail below.

- Investigation of the origin of the unexpectedly large deviation between density functional theory calculated dipole strengths and measured dipole strengths (section 5.5.3).

- Determination of the reason for the increase in radiative quantum yield as cysteinyldopa polymerises (section 8.4.4). Spectroscopic observation of the polymerisation process from monomer units to the macromolecule and an analysis of the dipole strength during this process (like those presented in chapters 10 and 5 for eumelanin respectively) may be extremely informative.

- Investigation of the effects of the solvent upon the spectroscopic properties of DHICA. Particularly, accurate characterisation and understanding of the effects of pH, and investigation of the possibility of the formation of a complex between the DHICA catecholate groups and the borax buffer, inhibiting polymerisation (section 9.4.1). The measurement of a full fluorescence map for DHICA similar to that in chapter 7 (for eumelanin) for a variety of pHs and solvents would be extremely beneficial (section 9.4.4).

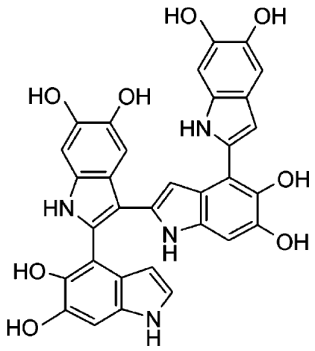

FIGURE 12.1: The first isolated tetramer of DHI (from [36]).

- Measurement of the inelastic neutron scattering spectrum of deuterated DHICA for accurate assignment of the vibrational peaks of DHICA (section 11.4.3).

Beyond these specific experiments, we aim in this chapter to describe in broader terms a few approaches to this system that we believe may be most fruitful in the near future, in the light of the ideas and discussions presented in this thesis.

12.1 Isolation and characterisation of oligomers

As described in chapter 3, an absolutely essential contribution to our understanding of the structure of eumelanin has come from an organic chemistry approach, isolating and synthesising the dimers and trimers that are naturally formed from the eumelanin monomers. This work has allowed identification of the most likely covalent binding sites of DHI and DHICA, and given substantial clues as to the way in which polymerisation occurs in this system. This work, conducted largely by the melanin group at Naples, continues to be massively important. For instance, they very recently published an article reporting the isolation of an eumelanin tetramer for the first time [36]. The tetramer structure, shown in figure 12.1 reveals a previously unseen 2,3' binding between monomers, which should now be included in our considerations of the possible structures that eumelanin might take. We believe that this organic chemistry approach will continue to be extremely fruitful, and should be continued with vigour.

The yields of the DHI and DHICA dimers and larger oligomers obtained from these studies are currently extremely low, and prohibit extensive investigation of their properties. This is unfortunate, since we believe that spectroscopic analysis of these species would be extremely helpful for comparison to quantum chemical analysis, and would lead ultimately to an understanding of the spectroscopic features of eumelanin. We hope that in future it may be possible to isolate larger quantities of these species for extensive quantum chemical and spectroscopic analysis, to understand their de-excitation pathways and contributions to eumelanin photobehaviour.

The work reported in chapter 9 of this thesis on the DHICA molecule highlights how powerful a combined spectroscopic and quantum chemical approach can be for a well defined system. Our research efforts continue in this vein, since by first understanding the

properties of this simple system in detail, we can begin to understand the properties of the larger eumelanin system. Over time, improvements in computational methods will allow for more accurate modelling of larger systems, and methods will be developed to isolate larger quantities of the experimental samples of interest. We look forward to the advances that this combined approach will bring.

12.2 Comparison with other model compounds

Most biological molecules rely on extreme order for functionality; a change in a single base in a DNA molecule can completely destroy its functionality, and similarly for proteins. Melanins, on the other hand, rely on extreme chemical disorder for biofunctionality, and appear to be somewhat unique in this regard. This makes the study of melanin challenging, since the disorder makes characterisation problematic, and methods that have been well developed for proteins cannot be easily applied.

It was suggested some time ago, however, that we should consider looking to non-biological systems for novel approaches to melanins. Zeise et al. suggested in 1992 that carbon black particles might be an excellent model system, since they have many similar properties to melanins, and have been well studied due to their commercial importance [122]. This, and several other systems that appear to have qualities similar to melanins might provide substantial inspiration and are outlined below.

12.2.1 Humic substances

Humic substances are the dark organic materials that result from the decay of plant and animal matter. They are highly disordered, and exhibit the following spectroscopic features:

- A broadband absorption spectrum that increases exponentially towards UV wavelengths [333], identical to melanins.
- A broad and featureless emission spectrum that decreases in intensity and shifts continuously to the red with decreasing excitation energy [334], very similar to melanins.
- The radiative quantum yield is dependant upon the excitation wavelength in a complex manner [333], similar to melanins (although melanins exhibit a different spectral shape in the radiative yield).
- The excitation spectrum has a complex emission wavelength dependance that is unlike the absorption spectrum [335], similar to melanins (although melanins exhibit a different spectral shape).

Although humic substances are biological in origin, they are not biologically functional in the same way that melanins are (being mostly waste matter). This makes the similarity between melanins and humic substances somewhat surprising. Nevertheless, we believe that the similarities between these two systems makes it worth keeping a close eye on the literature concerning humic substances for new theories, ideas and approaches.

As for melanins, the broadband absorbance of humic substances remains unexplained, although it has long been assumed to be due to chemical heterogeneity (as is proposed for melanins in the chemical disorder model). Interestingly, a recent paper by Del Vecchio and Blough reports laser photobleaching experiments that suggest that a linear superposition of absorption spectra from chemical disorder may not be sufficient to explain the broadband absorption spectrum of humic substances [336]. They propose instead that the broadband absorbance is due to a continuum of coupled states resulting from intramolecular charge-transfer interactions, and hypothesise that this model is likely to also apply to melanins. This is a fascinating proposal and certainly deserves further investigation. For this reason, the application of hole burning techniques to melanins is discussed below.

12.2.2 Soots, carbon black and amorphous carbon

Soots and carbon black are the black carbonaceous byproducts obtained from the combustion of fossil fuels. Soots are thought to be co-responsible for global warming processes (since they strongly absorb UV and visible light in the atmosphere), and have therefore been the topic of considerable interest in recent years. A great deal of recent research aims to characterise the particles produced and their spectroscopic properties, and it seems that soots, consisting mostly of carbon and hydrogen in a strongly disordered graphitic structure [337], are extremely similar to melanins in many ways.

High resolution transmission electron microscope (HRTEM) images of soot particles appear to be remarkably similar to those of melanin particles. A fundamental crystallite unit is commonly identified, consisting of 5-10 sheets of carbon atoms with an external size of 2 - 3 nm, very similar to the structures identified for melanins [338–340]. Typical HRTEM images of soot particles are shown in figure 12.2 for comparison with those of melanin in figures 3.15 and 3.16 [341]. Note that both form graphitic sheets and onion-like structures [342, 343]. The formation of these structures in soot is known to be strongly temperature dependant (higher temperatures produce more ordered structures with lower curvature), and it is fascinating to consider what equivalent processes might dictate structure at this level in melanins. HRTEM has been so useful for the analysis of structure in these systems that we have included it below as a technique that should be applied much more extensively to our system.

Studies on carbon blacks have shown direct links between nanostructure and optical properties. $\sigma - \sigma^*$ transitions are known to occur in the far UV, between 60 and 100 nm, whereas $\pi - \pi^*$ transitions occur in the range 180 to 260 nm [344]. This lower energy band has been shown to disappear for sp^3/sp^2 ratios less than 1, because the $\pi - \pi^*$ band is lost in the slope of the much more intense $\sigma - \sigma^*$ transition; this may suggest that melanins have very low sp^3 character (since we have not observed a $\pi - \pi^*$ peak in UV/visible absorption spectra) [345]. The position of the lower energy band is also extremely sensitive to nanostructural changes [346, 347]; for example, the graphitization process (heating to produce ordered lattice planes) redshifts the absorption peak by 220 nm [348, 349], and the width of the $\pi - \pi^*$ transition is known to be strongly affected by the state of agglomeration [350, 351]. Secondary structure also significantly affects the complex refractive index of soot particles [349, 352]. These features strongly suggest that detailed spectroscopic analysis can be a

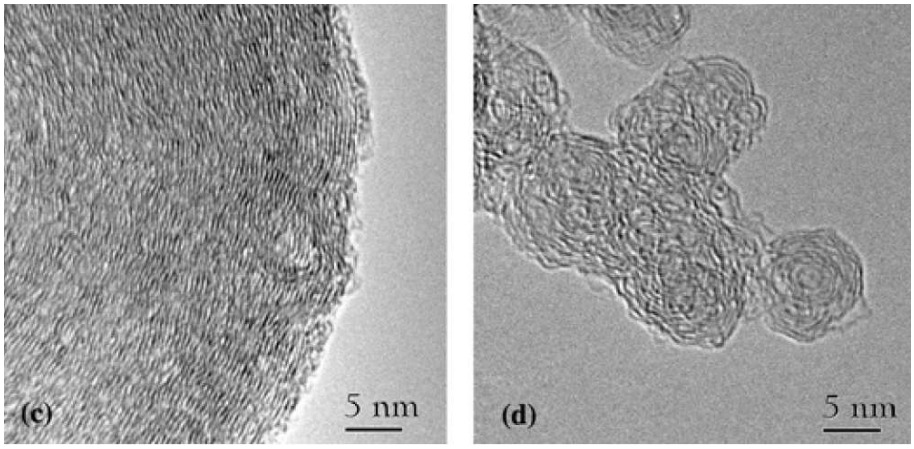

(a) Soots derived from acetylene

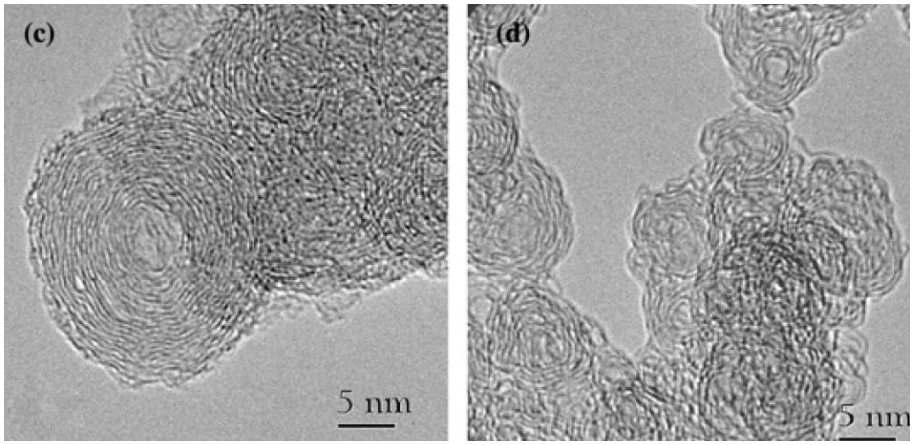

(b) Soots derived from ethanol

Figure 12.2: HRTEM images of soot particles formed at 1650°C (from [341]).

powerful non-invasive probe of structure in these systems, and empahsise the importance of accurately characterising the structure of melanin for interpretation of UV/visible spectra.

The way in which the nanoscale structure of soot particles influences other properties has also been a topic of interest, including investigations of their electrical properties and water adsorbability [337]. New techniques are constantly being developed and applied to these carbon based systems; for example the near edge X-ray absorption fine structure (NEXAFS) spectrum of soot particles has recently been characterised, giving important microstructural details such as the degree of graphitization [349, 353]. Electron energy loss spectroscopy (EELS) has also been an extremely important technique for investigating the relative amounts of sp^2 and sp^3 carbon hybridisation in soots for quantitative structural analysis [345, 354].

Given the similarities of these systems to melanins, and the rapidly growing interest in environmental monitoring and the impacts of pollution, we believe that the ongoing research in this field will have a lot to offer melanin scientists.

12.2.3 Disordered polymers

We believe that polymer science could be extremely useful when applied to melanins. Polymer chemists are skilled at dealing with disordered systems with a wide range of molecular weights, and have developed methods and a nomenclature for characterising and describing systems in terms of statistical averages, rather than strictly defined structures. Methods such as solid state NMR, Raman scattering, infrared spectroscopy, X-ray diffraction, TEM and dynamic light scattering have all been applied to a wide variety of disordered organic polymer systems with great success [355, 356]. Of these, we discuss dynamic light scattering below, since we believe this has not been yet been applied to the melanin system. Polymer scientists also continue to develop theoretical microstructural models for disordered systems, and these could provide a wealth of inspiration for ways of modelling the melanin system [357]. For these reasons, we propose that collaboration with polymer scientists with experience working on disordered organic polymers could be extremely productive.

12.3 Application of specific methods

An analysis of the literature regarding the model systems described above has highlighted several experimental methods that might be successfully applied to melanins. We outline these briefly in this section.

12.3.1 High resolution transmission electron microscopy (HRTEM)

HRTEM has become the preferred method for characterising the nanostructure of carbonaceous materials because it is easy to interpret, and is so sensitive to subtle differences in structure [341]. It has been extremely successfully applied to the analysis of soot particles, and other carbonaceous materials and we believe that the initial meaurements made by our group only begin to show how useful this technique will be for the analysis of nanoscale structure in melanins.

12.3.2 Dynamic light scattering

Dynamic light scattering is a powerful method that is commonly used for measuring particle sizes in colloidal solutions. In this method, a beam of light is scattered from the solution. The intensity of the scattering varies over short time scales due to Brownian motion of the particles (which is strongly dependant upon particle size). The time that it takes a particle to traverse the beam can be detected via the change in the scattering signal and the size of that particle therefore determined [358]. We did attempt to apply dynamic light scattering to melanin solutions through the course of our research but were hindered by the fact that the particles appeared to be too small and weakly scattering to give sufficient signal. However, the massive usefulness of this method to polymer scientists and biologists means that there are continual improvements in the technology, and the latest instruments are now reaching the sensitivities required for measuring particles of the size thought to be present in melanin

solutions [358, 359]. This may be another method that can be used for characterising our system conveniently, rapidly and non-invasively under various conditions.

12.3.3 Hole burning spectroscopy

Hole burning spectroscopy has been extremely useful for examining the electronic absorption and de-excitation processes of many important materials and biomolecules, including various polymers [360–362] and the photosynthetic complexes [363]. The method involves exciting the sample of interest with intense monochromatic light (with a very narrow spectral width) to deplete the electronic ground state. The sample is then probed (either in absorbance or emission) to observe the remaining spectral hole. The natural spectral width of a chemical species is subject to many forms of inhomogeneous broadening (spectral broadening due to the fact that each chemical species is in a slightly different environment). Hole burning spectroscopy allows probing of the homogenous line width and other properties of a single species within the distribution [364]. There are many variations on this broad type of experiment, including persistent spectral hole burning, transient spectral hole burning (pump probe, or single laser), fluorescence line narrowing and photobleaching [365].

Our interest in this technique stems from the fact that it has been applied to humic substances, with the results suggesting that the chemical disorder model is not sufficient to explain the broadband absorbance spectrum [336]. The authors used a laser to selectively destroy species absorbing at specific wavelengths, and used absorption spectroscopy to follow the photobleaching. They observed a variety of interesting features that were inconsistent with the chemical disorder model including a high energy absorption band centered at 300 nm for all species in solution, and absorption losses only within a broad hole near the irradiation wavelength for short irradiation times. These intriguing results suggest that photobleaching and/or hole burning spectroscopy could be an excellent probe of the chemical disorder model for melanins. We propose that an extensive hole burning study of melanins could provide genuine confirmation of the chemical disorder model.

12.4 Chapter conclusions

There are many interesting experiments that could be conducted for melanins, and we have outlined in this chapter several that we believe might be most fruitful. The best approach is likely to be a thorough investigation of literature concerning soots, carbon blacks, amorphous carbon, and humic substances for an analysis of the methods and theories that have made the most progress towards understanding these systems. Transmission electron microscopy, dynamic light scattering and spectral hole burning are several techniques that appear to show particular promise for melanins.

13
Conclusions

Explaining the broadband absorbance of melanin

Melanins are a fascinating biological material with many interesting macroscopic properties that remain thus far unexplained, despite substantial research efforts. They have a broadband absorbance spectrum that is atypical for an organic chromophore, the explanation of which remains one of the most important questions facing the melanin research community. In chapter 2 we discussed three possible explanations for this broadband absorption spectrum that have been proposed in the literature. The first of these is that the broadband spectrum is due to scattering rather than electronic absorbance. We have successfully eliminated this option through a careful measurement of the integrated scattering from a solution of eumelanin, as presented in chapter 4. This showed that the scattering intensity is negligible and that the majority of the optical density of eumelanin solutions is due to true electronic absorbance. This result also has very significant implications for the spectroscopy of eumelanin, since it allows the uninhibited measurement of properties such as the radiative quantum yield (the contribution of scattering to this measurement was previously a serious concern).

A second explanation for the broadband absorbance spectrum of melanin that has perpetuated for decades is the amorphous semiconductor model. In this model, eumelanin is an amorphous semiconductor that has an electronic band structure which gives rise to a broadband absorption spectrum. A review of the literature concerning the structure of eumelanin (chapter 3) reveals that eumelanin consists of a highly heterogeneous collection of small oligomeric species. As discussed in section 2.3, organic semiconductors are typically either large polymers, or relatively structurally homogeneous small oligomers. This casts doubt upon the amorphous semiconductor model for eumelanin, although we cannot definitively eliminate this model based upon the evidence currently available.

The data presented in this thesis is most consistent with the chemical disorder model, the

third and final explanation of the broadband absorption spectrum. In this model, broadband absorbance is due to the superposition of the peaked absorption spectra of many chemically distinct species. Detailed spectroscopic analysis of eumelanin, reported in chapters 6 and 7, reveals a variety of features that are atypical for an organic chromophore, including

- violation of the mirror image rule,
- violation of Kasha's rule (excitation energy dependance in the shape of the emission spectrum), and
- excitation energy dependance in the radiative quantum yield.

All of these features are logically explained by the chemical disorder model. We propose that hole burning experiments may provide definitive evidence for the chemical disorder model and should be conducted as future research (as discussed in chapter 12).

Through our investigation of the literature concerning the molecular structure of eumelanin (reported in chapter 3) we have come to appreciate that the structure of eumelanin is poorly defined. This hinders almost all analysis on this system and makes modelling extremely challenging. We emphasise that the 'stacked protomolecule' structural model of eumelanins has become accepted as dogma in some cases, but the original experiments upon which this model was based were not definitive. Further confirmation of this model should be sought before it is accepted, and the degree of chemical heterogeneity in this system should be included more rigorously in future structural models. The techniques and nomenclature used for the analysis of disordered polymers may be of significant use in this endeavour. Additionally, transmission electron microscope (TEM) images of eumelanin suggest that this technique shows great promise for the investigation of the structure of melanins.

We have measured the transition dipole strength of eumelanin and shown that it is not exceptionally large (as might be expected of a photoprotectant), but is, in fact, typical of an organic chromophore (chapter 5). We have also shown that *ab-initio* density functional theory calculations can predict trends in the transition dipole strength, although we discover an unexpectedly large quantitative deviation from experimental values. This fascinating finding is believed to be related to the system under study, rather than to the computational technique, and warrants further investigation. The per-monomer dipole strength has been shown to increase slightly upon polymerisation from DHICA into the eumelanin macromolecule, with the magnitude of hyperchromism being typical of an organic macromolecule. Most significantly, the small magnitude of the increase is consistent with the chemical disorder model.

In summary, of the three explanations of the broadband absorbance spectrum of eumelanin discussed in this thesis, the chemical disorder model is supported by all experimental evidence and appears to be the most likely.

Energy dissipation in melanins

In the second half of this thesis we reported a detailed study of the dissipation process that occur in melanins, with a particular focus on radiative dissipation. Previous measurements

of the spectroscopic properties of eumelanin (such as emission and excitation spectra) have shown a great lack in consistency due to a variety of effects. Two of the most significant of these are re-absorption and inner filter effects. We presented in chapter 6 a method to correct for these, and showed that it is highly effective. This method has been applied to perform the most accurate and detailed characterisation of the spectroscopic properties of eumelanin to date, including

- emission spectra for a variety of excitation wavelengths,
- excitation spectra for a variety of emission wavelengths,
- the radiative quantum yield as a function of excitation wavelength,
- a UV/visible fluorescence map, and
- a UV/visible specific radiative quantum yield map

(as presented in chapters 6 and 7). We recommend that all future spectroscopic studies on melanins utilize this method. Significantly, we have used it to make the first accurate measurement of the radiative yield of eumelanin showing it to be extremely low ($< 0.1\%$), consistent with the pigment's role as a photoprotectant.

Additionally, we reported in chapter 8 a detailed characterisation of the spectroscopic properties of pheomelanin. Pheomelanin was discovered to exhibit a dual peaked emission spectrum (as opposed to the single emission peak observed for eumelanin), and was found to have a radiative yield of $\sim 0.2\%$, double that of eumelanin. As a significant biomolecule that is closely related to melanoma skin cancer, pheomelanin warrants further investigation, and we have shown that spectroscopic methods provide a sensitive probe for this purpose.

Spectroscopic analysis of the key eumelanin monomer 5,6-dihydroxyindole-2-carboxylic acid (DHICA), reported in chapter 9, showed that it is a well behaved organic chromophore with a typical extinction coefficient, emission and excitation spectra and radiative quantum yield. The radiative yield was revealed to be much larger than that of eumelanin, being $\sim 60\%$. Violation of the mirror image rule was discovered by the presence of a shoulder in the absorption spectrum that is absent in the emission spectrum. This was investigated via highly sophisticated quantum chemical calculations which suggest that DHICA may undergo convergent adiabatic and nonadiabatic excited-state intramolecular proton-transfer (ESIPT) processes. This has the interesting implication that proton-transfer processes may be involved in energy dissipation in eumelanin. Spectroscopic observation of the formation of eumelanin from DHICA suggests that the emission spectrum can be used as an effective probe of the concentration of DHICA remaining in solution (chapter 10). Additionally, emission and excitation spectra suggest that all the oligomeric species formed from DHICA have substantially lower radiative quantum yields than the monomer.

Finally, in chapter 11 we reported preliminary research into the non-radiative dissipation processes in eumelanin. We conducted the first inelastic neutron scattering (INS) study of eumelanin precursors, measuring the INS spectrum of indole-2-carboxylic acid (ICA) and DHICA. The peaks in these spectra were assigned to vibrational modes calculated using *ab-initio* density functional theory based upon our previous assignment of the INS spectrum

of indole and other published vibrational spectra (infra-red and Raman). This study forms a careful foundation for analysis of the vibrational properties of eumelanin in later studies.

The work reported in this thesis forms the essential and critical first steps towards understanding the energy processes in melanin. We believe we have conducted an accurate, quantitative, careful and thoughtful foundation on which we can build extremely sophisticated analyses of this fascinating system.

References

[1] P. A. Riley. *Melanin.* International journal of biochemistry and cell biology **29(11)**, 1235 (1997).

[2] G. A. Swan. *Structure, chemistry and biosynthesis of the melanins.* In *Progress in the Chemistry of organic natural products* (Springer-Verlag, New York, 1974).

[3] G. Prota. *Melanins and Melanogenesis* (Academic Press, San Diego, 1992).

[4] N. Kollias, R. M. Sayer, L. Zeise, and M. R. Chedekel. *Photoprotection by melanin.* Journal of Photochemistry and Photobiology B Biol **9**, 135 (1991).

[5] V. J. Hearing. *Biochemical control of melanogenesis and melanosomal organization.* Journal of Investigative Dermatology **4**, 25 (1999).

[6] V. J. Hearing. *The regulation of melanin production.* In J. J. Norlund, R. E. Boissy, and V. J. Hearing, eds., *The Pigmentary System: Physiology and Pathophysiology*, pp. 423–38 (Oxford University Press, New York, 1998).

[7] T. B. Fitzpatrick, A. Z. Eisen, K. Wolf, I. M. Freeberg, and K. F. Austen. *Biology of Melanocytes* (McGraw-Hill Book Co., Sydney, 1987), 3rd ed.

[8] Y. M. Chen and W. Chavin. *Radiometric assay of tyrosinase and theoretical considerations of melanin formation.* Analytical Biochemistry **13**, 234 (1965).

[9] M. D'Ischia and G. Prota. *Biosynthesis, structure, and function of neuromelanin and its relation to parkinson's disease: A critical update.* Pigment Cell Research **10**, 370 (1997).

[10] B. J. R. Nicolaus. *A critical review of the function of neuromelanin and an attempt to provide a unified theory.* Medical Hypotheses **65**, 791 (2005).

[11] R. Anderson and J. Parrish. *The optics of human skin.* Journal of Investigative Dermatology **77(1)**, 13 (1981).

[12] M. Doi and S. Tominaga. *Spectral estimation of human skin color using the kubelka-munk theory.* SPIE/IS&T Electronic Imaging **5008**, 221 (2003).

[13] V. Basrur, F. Yang, T. Kushimoto, Y. Higashimoto, K. ichi Yasumoto, J. Valencia, J. Muller, W. D. Vieira, H. Watabe, J. Shabanowitz, V. J. Hearing, D. F. Hunt,

and E. Appella. *Proteomic analysis of early melanosomes: Identification of novel melanosomal proteins*. Journal of Proteome Research **2**, 69 (2003).

[14] J. L. Bolognia, J. L. Jorizzo, and R. P. Rapini. *Dermatology* (Mosby, Sydney, 2003).

[15] R. A. Nicolaus. *Melanins* (Hermann, Paris, 1968).

[16] L. Zeise, M. Chedekel, and T. Fitzpatrick. *Is melanin photoprotective or photosensitising?* (Vladenmar Press, Overland Park, KS, 1995).

[17] J. Nofsinger, S. Forest, and J. Simon. *Explanation for the disparity among absorption and action spectra of eumelanin*. Journal of Physical Chemistry B. **103**, 11428 (1999).

[18] I. Menon and H. Haberman. *Mechanisms of action of melanins*. British Journal of Dermatology **97**, 109 (1997).

[19] J. Y. Lin and D. E. Fisher. *Melanocyte biology and skin pigmentation*. Nature **445**, 843 (2007).

[20] C. Kennedy, J. ter Huurne, M. Berkhout, N. Gruis, M. Bastiaens, W. Bergman, R. Willemze, and J. N. B. Bavinck. *Melanocortin 1 receptor (mc1r) gene variants are associated with an increased risk for cutaneous melanoma which is largely independent of skin type and hair color*. Journal of Investigative Dermatology **117**, 294 (2001).

[21] M. C. Scott, K. Wakamatsu, S. Ito, A. L. Kadekaro, N. Kobayashi, J. Groden, R. Kavanagh, T. Takakuwa, V. Virador, V. J. Hearing, and Z. A. Abdel-Malek. *Human melanocortin 1 receptor variants, receptor function and melanocyte response to UV radiation*. Journal of Cell Science **115**, 2349 (2002).

[22] E. Wenczl, G. P. V. der Schans, L. Roza, R. M. Kolb, A. J. Timmerman, N. P. Smit, S. Pavel, and A. A. Schothorst. *(Pheo)melanin photosensitizes UVA-induced DNA damage in cultured human melanocytes*. Journal of Investigative Dermatology **111**, 678 (1998).

[23] L. A. G. Ries, D. Melbert, M. Krapcho, A. Mariotto, B. A. Miller, E. J. Feuer, L. Clegg, M. J. Horner, N. Howlader, M. P. Eisner, M. Reichman, and B. K. Edwards. *SEER cancer statistics review, 1975-2004*. National Cancer Institute (2006).

[24] R. Lucas. *Global burden of disease of solar ultraviolet radiation, environmental burden of disease series*. News release, World Health Organization **13** (2006).

[25] G. Prota, M. D'Ischia, and A. Napolitano. *The chemistry of melanins and related metabolites*. In J. J. Norlund, R. E. Boissy, V. J. Hearing, R. A. King, and J. P. Ortonne, eds., *The Pigmentary System: Its physiology and Pathophysiology*, chap. 24, pp. 307–332 (Oxford University Press, New York, 1998).

[26] H. Xie, S. Vucetic, L. I. C. J. Oldfield, A. K. D. Z. Obradovic, and V. N. Uversky. *Functional anthology of intrinsic disorder. 3. Ligands, post-translational modifications, and diseases associated with intrinsically disordered proteins.* Journal of Proteome Research **6(5)**, 1917 (2007).

[27] K. Shimizu, Y. Muraoka, S. Hirose, K. Tomii, and T. Noguchi. *Predicting mostly disordered proteins by using structure-unknown protein data.* BMC Bioinformatics **8**, 78 (2007).

[28] A. Loettgers. *Getting abstract mathematical models in touch with nature.* Science in Context **20(1)**, 97 (2007).

[29] M. G. Bridelli, A. Ciati, and P. R. Crippa. *Binding of chemicals to melanins re-examined: Adsorption of some drugs to the surface of melanin particles.* Biophysical Chemistry **119**, 137 (2006).

[30] L. Hong, Y. Liu, and J. D. Simon. *Binding of metal ions to melanin and their effects on the aerobic reactivity.* Photochemistry and Photobiology **80**, 477 (2004).

[31] A. Samokhvalov, Y. Liu, and J. D. Simon. *Characterization of the Fe(III)-binding site in Sepia eumelanin by resonance Raman confocal microspectroscopy.* Photochemistry and Photobiology **80**, 84 (2004).

[32] B. S. Larsson. *Interaction between chemicals and melanin.* Pigment Cell Research **6**, 127 (1993).

[33] P. Meredith and T. Sarna. *The physical and chemical properties of eumelanin.* Pigment Cell Research **19(6)**, 572 (2006).

[34] B. Mostert. *Humidity dependence of charge transport in melanin.* B. Sc. (Hons.) Thesis, University of Queensland (2006).

[35] P. Meredith, B. J. Powell, J. Riesz, R. Vogel, D. Blake, S. Subianto, G. Will, and I. Kartini. *Broad band photon-harvesting biomolecules for photovoltaics.* In A. Collings and C. Critchley, eds., *Artificial Photosynthesis: From Basic Biology to Industrial Application*, chap. 3, p. 37 (2005).

[36] L. Panzella, A. Pezzella, A. Napolitano, and M. d'Ischia. *The first 5,6-dihydroxyindole tetramer by oxidation of 5,5',6,6'-tetrahydroxy-2,4'-biindolyl and an unexpected issue of positional reactivity en route to eumelanin-related polymers.* Organic Letters **9(7)**, 1411 (2007).

[37] H. S. Raper. *The tyrosinase-tyrosine reaction. VI. production from tyrosine of 5,6-dihydroxyindole and 5,6-dihydroxyindole-2-carboxylic acid - the precursors of melanin.* Journal of Biochemistry **21**, 89 (1927).

[38] H. S. Raper. *The aerobic oxidases.* Physiology Reviews **8**, 245 (1928).

[39] S. Ito. *A chemist's view of melanogenesis.* Pigment Cell Research **16(3)**, 230 (2003).

[40] A. Pezzella, M. D'Ischia, A. Napolitano, A. Palumbo, and G. Prota. *An integrated approach to the structure of sepia melanin. Evidence for a high proportion of degraded 5,6-dihydroxyindole-2-carboxylic acid units in the pigment backbone.* Tetrahedron **153**, 8281 (1997).

[41] S. Ito. *Re-examination of the structure of eumelanin.* Biochimica Biophysica Acta **883**, 155 (1986).

[42] Y. Liu, V. R. Kempf, J. B. Nofsinger, E. E. Weinert, M. Rudnicki, K. Wakamatsu, S. Ito, and J. D. Simon. *Comparison of the structural and physical properties of human hair eumelanin following enzymatic or acid/base extraction.* Pigment Cell Research **16**, 355 (2003).

[43] G. Prota. *Progress in the chemistry of melanins and related metabolites.* Medical Research Reviews **8**, 525 (1988).

[44] M. d'Ischia, A. Napolitano, K. Tsiakas, and G. Prota. *New intermediates in the oxidative polymerisation of 5,6-dihydroxyindole to melanin promoted by the peroxidase/H_2O_2 system.* Tetrahedron **46**, 5789 (1990).

[45] J. Riesz, J. Gilmore, and P. Meredith. *Quantitative scattering of melanin solutions.* Biophysical Journal **90(11)**, 1 (2006).

[46] J. Riesz, J. Gilmore, R. H. McKenzie, B. J. Powell, M. R. Pederson, and P. Meredith. *The transition dipole strength of melanin.* Physical Review E **76**, 021915 (2007).

[47] P. Meredith and J. Riesz. *Radiative relaxation quantum yields for synthetic eumelanin.* Photochemistry and Photobiology **79(2)**, 211 (2004).

[48] S. Nighswander-Rempel, J. Riesz, J. Gilmore, and P. Meredith. *A quantum yield map for synthetic eumelanin.* The Journal of Chemical Physics. Also selected for the November 15 issue of Virtual Journal of Biological Physics Research **123**, 194901 (2005).

[49] J. Riesz, T. Sarna, and P. Meredith. *Radiative relaxation in synthetic pheomelanin.* Journal of Physical Chemistry B **110(28)**, 13985 (2005).

[50] S. Olsen, J. Riesz, I. Mahadevan, A. Coutts, J. P. Bothma, B. J. Powell, R. H. McKenzie, S. C. Smith, and P. Meredith. *Convergent proton-transfer photocycles violate mirror-image symmetry in a key melanin monomer.* Journal of the American Chemical Society **129 (21)**, 6672 (2007).

[51] G. A. Blackburn. *Hyperspectra remote sensing of plant pigments.* Journal of Experimental Botany **58(4)**, 855 (2007).

[52] A. Krishnaswamy and G. Baranoski. *A biologically-based spectral model of light interaction with human skin.* Eurographics **23(3)**, 331 (2004).

[53] P. Meredith, B. J. Powell, J. Riesz, S. Nighswander-Rempel, M. R. Pederson, and E. Moore. *Towards structure-property-function relationships for eumelanin.* Soft Matter **2**, 37 (2006).

[54] M. Wolbarsht, A. Walsh, and G. George. *Melanin, a unique biological absorber.* Applied Optics **20 (13)**, 2184 (1981).

[55] H. C. Longuet-Higgins. *On the origin of the free radical property of melanins.* Archives of Biochemistry and Biophysics **86**, 231 (1960).

[56] J. E. McGinness, P. Corry, and P. Proctor. *Amorphous semiconductor switching in melanins.* Science **183**, 853 (1974).

[57] M. M. Jastrzebska and T. Wilczok. *Thermoelectric effect in synthetic DOPA-melanin.* Studia Biophysica **122**, 39 (1987).

[58] W. Osak, T. Katarzyna, H. Czternastek, and J. Slawinski. *I-V characteristics and electrical conductivity of synthetic melanin.* Biopolymers **28**, 1885 (1989).

[59] M. M. Jastrzebska and T. Wilczok. *Electrical conductivity of synthetic DOPA-melanin polymer for different hydration states and temperatures.* Journal of Biomaterials Science, Polymer Edition **7**, 577 (1995).

[60] A. Pullman and B. Pullman. *The band structure of melanins.* Biochimica Biophysica Acta **54**, 384 (1961).

[61] D. Galvao and M. Caldas. *Polymerization of 5,6-indolequinone: A view into the band structure of melanins.* Journal of Chemical Physics **88(6)**, 4088 (1988).

[62] D. Galvao and M. Caldas. *Theoretical investigations of model polymers for eumelanins. I. Finite and infinite polymers.* Journal of Chemical Physics **92(4)**, 2630 (1990).

[63] D. Galvao and M. Caldas. *Theoretical investigations of model polymers for eumelanins. II. Isolated defects.* Journal of Chemical Physics **93(4)**, 2848 (1990).

[64] L. Bolivar-Marinez, D. Galvao, and M. Caldas. *Geometric and spectroscopic study of some molecules related to eumelanins. 1. monomers.* Journal of Physical Chemistry B. **103**, 2993 (1999).

[65] E. M. Trukhan, N. F. Perevoschikoff, and A. M. Ostrovski. *Investigation of the photoconductivity of the pigment epithelium of the eye.* Biofizika **15**, 1052 (1970).

[66] M. Powell and B. Rosenberg. *The nature of charge carriers in solvated biomacromolecules.* Bioenergetics **1**, 493 (1970).

[67] T. Strzelecka. *A band model for synthetic DOPA-melanin.* Physiological Chemical Physics **14**, 219 (1982).

[68] P. R. Crippa, V. Cristofoletti, and N. Romeo. *A band model for melanin deduced from optical absorption and photoconductivity measurements.* Biochimica et Biophysica Acta **583**, 164 (1978).

[69] V. P. Grishchuk, S. A. Davidenko, I. D. Zholner, A. B. Verbitskii, M. V. Kurik, and Y. P. Piryatinskii. *Optical absorption and luminescent properties of melanin films.* Technical Physics Letters **28**, 36 (2002).

[70] J. E. Albuquerque, C. Giacomantonio, A. G. White, and P. Meredith. *Determination of thermal and optical parameters of melanins by photopyroelectric spectroscopy.* Applied Physics Letters **87**, 061920 (2005).

[71] J. Albuquerque, C. Giacomantonio, A. White, and P. Meredith. *Study of optical properties of electropolymerised melanin films by photopyroelectric spectroscopy.* European Journal of Biophysics **35**, 190 (2006).

[72] B. Rosenberg. *Electrical conductivity of proteins II. Semiconduction in crystalline bovine hemoglobin.* The Journal of Chemical Physics **36(3)**, 816 (1962).

[73] K. Stark, J. Gallas, G. Zajac, M. Eisner, and J. Golab. *Spectroscopic study and simulation from recent structural models for eumelanin: I. Monomer, dimers.* Journal of Physical Chemistry B. **107**, 3061 (2003).

[74] K. Stark, J. Gallas, G. Zajac, M. Eisner, and J. Golab. *Spectroscopic study and simulation from recent structural models for eumelanin: II. Oligomers.* Journal of Physical Chemistry B. **107**, 11558 (2003).

[75] K. Bochenek and E. Gudowska-Nowak. *Electronic properties of random polymers: modelling optical spectra of melanins.* Chemical Physics Letters **373**, 523 (2003).

[76] M. L. Tran, B. J. Powell, and P. Meredith. *Chemical and structural disorder in eumelanins: A possible explanation for broadband absorbance.* Biophysical Journal **90**, 743 (2006).

[77] B. J. Powell. *5,6-dihydroxyindole-2-carboxylic acid: a first principles density functional study.* Chemical Physics Letters **204**, 111 (2005).

[78] B. J. Powell, T. Baruah, N. Bernstein, K. Brake, R. H. McKenzie, P. Meredith, and M. R. Pederson. *A first principles density-functional theory calculation of the electronic and vibrational structure of the key melanin monomers.* Journal of Chemical Physics **120(18)**, 8608 (2004).

[79] Y. Il'ichev and J. Simon. *Building blocks of eumelanin: Relative stability and excitation energies of tautomers of 5,6-dihydroxyindole and 5,6-indolequinone.* Journal of Physical Chemistry B **107**, 7162 (2003).

[80] K. Stark, J. Gallas, G. Zajac, J. Golab, S. Gidanian, T. McIntire, and P. Farmer. *Effect of stacking and redox state on optical absorption spectra of melanins - comparison of theoretical and experimental results.* Journal of Physical Chemistry B **109**, 1970 (2005).

[81] K. Bochenek and E. Gudowska-Nowak. *Electronic properties of random polymers: modelling optical spectra of melanins.* Acta Physica Polonica B **34(5)**, 2775 (2003).

[82] E. Kaxiras, A. Tsolakidis, G. Zonios, and S. Meng. *Structural model of eumelanin.* Physical Review Letters **97**, 218102 (2006).

[83] S. Ito and J. A. C. Nicol. *Isolation of oligomers of 5,6-dihydroxyindole-2-carboxylic acid from the eye of the catfish.* Biochemical Journal **143**, 207 (1974).

[84] R. Edge, M. D'Ischia, E. J. Land, A. Napolitano, S. Navaratnam, L. Panzella, A. Pezzella, C. A. Ramsden, and P. A. Riley. *Dopaquinone redox exchange with dihydroxyindole and dihydroxyindole carboxylic acid.* Pigment Cell Research **19**, 443 (2006).

[85] Y. Liu, L. Hong, K. Wakamatsu, S. Ito, B. Adhyaru, C. Cheng, C. Bowers, and J. Simon. *Comparison of structural and chemical properties of black and red human hair melanosomes.* Photochemistry and Photobiology **81**, 135 (2005).

[86] A. Slominski, D. J. Tobin, S. Shibahara, and J. Wortsman. *Melanin pigmentation in mammalian skin and its hormonal regulation.* Physiological Reviews **84**, 1155 (2004).

[87] S. Alaluf, A. Heath, N. Carter, D. Atkins, H. Mahalingam, K. Barrett, R. Kolb, and N. Smith. *Variation in melanin content and composition in type V and VI photoexposed and photoprotected human skin: The dominant role of dhi.* Pigment Cell Research **14**, 337 (2001).

[88] H. Nakagawa and G. Imokawa. *Characterisation of melanogenesis in normal human epidermal melanocytes by chemical and ultrastructural analysis.* Pigment Cell Research **9**, 175 (1996).

[89] S. Alaluf, D. Atkins, K. Barrett, M. Blount, N. Carter, and A. Heath. *Ethnic variation in melanin content and composition in photoexposed and photoprotected human skin.* Pigment Cell Research **15**, 112 (2002).

[90] L. Zeise, B. L. Murr, and M. R. Chedekel. *Melanin standard method: Particle description.* Pigment Cell Research **5**, 132 (1992).

[91] L. Zeise. *Analytical methods for characterization and identification of melanins.* In L. Zeise, M. Chedekel, and T. Fitzpatrick, eds., *Melanin: Its role in human photoprotection* (Vladenmar Publishing Company, Overland Park, KS, 1995).

[92] M. Seiji, T. B. Fitzpatrick, and R. T. Simpson. *Chemical composition and terminology of specialized organelles (melanosomes and melanin granules) in mammalian melanocytes.* Nature **197**, 1082 (1963).

[93] J. Duchon, J. Borovansky, and P. Hach. *Chemical composition of ten kinds of various melanosomes.* Pigment Cell Research **1**, 165 (1973).

[94] J. D. Simon and S. Ito. *The chemical structure of melanin.* Pigment Cell Research **17**, 422 (2004).

[95] K. E. van Holde, W. C. Johnson, and P. S. Ho. *Principles of Physical Biochemistry* (Prentic Hall, Upper Saddle River, New Jersey, 1998).

[96] M. D'Ischia, A. Napolitano, and G. Prota. *Oxidative polymerisation of 5,6-dihydroxyindoles. Tracking the biosynthetic pathway to melanin pigments.* Gazzetta Chimica Italiana **126**, 783 (1996).

[97] A. Napolitano, A. Pezzella, M. R. Vincensi, and G. Prota. *Oxidative degradation of melanins to pyrrole acids: a model study.* Tetrahedron **51(20)**, 5913 (1995).

[98] A. Pezzella, A. Napolitano, M. D'Ischia, and G. Prota. *Oxidative polymerisation of 5,6-dihydroxyindole-2-carboxylic acid to melanin: A new insight.* Tetrahedron **52(23)**, 7913 (1996).

[99] A. Pezzella, D. Vogna, and G. Prota. *Atropoisomeric melanin intermediates by oxidation of the melanogenic precursor 5,6-dihydroxyindole-2-carboxylic acid under biomimetic conditions.* Tetrahedron **58**, 3681 (2002).

[100] A. Pezzella, D. Vogna, and G. Prota. *Synthesis of optically active tetrameric melanin intermediates by oxidation of melanogenic precursor 5,6-dihydroxyindole-2-carboyxlic acid under biomimetic conditions.* Tetrahedron Asymmetry **14**, 1133 (2003).

[101] A. Pezzella, L. Panzella, O. Crescenzi, A. Napolitano, S. Navaratman, R. Edge, E. J. Land, V. Barone, and M. d'Ischia. *Short-lived quinoid species from 5,6-dihydroxyindole dimers en route to eumelanin polymers: Integrated chemical, pulse radiolytic and quantum mechanical investigation.* Journal of the American Chemical Society **128**, 15490 (2006).

[102] P. Reinheimer, J. Hirschinger, P. Granger, P. Breton, A. Lagrange, P. Gilard, M. A. Lefebvre, and N. Goetz. *Cross-polarization/magic-angle-spinning nuclear magnetic resonance in selectively ^{13}C-labeled synthetic eumelanins.* Biochimica et Biophysica Acta **1472**, 240 (1999).

[103] A. Napolitano, O. Crescenzi, and G. Prota. *Copolymerisation of 5,6-dihydroxyindole and 5,6-dihydroxyindole-2-carboxylic acid in melanogenesis: Isolation of a cross coupling product.* Tetrahedron Letters **34(5)**, 885 (1993).

[104] S. J. Orlow, M. P. Osber, and J. M. Pawelek. *Synthesis and characterisation of melanins from dihydroxyindole-2-carboxylic acid and dihydroxyindole.* Pigment Cell Research **5**, 113 (1992).

[105] A. Napolitano, A. Pulumbo, G. Misuraca, and G. Prota. *Inhibitory effect of melanin precursors on arachidonic acid peroxidation.* Biochimica et Biophysica Acta **1168**, 175 (1993).

[106] A. Napolitano, A. Pezzella, G. Prota, R. Seraglia, and P. Traldi. *A reassessment of the structure of 5,6-dihydroxyindole-2-carboxylic acid melanins by matrix-assisted laser desorption/ionization mass spectrometry.* Rapid Communications in Mass Spectrometry **10**, 204 (1996).

[107] A. Napolitano, A. Pezzella, and G. Prota. *Structural analysis of synthetic melanins from 5,6-dihydroxyindole by matrix-assisted laser desorption/ionization mass spectrometry.* Rapid Communications in Mass Spectrometry **10**, 468 (1996).

[108] A. Pezzella, A. Napolitano, M. d'Ischia, G. Prota, R. Seraglia, and P. Traldi. *Identification of partially degraded oligomers of 5,6-dihydroxyindole-2-carboxylic acid in sepia melanin by matrix-assisted laser desorption/ionization mass spectrometry.* Rapid Communications in Mass Spectrometry **11**, 368 (1997).

[109] A. Bertazzo, C. Costa, G. Allegri, R. Seraglia, and P. Traldi. *Biosynthesis of melanin from dopamine.* Rapid Communications in Mass Spectrometry **9**, 634 (1995).

[110] A. Bertazzo, C. Costa, G. Allegri, M. Schiavolin, D. Favretto, and P. Traldi. *Enzymatic oligomerization of tyrosine by tyrosine and peroxidase studied by matrix-assisted laser desorption/ionization mass spectrometry.* Rapid Communications in Mass Spectrometry **13**, 542 (1999).

[111] C. Costa, A. Bertazzo, G. Allegri, G. Toffano, O. Curcuruto, and P. Traldi. *Melanin biosynthesis from dopamine. II. A mass spectrometric and collisional spectroscopic investigation.* Pigment Cell Research **5**, 122 (1992).

[112] C. Kroesche and M. G. Peter. *Detection of melanochromes by MALDI-TOF mass spectrometry.* Tetrahedron **52**, 3947 (1996).

[113] M. G. Peter and H. Forster. *On the structure of eumelanins: Identification of constitutional patterns by solid-state NMR spectroscopy.* Angewandte Chemie, International Edition, English **28(6)**, 741 (1989).

[114] S. Aime, M. Fasano, and C. Croombridge. *Solid-state ^{13}C NMR characterization of melanin free acids from biosynthetic and natural melanins.* Gazzetta Chimica Italiana **120**, 663 (1990).

[115] G. A. Duff, J. E. Robers, and N. Foster. *Analysis of the structure of synthetic and natural melanins by solid-phase NMR.* Biochemistry **27**, 7112 (1988).

[116] M. Herve, J. Hirschinger, P. Granger, P. Gilard, and N. Goetz. *Quantitative analysis by ^{13}C solid-state NMR of eumelanins.* Journal De Chimie Physique **91**, 881 (1994).

[117] M. Herve, J. Hirschinger, P. Granger, P. Gilard, A. Deflandre, and N. Goetz. *A ^{13}C solid-state NMR study of the structure and auto-oxidation process of natural and synthetic melanins.* Biochimica et Biophysica Acta **1204**, 19 (1994).

[118] A. V. Golounin. *NMR study of the structure of the soluble fraction of natural melanin.* Russian Journal of Applied Chemistry **69(1)**, 103 (1996).

[119] A. R. Katritzky, N. G. Akhmedov, S. N. Denisenko, and O. V. Denisko. *^{1}H NMR spectroscopic characterization of solutions of Sepia melanin, Sepia melanin free acid and human hair melanin.* Pigment Cell Research **15**, 93 (2002).

[120] B. B. Adhyaru, N. G. Akhmedov, A. R. Katritzky, and C. R. Bowers. *Solid-state cross-polarization magic angle spinning ^{13}C and ^{15}N NMR characterisation of Sepia melanin, Sepia melanin free acid and human hair melanin in comparison with several model compounds.* Magnetic Resonance in Chemistry **41**, 466 (2003).

[121] S. E. Forest, W. C. Lam, D. P. Millar, J. B. Nofsinger, and J. D. Simon. *A model for the activated energy transfer within eumelanin aggregates.* Journal of Physical Chemistry B **104**, 811 (2000).

[122] L. Zeise, R. B. Addison, and M. R. Chedekel. *Bioanalytical studies of eumelanins. I. Characterisation of melanin the particle.* Pigment Cell Research Supplement **2**, 48 (1992).

[123] M. R. Chedekel, A. B. Ahene, and L. Zeise. *Melanin standard method: empirical formula 2.* Pigment Cell Research **5**, 240 (1992).

[124] A. Vitkin, J. Woolsey, B. C. Wilson, and R. R. Anderson. *Optical and thermal characterization of natural (sepia officinalis) melanin.* Photochemistry and Photobiology **59(4)**, 455 (1994).

[125] Y. Liu and J. D. Simon. *The effect of preparation procedures on the morphology of melanin from the ink sac of Sepia officinalis.* Pigment Cell Research **16**, 72 (2003).

[126] J. Nofsinger, S. Forest, L. Eibest, K. Gold, and J. Simon. *Probing the building blocks of eumelanins using scanning electron microscopy.* Pigment Cell Research **13**, 179 (2000).

[127] C. M. R. Clancy, J. B. Nofsinger, R. K. Hanks, and J. D. Simon. *A hierachical self-assembly of eumelanin.* Journal of Physical Chemistry B **104**, 7871 (2000).

[128] C. Clancy and J. Simon. *Ultrastructural organization of eumelanin from* Sepia officinalis *measured by atomic force microscopy.* Biochemistry **40**, 13353 (2001).

[129] Y. Liu and J. D. Simon. *Isolation and biophysical studies of natural eumelanins: applications of imaging technologies and ultrafast spectroscopy.* Pigment Cell Research **16**, 606 (2003).

[130] G. W. Zajac, J. M. Gallas, J. Cheng, M. Eisner, S. C. Moss, and A. E. Alvarado-Swaisgood. *The fundamental unit of synthetic melanin: a verification by tunneling microscopy of X-ray scattering results.* Biochimica et Biophysica Acta **1199**, 271 (1994).

[131] G. Zajac, J. Gallas, and A. Alvarado-Swaisgood. *Tunneling microscopy verification of an X-ray scattering-derived molecular model of tyrosine-based melanin.* Journal of Vacuum Science and Tecnology B **12(3)**, 1512 (1994).

[132] J. M. Gallas, K. C. Littrell, S. Seifert, G. W. Zajac, and P. Thiyagarajan. *Solution structure of copper ion-induced molecular aggregates of tyrosine melanin.* Biophysical Journal **77**, 1135 (1999).

[133] Y. Miyake, Y. Izumi, A. Tsutsumi, and K. Jimbow. *Structure and function of melanin 2: Chemico-physical properties of melanin III.* In Jimbow K (ed.) Sappora, Japan: Fuji-shoin Co. Ltd. pp. 3–18 (1985).

[134] Y. Miyake, Y. Izumi, K. Yasuda, and K. Jimbow. *Chemico-physical properties of melanin (II).* In K. Jimbow, ed., *Structure and Function of Melanin, 2*, pp. 3–10 (Fuji-shoin Co. Ltd., Sappora, Japan, 1985).

[135] Y. Miyake, Y. Izumi, A. Tsutsumi, and K. Jimbow. *Chemico-physical properties of melanin III.* In K. Jimbow, ed., *Structure and Function of Melanin, 3*, pp. 3–18 (Fuji-shoin Co. Ltd., Sappora, Japan, 1986).

[136] J. Cheng, S. C. Moss, M. Eisner, and P. Zschack. *X-ray characterization of melanins - I.* Pigment Cell Research **7**, 255 (1994).

[137] Y. Miyake, Y. Izumi, A. Tsutsumi, and K. Jimbow. *Chemico-physical properties of melanin IV.* In K. Jimbow, ed., *Structure and Function of Melanin, 4*, pp. 32–43 (Fuji-shoin Co. Ltd., Sappora, Japan, 1987).

[138] Y. Thathachari and M. Blois. *Physical studies on melanins II. X-ray diffraction.* Biophysical Journal **9**, 77 (1969).

[139] Y. Thathachari. *Structure of melanins.* Pigment Cell **1**, 158 (1973).

[140] Y. Miyake and Y. Izumi. *Chemico-physical properties of melanin.* In K. Jimbow, ed., *Structure and Function of Melanin, 1*, pp. 3–13 (Fuji-shoin Co. Ltd., Sappora, Japan, 1984).

[141] S. Chio. *X-ray diffraction and ESR studies on amorphous melanin.* Ph.D. thesis, University of Houston (1977).

[142] M. G. Bridelli, P. R. Crippa, and F. Ugozzoli. *X-ray diffraction studies on melanins in lyophylized melanosomes.* Pigment Cell Research **3**, 187 (1990).

[143] G. Albanese, M. G. Bridelli, and A. Deriu. *Structural dynamics of melanin investigated by Rayleigh scattering of messbauer radiation.* Biopolymers **23**, 1481 (1984).

[144] J. Cheng. *X-ray studies of amorphous melanins.* Ph.D. thesis, University of Houston (1992).

[145] J. Cheng, S. C. Moss, and M. Eisner. *X-ray characterization of melanins - II.* Pigment Cell Research **7**, 263 (1994).

[146] A. W. Moore. *Highly oriented pyrolytic graphite.* In P. L. Walker and P. A. Thrower, eds., *Chemistry and Physics of Carbon*, chap. 11, pp. 69–187 (Marcel Dekker Inc., New York, 1973).

[147] J. M. Gallas, G. W. Zajac, T. Sarna, and P. L. Stotter. *Structural differences in unbleached and mildly-bleached synthetic tyrosine-derived melanins identified by scanning probe microscopies*. Pigment Cell Research **13**, 99 (2000).

[148] K. Littrell, J. Gallas, G. Zajac, and P. Thiyagarajan. *Structural studies of bleached melanin by synchrotron small-angle X-ray scattering*. Photochemistry and Photobiology **77(2)**, 115 (2003).

[149] G. S. Lorite, V. R. Coluci, M. I. N. da Silva, S. N. Deziderio, C. F. O. Graeff, D. S. Galvao, and M. A. Cotta. *Synthetic melanin films: Assembly mechanisms, scaling behaviour, and structural properties*. Journal of Applied Physics **99**, 113511 (2006).

[150] C. C. Felix, J. S. Hyde, T. Sarna, and R. C. Sealy. *Interactions of melanin with metal ions. Electron spin resonance evidence for chelate complexes of metal ions with free radicals*. Journal of the American Chemical Society **100**, 3922 (1978).

[151] C. A. Hunger and K. M. Sanders. *The nature of $\pi - \pi$ interactions*. Journal of the American Chemical Society **112**, 5525 (1990).

[152] N. Roberston, S. Parsons, E. J. Maclean, R. A. Coxal, and A. R. Mount. *Preparation X-ray structure and properties of a hexabrominated, symmetric indole trimer and its tcnq adduct: a new route to functional molecular systems*. Journal of Materials Chemistry **10**, 2043 (2000).

[153] M. P. Waller, A. Robertazzi, J. A. Platts, D. E. Hibbs, and P. A. Williams. *Hybrid density functional theory for p-stacking interactions: application to benzenes, pyridines and DNA bases*. Journal of Computational Chemistry **27**, 491 (2006).

[154] M. Rzanowska, J. Jarvis-Evans, W. Korytowski, M. E. Boulton, J. M. Burke, and T. Sarna. *Blue light-induced reactivity of retinal age pigment - in vitro generation of oxygen-reactive species*. Journal of Biological Chemistry **270(32)**, 18825 (1995).

[155] M. G. Bridelli. *Self-assembly of melanin studied by laser light scattering*. Biophysical Chemistry **73**, 227 (1998).

[156] Y. Liu, L. Hong, V. R. Kempf, K. Wakamatsu, S. Ito, and J. D. Simon. *Ion-exchange and adsorption of Fe(III) by sepia melanin*. Pigment Cell Research **17**, 262 (2004).

[157] S. Bratosin. *Disassembly of melanosomes in detergents*. Journal of Investigative Dermatology **60(4)**, 224 (1973).

[158] R. C. Sealy, C. C. Felix, J. S. Hyde, and H. M. Swartz. *Structure and reactivity of melanins: influence of free radicals and metal ions*. In W. A. Pryor, ed., *Free radicals in biology*, pp. 209–259 (Academic Press, New York, 1980).

[159] J. S. Huang, J. Sung, M. Eisner, S. C. Moss, and J. Gallas. *The fractal structure and the dynamics of aggregation of synthetic melanin in low pH aqueous solutions*. Journal of Physical Chemistry **90(1)**, 25 (1989).

[160] P. R. Crippa, C. Giorcelli, and L. Zeise. *Determination of surface characteristics and fractal dimensions of natural and synthetic eumelanins from nitrogen adsorption isotherms.* Langmuir **19**, 348 (2003).

[161] J. Nofsinger and J. Simon. *Radiative relaxation of* Sepia *eumelanin is affected by aggregation.* Photochemistry and Photobiology **74(1)**, 31 (2001).

[162] S. Forest and J. Simon. *Wavelength-dependant photoacoustic calorimetry study of melanin.* Photochemistry and Photobiology **68(3)**, 296 (1998).

[163] J. Riesz, J. Gilmore, and P. Meredith. *Quantitative photoluminescence of broad band absorbing melanins: a procedure to correct for inner filter and re-absorption effects.* Spectrochimica Acta A **61(9)**, 2153 (2005).

[164] S. Nighswander-Rempel, J. Riesz, J. Gilmore, J. Bothma, and P. Meredith. *Quantitative fluorescence excitation spectra of synthetic eumelanin.* Journal of Physical Chemistry B **109(43)**, 20629 (2005).

[165] J. Krysciak. *Light scattering and absorption spectrum of alkaline melanin solutions.* Folia biologica (Krakow) **33(1-2)**, 49 (1985).

[166] S. Kurtz. *Light scattering calculations for melanin pigments from the Rayleigh to the Mie regime.* Journal of Investigative Dermatology **87(3)**, 400 (1986).

[167] D. Sardar, M. Mayo, and R. Glickman. *Optical characterisation of melanin.* Journal of Biomedical Optics **6(4)**, 404 (2001).

[168] E. Caiti, P. Crippa, and C. Viappiani. *Application of photoacoustic phase angle spectroscopy (ϕas) to eumelanins and pheomelanins.* Pigment Cell Research **6**, 140 (1993).

[169] A. Bricaud, A. Morel, and L. Prieur. *Optical efficiency factors of some phytoplankters.* Limnology and Oceanography **28(5)**, 816 (1983).

[170] N. Nelson and B. Prezelin. *Calibration of an integrating sphere for determining the absorption coefficient of scattering suspensions.* Applied Optics **32(33)**, 6710 (1993).

[171] H. Ou-Yang, G. Stamatas, and N. Kollias. *Spectral responses of melanin to ultraviolet A irradiation.* Journal of Investigative Dermatology **122**, 492 (2004).

[172] J. Nofsinger, T. Ye, and J. Simon. *Ultrafast nonradiative relaxation dynamics of eumelanin.* Journal of Physical Chemistry B **105**, 2864 (2001).

[173] J. Nofsinger, E. Weinert, and J. Simon. *Establishing structure-function relationships for eumelanin.* Biopolymers (Biospectroscopy) **67**, 302 (2002).

[174] J. Jackson. *Classical electrodynamics* (John Wiley and Sons, Inc., 1999), 3rd ed.

[175] S. Kurtz, S. Kozikowski, and L. Wolfram. *Optical constants of solid melanins determined from reflection measurements in the visible spectrum.* Journal of Investigative Dermatology **87**, 401 (1986).

[176] S. Kurtz, S. Kozikowski, and L. Wolfram. *Non-linear optical and electro-optical properties of biopolymers*, pp. 110–130 (Springer-Verlag, Berlin, 1986).

[177] R. Pope and E. Fry. *Absorption spectrum (380-700nm) of pure water. II. Integrating cavity measurements.* Applied Optics **36**, 8710 (1997).

[178] D. Segelstein. *The Complex Refractive Index of Water.* Ph.D. thesis, University of Missouri, Kansas City (1981).

[179] T. Sarna and H. Swartz. *The physical properties of melanins.* In J. J. Nordlund, R. E. Boissy, V. J. Hearing, R. A. King, and J.-P. Ortonne, eds., *The Pigmentary System*, pp. 333–357 (Oxford University Press, Oxford, 1998).

[180] R. S. Knox. *Dipole and oscillator strengths of chromophores in solution.* Photochemistry and Photobiology **77(5)**, 492 (2003).

[181] P. W. Atkins. *Molecular Quantum Mechanics* (Oxford University Press, New York, 1996), 3rd ed.

[182] D. Magde, R. Wong, and P. G. Seybold. *Fluorescence quantum yields and their relation to lifetimes of Rhodamine 6G and fluorescein in nine solvents: Improved absolute standards for quantum yields.* Photochemistry and Photobiology **75(4)**, 327 (2002).

[183] R. S. Knox. *Dipole strengths in chlorophyll-A and bacteriochlorophyll-A.* Proceedings of the 12th International Congress on Photosynthesis (2001).

[184] A. Bartczak, A. Dudkowiak, and D. Frackowiak. *Dipole strengths of the $q_y(0,0)$ bacteriochlorophyll C transition.* Photochemistry and Photobiology **78(5)**, 525528 (2003).

[185] L. Onsager. *Electric moments of molecules in liquids.* Journal of the American Chemical Society **58**, 1486 (1936).

[186] G. D. Mahan. *Many-Particle Physics* (Plenum Press, New York and London, 1990), 2nd ed.

[187] C. Bottcher. *Theory of electric polarization*, vol. 1 (Elsevier, Amsterdam, 1973).

[188] X. Zhang, C. Erb, J. Flammer, and W. M. Nau. *Absolute rate constants for the quenching of reactive excited states by melanin and related 5,6-dihydroxyindole metabolites: Implications for their antioxidant activity.* Photochemistry and Photobiology **71(5)**, 524 (2000).

[189] A. Tamulis, J. Tamuliene, M. L. Balevicius, Z. Rinkevicius, and V. Tamulis. *Quantum mechanical studies of intensity in electronic spectra of fluorescein dianion and monoanion forms.* Structural Chemistry **14(6)**, 643 (2003).

[190] M. Pederson, D. Porezag, J. Kortus, and D. Patton. *Strategies for massively parallel local-orbital-based electronic structure methods.* Physica status solidi (b) **217**, 197 (2000).

[191] M. R. Pederson and K. A. Jackson. *Variational mesh for quantum-mechanical simulations.* Physical Review B **41**, 7453 (1990).

[192] K. A. Jackson and M. R. Pederson. *Accurate forces in a local-orbital approach to the local-density approximation.* Physical Review B **42**, 3276 (1990).

[193] M. R. Pederson and K. A. Jackson. *Pseudoenergies for simulations on metallic systems.* Physical Review B **43(9)**, 7312 (1991).

[194] A. A. Quong, M. R. Pederson, and J. L. Feldman. *First principles determination of the interatomic force-constant tensor of the fullerene molecule.* Solid State Communications **87(6)**, 535 (1993).

[195] D. V. Porezag and M. R. Pederson. *Infrared intensities and Raman-scattering activities within density-functional theory.* Physical Review B **54(11)**, 7830 (1996).

[196] D. V. Porezag. *http://archiv.tuchemnitz.de/pub/1997/0025.* Ph.D. thesis, Technische Universitait (1997).

[197] A. Briley, M. R. Pederson, K. A. Jackson, D. C. Patton, and D. V. Porezag. *Vibrational frequencies and intensities of small molecules: All-electron, pseudopotential, and mixed-potential methodologies.* Physical Review B **58(4)**, 1786 (1998).

[198] J. P. Perdew, K. Burke, and M. Ernzerhof. *Generalized gradient approximation made simple.* Physical Review Letters **77(18)**, 3865 (1996).

[199] H. G. Kuhn. *Atomic Spectra*, p. 337 (Academic Press, New York, 1969), 2nd ed.

[200] G. D. Fasman. *Proteins*, vol. 1, pp. 183–203 (CRC Press, Cleveland, Ohio, 1976), 3rd ed.

[201] P. C. DeRose and G. W. Kramer. *Bias in the absorption coefficient determination of a fluorescent dye, standard reference material 1932 fluorescein solution.* Journal of Luminescence **113**, 314 (2005).

[202] H. Du, R.-C. A. Fuh, J. Li, L. A. Corkan, and J. S. Lindsey. *Photochemcad†† : A computer-aided design and research tool in photochemistry.* Photochemistry and Photobiology **68(2)**, 141 (1998).

[203] T. Sarna and H. M. Swartz. *The Physical Properties of Melanins* (Oxford University Press, New York, 1987).

[204] K. Wakamatsu and S. Ito. *Advanced chemical methods in melanin determination.* Pigment Cell Research **15**, 174 (2002).

[205] A. Nagy. *Density functional. theory and application to atoms and molecules.* Physics Reports - Review section of Physics Letters **298(1)**, 2 (1998).

[206] R. O. Jones and O. Gunnarsson. *The density functional formalism, its applications and prospects.* Reviews of Modern Physics **61**, 689 (1989).

[207] E. K. U. Gross, J. F. Dobson, and M. Petersilka. *Density Functional Theory* (Springer, Berlin, 1996).

[208] M. Petersilka, U. J. Gossmann, and E. K. U. Gross. *Excitation energies from time-dependent density-functional theory.* Physics Review Letters **76**, 1212 (1996).

[209] M. Pederson, T. Baruah, P. Allen, , and C. Schmidt. *Density-functional-based determination of vibrational polarizabilities in molecules within the double-harmonic approximation: Derivation and application.* Journal of Chemical Theory and Computation **1**, 590 (2005).

[210] J. R. Chelikowsky, L. Kronik, and I. Vasiliev. *Time-dependent density-functional calculations for the optical spectra of molecules, clusters, and nanocrystals.* Journal of Physics: Condensed Matter **15**, R1517 (2003).

[211] K. Yabana and G. F. Bertsch. *Time-dependent local-density approximation in real time: Application to conjugated molecules.* International Journal of Quantum Chemistry **75**, 55 (1999).

[212] *A Guide to Recording Fluorescence Quantum Yields.* Jobin Yvon Horiba, Stanmore, http://www.jobinyvon.co.uk (2007).

[213] K. Guzow, R. Ganzynkowicz, A. Rzeska, J. Mrozek, M. Szabelski, J. Karolczak, A. Liwo, and W. Wiczk. *Photophysical properties of tyrosine and its simple derivatives studied by time-resolved fluorescence spectroscopy, global analysis, and theoretical calculations.* Journal of Physical Chemistry B **108(12)**, 3879 (2004).

[214] W. H. Koch and M. R. Chedekel. *Photochemistry and photobiology of melanogenic metabolites: formation of free radicals.* Photochemistry and Photobiology **46(2)**, 229 (1987).

[215] M. T. Vala and S. A. Rice. *Solvent effects and a test of the theory of hypochromism.* Journal of Chemical Physics **39**, 2348 (1963).

[216] J. Kowal and D. Jamroz. *Hypochromy in polystyrene systems.* Makromolekulare Chemie **192(2)**, 461 (1991).

[217] J. Kowal. *Hypochromism of poly(N-vinylcarbazole).* Macomolecular Chemical Physics **196(4)**, 1195 (1995).

[218] I. Tinoco. *Hypochromism in polynucleotides.* Journal of the American Chemical Society **82**, 4785 (1960).

[219] C. R. Cantor and P. R. Schimmel. *Biophysical Chemistry Part II: Techniques for the study of biological structure and function*, p. 399 (Freeman, San Francisco, CA, 1980).

[220] H. Neuhacher and W. Lohmann. *Biophysics.* chap. 3.2.5, p. 106 (Springer, Berlin, 1983).

[221] F. Peral and E. Gallego. *Self-association of pyridine-2,6-dicarboxylic acid in aqueous solution as determined from ultraviolet hypochromic and hyperchromic effects.* Spectrochimica Acta Part A **56**, 2149 (2000).

[222] E. Dadachova, R. A. Bryan, X. Huang, T. Moadel, A. D. Schweitzer, P. Aisen, J. D. Nosanchuk, and A. Casadevall. *Ionizing radiation changes the electronic properties of melanin and enhances the growth of melanized fungi.* PLoS ONE **5**, e457 (2007).

[223] K. Stratton and M. Pathak. *Photoenhancement of the electron spin resonance signal from melanins.* Archives of Biochemistry and Biophysics **123**, 477 (1968).

[224] H. W. Sachs. *Uber die autogenen pigmente, besonders das lipfuscin und seine abrenzung von melanin.* Betir Pathol Anat **108**, 268 (1943).

[225] M. Boulton, F. Docchio, P. Dayhaw-Barker, R. Ramponi, and R. Cubeddu. *Age related changes in the morphology, absorption and fluorescence of melanosomes and lipfuscin granules of the retinal pigment epithelium.* Vision Research **30(9)**, 1291 (1990).

[226] T. S. Dintelmann, K. Heimann, P. Kayatz, and U. Schrayermeyer. *Comparative study of ROS degradation by IPE and RPE cells in vitro.* Graefe's archive for clinical and experimental ophthalmology **237**, 830 (1999).

[227] B. Falck, S. Jacobson, H. Olivercrona, and H. Rorsman. *Pigmented nevi and malignant melanomas as studied with a specific fluorescence method.* Science **149**, 439 (1965).

[228] D. Slawinska and J. Slawinski. *Electronically excited molecules in the function and degradation of melanins.* Physiological Chemical Physics **14**, 363 (1982).

[229] M. Elleder and J. Borovansky. *Autofluorescence of melanins induced by ultraviolet radiation and near ultraviolet light. A histochemical and biochemical study.* The Histochemical Journal **33**, 273 (2001).

[230] S. D. Kozikowski, L. J. Wolfram, and R. R. Alfano. *Fluorescence spectroscopy of eumelanins.* IEEE J. Quantum Electron **QE-20**, 1379 (1984).

[231] T. Ikejima and T. Takeuchi. *Fluorescence spectrophotometric analysis of melanins in the house mouse.* Biochemical Genetics **16(7/8)**, 673 (1978).

[232] J. Gallas and M. Eisner. *Fluorescence of melanin-dependence upon excitation wavelength and concentration.* Photochemistry and Photobiology **45(5)**, 595 (1987).

[233] L. Mosca, C. D. Marco, M. Fontana, and M. A. Rosei. *Fluorescence properties of melanins from opioid peptides.* Archives of Biochemistry and Biophysics **371(1)**, 63 (1999).

[234] K. Teuchner, W. Freyer, D. Leupold, A. Volkmer, D. J. S. Birch, P. Altmeyer, M. Stucker, and K. Hoffmann. *Femtosecond two-photon excited fluorescence of melanin.* Photochemistry and Photobiology **70(2)**, 146 (1999).

[235] K. Teuchner, J. Ehlert, W. Freyer, D. Leupold, P. Altmeyer, M. Stucker, and K. Hoffmann. *Fluorescence studies of melanin by stepwise two-photon femtosecond laser excitation.* Journal of Fluorescence **10(3)**, 275 (2000).

[236] J. D. Simon. *Spectroscopic and dynamic studies of the epidermal chromophores trans-urocanic acid and eumelanin.* Accounts of Chemical Research **33**, 307 (2000).

[237] P. Kayatz, G. Thumann, T. Luther, J. Jordan, K. Bartz-Schmidt, P. Esser, and U. Schraermeyer. *Oxidation causes melanin fluorescence.* Investigative Opthamology and Visual Science **41(1)**, 241 (2001).

[238] D. J. S. Birch, A. Ganesan, and J. Karolin. *Metabolic sensing using fluorescence.* Synthetic Metals **155**, 410 (2005).

[239] L. P. Korzhova, E. V. Frolova, Y. A. Romakov, and N. A. Kuznetsova. *The photoinduced destruction of DOPA melanin (in Russian).* Biokhimija **54**, 992 (1989).

[240] M. H. Rosenthal, J. W. Kreider, and R. Shiman. *Quantitative assay of melanin in melanoma cells in culture and in tumors.* Analytical Biochemistry **56**, 91 (1973).

[241] L. P. Korzhova, E. V. Frolova, and Y. A. Romakov. *Spectrofluorimetric procedure for registration of products developed after oxidative destruction of eumelanins (in russian).* Vopr Med Khim **35**, 139 (1989).

[242] S. P. Nighswander-Rempel, J. Riesz, J. Gilmore, J. P. Bothma, and P. Meredith. *Quantitative excitation spectra of synthetic eumelanin.* Journal of Physical Chemistry B **109**, 20629 (2005).

[243] T. Sarna, A. Duleba, W. Korytowski, and H. Swartz. *Interaction of melanin with oxygen.* Archives of Biochemistry and Biophysics **200(1)**, 140 (1980).

[244] T. Sarna and R. C. Sealy. *Photoinduced oxygen consumption in melanin systems. Action spectra and quantum yields for eumelanin and synthetic melanin.* Photochemistry and Photobiology **39(1)**, 69 (1984).

[245] J. R. Lakowicz. *Principles of Fluorescence Spectroscopy* (Kluwer Academic-Plenum Publishers, New York, 1999), 2nd ed.

[246] K. Adachi, K. Wakamatsu, S. Ito, N. Miyamoto, T. Kokubo, T. Nishioka, and T. Hirata. *An oxygen transporter hemocyanin can act on the late pathway of melanin synthesis.* Pigment Cell Research **18**, 214 (2005).

[247] J. N. Demas and G. A. Crosby. *Measurement of photoluminescence quantum yields.* Journal of Physical Chemistry **75**, 991 (1971).

[248] J. Butcher and S. Nighswander-Rempel. *University of Queensland.* Master's thesis, University of Queensland (2006).

[249] J. Hartleb and R. Arndt. *Cysteine and indole derivatives as markers for malignant melanoma.* Journal of Chromatography B **764**, 409 (2001).

[250] Z. Harsanyi, P. Post, J. Brinkmann, M. Chedekel, and R. Deibel. *Mutagenicity of melanin from human red hair.* Experientia **36**, 291 (1980).

[251] H. Hill and G. Hill. *UVA, pheomelanin and the carcinogenesis of melanoma.* Pigment Cell Research **13 (Suppl. 8)**, 140 (2000).

[252] M. R. Chedekel, P. W. Post, R. M. Deibel, and M. Kalus. *Photodestruction of phaeomelanin.* Photochemistry and Photobiology **26**, 651 (1977).

[253] M. R. Chedekel, S. K. Smith, P. W. Post, and D. L. Vessell. *Photodestruction of pheomelanin: role of oxygen.* Proceedings of the National Academy of Science, USA **75**, 5395 (1978).

[254] M. R. Chedekel, P. P. Agin, and R. M. Sayre. *Photochemistry of pheomelanin: action spectrum for superoxide production.* Photochemistry and Photobiology **31**, 553 (1980).

[255] S. Takeuchi, W. Zhang, K. Wakamatsu, S. Ito, V. Hearing, K. Kraemer, and D. Brash. *Melanin acts as a potent UVB photosensitizer to cause an atypical mode of cell death in murine skin.* PNAS **101(42)**, 15076 (2004).

[256] D. G. Sanderson and M. R. Chedekel. *Spin trapping of the superoxide radical by 4-(n-methylpyridinium)t-butyl nitrone.* Photochemistry and Photobiology **32**, 573 (1980).

[257] J. Bliss, D. Ford, A. Swerdlow, B. Armstrong, M. Cristofolini, J. Elwood, A. Green, E. Holly, T. Mack, R. Mackie, A. Osterlind, S. Walter, J. Peto, and D. Easton. *Risk of cutaneous melanoma associated with pigmentation characteristics and freckling: systematic overview of 10 case-control studies.* The International Melanoma Analysis Group (IMAGE), International Journal of Cancer **62**, 367 (1995).

[258] J. Elwood, S. Whitehead, J. Davison, M. Stewart, and M. Galt. *Malignant melanoma in England: Risks associated with naevi, freckles, social class, hair colour, and sunburn.* International Journal of Epidemiology **19**, 801 (1990).

[259] A. Hennessy, C. Oh, B. Diffey, K. Wakamatsu, S. Ito, and J. Rees. *Eumelanin and pheomelanin concentrations in human epidermis before and after UVB irradiation.* Pigment Cell Research **18**, 220 (2005).

[260] M. Vincensi, M. d'Ischia, A. Napolitano, E. Procaccini, G. Riccio, G. Monfrecola, P. Santonianni, and G. Prota. *Phaeomelanin versus eumelanin as a chemical indicator of ultraviolet sensitivity in fair-skinned subjects at high risk for melanoma: a pilot study.* Melanoma Research **8**, 53 (1998).

[261] A. Losi, R. Bedotti, L. Brancaleon, and C. Viappiani. *Porphyrin-melanin interaction: effect on fluorescence and non-radiative relaxations.* Journal of Photochemistry and Photobiology B: Biology **21(1)**, 69 (1993).

[262] W. D. Bush, J. Garguilo, F. A. Zucca, A. Albertini, L. Zecca, G. S. Edwards, R. J. Nemanich, and J. D. Simon. *The surface oxidation potential of human neuromelanin reveals a spherical architecture with a pheomelanin core and a eumelanin surface.* Proceedings of the National Academy of Sciences of the United States of America **103 (40)**, 14785 (2006).

[263] S. Ito and K. Jimbow. *Quantitative analysis of eumelanin and pheomelanin in hair and melanomas.* The Journal of Investigative Dermatology **80**, 268 (1983).

[264] R. H. Thomson. *The pigments of reddish hair and feathers.* Angewandte Chemie, International Edition, English **13**, 305 (1974).

[265] A. Napolitano, S. Memoli, O. Crescenzi, and G. Prota. *Oxidative polymerization of the pheomelanin precursor 5-hydroxy-1,4-benzothiazinylalanine: A new hint to the pigment structure.* Journal of Organic Chemistry **61(2)**, 598 (1996).

[266] C. Costantini, O. Crescenzi, G. Prota, and A. Palumbo. *New intermediates of pheomelanogenesis in vitro beyond the 1,4-benzothiazine stage.* Tetrahedron **46**, 6831 (1990).

[267] P. D. Donato and A. Napolitano. *1,4-benzothiazines as key intermediates in the biosynthesis of red hair pigment pheomelanins.* Pigment Cell Research **16**, 532 (2003).

[268] P. D. Donato, A. Napolitano, and G. Prota. *Isolation and structural characterisation of pheomelanins from red human hair.* Pigment Cell Research (Proc. 9th ESPCR Meething, Ulm) **13**, 404 (2000).

[269] R. Deibel and M. Chedekel. *Biosynthetic and structural studies on pheomelanin.* Journal of the American Chemical Society **104**, 7306 (1982).

[270] R. M. B. Deibel and M. R. Chedekel. *Biosynthetic and structural studies on pheomelanin. 2.* Journal of the American Chemical Society **106**, 5884 (1984).

[271] M. Chedekel, K. Subbarao, P. Bhan, and T. Schultz. *Biosynthetic and structural studies on pheomelanin.* Biochimica et Biophysica Acta **912**, 239 (1987).

[272] D. Slawinska, J. Slawinski, and M. R. Chedekel. *Chemiluminescent monitoring of oxidative damage during the extraction of pheomelanin.* XII International Pigment Cell Conference Abstracts **57(3)**, 418 (1984).

[273] H. Olivecrona and H. Rorsman. *Specific fluorescence in guinea-pig melanocytes.* Acta Dermato-venereologica **46**, 497 (1966).

[274] T. Ye and J. Simon. *Ultrafast spectroscopic study of pheomelanin: implications on the mechanism of superoxide anion formation.* Journal of Physical Chemistry B **106**, 6133 (2002).

[275] T. Ye, J. Simon, and T. Sarna. *Ultrafast energy transfer from bound tetra(4-N,N,N,N-trimethylanilinium)porphyrin to synthetic DOPA and cysteinyldopa melanins.* Photochemistry and Photobiology **77(1)**, 1 (2003).

[276] T. Ye and J. Simon. *Comparison of the ultrafast absorption dynamics of eumelanin and pheomelanin.* Journal of Physical Chemistry B **107**, 11240 (2003).

[277] T. Ye and J. Simon. *The action spectrum for generation of the primary intermediate revealed by ultrafast absorption spectroscopy studies of pheomelanin.* Photochemistry and Photobiology **77(1)**, 41 (2003).

[278] H. Ozeki, S. Ito, K. Wakamatsu, and A. Thody. *Spectrophotometric characterization of eumelanin and pheomelanin in hair.* Pigment Cell Research **9**, 265 (1996).

[279] S. Ito. *Optimization of conditions for preparing synthetic pheomelanin.* Pigment Cell Research **2**, 53 (1989).

[280] M. Rozanowska, T. Sarna, E. Land, and T. Truscott. *Free radical scavenging properties of melanin: Interaction of eu- and pheo-melanin models with reducing and oxidising radicals.* Free Radical Biology and Medicine **26(5-6)**, 518 (1999).

[281] S. Schmitz, P. D. Thomas, T. M. Allen, M. J. Poznansky, and K. Jimbow. *Dual role of melanins and melanin precursors as photoprotective and phototoxic agents: inhibition of ultraviolet radiation-induced lipid peroxidation.* Photochemistry and Photobiology **61**, 650 (1995).

[282] G. Prota. *Pigment cell research: what directions?* Pigment Cell Research **10**, 5 (1997).

[283] G. Prota and G. Misuraca. *Melanin-related metabolites: a new look at their functional role.* In Y. Hori, V. F. Hearing, and F. Nakayama, eds., *Melanogenesis and Malignant Melanoma: Biochemistry, cell biology, molecular biology, pathophysiology, diagnosis and treatment*, pp. 49–61 (Elsevier, Amsterdam, 1996).

[284] W. H. Koch and M. R. Chedekel. *Photoinitiated DNA damage by melanogenic intermediates in vitro.* Photochemistry and Photobiology **44**, 703 (1986).

[285] C. Costantini, M. d'Ischia, A. Palumbo, and G. Prota. *Photochemistry of 5-S-cysteinyldopa.* Photochemistry and Photobiology **60**, 33 (1994).

[286] J. M. Pawelek and A. B. Lerner. *5,6-dihydroxyindole is a melanin precursor showing potent cytotoxicity.* Nature **276**, 627 (1978).

[287] C. Kipp and A. R. Young. *The soluble eumelanin precursor 5,6-dihydroxyindole-2-carboxylic acid enhances oxidative damage in human kerationocyte DNA after UVA irradiation.* Photochemistry and Photobiology **70(2)**, 191 (1999).

[288] C. Routaboul, C. L. Serpentini, P. Msika, J. P. Cesarini, and N. Paillous. *Photosensitization of supercoiled DNA damage by 5,6-dihydroxyindole-2-carboxylic acid, a precursor of eumelanin.* Photochemistry and Photobiology **62(3)**, 469 (1995).

[289] F. D'Acquisto, R. Carnuccio, M. d'Ischia, and G. Miscuraca. *5,6-dihydroxyindole-2-carboxylic acid, a diffusible melanin precursor, is a potent stimulator of lipopolysaccharide-induced production of nitric oxide by J774 macrophages.* Pharmacology Letters, Life Sciences **57(26)**, 401 (1995).

[290] B. P. Murphy and T. M. Schultz. *Synthesis and physical properties of 5,6-dihydroxyindole.* Journal of Organic Chemistry **50**, 2790 (1985).

[291] M. D'Ischia, A. Plumbo, and G. Prota. *5,6-dihydroxyindole-2-carboxylic acid by treatment of sepiomelanin with sodium borohydride.* Tetrahedron Letters **26(23)**, 2801 (1985).

[292] L. K. Charkoudian and K. J. Franz. *Fe(III)-coordination properties of neuromelanin components: 5,6-dihydroxyindole and 5,6-dihydroxyindole-2-carboxylic acid.* Inorganic Chemistry **45**, 3657 (2006).

[293] A. Onufriev, D. A. Case, and G. M. Ullman. *A novel view of pH titration in biomolecules.* Biochemistry **40(12)**, 3414 (2001).

[294] A. L. Sobolewski and W. Domcke. *Photophysics of eumelanin: ab initio studies on the electronic spectroscopy and photochemisry of 5,6-dihydroxyindole.* Chemphyschem **8**, 756 (2007).

[295] O. Crecenzi, M. D'Ischia, A. Napolitano, and G. Prota. *The alleged stability of DOPA-melanins revisited.* Gazzetta Chimica Italiana **123**, 241 (1993).

[296] A. Wilczek, H. Kondoh, and Y. Mishima. *Composition of mammalian eumelanins: Analysis of DHICA-derived units in pigments from hair and melanoma cells.* Pigment Cell Research **9**, 63 (1996).

[297] H. Okuda, A. Nakamura, K. Wakamatsu, S. Ito, and T. Sota. *Mid-infrared absorption spectrum of 5,6-dihydroxyindole-2-carboxylic acid.* Chemical Physics Letters **433**, 355 (2007).

[298] A. J. Nappi and E. Vass. *Hydrogen peroxide generation associated with the oxidations of the eumelanin precursors 5,6-dihydroxyindole and 5,6-dihydroxyindole-2-carboxylic acid.* Melanoma Research **6**, 341 (1996).

[299] K. Wakamatsu and S. Ito. *Preparation of eumelanin-related metabolites 5,6-dihydroxyindole, 5,6-dihydroxyindole-2-carboxylic acid, and their O-methyl derivatives.* Analytical Biochemistry **170**, 335 (1988).

[300] D. D. Perrin and W. L. F. Armarego. *The purification of laboratory chemicals.* Pergamon Press, Sydney **3rd Ed.**, 52 (1988).

[301] W. H. Melhuish. *Quantum efficiencies of fluorescence of organic substances: Effect of solvent and concentration of the fluorescence solute.* Journal of Physical Chemistry **65**, 229 (1961).

[302] L. E. Arnow. *The formation of DOPA by the exposure of tyrosine solutions to ultraviolet radiation.* The Journal of Biological Chemistry **120**, 151 (1937).

[303] M. R. Chedekel, E. J. Land, A. Thompson, and T. G. Truscott. *Early steps in the free radical polymerisation of 3,4-dihydroxyphenylanaline (DOPA) into melanin.* Journal of the Chemical Society, Chemical Communications **770**, 1170 (1984).

[304] J. McGinness and P. Proctor. *The importance of the fact that melanin is black.* Journal of Theoretical Biology **39**, 677 (1973).

[305] P. R. Crippa and C. Viappiani. *Photoacoustic studies of non-radiative relaxation of excited states in melanin.* European Biophysical Journal **17**, 299 (1990).

[306] C. C. Felix, J. S. Hyde, and R. C. Sealy. *Photoreactions of melanin: a new transient species and evidence for triplet state involvement.* Biochemical and Biophysical Research Communications **88(2)**, 456 (1979).

[307] M. G. Bridelli, D. Tampellini, and L. Zecca. *The structure of neuromelanin and its iron binding site studied by infrared spectroscopy.* FEBS Letters **457**, 18 (1999).

[308] J. A. Pierce and D. M. Rast. *Permanganate degradation of a fungal melanin and characterization of the decomposition products by infrared spectrometry.* Physiological chemistry and physics and medical NMR **23**, 161 (1991).

[309] J. A. Pierce and D. M. Rast. *A comparison of native and synthetic mushroom melanins by fourier-transform infrared spectroscopy.* Phytochemistry **39(1)**, 49 (1995).

[310] J. D. Russell, D. Jones, D. Vaughan, and A. R. Fraser. *A preliminary study of fungal melanin by infrared spectroscopy.* Geoderma **24**, 207 (1980).

[311] R. C. Gomes, A. S. Mangrich, R. R. R. Coelho, and L. F. Linhares. *Elemental, functional group and infrared spectroscopic analysis of actinomycete melanins from brazilian soils.* Biol Fertil Soils **21**, 84 (1996).

[312] J. A. Pierce-Liebisch. *Diffuse reflectance infrared spectrometry of base solubilized fungal melanin.* Physiological chemistry and physics and medical NMR **21**, 81 (1989).

[313] T. M. Cooper, D. L. Bolton, S. T. Schuscherba, and E. T. Schmeisser. *Spectroscopic studies of melanin.* Environment Information Division, Air Training Command, Maxwell Air Force Base, AL. Report LAIR-215 **Order No. AD-A 168242/6/GAR23** (1986).

[314] L. K. Panina, N. F. Kartenko, Y. A. Kumzerov, and M. F. Limonov. *Comparative study of the spatial organization of biological carbon nanostructures and fullerene-related carbon.* Molecular crystals and liquid crystals science technology, Section C. Molecular materials **11**, 117 (1998).

[315] R. J. Wegmann. *Melanins: an old problem revisited, or, the usefulness of infrared spectroscopy.* Cell Molecular Biology **45(7)**, 895 (1999).

[316] B. Bilinska. *On the structure of human hair melanins from an infrared spectroscopy analysis of their interactions with Cu^{2+} ions.* Spectrochimica Acta Part A **57**, 2525 (2001).

[317] Z. Huang, H. Lui, X. K. Chen, A. Alajlan, D. I. McLean, and H. Zeng. *Raman spectroscopy of in vivo cutaneous melanin.* Journal of Biomedical Optics **9(6)**, 1198 (2004).

[318] P. C. H. Mitchell, S. F. Parker, A. J. Ramirez-Cuesta, and J. Tomkinson. *Vibrational spectroscopy with neutrons.* World Scientific Press, Singapore (2005).

[319] J. Tomkinson, S. Parker, J. Riesz, and P. Meredith. *The vibrational spectrum of indole: an inelastic neutron scattering study.* J. Biomolecular Structure and Dynamics (2007).

[320] A. K. Singh and D. Prakash. *Studies of some metal complexes with heterocyclic base - I. Coordination compounds of Fe(III), Cu(II), Hg(II), Pb(II) and Ag(I) with indole-2-carboxylic acid.* Journal of Inorganic Nuclear Chemistry **40**, 579 (1977).

[321] V. Viossat, P. Lemoine, E. Dayan, N. Dung, and B. Viossat. *Synthesis, crystal structures and IR spectra of isotypic pseudopolymorphs complexes of Zn(II) by indole-2-carboxylic acid and 2,9-dimethyl-1,10-phenanthroline with different solvates (DMA, DMF or DMSO).* Journal of Molecular Structure **741**, 45 (2005).

[322] M. Rele, S. Kapoor, S. Hegde, S. Naumov, and T. Mukherjee. *Photophysical characteristics and density functional theory calculations of indole-2-carboxylic acid in the presence of mercurous ions.* Res. Chem. Intermed. **32(7)**, 637 (2006).

[323] I. Ahmed. *Spectral and thermal studies of divalent transition metal complexes with indole-2-carboxylic acid and 4-substituted hydrazienthiocarbamide.* Spectrochimica Acta Part A **63**, 416 (2006).

[324] I. Ahmed. *Spectral and thermal studies of divalent transition metal with indole-2-carboxylic acid and 4-substituted hydrazienthiocarbamide.* Spectrochimica Acta Part A **65**, 5 (2006).

[325] A. Tine, P. Guillaume, A. Massat, and J. Aaron. *Infrared study of indolecarboxylic acids associations with lanthanide acetates.* Spectrochimica Acta A **54**, 1451 (1998).

[326] B. Morzyk-Ociepa, D. Michalska, and A. Pietraszko. *Structures and vibrational spectra of indole carboxylic acids. part I. Indole-2-carboxylic acid.* Journal of Molecular Science **688**, 79 (2004).

[327] D. Colognesi, M. Celli, F. Cilloco, R. J. Newport, S. F. Parker, V. Rossi-Albertini, F. Sacchetti, J. Tomkinson, and M. Zoppi. *Tosca neutron spectrometer: The final configuration.* Applied Physics A: Materials Science and Processing, Supplement **74**, S64 (2002).

[328] M. J. Frisch, G. Trucks, H. Schlegel, G. Scuseria, M. Robb, J. Cheeseman, V. Zakrzewski, J. M. Jr., R. Stratmann, J. Burant, S. Dapprich, J. Millam, A. Daniels, K. Kudin, M. Strain, O. Farkas, J. Tomasi, V. Barone, M. Cossi, R. Cammi, B. Mennucci, C. Pomelli, C. Adamo, S. Clifford, J. Ochterski, G. Petersson, P. Ayala, Q. Cui, K. Morokuma, D. Malick, A. Rabuck, K. Raghavachari, J. Foresman, J. Cioslowski, J. Ortiz, B. Stefanov, G. Liu, A. Liashenko, P. Piskorz, I. Komaromi, R. Gomperts, R. Martin, D. Fox, T. Keith, M. Al-Laham, C. Peng, A. Nanayakkara, C. Gonzalez, M. Challacombe, P. Gill, B. Johnson, W. Chen, M. Wong, J. Andres, C. Gonzalez, M. Head-Gordon, E. Replogle, and J. Pople. *GAUSSIAN98*, vol. Revision A.3 (Gaussian Inc., Pittsburgh, 1998).

[329] D. Porezag and M. R. Pederson. *Optimization of gaussian basis sets for density-functional calculations.* Physical Review A **60(4)**, 2840 (1999).

[330] D. C. Patton and M. R. Pederson. *Application of the generalized-gradient approximation to rare-gas dimers.* Physical Review A **56**, R2496 (1997).

[331] A. J. Ramirez-Cuesta. *aClimax 4.0.1, the new version of the software for analyzing and interpreting ins spectra.* Computational Physics Communcations **157**, 226 (2004).

[332] A. K. Grafton and R. A. Wheeler. *ViPA: A computer program for vector projection analysis of normal vibrational modes of molecules.* Computer Physics Communications **113**, 78 (1998).

[333] S. A. Green and N. V. Blough. *Optical absorption and fluorescence properties of chromophoric dissolved organic matter in natural waters.* Limnology and Oceanography **39(8)**, 1903 (1994).

[334] N. V. Blough and S. A. Green. In R. G. Zepp and C. Sonntag, eds., *The role of nonliving organic matter in the earth's carbon cycle*, pp. 23–45 (John Wiley and Sons, Chinchester, 1995).

[335] T. Miano, G. Sposito, and J. P. Martin. *Fluorescence spectroscopy of model humic acid type polymers.* Geoderma **47**, 349 (1990).

[336] R. D. Vecchio and N. V. Blough. *On the origin of the optical properties of humic substances.* Environmental Science and Technology **38**, 3885 (2004).

[337] O. B. Popovicheva, N. M. Persiantseva, B. V. Kuzentsov, T. A. Rakhmanova, N. K. Shonija, J. Suzanne, and D. Ferry. *Microstructure and water adsorbability of aircraft combustor soots and kerosene flame soots: toward an aircraft-generated soot laboratory surrogate.* Journal of Physical Chemistry B **107**, 10046 (2003).

[338] R. L. V. Wal. *Soot precursor carbonization: visualization using LIF and LII and comparison using bright and dark field TEM.* Combust. Flame **112(4)**, 607 (1998).

[339] D. C. Siegla and G. W. Smith. *Particulate carbon* (Plenum, New York, 1981).

[340] H. B. Palmer and C. F. Cullins. In P. L. Walker, ed., *The chemistry and physics of carbon*, vol. 1, p. 265 (Dekker, New York, 1965).

[341] R. L. V. Wal, A. J. Tomasek, M. I. Pamphlet, C. D. Taylor, and W. K. Thompson. *Analysis of HRTEM images for carbon nanostructure quantification.* Journal of Nanoparticle Research **6**, 555 (2004).

[342] D. S. Su, R. E. Jentoft, J. O. Muller, D. Rothe, E. Jacob, C. D. Simpson, Z. Tomovic, K. Mullen, A. Messerer, U. Poschl, R. Niessner, and R. Schlogl. *Microstructure and oxidation behaviour of Euro IV diesel engine soot: a comparative study with synthetic model soot substances.* Catalysis Today **90**, 127 (2004).

[343] M. Wentzel, H. Gorzawski, K. H. Naumann, H. Saathoff, and S. Weinbruch. *Transmission electron microscopical and aerosol dynamical characterization of soot aerosols.* Journal of Aerosol Science **34**, 1347 (2003).

[344] D. C. Green, D. R. McKenzie, and P. B. Lukins. In J. J. Pouch and S. A. Alterovitz, eds., *Properties and characterisation of amorphous carbon films*, vol. 52 and 53 (Transactions Technical Publications, Zurich, 1990).

[345] C. Jager, T. Henning, R. Schlogl, and O. Spillecke. *Spectral properties of carbon black.* Journal of Non-crystalline Solids **258**, 161 (1999).

[346] J. Robertson and E. P. O'Reilly. *Electronic and atomic structure of amorphous carbon.* Physical Review B **35**, 2946 (1987).

[347] B. Michel, T. Henning, C. Jager, and U. Kreibig. *Optical extinction by spherical carbonaceous particles.* Carbon **37**, 391 (1999).

[348] K. Y, T. Sato, and C. Kaito. *Production and structural characterization of carbon soot with narrow UV absorption feature.* Carbon **42**, 33 (2004).

[349] S. di Stasio and A. Braun. *Comparative NEXAFS study on soot obtained from an ethylene/air flame, a diesel engine, and graphite.* Energy and Fuels **20**, 187 (2006).

[350] F. Rouleau, T. Henning, and R. Stognienko. *Constraints on the properties of the 2175å interstellar feature carrier.* Astronomy and Astrophysics **322**, 633 (1997).

[351] M. Schnaiter, H. Mutschke, J. Dorschner, T. Henning, and F. Salama. *Matrix-isolated nano-sized carbon grains as an analog for the 217.5 nm feature carrier.* Astrophysics Journal **498**, 486 (1998).

[352] C. F. Bohren and D. R. Huffman. *Absorption and scattering of light* (Wiley, New York, 1983).

[353] A. J. Braun. *Carbon speciation in airborne particulate matter with C (1s) NEXAFS spectroscopy.* Journal of Environmental Monitoring **7**, 1059 (2005).

[354] J. Robertson. *Amorphous carbon.* Advances in Physics **35(4)**, 317 (1986).

[355] K. S. Burnham, R. Roth, F. Zhou, W. Fan, E. Brouk, and M. Stifanos. *Dimensionally and thermally stable polymer, containing disordered graphitic structure and adamantane.* Journal of Polymer Science: Part A: Polymer Chemistry **44**, 6909 (2006).

[356] M. A. Valente, L. C. Costa, S. K. Mendiratta, F. Henry, and L. Ramanitra. *Structural and electrical properties of polystyrene-carbon composites.* Solid State Communications **112**, 67 (1999).

[357] A. P. Roberts. *Cross-property correlations for disordered materials.* Colloids and Surfaces, A. Physicochemical and Engineering Aspects **129–130**, 377 (1997).

[358] M. Kaszuba and M. T. Connah. *Protein and nanoparticle characterisation using light scattering techniques.* Particle And Particle Systems Characterization **23**, 193 (2006).

[359] M. Medebach, C. Moitzi, N. Freiberger, and O. Glatter. *Dynamic light scattering in turbid colloidal dispersions: a comparison between modified flat-cell light-scattering instrument and 3d dynamic light-scattering instrument.* Journal of Colloid and Interface Science **305**, 88 (2007).

[360] A. Laisaar and J. Kikas. *Persistent spectral hole-burning in doped organic crystals and polymers at high hydrostatic pressures.* Journal of Luminescence **72–74**, 515 (1997).

[361] Y. V. Romanovskii and H. Bassler. *Spectral hole burning in conjugated organic polymers.* Journal of Luminescence **113**, 156 (2005).

[362] A. Tilgner, H. P. Trommsdorff, J. M. Zeigler, and R. M. Hochstrasser. *Poly(di-n-hexylsilane) in solid solutions: Experimental and theoretical studies of electronic excitations of a disordered linear chain.* Journal of Chemical Physics **96**, 781 (1992).

[363] M. Ratsep, H. M. Wu, J. M. Hayes, R. E. Blankenship, R. J. Cogdell, and G. J. Small. *Stark hole-hurning studies of three photosynthetic complexes.* Journal of Physical Chemistry B **102**, 4035 (1998).

[364] A. B. Myers. *Molecular electronic spectral broadening in liquids and glasses.* Annual Reviews in Physical Chemistry **49**, 267 (1998).

[365] H. Riesen. *Hole-burning spectroscopy of coordination compounds.* Coordination chemistry reviews **250**, 1737 (2006).